frontiers | Research Topics

Simultaneous multiparametric and multidimensional cardiovascular magnetic resonance imaging

Edited by
Aleksandra Radjenovic and Anthony G. Christodoulou

Published in
Frontiers in Cardiovascular Medicine

ISSN 1664-8714
ISBN 978-2-8325-2743-6
DOI 10.3389/978-2-8325-2743-6

About Frontiers

Frontiers is more than just an open access publisher of scholarly articles: it is a pioneering approach to the world of academia, radically improving the way scholarly research is managed. The grand vision of Frontiers is a world where all people have an equal opportunity to seek, share and generate knowledge. Frontiers provides immediate and permanent online open access to all its publications, but this alone is not enough to realize our grand goals.

Frontiers journal series

The Frontiers journal series is a multi-tier and interdisciplinary set of open-access, online journals, promising a paradigm shift from the current review, selection and dissemination processes in academic publishing. All Frontiers journals are driven by researchers for researchers; therefore, they constitute a service to the scholarly community. At the same time, the *Frontiers journal series* operates on a revolutionary invention, the tiered publishing system, initially addressing specific communities of scholars, and gradually climbing up to broader public understanding, thus serving the interests of the lay society, too.

Dedication to quality

Each Frontiers article is a landmark of the highest quality, thanks to genuinely collaborative interactions between authors and review editors, who include some of the world's best academicians. Research must be certified by peers before entering a stream of knowledge that may eventually reach the public - and shape society; therefore, Frontiers only applies the most rigorous and unbiased reviews. Frontiers revolutionizes research publishing by freely delivering the most outstanding research, evaluated with no bias from both the academic and social point of view. By applying the most advanced information technologies, Frontiers is catapulting scholarly publishing into a new generation.

What are Frontiers Research Topics?

Frontiers Research Topics are very popular trademarks of the *Frontiers journals series*: they are collections of at least ten articles, all centered on a particular subject. With their unique mix of varied contributions from Original Research to Review Articles, Frontiers Research Topics unify the most influential researchers, the latest key findings and historical advances in a hot research area.

Find out more on how to host your own Frontiers Research Topic or contribute to one as an author by contacting the Frontiers editorial office: frontiersin.org/about/contact

Simultaneous multiparametric and multidimensional cardiovascular magnetic resonance imaging

Topic editors

Aleksandra Radjenovic — University of Glasgow, United Kingdom

Anthony G. Christodoulou — Cedars Sinai Medical Center, United States

Citation

Radjenovic, A., Christodoulou, A. G., eds. (2023). *Simultaneous multiparametric and multidimensional cardiovascular magnetic resonance imaging*. Lausanne: Frontiers Media SA. doi: 10.3389/978-2-8325-2743-6

The authors declare that the research was conducted in the absence of any commercial or financial relationships that could be construed as a potential conflict of interest

Table of contents

frontiers | Frontiers in Cardiovascular Medicine

TYPE Editorial
PUBLISHED 05 June 2023
DOI 10.3389/fcvm.2023.1205994

OPEN ACCESS

EDITED AND REVIEWED BY
Ruud B. van Heeswijk,
Centre Hospitalier Universitaire Vaudois (CHUV), Switzerland

*CORRESPONDENCE
Aleksandra Radjenovic
aleksandra.radjenovic@glasgow.ac.uk

RECEIVED 14 April 2023
ACCEPTED 17 May 2023
PUBLISHED 05 June 2023

CITATION
Radjenovic A and Christodoulou AG (2023) Editorial: Simultaneous multiparametric and multidimensional cardiovascular magnetic resonance imaging.
Front. Cardiovasc. Med. 10:1205994.
doi: 10.3389/fcvm.2023.1205994

Editorial: Simultaneous multiparametric and multidimensional cardiovascular magnetic resonance imaging

Aleksandra Radjenovic[1]* and Anthony G. Christodoulou[2]

[1]School of Cardiovascular & Metabolic Health, University of Glasgow, Glasgow, United Kingdom, [2]Biomedical Imaging Research Institute, Cedars-Sinai Medical Center, Los Angeles, CA, United States

KEYWORDS

magnetic resonance imaging (MRI), heart imaging, cardiac magnetic resonance (CMR), multiparametric imaging, quantitative imaging, SMART CMR, cardiovascular imaging, artificial intelligence-AI

Editorial on the Research Topic
Simultaneous multiparametric and multidimensional cardiovascular magnetic resonance imaging

Multiparametric quantitative cardiovascular magnetic resonance (CMR) imaging is a powerful tool for evaluating myocardial morphology, function, and tissue status. It provides objective, reproducible measurements appropriate for diagnosing and longitudinally monitoring both focal and diffuse cardiovascular diseases. CMR has unparalleled flexibility: it is sensitive to a wide range of physical and physiological processes such as motion, T1 and T2 relaxation (biomarkers for e.g., fibrosis, edema, and inflammation), blood flow, diffusion, and more. However, the multiparameter sensitivity of CMR is also its weakness, as sequentially targeting each of these individual processes requires an inefficient combination of electrocardiogram (ECG) triggering, respiratory control, and precise pulse sequence timing. This complicated, disjointed imaging paradigm has limited the adoption of multiparametric quantitative CMR to only specialized imaging centers, preventing it from reaching its full potential.

In this article collection, we showcase the results of ongoing research in Simultaneous Multiparameter Acquisition and Reconstruction Techniques (SMART) for CMR (1), which will facilitate the transition from the current sequential MR imaging model into a new, single push-button MRI model. This new model is capable of simultaneously capturing multiple types of contrast and quantitative maps of tissue properties from one comprehensive, continuous dataset (**Figure 1**).

This transition is analogous to moving from sequential "single color" imaging to simultaneous "prismatic" imaging. It has the potential to revolutionize all branches of diagnostic MRI, but its impact will undoubtedly be most profound in the cardiovascular domain. Here, it can eliminate the need for respiratory or ECG triggering or gating, making CMR accessible to patient groups who currently cannot benefit from its full diagnostic potential.

So far, multidimensionality has been used to achieve a better workflow with equivalent results. This in itself can increase access to CMR for patients suffering from various types of arrhythmia, breathing difficulties, and in low- to middle-income countries where

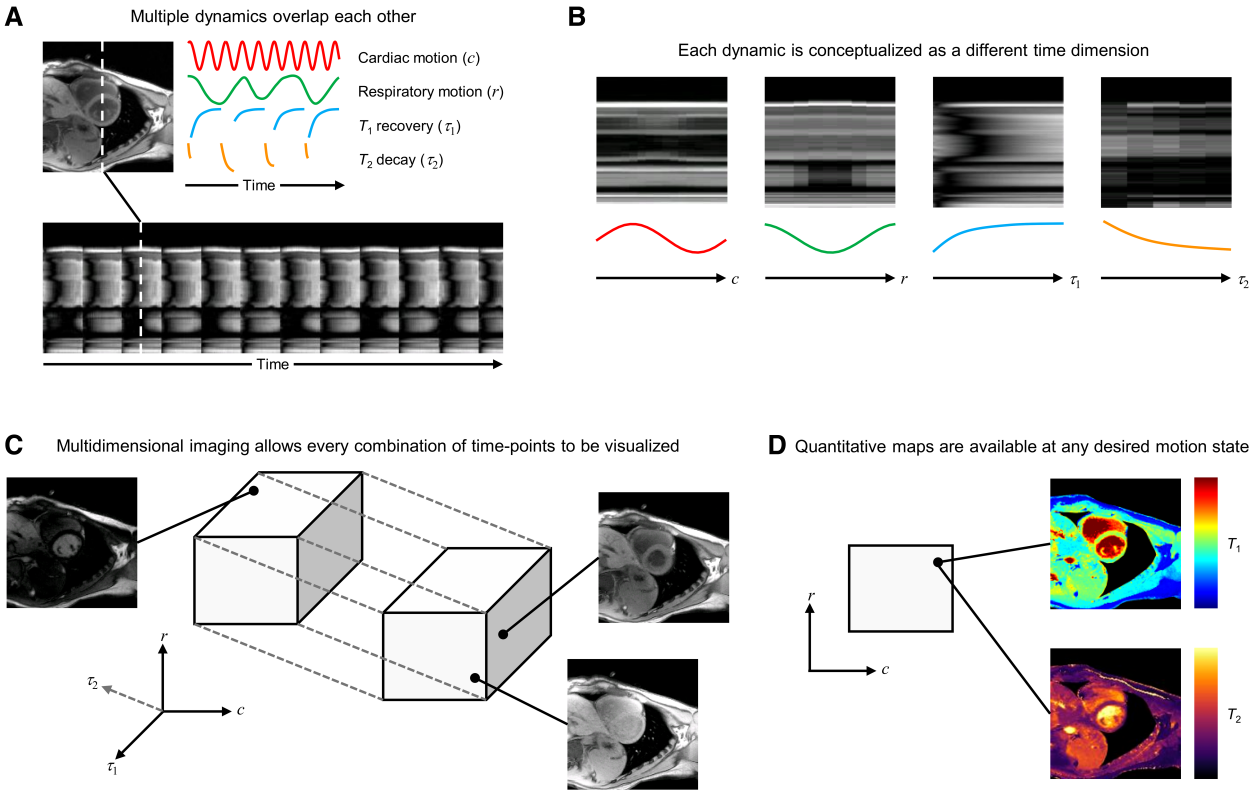

FIGURE 1
Multidimensional imaging example. (A) Continuous data acquisition without electrocardiography (ECG) triggering during free-breathing results in overlapped cardiovascular dynamics. This example shows cardiac motion, respiratory motion, T1 recovery, and T2 decay. (B) Multidimensional approaches consider each dynamic as a separate time dimension, disentangling the different dynamics. (C,D), The resulting multidimensional dataset enables the visualization of arbitrary combinations of time points (C) and can provide co-registered quantitative maps for each cardiac or respiratory motion state (D). Figure adapted from Otazo 2018 (2).

technologist training is a burden or scanner throughput is at a premium due to scarce imaging resources. Looking even farther ahead: in addition to improving workflow and access, multidimensional imaging may provide additional value through novel time-resolved quantification and study of interactions between dimensions. Furthermore, the rich multiparametric information in multidimensional CMR images is spatiotemporally co-registered, and therefore ready-made for the development of artificial intelligence tools for diagnosis, risk prediction, therapy monitoring and more.

Another advantage of SMART CMR is its potential to address the issue of reproducibility, another significant barrier to wide adoption for quantitative mapping techniques. Although quantitative maps are ideally absolute biomarkers, differences in cut-off values for healthy and pathological tissues exist across imaging centers. This inconsistency stems from factors like incomplete modeling and variable segmentation, limiting the adoption of these techniques by those not directly involved in their development (Ogier et al.). SMART CMR can potentially improve reproducibility in several ways. For instance, it can provide standardized timing not reliant on patients' ECG signals, use co-registered parameter maps to improve region drawing and segmentation, and employ multiparameter mapping to model confounding factors that affect repeatability, such as B1 + and magnetization transfer. These improvements may lead to more consistent results across imaging centers, ultimately enhancing the clinical utility of these techniques.

This collection of articles contains reports on existing research that is already producing tangible, peer-reviewed scientific results in this emerging field while also offering a projection of what lies in the future, just beyond the horizon.

An overview of simultaneous multiparametric acquisition and reconstruction techniques (SMART) in CMR was provided by Eyre et al. They discuss the theory of SMART CMR, its clinical testing, validation, and examples of how it improves clinical workflows. A further policy and practices review by Fotaki and Velasco et al. (2) highlights the cardiac–liver axis, discussing quantitative MRI methods for non-invasive myocardial and liver tissue characterization in cardiometabolic diseases. It covers current approaches, technical developments, limitations, challenges, and recommendations for clinical validation.

In the realm of cardiac MR fingerprinting (MRF) (3, 4), Hamilton presents deep image prior MRF, a novel reconstruction approach that shortens breathhold and diastolic acquisition window in cardiac MRF, thereby improving scan efficiency and reducing motion artifacts. Liu et al. extend cardiac MRF to simultaneous T1, T2, and proton density fat fraction mapping in the heart through the use of rosette k-space trajectories.

Velasco and Fletcher et al. review the latest developments in applying artificial intelligence (AI) to cardiac MRF, discussing how AI optimizes sequences, reduces memory demand, and minimizes computational time for image reconstruction and post-processing.

Expanding the MR Multitasking framework (5), Mao et al. present a simultaneous multi-slice (SMS) technique for motion-resolved, non-ECG, free-breathing T1-T2 mapping, demonstrating its potential for reducing three-slice mapping time without ECG or breath-holds. Building on the TOPAZ technique (6), Weingartner et al. introduce a three-step approach for cardiac phase-resolved LGE imaging, allowing assessment of scar motility and cross-comparison between multiple phases, overcoming limitations of single-phase LGE techniques. Moving to clinical validation, Jarkman et al. evaluate the Multimapping framework (7) for simultaneous myocardial T1 and T2 mapping in patients with a range of cardiovascular diseases, showing high correlation with reference techniques and better image quality in a short breath-hold.

Finally, Axel et al. discuss challenges and opportunities in visualizing and analyzing multidimensional cardiovascular magnetic resonance imaging data, addressing new computational methods, limitations of human perception, and conventional display devices. They suggest that significant breakthroughs in this field may result from exploiting advances in other areas of applied science and technology, such as hyperspectral remote sensing of environment or astronomy.

The articles in this collection present a convincing case that the transition to continuous, multiparametric and multidimensional MRI is within our reach. The question is not if, but when this will happen.

Author contributions

AR and AC made an equal contribution to this research topic and jointly authored this editorial. All authors contributed to the article and approved the submitted version.

Conflict of interest

The authors declare that the research was conducted in the absence of any commercial or financial relationships that could be construed as a potential conflict of interest.

Publisher's note

References

1. Friedrich MG. Steps and leaps on the path toward simpler and faster cardiac MRI scanning. *Radiology*. (2021) 298(3):587–8. doi: 10.1148/radiol.2021204084

2. Otazo R. Motion-Tolerant quantitative cardiovascular MRI. *Nat Biomed Eng*. (2018) 2(4):199–200. doi: 10.1038/s41551-018-0228-8

3. Ma D, Gulani V, Seiberlich N, Liu K, Sunshine JL, Duerk JL, et al. Magnetic resonance fingerprinting. *Nature*. (2013) 495(7440):187–92. doi: 10.1038/nature11971

4. Hamilton JI, Jiang Y, Chen Y, Ma D, Lo WC, Griswold M, et al. MR fingerprinting for rapid quantification of myocardial T1, T2, and proton spin density. *Magn Reson Med*. (2017) 77(4):1446–58. doi: 10.1002/mrm.26216

5. Christodoulou AG, Shaw JL, Nguyen C, Yang Q, Xie Y, Wang N, et al. Magnetic resonance multitasking for motion-resolved quantitative cardiovascular imaging. *Nature Biomed Eng*. (2018) 2(4):215–26. doi: 10.1038/s41551-018-0217-y

6. Weingartner S, Shenoy C, Rieger B, Schad LR, Schulz-Menger J, Akcakaya M. Temporally resolved parametric assessment of Z-magnetization recovery (TOPAZ): dynamic myocardial T1 mapping using a cine steady-state look-locker approach. *Magn Reson Med*. (2018) 79(4):2087–100. doi: 10.1002/mrm.26887

7. Henningsson M. Cartesian dictionary-based native T1 and T2 mapping of the myocardium. *Magn Reson Med*. (2022) 87(5):2347–62. doi: 10.1002/mrm.29143

frontiers in Cardiovascular Medicine

ORIGINAL RESEARCH
published: 04 March 2022
doi: 10.3389/fcvm.2022.833257

Simultaneous Multi-Slice Cardiac MR Multitasking for Motion-Resolved, Non-ECG, Free-Breathing T1–T2 Mapping

*Xianglun Mao[1], Hsu-Lei Lee[1], Zhehao Hu[2,3], Tianle Cao[1,2], Fei Han[4], Sen Ma[1], Fardad M. Serry[1], Zhaoyang Fan[3], Yibin Xie[1], Debiao Li[1,2] and Anthony G. Christodoulou[1,2]**

[1] Biomedical Imaging Research Institute, Cedars-Sinai Medical Center, Los Angeles, CA, United States, [2] Department of Bioengineering, University of California, Los Angeles, Los Angeles, CA, United States, [3] Department of Radiology, University of Southern California, Los Angeles, CA, United States, [4] Siemens Medical Solutions, Inc., Los Angeles, CA, United States

OPEN ACCESS

Edited by:
Rene M. Botnar,
King's College London,
United Kingdom

Reviewed by:
Aurelien Bustin,
Institut De Rythmologie Et Modélisation Cardiaque (IHU-Liryc), France
Haikun Qi,
ShanghaiTech University, China
Filippo Cademartiri,
Gabriele Monasterio Tuscany Foundation (CNR), Italy

***Correspondence:**
Anthony G. Christodoulou
anthony.christodoulou@cshs.org

Specialty section:
This article was submitted to Cardiovascular Imaging, a section of the journal Frontiers in Cardiovascular Medicine

Received: 10 December 2021
Accepted: 27 January 2022
Published: 04 March 2022

Citation:
Mao X, Lee H-L, Hu Z, Cao T, Han F, Ma S, Serry FM, Fan Z, Xie Y, Li D and Christodoulou AG (2022) Simultaneous Multi-Slice Cardiac MR Multitasking for Motion-Resolved, Non-ECG, Free-Breathing T1–T2 Mapping. Front. Cardiovasc. Med. 9:833257. doi: 10.3389/fcvm.2022.833257

The aim of this study is to simultaneously quantify T1/T2 across three slices of the left-ventricular myocardium without breath-holds or ECG monitoring, all within a 3 min scan. Radial simultaneous multi-slice (SMS) encoding, self-gating, and image reconstruction was incorporated into the cardiovascular magnetic resonance (CMR) Multitasking framework to simultaneously image three short-axis slices. A T2prep-IR FLASH sequence with two flip angles was designed and implemented to allow B1+-robust T1 and T2 mapping. The proposed Multitasking-SMS method was validated in a standardized phantom and 10 healthy volunteers, comparing T1 and T2 measurements and scan-rescan repeatability against corresponding reference methods in one layer of phantom vials and in 16 American Heart Association (AHA) myocardial segments. In phantom, Multitasking-SMS T1/T2 measurements showed substantial correlation ($R^2 > 0.996$) and excellent agreement [intraclass correlation coefficients (ICC) ≥ 0.999)] with reference measurements. In healthy volunteers, Multitasking-SMS T1/T2 maps reported similar myocardial T1/T2 values (1,215 ± 91.0/41.5 ± 6.3 ms) to the reference myocardial T1/T2 values (1,239 ± 67.5/42.7 ± 4.1 ms), with $P = 0.347$ and $P = 0.296$, respectively. Bland–Altman analyses also demonstrated good *in vivo* repeatability in both the multitasking and references, with segment-wise coefficients of variation of 4.7% (multitasking T1), 8.9% (multitasking T2), 2.4% [modified look-locker inversion recovery (MOLLI)], and 4.6% (T2-prep FLASH), respectively. In summary, multitasking-SMS is feasible for free-breathing, non-ECG, myocardial T1/T2 quantification in 16 AHA segments over 3 short-axis slices in 3 min. The method shows the great potential for reducing exam time for quantitative CMR without ECG or breath-holds.

Keywords: multiparametric magnetic resonance imaging, simultaneous multi slice, cardiovascular imaging, free breathing cardiac MR, non-ECG gated, low rank tensor completion

INTRODUCTION

Cardiac magnetic resonance (CMR) imaging is rapidly evolving toward quantitative multiparameter measurement for myocardial tissue characterization (1–6). Quantitative myocardial T1 and T2 mapping techniques are especially useful for tissue characterization, clinical diagnosis, and disease monitoring (7–19). For example, T1 is sensitive to amyloidosis (11–13), fibrosis (15, 17), and inflammation (20); T2 is sensitive to water content in tissue, characterizing myocardial edema (16, 21), ischemia (21), inflammation (14), sarcoidosis (22), and more. Quantitative imaging techniques also enable comparison between patients scanned with differing scanners or timepoints and are therefore promising imaging biomarkers for multi-center or longitudinal studies (23).

Conventional cardiac T1 (24–27) and T2 (28) mapping techniques are inherently inefficient because (1) they rely on breath-holds (often one per slice, with pauses between acquisitions for patients to recover before the next breath-hold) and pauses in acquisition (*via* ECG triggering) to avoid respiratory and cardiac motion; and (2) are performed in series (slice-by-slice, biomarker-by-biomarker) instead of simultaneously. This approach becomes impractical for patients having difficulty holding their breath or for whom ECG triggering fails. Respiratory gating (29) is an alternative to breath-holding, but typically comes with low scan efficiency as well.

Multidimensional continuous-acquisition methods, such as MR Multitasking (5), have shown promise for free-breathing, non-ECG, simultaneous parameter mapping by simultaneously resolving the overlapping dynamics (i.e., cardiac/respiratory motions, relaxations, etc.) involved in quantitative CMR. Multitasking uses a low-rank tensor (LRT) imaging approach with subspace modeling to address the curse of dimensionality associated with imaging multiple motions and relaxations. This approach removes the conventional inefficiencies of scan pauses and serial biomarker acquisition; however, 2D multitasking still uses serial slice acquisition, and so has the same slice coverage inefficiencies as conventional scans. Clinical protocols for quantitative CMR typically include T1 and T2 maps in mid, basal, and apical short-axis slices. Therefore, slice-by-slice 2D multitasking is not fully efficient for the simultaneous acquisition of all biomarkers at all slices. Volumetric 3D Multitasking (30, 31) has been preliminarily demonstrated over 14 short-axis slices (whole ventricle coverage) with 1.4 mm × 1.4 mm × 8 mm resolution in 9:14 min, but provides more slice coverage than is currently used in clinical protocols, at the expense of scan time.

Simultaneous multislice (SMS) imaging (32, 33) has the potential to address the slice inefficiencies of 2D Multitasking without the scan time extension required by full 3D coverage. Here, we redesign MR Multitasking sampling and reconstruction to incorporate SMS imaging, performing three-slice myocardial T1/T2 mapping in a 3 min, non-ECG, free-breathing MRI scan. The repeatability of quantitative measurements and the agreement with reference approaches were evaluated in phantom and in healthy volunteers.

MATERIALS AND METHODS

Cardiac MR Multitasking Framework

Pulse Sequence Design With SMS Acceleration

A prototype MR pulse sequence was developed based on our previous CMR Multitasking implementations (5). T2prep-IR pulses were employed to generate the T1 and T2 contrasts (as shown in **Figure 1**). The T2 prep-IR module was modified from an adiabatic T2-preparation module (34) by adding one adiabatic 180 inversion pulse after the 90 tip-up pulse in the T2-preparation module to achieve the inversion effect. The sequence cycled through five T2 prep-IR durations and the special case of "0 ms" preparation duration used only the IR pulse without any T2 preparation. A continuous-acquisition FLASH sequence collected readouts throughout the entire T1 recovery process. Successive recovery periods alternated between two FLASH excitation flip angles to allow $B1^+$–and through-plane-motion–robust T1 mapping (35). Interleaving five T2prep-IR durations while also interleaving two flip angles produces a cycle of 10 T2prep-IR duration/flip angle combinations, which was repeated throughout the scan. The sequence employed radial k-space sampling, alternating between imaging data readouts incremented by the golden angle (111.24°) and between training data at a fixed radial angle (0°). The image data target spatially resolvable information through (0° and 360°) angular coverage of k-space, whereas the training data collect one projection line at a high temporal sampling rate to facilitate self-gating and will be used to define temporally resolved model parameters during image reconstruction.

A multiband factor of three was used to acquire three slices at the same time. The simultaneous excitation of multiple slices was achieved by superimposing single-band excitation pulses at equally spaced center frequencies, corresponding to equally spaced slice locations. The phase of each band was cycled by different increments ($-2\pi/3$, 0, and $+2\pi/3$), mimicking the discrete Fourier transform and defining a discrete k_z dimension. This encoding scheme is a generalization of the controlled aliasing in volumetric parallel imaging (CAIPIRINHA) technique (36). SMS encoding was applied on every FLASH excitation pulse to always excite three slices simultaneously. No phase cycling was used on the mid-ventricular slice, the $+2\pi/3$ phase increment was used on the basal slice, and the $-2\pi/3$ phase increment on the apical slice. The phase cycle was incremented by one step for each imaging data readout, corresponding to linear k_z encoding; no phase modulation was used for the training data, corresponding to $k_z = 0$. The training data contain contributions from all 3 slices with matched phases, akin to a projection along the slice direction.

Low-Rank Tensor Imaging Model

The images acquired in the Multitasking framework can be represented as a 5-way tensor $\mathcal{A}$ (5, 37). Multitasking conceptualizes different sources of image dynamics involved in quantitative cardiovascular imaging as an image array/tensor with images sorted according to different time dimensions. These image dynamics (e.g., cardiac, respiratory motions, T1/T2 relaxations) overlap in real-time, but by organizing them

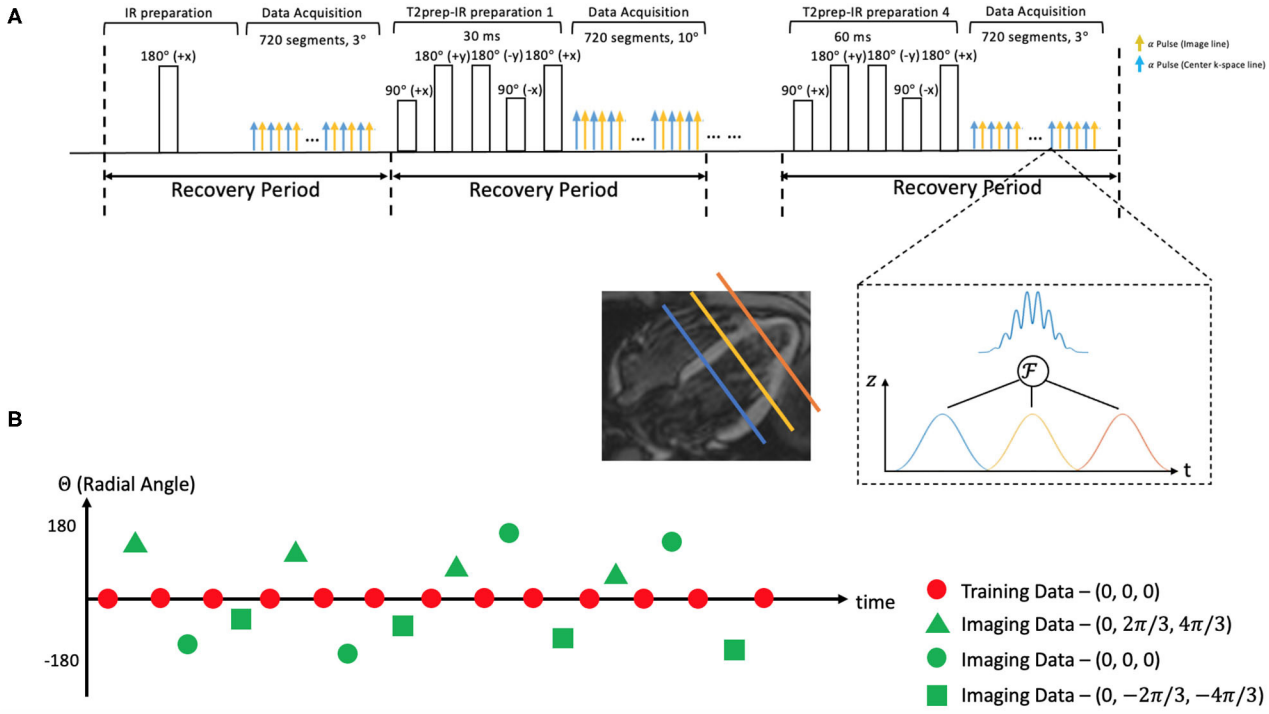

FIGURE 1 | (A) Schematic diagram of the proposed 2D magnetic resonance (MR) Multitasking sequence with simultaneous multislice (SMS)-acceleration, where 5 different preparations (IR and T2prep-IR with 4 different preparation times) are repeated throughout the scan. Each FLASH excitation pulse can excite three slices simultaneously. **(B)** k-Space sampling demonstration. Imaging data are collected with a 2D radial trajectory, and they are incremented by a golden angle (i.e., 111.24°) for each readout. Training data periodically sample the center k-space line every other readouts. Three short-axis slices are excited simultaneously with different phase modulation schemes, resulting in a $2\pi/3$, 0, $-2\pi/3$ shift in their phase increment, respectively.

into a tensor and exploiting the correlation between images, Multitasking can simultaneously resolve all of them. As a result, we can capture and view different image dynamics along different time dimensions.

We model $\mathcal{A}$ as a LRT, leveraging image correlation laterally along each of the N time dimensions and diagonally throughout the multidimensional temporal space, reducing the images to the product of a small core tensor and five factor matrices:

$$\mathcal{A} = \mathcal{G} \times_1 \mathbf{U_x} \times_2 \mathbf{U}_{T_1} \times_3 \mathbf{U}_{\tau,\alpha} \times_4 \mathbf{U}_c \times_5 \mathbf{U}_r, \qquad (1)$$

where $\mathbf{U_x}$ contains spatial basis functions with voxel location index $\mathbf{r} = (x, y, z)$, $\mathbf{U}_{T_1}$ contains basis functions for the T1 relaxation, $\mathbf{U}_{\tau,\alpha}$ contains basis functions that index the 10 different recovery modules with varying T2prep-IR duration τ and flip angle α combinations, $\mathbf{U}_c$ contains cardiac motion basis functions, $\mathbf{U}_r$ contains respiratory motion basis functions, and $\mathcal{G}$ is the core tensor governing the interaction between factor matrices. This constrains the image tensor $\mathcal{A}$ to the intersection of the five low-dimensional subspaces spanned by the $\mathbf{U}$ matrices. The factor matrices and core tensor have far fewer elements than the full image tensor $\mathcal{A}$, which reduces the degrees of freedom for the LRT recovery problem and allows memory-efficient image reconstruction. A diagram of the LRT imaging model is shown in **Figure 2**.

Image Reconstruction

Image reconstruction in the CMR Multitasking framework is divided into the following steps: (1) preliminary "real-time" (ungated) image reconstruction; (2) predetermining the temporal basis functions in $\mathbf{U}_{T_1}$ and $\mathbf{U}_{\tau,\alpha}$ from a training dictionary of signal curves; (3) cardiac and respiratory binning of the real-time images; (4) determining the motion bases and core tensor from the training data; and finally, (5) solving for the spatial coefficients $\mathbf{U_x}$ from the imaging data.

Real-Time Image Reconstruction

"Real-time" (i.e., one single time dimension representing elapsed time) image reconstruction generates ungated images with a low-rank matrix imaging strategy (37), to facilitate image-based binning. The temporal basis functions are estimated from the singular value decomposition (SVD) of the training data, and the spatial coefficients are estimated by least-squares fitting to the imaging data (37).

Dictionary Generation for T1 and Recovery Index Basis Functions

We generated a training dictionary of feasible T2-IR-FLASH signal curves governed by the Bloch equations, with a range of variable T1/T2 values, B1 inhomogeneities, and inversion efficiencies (30, 31). We used 21 T1 values logarithmically spaced

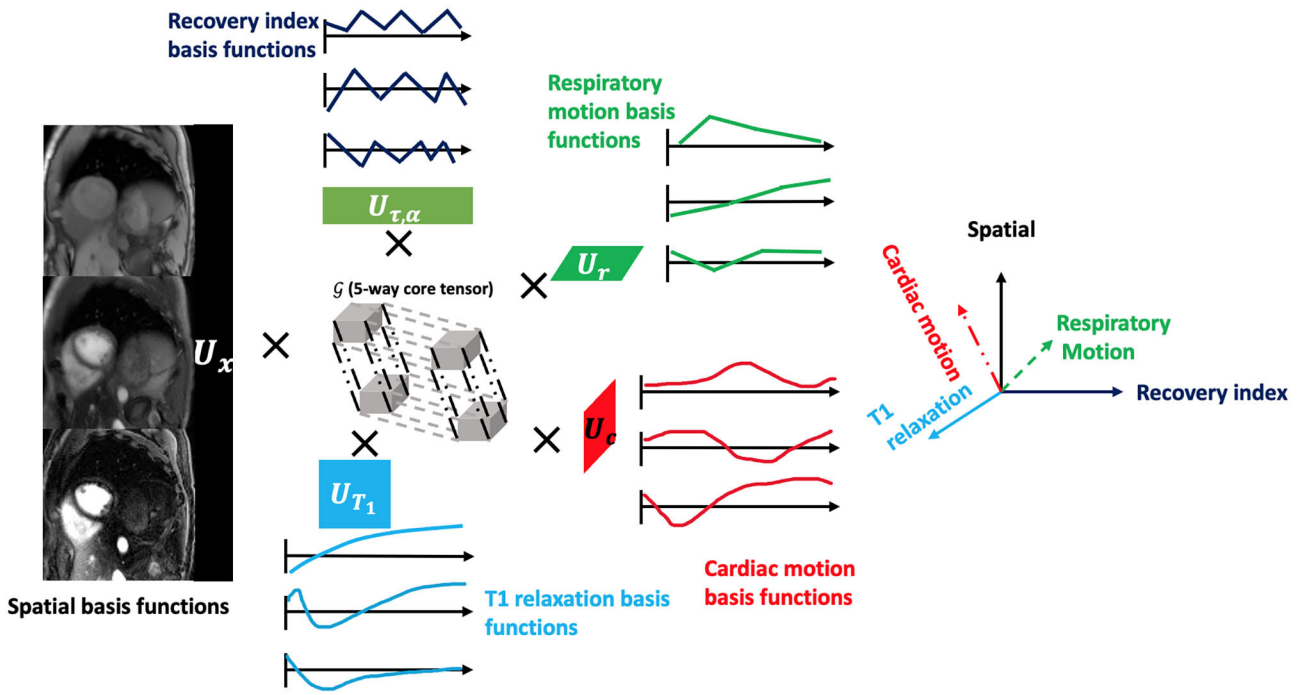

FIGURE 2 | The framework of the low-rank tensor (LRT) imaging model. The underlying image can be represented as a 5-way tensor with one spatial dimension and 4 time dimensions representing 4 dynamic processes: T1 relaxation process, recovery weights with different T2prep-IR duration and flip angles, respiratory motion, and cardiac motion. With the LRT image model, the tensor can be factorized into five factor matrices with much smaller sizes, reducing the degrees of freedom for the LRT recovery problem.

between 100 and 3,000 ms, 21 T2 values logarithmically spaced between 10 and 3,000 ms, seven B1+ efficiency values between 0 and 1.5 modulating the excitation flip angles, and seven inversion efficiency factors controlling the effects of inversion efficiency for the IR and T2prep-IR pulses. The T1 and recovery index relaxation basis functions in $\mathbf{U}_{T_1}$ and $\mathbf{U}_{\tau,\alpha}$ are estimated from the SVD of this training dictionary.

Respiratory and Cardiac Motion Binning

The respiratory and cardiac motion binning algorithm is derived from the methods described in the original MR Multitasking work (5). Briefly, we used an unsupervised machine learning approach to identify motion states by employing a modified k-means clustering algorithm incorporating a low-rank NMR relaxation model (i.e., the known $\mathbf{U}_{T_1}$ and $\mathbf{U}_{\tau,\alpha}$) to address the variable contrast weighting of the training data. We used 6 respiratory bins and 20 cardiac bins in the binning procedure.

Temporal Factor Estimation

Once the motion states have been identified, the training data can be reorganized as a 5-way tensor $\mathcal{D}_{tr}$ which shares temporal factors and core tensor with the image tensor $\mathcal{A}$. These training data will cover several—but not all—combinations of cardiac phase, respiratory phase, recovery index, and inversion time. To recover missing combinations, we apply an LRT completion algorithm, solving the optimization problem below:

$$\begin{aligned}\hat{\mathcal{D}}_{tr} = \min_{\mathcal{D}_{tr},} \quad & \|\mathbf{d}_{tr} - \Omega_{tr}(\mathcal{D}_{tr})\|_2^2 \\ & \mathbf{D}_{tr,(2)} \in range\left(\mathbf{U}_{T_1}\right) \\ & \mathbf{D}_{tr,(3)} \in range\left(\mathbf{U}_{\tau,\alpha}\right) \\ & +\lambda \sum_{i=1,4,5} \left\|\mathbf{D}_{tr,(i)}\right\|_* + R_t(\mathcal{D}_{tr}),\end{aligned} \tag{2}$$

where $\mathbf{d}_{tr}$ is the collected training data, $\Omega_{tr}(\cdot)$ is the sampling operator for the training dataset, $\mathbf{D}_{tr,(i)}$ is the mode-i unfolding of the training tensor, $\|\cdot\|_*$ denotes the matrix nuclear norm, and $R_t(\cdot)$ is a temporal regularizer, which was chosen as temporal total variation (TV) along the respiratory and cardiac dimensions in this work (38). $R_t(\mathcal{D}_{tr})$ in Eq. (2) can be expressed as

$$R_t(\mathcal{D}_{tr}) = \lambda_c \left\|\mathbf{D}_{tr,(4)}\right\|_1 + \lambda_r \left\|\mathbf{D}_{tr,(5)}\right\|_1, \tag{3}$$

where λ_c and λ_r are the two regularization parameters that control the TV smoothing along the cardiac and respiratory dimensions.

Once the training data tensor $\hat{\mathcal{D}}_{tr}$ is complete, the core tensor $\mathcal{G}$ and the remaining unknown temporal factor matrices $\mathbf{U}_c$ and $\mathbf{U}_r$ are extracted from the higher-order SVD (HOSVD) (39) of $\mathcal{D}_{tr}$. At this stage, the core tensor and all temporal factor matrices are known, permitting the definition of a combined temporal factor tensor $\Phi = \mathcal{G} \times_2 \mathbf{U}_{T_1} \times_3 \mathbf{U}_{\tau,\alpha} \times_4 \mathbf{U}_c \times_5 \mathbf{U}_r$.

Spatial Factor Estimation

The spatial factor $\mathbf{U_x}$ was then recovered by fitting the known Φ to the acquired imaging data $\mathbf{d}$, using the following optimization problem:

$$\hat{\mathbf{U}}_\mathbf{x} = \arg\min_{\mathbf{U_x}} ||\mathbf{d} - \Omega\left(\Phi \times_1 \mathbf{F}\mathbf{S}\mathbf{U_x}\right)||_2^2 + R(\mathbf{U_x}), \quad (4)$$

where Ω is the undersampling operator, $\mathbf{F}$ is the Fourier transform operator comprising non-uniform in-plane Fourier encoding and Fourier slice encoding, $\mathbf{S}$ is the coil sensitivity operator, and $R(\cdot)$ is an optional regularization functional to promote transform sparsity (chosen as a wavelet transform in this implementation). $R\left(\mathbf{U}_x\right)$ in Eq. (4) can be expressed as

$$R\left(\mathbf{U}_x\right) = \lambda_w \|\mathbf{W}\mathbf{U}_x\|_1, \quad (5)$$

where $\mathbf{W}$ is the wavelet operator and λ_w is the regularization parameter that controls the wavelet sparsity. Once Φ and $\mathbf{U_x}$ have both been determined, the final reconstructed image can be calculated as $\mathcal{A} = \Phi \times_1 \mathbf{U_x}$.

Multiparametric Mapping

The signal equation at the k^{th} recovery period of the Multitasking-SMS pulse sequence is:

$$s\left(A, B, T_1, T_2, \beta\right) = A\frac{1 - e^{-TR/T_1}}{1 - e^{-TR/T_1}\cos(\beta\alpha_k)}$$

$$\cdot\left[1 + \left(BQ_k e^{-\frac{\tau}{T_2}} - 1\right)\left(e^{-\frac{TR}{T_1}}\cos\left(\beta\alpha_k\right)\right)^n\right]\cdot\sin\left(\beta\alpha_k\right), \quad (6)$$

with amplitude factor A, IR/T2prep-IR pulse efficiency B, FLASH readout interval TR, flip angle for the kth recovery period α_k, B1+ field weights β (to account for B1+ inhomogeneity), and recovery time points $n = 1, 2, \ldots, N$ (where N is the total number of excitations in each recovery period). The Q_k absorbs the effects of having inverted the magnetization from the steady-state for the previous recovery period's excitation flip angle. Assuming a steady-state established at the final readout of each recovery period, Q_k is expressed as

$$Q_k = \frac{1 - e^{-TR/T_1}\cos(\beta\alpha_k)}{1 - e^{-TR/T_1}\cos(\beta\alpha_{k-1})}. \quad (7)$$

The native T1 and T2 measurements can be estimated from the signal model in Eqs. (6) and (7). Our previous work (35) showed the value of a dual flip-angle signal model for B1+ robust T1 mapping.

Phantom Study

An International Society for Magnetic Resonance in Medicine/National Institute of Standards and Technology (ISMRM/NIST) phantom (40) (model 130, High Precision Devices, Boulder, Colorado) was imaged on a 3T scanner (MAGNETOM Vida, Siemens). The layer with the vials closest to the T1 and T2 values for myocardium (T1 ∈ [200, 2,500] ms; T2 ∈ [20, 800] ms) was used in the study.

The proposed 2D Multitasking-SMS sequence was applied, as well as four reference methods: modified look-locker inversion recovery (MOLLI) 5(3)3 (41), T2-prepared fast low angle shot (T2-prep FLASH) mapping method (common product sequences used in the heart), and the gold standard static T1 and T2 mapping sequences inversion recovery spin echo (IRSE-T1) for T1 mapping, and T2-weighted spin-echo (SE-T2) for T2 mapping.

The following scan parameters were used for the proposed 2D Multitasking-SMS sequence: Field of View (FOV) = 270 mm × 270 mm (with 2-fold readout oversampling, the acquired FOV = 540 mm × 540 mm); spatial resolution = 1.7 mm × 1.7 mm × 8 mm; 3 slices with a multiband factor of 3; TR/TE = 3.5/1.6 ms; flip angle = 3 and 10; T2 preparation times = 0, 30, 40, 50, and 60 ms (with 0 corresponding to a standard IR pulse); recovery period = 2.5 s; scan time = 3 min 3 s. The 2D MOLLI imaging parameters were: Repetition Time/Echo Time (TR/TE) = 2.7/1.1 ms; flip angle = 35; FOV = 220 mm × 220 mm; in-plane resolution = 1.4 mm × 1.4 mm; slice thickness = 8 mm. The 2D T2-prep FLASH imaging parameters were: TR/TE = 3.3/1.4 ms; flip angle = 12; FOV = 220 mm × 220 mm; in-plane resolution = 1.4 mm^2 × 1.4 mm; slice thickness = 8 mm; T2 preparation times = 0, 35, and 55 ms. The IR-SE T1 protocol parameters were: FOV = 280 mm × 192 mm; in-plane resolution = 1.4 mm × 1.4 mm; slice thickness = 5 mm; TI = 150, 300, 500, 800, 1,200, 1,600, 2,000, and 4,500 ms. The SE-T2 protocol parameters were: FOV = 280 mm × 192 mm; in-plane resolution = 1.4 mm × 1.4 mm; slice thickness = 5 mm; TE = 15, 25, 45, 70, 100, 140, 180, 250, and 350 ms.

Linear regression, the Bland–Altman analyses, and intraclass correlation coefficients (ICC) with a two-way mixed model were performed on the vials with relevant T1 and T2 values (T1 < 2,000 ms; T2 < 120 ms) to evaluate the quantitative agreement between Multitasking and reference measurements. Pairwise t-tests were also performed to evaluate measurement biases, with a significance level of 0.05.

In-vivo Study

Healthy volunteer studies were approved by the institutional review board of Cedars-Sinai Medical Center. All subjects gave written informed consent before MRI. $N = 10$ human volunteers (3 men and 7 women, age 36.7 ± 12.3) were imaged on a 3T scanner (MAGNETOM Vida, Siemens) with an 18-channel body coil.

The 2D Multitasking-SMS pulse sequence imaged three short-axis slices over the left-ventricle, base, mid, and apex. It was applied twice to test scan-rescan repeatability. The scan parameters were the same as used in the phantom study. A 2-step fitting procedure was used to determine parameter maps. Step 1 estimates β and T2 from Eq. (6), and Step 2 uses the known β to fit T1 from the 3° recovery curve only, for which the Look–Locker effect is reduced.

The 2D single-slice multitasking (i.e., multitasking-SS) pulse sequence was also applied to sequentially image the same three short-axis slices. The scan parameters were: FOV = 270 × 270 mm (with two-fold readout oversampling, the acquired FOV = 540 mm × 540 mm); spatial resolution = 1.7 mm × 1.7 mm × 8

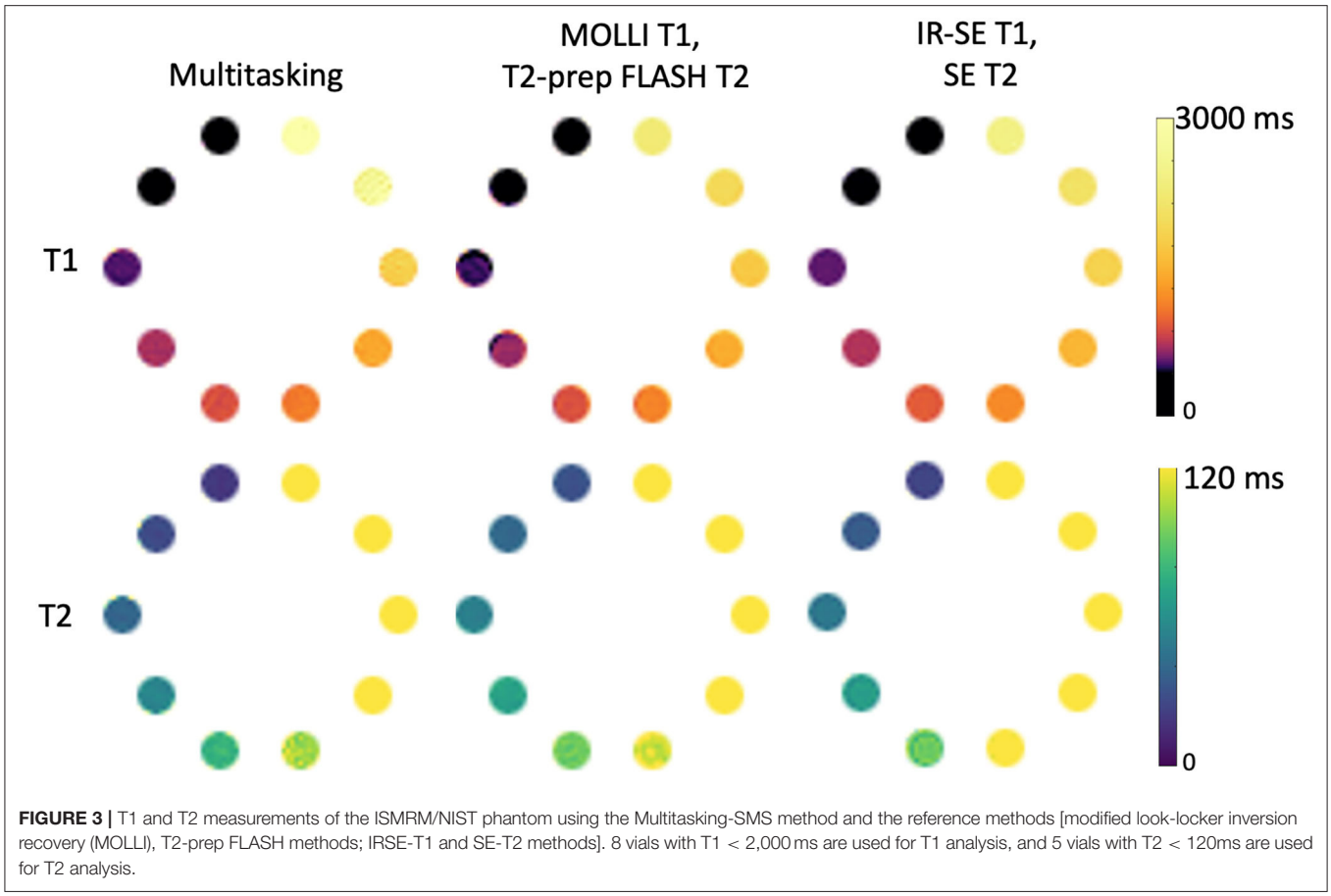

FIGURE 3 | T1 and T2 measurements of the ISMRM/NIST phantom using the Multitasking-SMS method and the reference methods [modified look-locker inversion recovery (MOLLI), T2-prep FLASH methods; IRSE-T1 and SE-T2 methods]. 8 vials with T1 < 2,000 ms are used for T1 analysis, and 5 vials with T2 < 120ms are used for T2 analysis.

TABLE 1 | Intraclass correlation coefficient (ICC) and *P*-values of the paired *t*-test for comparison analysis between cardiac mapping methods and the gold standard and reference values across vials in the ISMRM/NIST phantom.

	ICC	*P*-value (Paired *T*-Test)
MOLLI T1 vs. IRSE T1	0.999	<0.001
Multitasking T1 vs. IRSE T1	0.999	0.011
T2-prep FLASH T2 vs. SE T2	0.999	0.010
Multitasking T2 vs. SE T2	0.999	0.006

mm; TR/TE = 3.5 ms/1.6 ms; flip angle = 5; T2 preparation times = 0, 30, 40, 50, and 60 ms; recovery period = 2.5 s; scan time per slice = 1 min 31 s (4 min 33 s for 3 slices).

Reference 2D T1 maps with MOLLI and 2D T2 maps with T2-prep FLASH (1.4 mm × 1.4 mm × 8.0 mm) were acquired at both systole and diastole during end-expiration breath-holds and were also collected twice. The scan parameters of the reference sequences were the same as used in the phantom study.

T1 and T2 maps were segmented at the end-expiration respiratory and end-diastolic cardiac phases, using the AHA 16-segment model by drawing epi- and endocardial contours in commercially available software (CVI42; Circle Cardiovascular Imaging, Calgary, Alberta, Canada) (42).

Measurement of global and segmental myocardial T1/T2 in all healthy volunteers were compared between the Multitasking-SMS approach and the reference approaches. The pairwise *t*-tests were performed with a significance level of 0.05. Repeatability was evaluated using Bland–Altman analyses and coefficients of variation (CoVs) between the first and second scans of the proposed method and of reference methods. Global and segment-wise CoVs were calculated to assess repeatability. Global CoVs were calculated as the standard deviation of average Left Ventricle (LV) myocardial T1/T2 between two scans, divided by the mean T1/T2 for each subject, and were root-mean-square (RMS)-aggregated over all 10 subjects to provide an overall summary of global repeatability. Segment-wise CoVs were calculated as the standard deviation between two scans for each LV myocardial segment, and were first RMS-aggregated over segments to calculate the segment-wise CoV and divided by the mean T1/T2 for each individual subject; segment-wise CoVs between methods, with a significance level of 0.05. Segment-wise CoVs were then RMS-aggregated over all 10 subjects to provide an overall summary of segment-wise repeatability.

To determine the impact of dual-flip-angle SMS imaging on the accuracy and precision of multitasking measurements, pairwise *t*-tests were used to compare the segmental T1/T2 values, segment-wise Signal-to-noise ratio (SNR), and segment-wise SNR efficiency between Multitasking-SS and

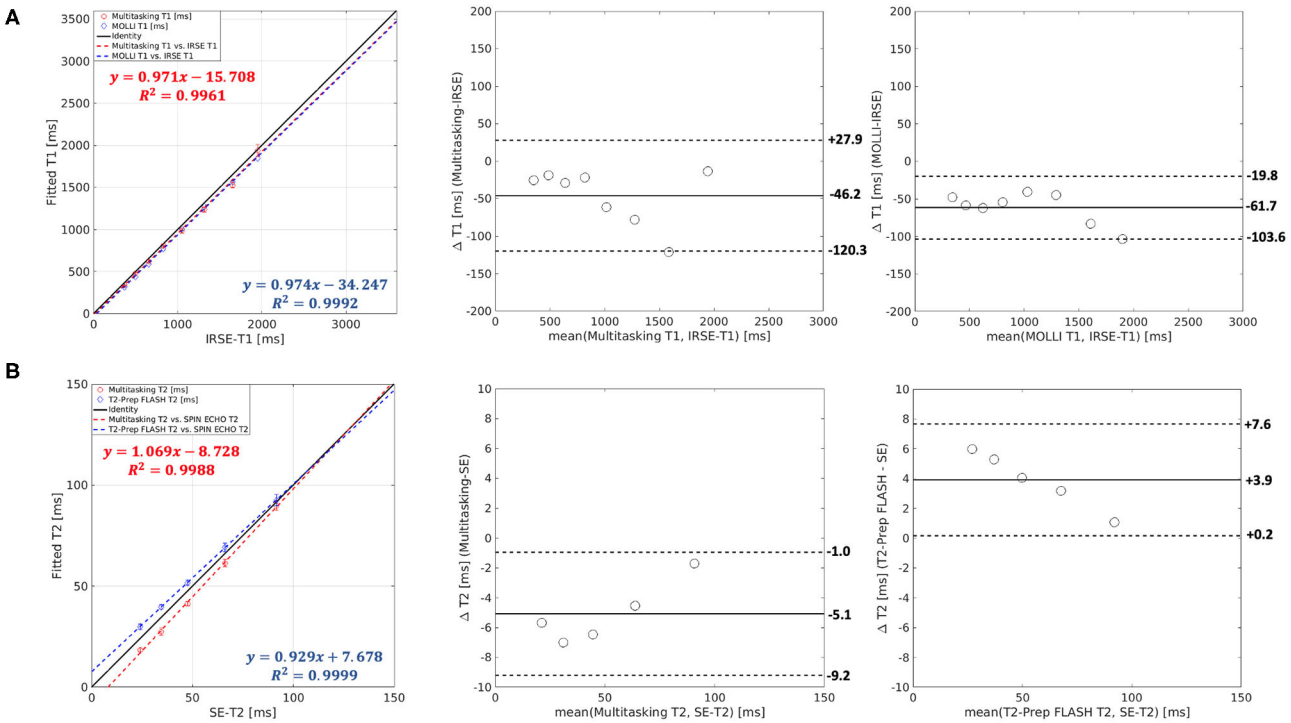

FIGURE 4 | (A) Both Multitasking-SMS and MOLLI showed high R^2 values against inversion recovery spin echo (IRSE)-T1 in the linear regression. The T1 bias and limits of agreement were −46.2 ± 74.1ms for Multitasking-SMS and IRSE-T1, and −61.7 ± 41.9 ms for MOLLI and IRSE-T1. **(B)** Both Multitasking-SMS and T2-prep FLASH showed a high R^2 value against SE-T2. The T2 bias and limits of agreement were −5.1 ± 4.1 ms for the Multitasking-SMS and SE-T2, and 3.9 ± 3.7 ms for T2-prep FLASH and SE-T2.

Multitasking-SMS. The segment-wise SNR was calculated as the mean T1/T2 within each segment divided by the voxelwise standard deviation of T1/T2 within that segment. SNR values were transformed into 3-slice SNR efficiency values by dividing by the square root of the total scan time required to collect 3 slices (4.5 min for Multitasking-SS and 3 min for Multitasking-SMS).

Materials and Software

All Multitasking image reconstructions were performed on a Linux workstation with a 2.90 GHz Intel Xeon processor in MATLAB 2018a (MathWorks, Natick, Massachusetts). Statistical analyses were performed using IBM SPSS Statistics (Armonk, New York, USA).

RESULTS

Phantom Results

Phantom T1 and T2 maps obtained from the 2D MOLLI, T2-prep FLASH, IRSE-T1, SE-T2, and the Multitasking-SMS approaches are shown in **Figure 3**. **Table 1** summarizes the ICC and Paired *t*-test results between Multitasking-SMS/MOLLI/T2-prep FLASH and gold standard IRSE/SE measurements. Multitasking-SMS measurements and IRSE/SE measurements showed excellent agreement with ICC = 0.999 for both T1 and T2. All pairwise method comparisons showed statistically significant biases.

Scatter plots and Bland–Altman plots of the T1 and T2 values in the relevant vials are shown in **Figure 4**. T1 measurements from Multitasking-SMS and MOLLI were each highly correlated ($R^2 > 0.996$) with the reference 2D IRSE-T1 acquisition. The 95% limits of agreement of the T1 values were 46.2 ± 74.1 ms for Multitasking-SMS and IRSE-T1, and −61.7 ± 41.9 ms for MOLLI and IRSE-T1. T2 measurements from Multitasking-SMS and T2-prep FLASH were also each highly correlated ($R^2 > 0.998$) with the reference 2D SE-T2 acquisition. The 95% limits of agreement of the T2 measurements were −5.1 ± 4.1ms for Multitasking-SMS and SE-T2, and 3.9 ± 3.7ms for T2-prep FLASH and SE-T2.

In-vivo Results

Figure 5 shows the cardiac and respiratory phases detected in the Multitasking-SMS framework in one subject. Motion videos are provided in **Supplementary Videos 1**, **2**. T1 and T2 mapping results from 2D Multitasking-SMS, 2D Multitasking-SS, and reference methods in two healthy subjects (including 3 short-axis slices) are shown in **Figure 6**. Additional cardiac phases from Multitasking-SMS are shown in **Supplementary Figures 1, 2**. Example fitted B1+ field maps (β) and inversion efficiency maps (B) obtained from Multitasking-SMS are given in **Supplementary Figure 6**. **Figures 7A,B** show the mean T1/T2 values in each of the 16 AHA segments across all 10 healthy subjects as a bull's eye plot, for the Multitasking-SMS and the reference methods. The Bland–Altman plots in **Figures 7C,D**

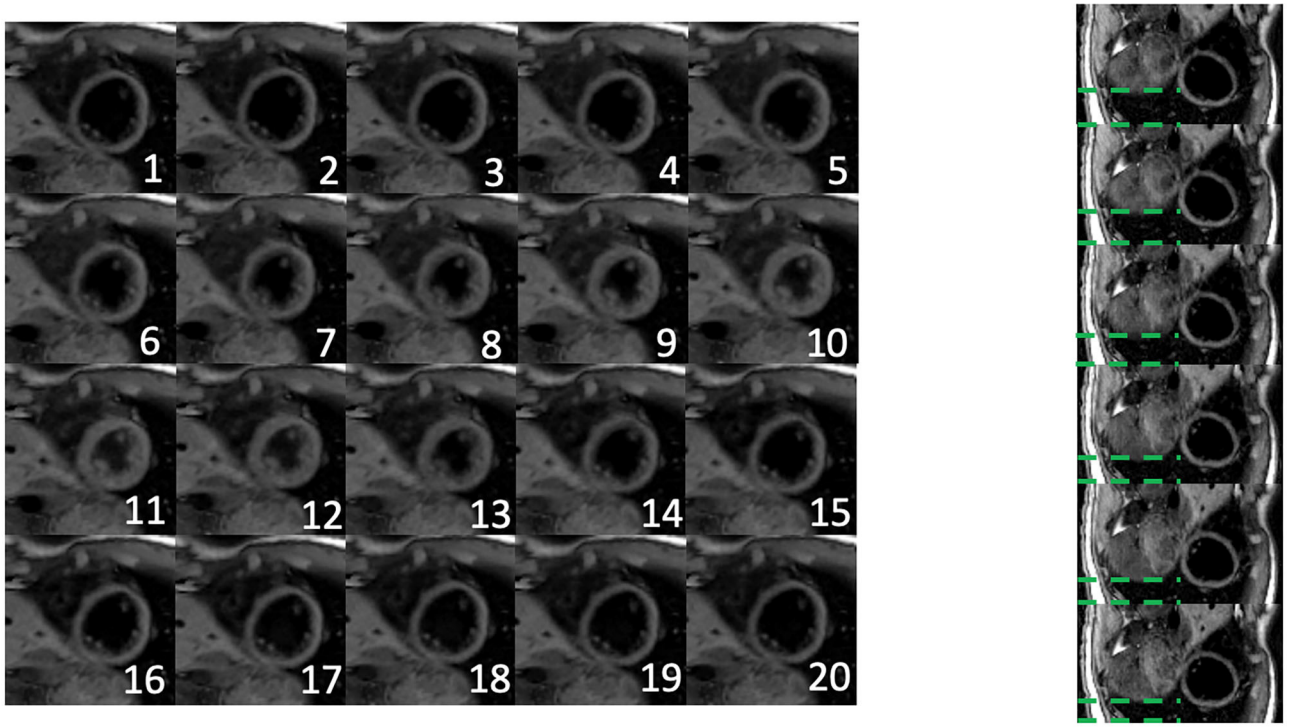

FIGURE 5 | (A) Twenty cardiac phases are generated after the binning procedure. **(B)** Six respiratory phases are generated after the binning, the displayed images show the exhalation process. The green dash line represents the distance between the liver dome and the bottom of the image. The liver dome position approaches the bottom of the image during exhalation.

further compare the Multitasking-SMS T1 values with the reference T1 values estimated by MOLLI, and the Multitasking-SMS T2 values with the reference T2 values estimated by T2-prep FLASH. Both subject-wise (averaged from whole myocardium for each subject, 10 values) and segment-wise (averaged from all subjects for each segment, 16 values) T1/T2 measurements are compared between Multitasking-SMS and references. **Supplementary Figure 3** shows these plots for all subject/segment combinations. Multitasking-SMS measured similar global T1 (1215 ± 91.0 ms) and T2 (41.5 ± 6.3 ms) values to MOLLI (1239 ± 67.5 ms) and T2-prep FLASH (42.7 ± 4.1 ms), with $P = 0.347$ and $P = 0.296$, respectively.

Additionally, Multitasking-SS T1/T2 mapping results were compared to the Multitasking-SMS measurements in **Figure 8**. **Supplementary Figure 4** further shows the Bland-Altman comparisons for all subject/segment combinations. 2D single-slice Multitasking measured similar global T1 ($1,191 \pm 106.5$ ms; $P = 0.323$) and higher T2 (51.6 ± 7.2 ms; $P = 0.002$) values compared to Multitasking-SMS T1/T2. The significant bias in T2 also exists between Multitasking-SS T2 and reference T2-prep FLASH measurements ($P < 0.001$).

The Bland–Altman plots in **Figure 9** show the subject-wise and segment-wise scan-rescan repeatability of multitasking-SMS and reference T1/T2 measurements. **Supplementary Figure 5** shows the Bland–Altman plots for all the subject/segment combinations. The RMS global CoVs of subject-wise T1/T2 values were 2.3% (multitasking T1), 4.4% (multitasking T2), 0.7% (MOLLI), 2.1% (T2-prep FLASH), respectively. The RMS segment-wise CoVs across all 16 segments' T1/T2 values in the 10 subjects were 4.7% (multitasking T1), 8.9% (multitasking T2), 2.4% (MOLLI), and 4.6% (T2-prep FLASH). Segment-wise CoVs were significantly larger for multitasking T1 than MOLLI T1 ($P = 0.002$), and significantly larger for multitasking T2 than T2-prep FLASH ($P = 0.001$).

The average SNR of multitasking measurements were 11.9 (multitasking-SMS T1), 6.2 (multitasking-SMS T2), 6.0 (multitasking-SS T1), and 6.1 (multitasking-SS T2). The average 3-slice SNR efficiencies were 6.9 $\text{min}^{-1/2}$ (multitasking-SMS T1), 3.6 $\text{min}^{-1/2}$ (multitasking-SMS T2), 2.8 $\text{min}^{-1/2}$ (multitasking-SS T1), and 2.9 $\text{min}^{-1/2}$ (multitasking-SS T2). The pairwise *t*-tests showed that multitasking-SMS had significantly higher T1 SNR and T1/T2 SNR efficiency than multitasking-SS ($P < 0.001$) and similar T2 SNR ($P = 0.692$).

DISCUSSION

In this study, a 2D SMS-accelerated, free-breathing, non-ECG, motion-resolved cardiac imaging method (i.e., multitasking-SMS) was introduced for simultaneous 2D myocardial T1/T2

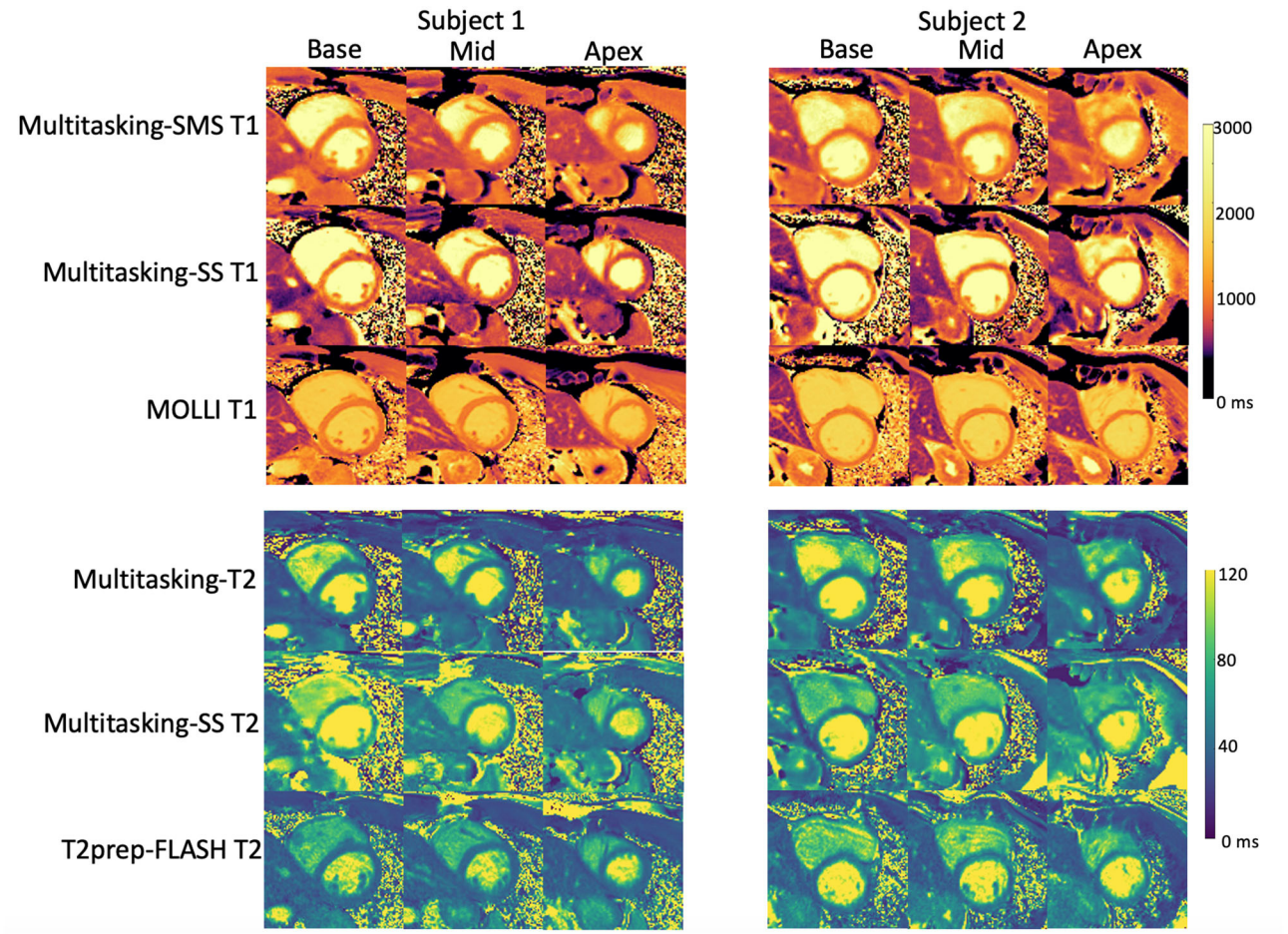

FIGURE 6 | Comparison between T1/T2 maps obtained with the proposed 2D Multitasking-SMS, the original Multitasking-SS, and the standard MOLLI/T2-prep FLASH approaches in two healthy subjects. The acquired Multitasking T1/T2 maps were the same slice position as the reference maps acquired in the short axis.

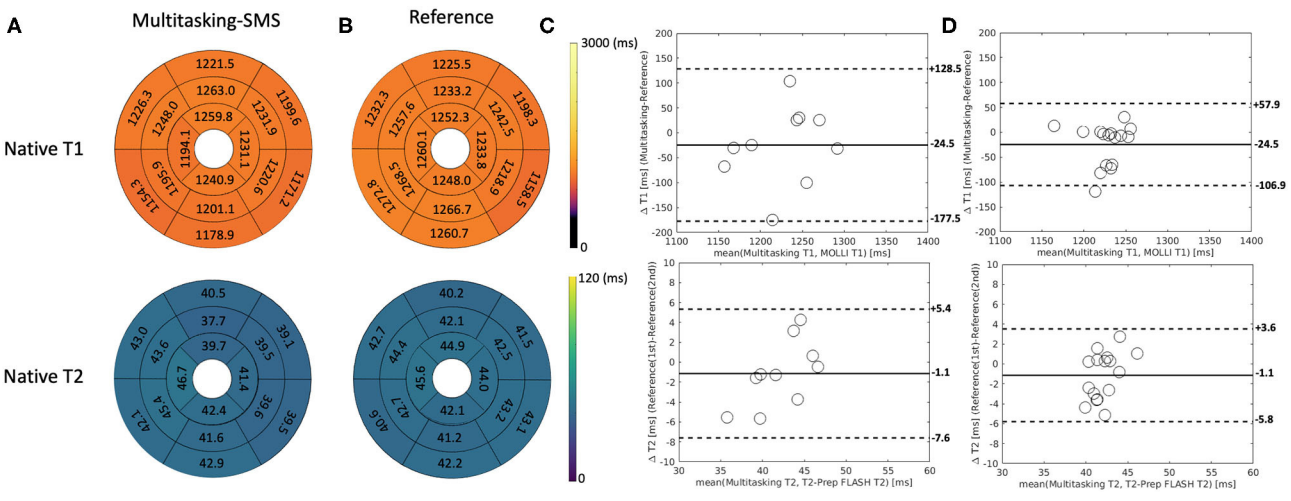

FIGURE 7 | (A,B) The 16-segment AHA model for the proposed Multitasking-SMS T1/T2 maps and the reference T1/T2 maps in the myocardium in all 10 healthy subjects. **(C)** The Bland-Altman plot compares the subject-wise global myocardium T1/T2 differences in 10 healthy subjects. **(D)** The Bland-Altman plot compares the segment-wise T1/T2 differences in 10 healthy subjects. The dash lines represent 95% limits of agreement, and the solid lines represent mean bias.

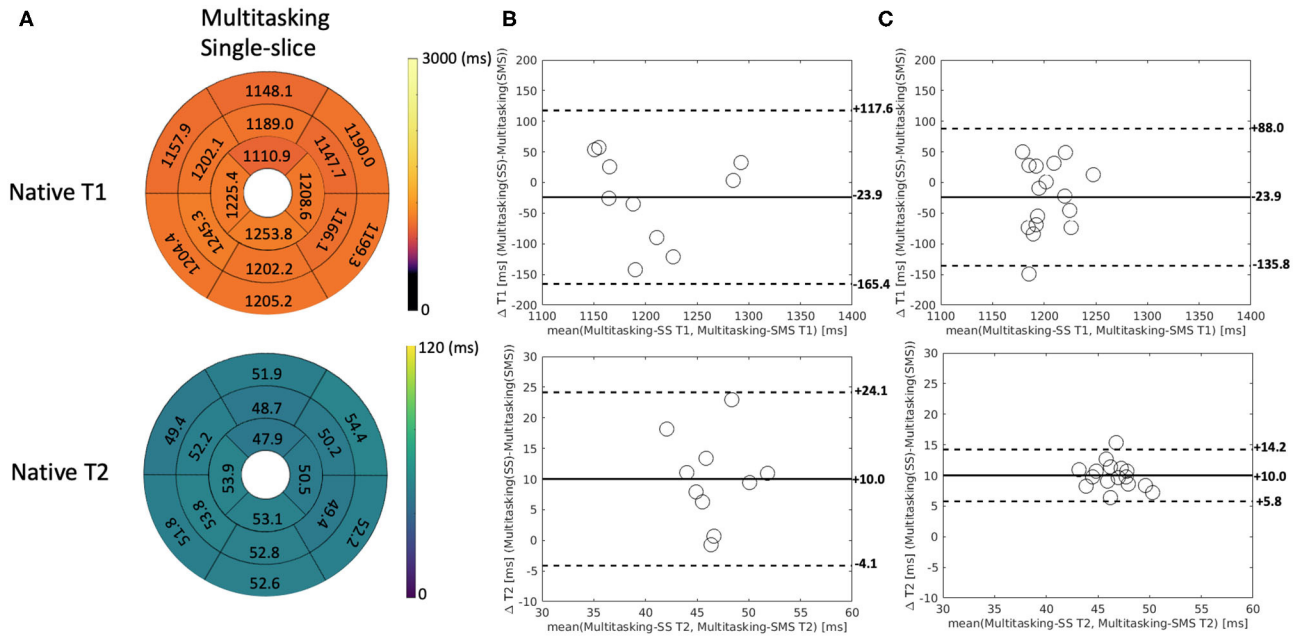

FIGURE 8 | (A) The 16-segment AHA model for the 2D single-slice Multitasking T1/T2 maps in the myocardium in all 10 healthy subjects. **(B)** The Bland-Altman plot compares the subject-wise global myocardium T1/T2 differences between Multitasking-SS and Multitasking-SMS in 10 healthy subjects. **(C)** The Bland-Altman plot compares the segment-wise T1/T2 differences between Multitasking-SS and Multitasking-SMS in 10 healthy subjects. The dash lines represent 95% limits of agreement, and the solid lines represent mean bias.

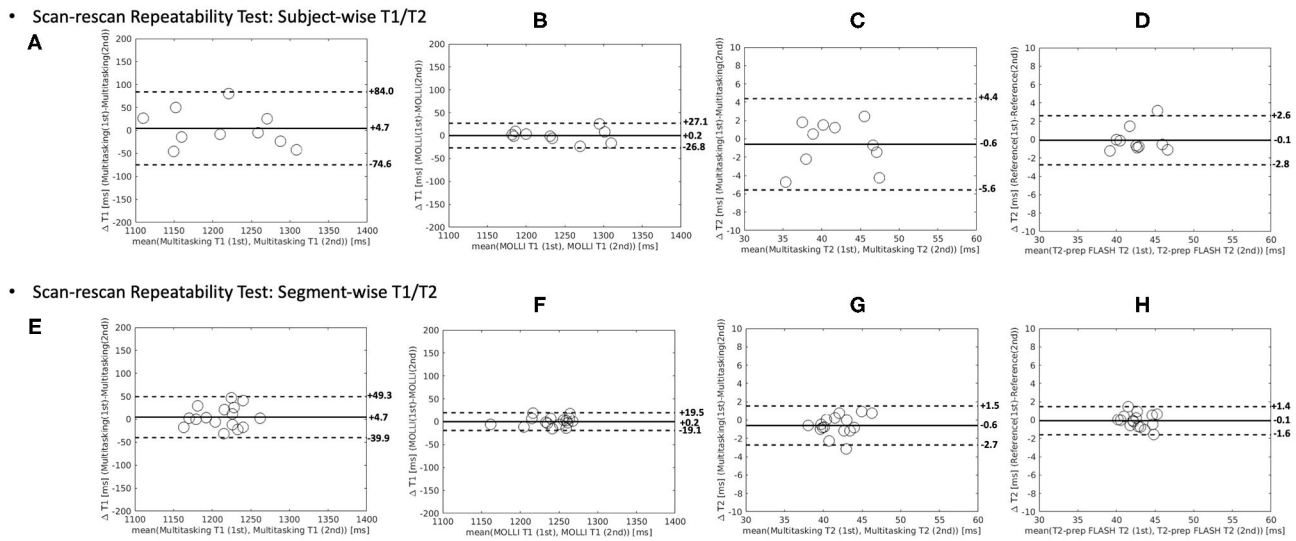

FIGURE 9 | The Bland–Altman plots comparing measurements from 1st and 2nd Multitasking-SMS scans and reference scans in subject-wise T1/T2 **(A–D)** and segment-wise T1/T2 **(E–H)**. Multitasking-SMS T1/T2 repeatability analysis are shown in **(A,C,E,G)**. Reference T1/T2 repeatability analysis are shown in **(B,D,F,H)**. The dash lines indicate the 95% limits of agreement and the solid line indicates mean bias.

mapping over three short-axis slices in 3 min. It represents several new developments that have not previously been a part of T1-T2 multitasking: (1) this is the first SMS acceleration with multitasking framework; and (2) the first use of a dual flip angle scheme interleaved with T2prep-IR blocks for B1+-robust T1-T2 mapping.

In the phantom study, the multitasking-SMS T1/T2 measurements and the typical cardiac mapping sequences MOLLI and T2-prep FLASH all showed statistically significant biases against the gold standard IRSE-T1 and SE-T2. For T1, multitasking-SMS and MOLLI both had small negative biases; for T2, multitasking-SMS and T2prep-FLASH had small biases

in opposite directions (underestimation by multitasking-SMS and overestimation by T2prep-FLASH). All the comparisons showed ICC $\geq$ 0.999, reflecting high agreement with gold standard references.

In healthy volunteers, multitasking-SMS T1/T2 measurements reported similar myocardial T1/T2 values compared to the reference T1/T2 measurements in healthy volunteers. The T1/T2 estimations from all methods were in the normal range of many 3T MRI studies (43–45). Multitasking-SMS was less repeatable than MOLLI and T2-prep FLASH in healthy volunteers, but may be an attractive choice for mapping in subjects who cannot comply with breath-holds or for whom ECG triggering fails, or when co-registration between T1 and T2 maps is desired. Multitasking-SMS underestimated T2 and T2-prep FLASH overestimated T2 in the phantom, but they achieved similar T2 quantification *in vivo*. This may be related to the difference in T2-prep modules between multitasking-SMS and T2prep-FLASH (T2prep-IR vs. T2prep, respectively). These different modules may have different responses to motion, inhomogeneity, and flow that are present in the *in vivo* scans, which could change their behavior relative to the phantom scans.

2D multitasking-SS scans from our original work (5) were also applied sequentially on the same short-axis slice locations. Multitasking-SS T2 values were significantly shorter than both the Multitasking-SMS and the T2prep-FLASH T2 values—which were not significantly different from each other—indicating that dual-flip-angle Multitasking-SMS was more accurate for T2 mapping *in vivo*. T1 values were not significantly different, suggesting similar accuracy in T1. Regarding precision, the combination of SMS and dual-flip angle excitation significantly increased 3-slice SNR efficiency for both T1 and T2 vs. multitasking-SS. When traded for a 1.5× reduction in 3-slice scan time (4.5 min to 3 min), this translated to the maintenance of T2 SNR and a 2.0× boost in T1 SNR.

Multitasking-SMS could be a potential alternative to the conventional series of multiple T1 and T2 mapping scans in clinical studies. Conventionally, each quantitative parameter (i.e., T1/T2) is typically mapped using one breath-hold per 2D slice. As a result, 3 slices (base, mid, apex) of native T1, and T2 at diastole phase would require 6 breath holds. In a typical scenario, 3-slice T1 and T2 mapping could take ∼3 min assuming a ∼20 s gap between each scan for the patient to recover from the breath-hold while the technologist sets up the next scan. With an experienced MR operator, the gap can often be reduced to ∼10 s and would take a total scan time of 2 min. However, shorter breath-hold recovery times may increase the likelihood of a repeat scan due to patients' difficulty in complying with breath-holds, which could then extend exam time. In our experiments, six breath-hold scans required 4–6 min. The proposed 2D CMR Multitasking-SMS removes this variability by offering a fixed 3-min scan, with the added benefits of push-button simplicity (no trigger delay times or cardiac acquisition windows to set up), free-breathing acquisition, and no ECG dependence. Further, Multitasking-SMS may have the opportunity to be extended to collect more slices in the heart with a multiband factor of 3 or more in the future.

SMS acceleration techniques have been adopted in other quantitative cardiac MRI studies (45, 46), but their data acquisition still requires breath-holding and/or ECG triggering. Multitasking-SMS is a promising free-breathing and non-ECG technique, which has tremendous potential in enhancing patient comfort, lowering technologist burden, and increasing scanner throughput. However, Multitasking-SMS also has some limitations. Qualitatively, T1 and T2 maps show some blurring, which may be due to unresolved motion or over-regularization during the reconstruction. This blurring is especially noticeable in systolic phases, although this cardiac phase is not standard for T1 and T2 analyses. A higher in-plane resolution can potentially be used to reduce the artifacts at the sacrifice of extending the scan time. Second, the reconstruction time was 2–3 h for each data acquisition, which is too long for online reconstruction in the clinic. Deep neural networks have shown promise for accelerating cardiac Multitasking reconstruction, cutting spatial factor estimation time by several orders of magnitude (47). A similar application of deep learning to the Multitasking-SMS sequence could potentially bring image reconstruction times within the clinically applicable range. Lastly, this study only evaluated Multitasking-SMS in healthy volunteers to demonstrate the feasibility of the technique. A larger study in patients is warranted.

In summary, SMS Multitasking provides co-registered T1 and T2 maps at the base, mid, and apex short-axis slices without ECG or breath-holding, all in one 3-min scan. T1 and T2 values agreed with reference measurements in a phantom and *in vivo*, and were repeatable *in vivo*. This new method improved T2 accuracy and T1 precision over the original Multitasking T1/T2 mapping method while maintaining T1 accuracy and T2 precision. The method shows potential for reducing exam time and setup time for quantitative CMR.

DATA AVAILABILITY STATEMENT

The original contributions presented in the study are included in the article/**Supplementary Materials**, further inquiries can be directed to the corresponding author.

ETHICS STATEMENT

The studies involving human participants were reviewed and approved by Cedars-Sinai Medical Center. The patients/participants provided their written informed consent to participate in this study.

AUTHOR CONTRIBUTIONS

XM, AC, and DL: study conception and design. XM, H-LL, and FH: pulse sequence development. XM: data collection. XM and

AC: analysis and interpretation of results. XM, H-LL, ZH, TC, FH, SM, FS, ZF, YX, DL, and AC: draft manuscript preparation. All authors reviewed the results and approved the final version of the manuscript.

FUNDING

This work was supported by the National Institutes of Health Grant R01 EB028146.

ACKNOWLEDGMENTS

The authors acknowledge with gratitude the Cedars-Sinai Medical Center Research Imaging Core staff.

SUPPLEMENTARY MATERIAL

The Supplementary Material for this article can be found online at: https://www.frontiersin.org/articles/10.3389/fcvm.2022.833257/full#supplementary-material

REFERENCES

1. Moon JC, Messroghli DR, Kellman P, Piechnik SK, Robson MD, Ugander M, et al. Myocardial T1 mapping and extracellular volume quantification: a Society for Cardiovascular Magnetic Resonance (SCMR) and CMR Working Group of the European Society of Cardiology consensus statement. *J Cardiovasc Magn Reson.* (2013) 15:1–12. doi: 10.1186/1532-429X-15-92
2. Kvernby S, Warntjes MJB, Haraldsson H, Carlhäll CJ, Engvall J, Ebbers T. Simultaneous three-dimensional myocardial T1 and T2 mapping in one breath hold with 3D-QALAS. *J Cardiovasc Magn Reson.* (2014) 16:1–14. doi: 10.1186/s12968-014-0102-0
3. Akçakaya M, Weingärtner S, Basha TA, Roujol S, Bellm S, Nezafat R. Joint myocardial T1 and T2 mapping using a combination of saturation recovery and T2-preparation. *Magn Reson Med.* (2016) 76:888–96. doi: 10.1002/mrm.25975
4. Hamilton JI, Jiang Y, Chen Y, Ma D, Lo WC, Griswold M, et al. MR fingerprinting for rapid quantification of myocardial T1, T2, and proton spin density. *Magn Reson Med.* (2017) 77:1446–58. doi: 10.1002/mrm.26216
5. Christodoulou AG, Shaw JL, Nguyen C, Yang Q, Xie Y, Wang N, et al. Magnetic resonance multitasking for motion-resolved quantitative cardiovascular imaging. *Nature Biomed Eng.* (2018) 2:215–26. doi: 10.1038/s41551-018-0217-y
6. Jaubert O, Cruz G, Bustin A, Schneider T, Koken P, Doneva M, et al. Free-running cardiac magnetic resonance fingerprinting: Joint T1/T2 map and Cine imaging. *Magn Reson Imaging.* (2020) 68:173–82. doi: 10.1016/j.mri.2020.02.005
7. Oh-Ici D, Jeuthe S, Al-Wakeel N, Berger F, Kuehne T, Kozerke S, et al. T1 mapping in ischaemic heart disease. *Eur Heart J Cardiovasc Imaging.* (2014) 15:597–602. doi: 10.1093/ehjci/jeu024
8. Messroghli DR, Walters K, Plein S, Sparrow P, Friedrich MG, Ridgway JP, et al. Myocardial T1 mapping: application to patients with acute and chronic myocardial infarction. *Magn Reson Med.* (2007) 58:34–40. doi: 10.1002/mrm.21272
9. Karamitsos TD, Piechnik SK, Banypersad SM, Fontana M, Ntusi NB, Ferreira VM, et al. Noncontrast T1 mapping for the diagnosis of cardiac amyloidosis. *JACC Cardiovasc Imaging.* (2013) 6:488–97. doi: 10.1016/j.jcmg.2012.11.013
10. Banypersad SM, Fontana M, Maestrini V, Sado DM, Captur G, Petrie A, et al. T1 mapping and survival in systemic light-chain amyloidosis. *Eur Heart J.* (2015) 36:244–51. doi: 10.1093/eurheartj/ehu444
11. Fontana M, Banypersad SM, Treibel TA, Maestrini V, Sado DM, White SK, et al. Native T1 mapping in transthyretin amyloidosis. *JACC Cardiovasc Imaging.* (2014) 7:157–65. doi: 10.1016/j.jcmg.2013.10.008
12. Puntmann VO, Carr-White G, Jabbour A, Yu CY, Gebker R, Kelle S, International T1 Multicentre CMR Outcome Study. T1-mapping and outcome in nonischemic cardiomyopathy: all-cause mortality and heart failure. *JACC Cardiovasc Imaging.* (2016) 9:40–50. doi: 10.1016/j.jcmg.2015.12.001
13. Hinojar R, Foote L, Arroyo Ucar E, Jackson T, Jabbour A, Yu CY, et al. Native T1 in discrimination of acute and convalescent stages in patients with clinical diagnosis of myocarditis: a proposed diagnostic algorithm using CMR. *JACC Cardiovasc Imaging.* (2015) 8:37–46. doi: 10.1016/j.jcmg.2014.07.016
14. Thavendiranathan P, Walls M, Giri S, Verhaert D, Rajagopalan S, Moore S, et al. Improved detection of myocardial involvement in acute inflammatory cardiomyopathies using T2 mapping. *Circ Cardiovasc Imaging.* (2012) 5:102–10. doi: 10.1161/CIRCIMAGING.111.967836
15. Kvernby S, Rönnerfalk M, Warntjes M, Carlhäll CJ, Nylander E, Engvall J, et al. Longitudinal changes in myocardial T1 and T2 relaxation times related to diffuse myocardial fibrosis in aortic stenosis; before and after aortic valve replacement. *J Magn Reson Imaging.* (2018) 48:799–807. doi: 10.1002/jmri.25980
16. Ugander M, Bagi PS, Oki AJ, Chen B, Hsu LY, Aletras AH, et al. Myocardial edema as detected by pre-contrast T1 and T2 CMR delineates area at risk associated with acute myocardial infarction. *JACC Cardiovasc Imaging.* (2012) 5:596–603. doi: 10.1016/j.jcmg.2012.01.016
17. Kim PK, Hong YJ, Im DJ, Suh YJ, Park CH, Kim JY, et al. Myocardial T1 and T2 mapping: techniques and clinical applications. *Korean J Radiol.* (2017) 18:113–31. doi: 10.3348/kjr.2017.18.1.113
18. Arai AE. Magnetic resonance imaging for area at risk, myocardial infarction, and myocardial salvage. *J Cardiovasc Pharmacol Ther.* (2011) 16:313–20. doi: 10.1177/1074248411412378
19. Mordi I, Carrick D, Bezerra H, Tzemos N. T 1 and T 2 mapping for early diagnosis of dilated non-ischaemic cardiomyopathy in middle-aged patients and differentiation from normal physiological adaptation. *Eur Heart J Cardiovasc Imaging.* (2016) 17:797–803. doi: 10.1093/ehjci/jev216
20. Taylor AJ, Salerno M, Dharmakumar R, Jerosch-Herold M. T1 mapping: basic techniques and clinical applications. *JACC Cardiovasc Imaging.* (2016) 9:67–81. doi: 10.1016/j.jcmg.2015.11.005
21. Giri S, Chung YC, Merchant A, Mihai G, Rajagopalan S, Raman SV, et al. T2 quantification for improved detection of myocardial edema. *J Cardiovasc Mag Reson.* (2009) 11:1–13. doi: 10.1186/1532-429X-11-56
22. Crouser ED, Ono C, Tran T, He X, Raman SV. Improved detection of cardiac sarcoidosis using magnetic resonance with myocardial T2 mapping. *Am J Respir Crit.* (2014) 189:109–12.
23. Luetkens JA, Homsi R, Sprinkart AM, Doerner J, Dabir D, Kuetting DL, et al. Incremental value of quantitative CMR including parametric mapping for the diagnosis of acute myocarditis. *Eur Heart J Cardiovasc Imaging.* (2016) 17:154–61. doi: 10.1093/ehjci/jev246
24. Messroghli DR, Radjenovic A, Kozerke S, Higgins DM, Sivananthan MU, Ridgway JP. Modified Look-Locker inversion recovery (MOLLI) for high-resolution T1 mapping of the heart. *Magn Reson Med.* (2004) 52:141–6. doi: 10.1002/mrm.20110
25. Piechnik SK, Ferreira VM, Dall'Armellina E, Cochlin LE, Greiser A, Neubauer S, Robson MD. Shortened Modified Look-Locker Inversion recovery (ShMOLLI) for clinical myocardial T1-mapping at 1.5 and 3 T within a 9 heartbeat breath-hold. *J Cardiovasc Magn Reson.* (2010) 12:1–11. doi: 10.1186/1532-429X-12-69
26. Chow K, Flewitt JA, Green JD, Pagano JJ, Friedrich MG, Thompson RB. Saturation recovery single-shot acquisition (SASHA) for myocardial T1 mapping. *Magn Reson Med.* (2014) 71:2082–95. doi: 10.1002/mrm.24878
27. Weingärtner S, Akçakaya M, Basha T, Kissinger KV, Goddu B, Berg S, et al. Combined saturation/inversion recovery sequences for improved evaluation of scar and diffuse fibrosis in patients with arrhythmia or heart rate variability. *Magn Reson Med.* (2014) 71:1024–34. doi: 10.1002/mrm.24761

28. Baeßler B, Schaarschmidt F, Stehning C, Schnackenburg B, Maintz D, Bunck AC. Cardiac T2-mapping using a fast gradient echo spin echo sequence-first *in vitro* and *in vivo* experience. *J Cardiovasc Magn Reson.* (2015) 17:1–8. doi: 10.1186/s12968-015-0177-2
29. Ehman RL, McNamara MT, Pallack M, Hricak H, Higgins CB. Magnetic resonance imaging with respiratory gating: techniques and advantages. *Am J Roentgenol.* (1984) 143:1175–82. doi: 10.2214/ajr.143.6.1175
30. Mao X, Serry F, Cokic I, Ma S, Hu Z, Han F, et al. 3D Free-Breathing, Non-ECG, T1-T2-B1+ Cine Mapping with Cardiac MR Multitasking. In: *Proceedings of 24th Annual International Conference of SCMR* (2021).
31. Mao X, Serry F, Ma S, Hu Z, Han F, Xie Y, et al. 3D Whole-ventricle, Free-Breathing, Non-ECG, T1-T2-B1+ Cine Mapping with Cardiac MR Multitasking. In *Proceedings of 30th Annual Meeting of ISMRM* (2021). p. 690.
32. Barth M, Breuer F, Koopmans PJ, Norris DG, Poser BA. Simultaneous multi-slice (SMS) imaging techniques. *Magn Reson Med.* (2016) 75:63–81. doi: 10.1002/mrm.25897
33. Breuer FA, Blaimer M, Heidemann RM, Mueller MF, Griswold MA, Jakob PM. Controlled aliasing in parallel imaging results in higher acceleration (CAIPIRINHA) for multi-slice imaging. *Magn Reson Med.* (2005) 53:684–91. doi: 10.1002/mrm.20401
34. Nezafat R, Stuber M, Ouwerkerk R, Gharib AM, Desai MY, Pettigrew RI. B1-Insensitive T2 preparation for improved coronary magnetic resonance angiography at 3 T. *Magn Reson Med.* (2006) 55:858–64. doi: 10.1002/mrm.20835
35. Serry F, Ma S, Mao X, Han F, Xie Y, Han H, et al. Dual flip angle (2FA) IR-FLASH with spin history mapping for B1+-insensitive T1 mapping: Application to T1 cardiovascular magnetic resonance multitasking. *Magn Reson Med.* (2021) 86:3182–91. doi: 10.1002/mrm.28935
36. Zahneisen B, Poser BA, Ernst T, Stenger VA. Three-dimensional Fourier encoding of simultaneously excited slices: generalized acquisition and reconstruction framework. *Magn Reson Med.* (2014) 71:2071–81. doi: 10.1002/mrm.24875
37. Liang Z-P. Spatiotemporal imaging with partially separable functions. *Proc IEEE Int Symp Biomed Imaging.* (2007) 988–91. doi: 10.1109/ISBI.2007.357020
38. Adluru G, DiBella EV. Reordering for improved constrained reconstruction from undersampled k-space data. *Int J Biomed Imaging.* (2008) 2008. doi: 10.1155/2008/341684
39. De Lathauwer L, De Moor B, Vandewalle J. A multilinear singular value decomposition. *SIAM J Matrix Anal Appl.* (2000) 21:1253–78. doi: 10.1137/S0895479896305696
40. Russek SE, Boss M, Jackson EF, Jennings DL, Evelhoch JL, Gunter JL, Sorensen AG. Characterization of NIST/ISMRM MRI system phantom. In: *Proceedings of the 20th Annual Meeting of ISMRM* (2012). p. 2456.
41. Xue H, Greiser A, Zuehlsdorff S, Jolly MP, Guehring J, Arai AE, et al. Phase-sensitive inversion recovery for myocardial T1 mapping with motion correction and parametric fitting. *Magn Reson Med.* (2013) 69:1408–20. doi: 10.1002/mrm.24385
42. American Heart Association Writing Group on Myocardial Segmentation and Registration for Cardiac Imaging, Cerqueira MD, Weissman NJ, Dilsizian V, Jacobs AK, Kaul S, Verani MS. Standardized myocardial segmentation and nomenclature for tomographic imaging of the heart: a statement for healthcare professionals from the Cardiac Imaging Committee of the Council on Clinical Cardiology of the American Heart Association. *Circulation*. (2002) 105:539–42. doi: 10.1161/hc0402.102975
43. Weingärtner S, Meßner NM, Budjan J, Loßnitzer D, Mattler U, Papavassiliu T, et al. Myocardial T1-mapping at 3T using saturation-recovery: reference values, precision and comparison with MOLLI. *J Cardiovasc Mag Reson.* (2017) 18:84. doi: 10.1186/s12968-016-0302-x
44. Von Knobelsdorff-Brenkenhoff F, Prothmann M, Dieringer MA, Wassmuth R, Greiser A, Schwenke C, et al. Myocardial T1 and T2 mapping at 3 T: reference values, influencing factors and implications. *J Cardiovasc Mag Reson.* (2013) 15:1–11. doi: 10.1186/1532-429X-15-53
45. Weingärtner S, Moeller S, Schmitter S, Auerbach E, Kellman P, Shenoy C, et al. Simultaneous multislice imaging for native myocardial T1 mapping: improved spatial coverage in a single breath-hold. *Magn Reson Med.* (2017) 78:462–71. doi: 10.1002/mrm.26770
46. Hamilton JI, Jiang Y, Ma D, Chen Y, Lo WC, Griswold M, et al. Simultaneous multislice cardiac magnetic resonance fingerprinting using low rank reconstruction. *NMR Biomed.* (2019) 32:e4041. doi: 10.1002/nbm.4041
47. Chen Y, Shaw JL, Xie Y, Li D, Christodoulou AG. Deep learning within a priori temporal feature spaces for large-scale dynamic MR image reconstruction: application to 5-D cardiac MR multitasking. In: *International Conference on MICCAI*. Springer, Cham (2019). p. 495–504. doi: 10.1007/978-3-030-32245-8_55

Conflict of Interest: FH is a full-time employee of Siemens Medical Solutions, Inc., USA.

The remaining authors declare that the research was conducted in the absence of any commercial or financial relationships that could be construed as a potential conflict of interest.

Publisher's Note: All claims expressed in this article are solely those of the authors and do not necessarily represent those of their affiliated organizations, or those of the publisher, the editors and the reviewers. Any product that may be evaluated in this article, or claim that may be made by its manufacturer, is not guaranteed or endorsed by the publisher.

frontiers | Frontiers in Cardiovascular Medicine

ORIGINAL RESEARCH
published: 23 June 2022
doi: 10.3389/fcvm.2022.928546

A Self-Supervised Deep Learning Reconstruction for Shortening the Breathhold and Acquisition Window in Cardiac Magnetic Resonance Fingerprinting

Jesse I. Hamilton[1,2]*

[1] Department of Radiology, University of Michigan, Ann Arbor, MI, United States, [2] Department of Biomedical Engineering, University of Michigan, Ann Arbor, MI, United States

The aim of this study is to shorten the breathhold and diastolic acquisition window in cardiac magnetic resonance fingerprinting (MRF) for simultaneous T_1, T_2, and proton spin density (M_0) mapping to improve scan efficiency and reduce motion artifacts. To this end, a novel reconstruction was developed that combines low-rank subspace modeling with a deep image prior, termed DIP-MRF. A system of neural networks is used to generate spatial basis images and quantitative tissue property maps, with training performed using only the undersampled k-space measurements from the current scan. This approach avoids difficulties with obtaining *in vivo* MRF training data, as training is performed *de novo* for each acquisition. Calculation of the forward model during training is accelerated by using GRAPPA operator gridding to shift spiral k-space data to Cartesian grid points, and by using a neural network to rapidly generate fingerprints in place of a Bloch equation simulation. DIP-MRF was evaluated in simulations and at 1.5 T in a standardized phantom, 18 healthy subjects, and 10 patients with suspected cardiomyopathy. In addition to conventional mapping, two cardiac MRF sequences were acquired, one with a 15-heartbeat(HB) breathhold and 254 ms acquisition window, and one with a 5HB breathhold and 150 ms acquisition window. In simulations, DIP-MRF yielded decreased nRMSE compared to dictionary matching and a sparse and locally low rank (SLLR-MRF) reconstruction. Strong correlation ($R^2 > 0.999$) with T_1 and T_2 reference values was observed in the phantom using the 5HB/150 ms scan with DIP-MRF. DIP-MRF provided better suppression of noise and aliasing artifacts *in vivo*, especially for the 5HB/150 ms scan, and lower intersubject and intrasubject variability compared to dictionary matching and SLLR-MRF. Furthermore, it yielded a better agreement between myocardial T_1 and T_2 from 15HB/254 ms and 5HB/150 ms MRF scans, with a bias of −9 ms for T_1 and 2 ms for T_2. In summary, this study introduces an extension of the deep image prior framework for cardiac MRF tissue property mapping, which does not require pre-training with *in vivo* scans, and has the potential to reduce motion artifacts by enabling a shortened breathhold and acquisition window.

Keywords: deep learning, deep image prior, cardiovascular imaging, low rank, multiparametric magnetic resonance imaging (MRI), magnetic resonance fingerprinting (MRF), T1 mapping, T2 mapping

OPEN ACCESS

Edited by:
Anthony G. Christodoulou, Cedars Sinai Medical Center, United States

Reviewed by:
Ruixi Zhou, Beijing University of Posts and Telecommunications (BUPT), China
Haikun Qi, ShanghaiTech University, China

***Correspondence:**
Jesse I. Hamilton
hamiljes@med.umich.edu

Specialty section:
This article was submitted to Cardiovascular Imaging, a section of the journal Frontiers in Cardiovascular Medicine

Received: *25 April 2022*
Accepted: *06 June 2022*
Published: *23 June 2022*

Citation:
Hamilton JI (2022) A Self-Supervised Deep Learning Reconstruction for Shortening the Breathhold and Acquisition Window in Cardiac Magnetic Resonance Fingerprinting. Front. Cardiovasc. Med. 9:928546. doi: 10.3389/fcvm.2022.928546

INTRODUCTION

Cardiac magnetic resonance (CMR) T_1 and T_2 mapping are useful for the detection of pathological changes in myocardial tissue, including acute (1) and chronic inflammation (2, 3), edema (4, 5), amyloid deposition (6), fatty infiltration (7), and infarct (8). Multiparametric methods have recently been developed to efficiently measure multiple tissue properties during one scan (9–12). Cardiac magnetic resonance fingerprinting (MRF) is one such technique that uses a time-varying pulse sequence to encode several properties in magnetization signal evolutions over time (13, 14). A time series of highly undersampled images is acquired, typically with a single image frame collected per repetition time (TR). Quantitative maps are obtained using pattern recognition, where the signal evolution (or "fingerprint") measured at each voxel is matched to a dictionary of fingerprints simulated for different tissue property values.

While simultaneous T_1, T_2, and proton spin density (M_0) mapping using cardiac MRF has been demonstrated in healthy subjects (15) and cardiomyopathy patients (16), respiratory and cardiac motion present significant challenges, even when breathholding and electrocardiogram (ECG) triggering are employed. The highly accelerated non-Cartesian sampling used in cardiac MRF introduces noise-like artifacts in the measured fingerprints, and thus many image frames are collected to enable accurate pattern recognition using the corrupted signals. Several previous studies employed a relatively long breathhold of 15 heartbeats and diastolic acquisition window of approximately 250 ms as a result (15). However, this sequence may be susceptible to motion if patients have difficulty holding their breath or have elevated heart rates. While retrospective motion correction can be used (17), an alternative strategy is to shorten the breathhold and acquisition window to avoid the need for such corrections.

Shortening the MRF acquisition will result in fewer time points in each fingerprint, which can impede accurate pattern recognition. Several classes of reconstruction methods have been developed to accelerate MRF scans, including model-based reconstructions (18, 19), low-rank subspace techniques (20–22), and deep learning (23). Deep learning methods have gained particular interest for their excellent denoising capabilities and fast computation times. While some MRF deep learning reconstructions operate on single-voxel fingerprints (23, 24), others use the fingerprints from many voxels within a spatial neighborhood to estimate the tissue properties at a target voxel (25), and thus can leverage both spatial and temporal correlations in the MRF data to reduce noise and k-space undersampling artifacts. Such a method was recently demonstrated for MRF in the brain, where a convolutional neural network (CNN) reconstruction enabled a 4-fold reduction in scan time compared to conventional dictionary matching (25) and allowed for high-resolution (submillimeter) mapping (26).

However, CNN reconstructions typically require training using *in vivo* datasets, which presents a challenge for cardiac MRF. It is difficult to collect ground truth tissue property maps in the heart due physiological motion, as a scan time of several minutes would be needed to obtain fully-sampled MRF data. Furthermore, because the MRF scan is prospectively triggered, the fingerprints depend on the subject's cardiac rhythm (14), and thus many datasets from subjects with different cardiac rhythms (including fast or irregular rhythms commonly seen in patients) would potentially be needed for training.

Recently, a deep image prior (DIP) technique was proposed for image processing tasks that does not require pre-training with ground truth datasets (27). Taking image denoising as an example, a randomly initialized CNN learns to generate a denoised image by minimizing the mean squared error loss compared to a noise-corrupted image, with no requirements for additional training data. The network architecture is typically based on a u-net (28) and is designed so that lower spatial frequencies are recovered before higher spatial frequencies (29). Therefore, the network learns to generate natural images before recovering higher frequency noise, so that training with early stopping avoids overfitting to the noisy image. When applied to inverse problems in medical imaging, a mathematical model of the image acquisition can be incorporated in the loss function, which has been applied to computed tomography (30), positron emission tomography (31), and diffusion MRI (32).

This study introduces a self-supervised deep learning reconstruction for cardiac MRF T_1, T_2, and M_0 mapping for the purpose of mitigating noise, reducing k-space undersampling artifacts, and enabling a shortened acquisition to reduce motion artifacts. The proposed method, termed DIP-MRF, combines low-rank MRF subspace modeling with the denoising capabilities of a deep image prior. A system of convolutional (u-net) and fully-connected networks is used to generate spatial basis images (i.e., images in a low-dimensional subspace derived from the MRF signal evolutions) and quantitative maps, without dictionary matching and without pre-training using *in vivo* data. For each MRF acquisition, training is performed *de novo* using only the undersampled k-space measurements from the current scan by incorporating a mathematical model of the cardiac MRF data acquisition in the loss function. DIP-MRF is shown to reduce noise and undersampling artifacts compared to conventional dictionary matching and low-rank subspace reconstructions. Furthermore, DIP-MRF is leveraged to shorten the breathhold duration from 15 to 5 heartbeats and diastolic acquisition window from 250 to 150 ms, with results shown in healthy subjects and cardiomyopathy patients, which has the potential to reduce motion artifacts.

MATERIALS AND METHODS

Previous work has shown that an MRF dictionary, denoted by $D \in \mathbb{C}^{p \times t}$, where p is the number of parameter combinations and t is the number of time points, can be compressed along time using a truncated singular value decomposition (SVD) that retains only the first k singular values (33). The temporal basis functions are denoted by $V_k \in \mathbb{C}^{t \times k}$, which is matrix whose columns contain the first k right singular vectors. A compressed dictionary, denoted by $D_k \in \mathbb{C}^{p \times k}$, can be obtained according to $D_k = DV_k$. Similarly, if $x \in \mathbb{C}^{n \times t}$ denotes a time series of MRF images with n voxels, then multiplication by V_k yields

a set of spatial basis images in this low-dimensional subspace, denoted by $x_k = xV_k$, where $x_k \in \mathbb{C}^{n \times k}$. Multiplying the spatial basis images by the complex conjugate V_k^* will yield a low-rank approximation to the original MRF image series, $x \approx x_k V_k^*$. Low-rank subspace reconstructions for MRF have been proposed that iteratively remove noise and undersampling artifacts from the spatial basis images, sometimes with additional regularization terms using spatial sparsity and/or locally low rank regularization, before matching to the compressed dictionary to obtain quantitative maps (21, 22, 34, 35).

This study extends the deep image prior framework using a low-rank cardiac MRF signal model. An overview of the DIP-MRF reconstruction pipeline is shown in **Figure 1**. A convolutional u-net generates spatial basis images, which are input to a fully-connected network that outputs quantitative maps, neither of which require pre-training with *in vivo* data. Rather, the networks are trained in a self-supervised manner to enforce consistency with the undersampled k-space data from a single scan by incorporating the MRF forward encoding model in the loss function. The forward model includes (1) simulation of a time series of MRF images from the tissue property maps, (2) projection of images onto the low-dimensional subspace, (3) coil sensitivity encoding, and (4) spiral k-space undersampling. Calculation of the forward model is accelerated by (1) a pre-trained neural network that rapidly outputs fingerprints instead of using a more time-consuming Bloch equation simulation (36), and (2) preprocessing the spiral MRF k-space data with GRAPPA operator gridding (GROG) to obtain data in Cartesian k-space (37). The following sections will describe the DIP-MRF pipeline in more detail.

Pre-trained Fingerprint Generator Network

Calculating the forward model requires repeated simulations of MRF signal evolutions at every iteration. To reduce computation time, this step is performed using a neural network called the Fingerprint Generator Network (FGN), which rapidly outputs signal evolutions for arbitrary T_1, T_2, and cardiac rhythm timings (**Figure 2A**) and has been described previously (36). The network is fully-connected with two hidden layers and 300 nodes per layer. The input consists of a T_1 value, a T_2 value, and the subject's cardiac rhythm timings (specifically, a vector of RR interval times) recorded by the ECG during the scan. The output is a vector of length $2t$ containing interleaved real and imaginary parts of the fingerprint. The FGN is the only neural network component in the DIP-MRF pipeline that requires pre-training. The pre-training is performed only one time using fingerprints produced by a Bloch equation simulation for different T_1, T_2, and cardiac rhythm timings, after which the same network can be applied to any subsequent scan regardless of the subject's cardiac rhythm. **Supplementary Figure 1** gives additional details about pre-training the FGN.

Low-Rank Signal Approximation

Although DIP-MRF does not use pattern recognition, a dictionary of fingerprints is calculated temporarily in order to derive the temporal basis functions V_k (33). The FGN is used to output a dictionary of approximately 23,000 fingerprints with T_1 between 50–3,000 ms and T_2 between 5–1,000 ms, which takes 30 ms on a GPU. Next, the SVD of the dictionary is calculated (taking approximately 1 s), and the temporal basis functions are obtained from the first k right singular vectors (**Figure 2B**). This study uses a rank of $k = 5$, which retains more than 99.9% of the energy compared to the uncompressed fingerprints.

GRAPPA Operator Gridding Preprocessing and Coil Sensitivity Estimation

The forward model calculation requires repeated iterations between image and k-space domains. To avoid time-consuming operations using the non-uniform fast Fourier Transform (NUFFT) (38), the MRF spiral k-space data are preprocessed using GROG, a parallel imaging technique that shifts non-Cartesian k-space data to unmeasured Cartesian locations using GRAPPA weight matrices (37). The weight matrices for unit shifts along k_x and k_y are calibrated using a fully-sampled dataset; this dataset is obtained by taking the temporal average of the multicoil MRF k-space data, gridding a time-averaged image using the NUFFT, and performing an FFT to obtain multicoil Cartesian k-space data. The central 48×48 region of the Cartesian k-space is used for GROG calibration. Coil sensitivity maps are estimated from the time-averaged multicoil images using the adaptive combination method (39). The GROG density compensation function, denoted by W, is obtained by counting the number of spiral k-space points that are shifted to each Cartesian coordinate. After calibration, the GROG weights are applied to shift undersampled spiral MRF k-space data onto a Cartesian grid, and each time frame of the resulting Cartesian k-space dataset is multiplied by W. A binary mask, denoted by P_i, is stored that indicates the sampled (acquired) points on the Cartesian grid at each time index i.

Neural Network Architectures

A convolutional u-net, which is not pre-trained, is used to output the MRF spatial basis images. This network will be called the image reconstruction network (IRN) and is shown in **Figure 3**. Inspired by the original DIP publication (27), the input is a tensor denoted by $z \in \mathbb{R}^{n_y \times n_x \times d}$ of uniform random numbers between -0.1 and 0.1, where n_y and n_x are the spatial dimensions in voxels, and d is a tunable parameter defining the number of feature channels in the first layer of the network. This study uses $d = 32$ to be consistent with the original DIP work, but this parameter was not found to have much impact on the reconstruction. The IRN performs a series of 2D convolutions followed by batch normalization, leaky ReLU activation, and an optional dropout layer. The data pass through five downsampling and upsampling paths with multiple skip connections. Downsampling is implemented using convolution with a 2×2 stride, and upsampling is performed using nearest neighbor interpolation followed by convolution. The network output has size $n_y \times n_x \times 2k$, where the channel

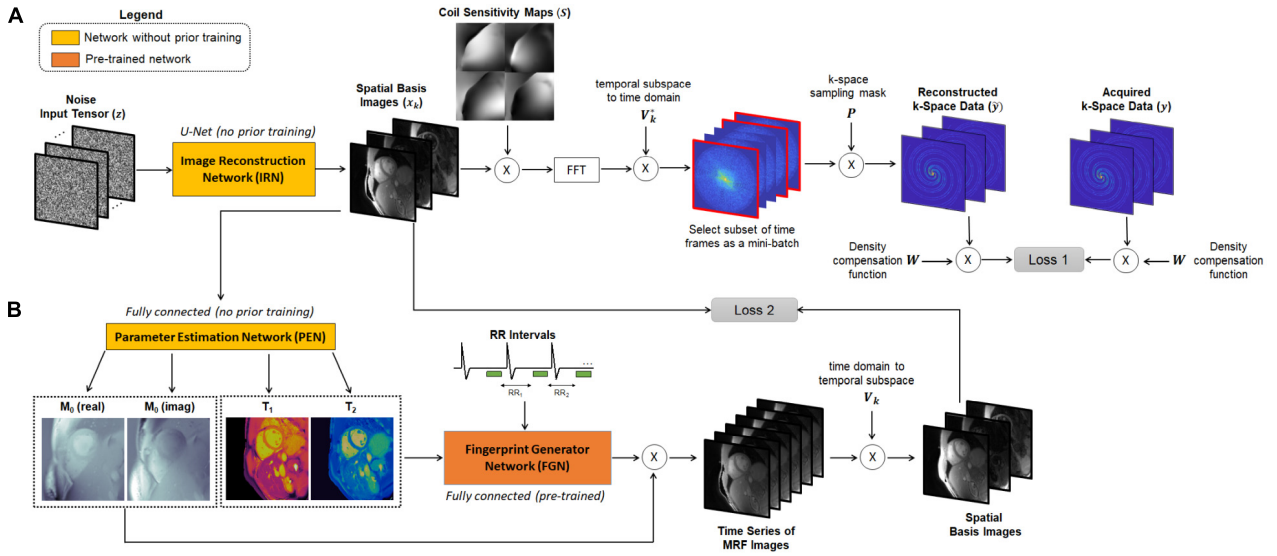

FIGURE 1 | Overview of the DIP-MRF reconstruction. A system of neural networks outputs spatial basis images and T_1, T_2, and M_0 maps, with no additional *in vivo* training data needed beyond the undersampled k-space data from the current scan. **(A)** The image reconstruction network (IRN) is a convolutional u-net that outputs a set of *k* spatial basis images. The input is a tensor of random numbers that remains fixed throughout training. Training is performed in a self-supervised manner by simulating the cardiac MRF forward encoding model. This step includes multiplication by coil sensitivity maps, fast Fourier transformation (FFT), projection of k-space data from the low-dimensional subspace to the time domain, and multiplication by spiral undersampling masks. The resulting k-space data are compared to the acquired k-space measurements, after density compensation, at the sampled locations using a mean squared error loss function (Loss 1), and IRN is updated using backpropagation. **(B)** A fully-connected network, referred to as the Parameter Estimation Network (PEN), uses the spatial basis images to output tissue property maps. Specifically, it outputs T_1, T_2, and a complex-valued M_0 scaling term. The T_1 map, T_2 map, and cardiac rhythm timings (RR intervals) from the ECG are input to the fingerprint generator network, which is a pre-trained fully-connected network that can be thought of as an efficient Bloch equation simulator that rapidly outputs cardiac MRF signal evolutions (fingerprints). The simulated fingerprints at all voxels are multiplied by the complex M_0 map to yield a time series of images. The images are projected onto the low-dimensional subspace and compared to the spatial basis images that were output by the IRN using a mean squared error loss function, and the PEN is updated using backpropagation (Loss 2). Note that the IRN and PEN are trained in parallel.

dimension contains the interleaved real and imaginary parts of the *k* spatial basis images.

A fully-connected network, which also is not pre-trained, outputs quantitative T_1, T_2, and M_0 maps from the spatial basis images. This network will be called the parameter estimation network (PEN) and is shown in **Figure 4**. The PEN has two hidden layers with 300 nodes per layer. Before being input to the network, the spatial basis images are vectorized to have size $(n_y n_x) \times (2k)$, where the second (channel) dimension contains interleaved real and imaginary signal intensities. The network output has one channel for each tissue property. As in previous MRF studies (13, 14), M_0 is modeled as a complex-valued scaling factor between the measured and simulated fingerprints, so the output has four channels for T_1, T_2, and the real and imaginary parts of M_0.

Self-Supervised Training

The IRN and PEN networks are trained *de novo* for each reconstruction in a self-supervised manner (**Figure 1**). Both networks are initialized with random weights and biases. Additionally, the input (z) to the IRN is initialized with random numbers and remains fixed throughout training. Both networks are trained in parallel using a loss function with two terms, one for updating each network. First, letting θ_{IRN} denote the network parameters of the IRN, the spatial basis images generated by the IRN can be written as,

$$x_k = \theta_{IRN}(z) \tag{1}$$

The spatial basis images are multiplied by coil sensitivity maps (S), transformed to k-space by performing an FFT, and multiplied by V_k^* to yield time series data. To reduce memory requirements, a subset of time frames is selected as mini-batch at this point. In practice, this is implemented by using $V_{i,k}^*$ instead of V_k, where $V_{i,k}^*$ denotes the i^{th} column vector from V_k^* (note that multiplication by $V_{i,k}^*$ projects data from the subspace to the time domain and extracts only the i^{th} time frame). The k-space data for time frame i are multiplied by the spiral undersampling mask for the corresponding time frame (P_i) and by the GROG density compensation function (W). The estimated multicoil k-space data for time frame i, denoted by $\tilde{y}_i$, can be written as,

$$\tilde{y}_i = WP_i\left((FSx_k)\,V_{i,k}^*\right) \tag{2}$$

The first loss term is calculated as the mean squared error between $\tilde{y}_i$ and the acquired multicoil k-space measurements after density compensation, denoted by y_i, at the sampled locations, and the IRN is updated using backpropagation.

$$\min_{\theta_{IRN}} \sum ||y_i - \tilde{y}_i||_2^2 \tag{3}$$

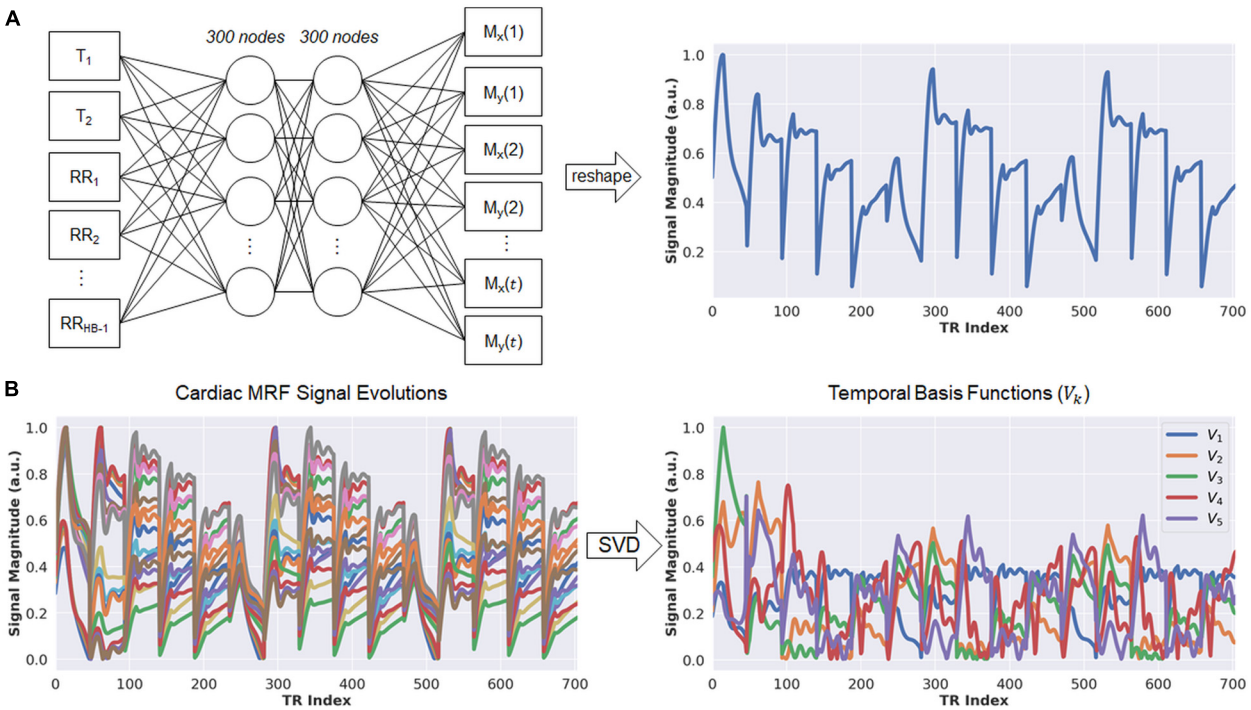

FIGURE 2 | Schematic of the fingerprint generator network (FGN) and derivation of the low-dimensional subspace. **(A)** The FGN is a fully-connected network with two hidden layers. The input consists of a T_1 value, T_2 value, and vector of RR interval times (RR_1, RR_2, …, RR_{HB-1}) recorded by the ECG, where RR_i denotes the elapsed time (in milliseconds) between the end of the acquisition window in heartbeat i and the beginning of the acquisition window in heartbeat $i+1$, and HB is the total number of heartbeats in the scan. The output is a vector of length $2t$, where t is the number of repetition times (i.e., number of time points), which contains the interleaved real and imaginary parts of an MRF fingerprint. **(B)** The FGN is used to calculate a dictionary of fingerprints for different T_1 and T_2 combinations specific for the patient's cardiac rhythm timings (left panel). The SVD of the dictionary is calculated in order to derive the low-rank approximation used in the DIP-MRF forward model calculation (right panel).

The PEN is updated in parallel using a second loss term. The T_1 and T_2 maps output by the PEN, along with the subject's RR interval times from the ECG, are input to the FGN to yield simulated fingerprints at each voxel location. These fingerprints are multiplied by the complex-valued M_0 map to obtain a time series of images that are projected onto the subspace by multiplication with V_k. Letting θ_{PEN} and θ_{FGN} denote the network parameters of the PEN and FGN, respectively, the second loss term is calculated as the mean squared error between the resulting images and the spatial basis images output by the IRN:

$$\min_{\theta_{PEN}} \sum ||x_k - (M_0 \theta_{FGN}(T_1, T_2, RR))\, V_k||_2^2 \qquad (4)$$

For all experiments, training was performed for 30,000 iterations using an Adam optimizer with learning rate 0.001. DIP-MRF was implemented in Tensorflow (v2.8) with Keras on a GPU (NVIDIA Tesla v100 16GB). A mini-batch size of 32 image frames was used to calculate the loss for the IRN.

Cardiac Magnetic Resonance Fingerprinting Acquisition Parameters

Data were collected using a fast imaging with steady state precession (FISP) cardiac MRF sequence with a 15-heartbeat (HB) breathhold and 254 ms ECG-triggered diastolic acquisition (15, 40). Variable flip angles (4–25°) and a constant TR/TE of 5.4/1.4 ms were employed. A total of 705 undersampled images were collected (one image per TR) with 47 images acquired every heartbeat. Magnetization preparation pulses were applied before the acquisition window in each heartbeat according to the following schedule, which repeated three times during the scan: HB1—inversion (21 ms), HB2—no preparation, HB3—T_2 prep (30 ms), HB4—T_2 prep (50 ms), HB5—T_2 prep (80 ms).

In addition, shortened MRF acquisitions were investigated having a five-heartbeat breathhold and progressively shorter acquisition windows. These were based on the same sequence structure, with the only difference being that the flip angle pattern within each heartbeat was truncated to fit within the desired scan window. An example of a flip angle series for a shortened scan is shown in **Supplementary Figure 2**. All data were acquired using a 48-fold undersampled spiral k-space trajectory (41) with a readout duration of 3.4 ms, matrix size of 192 × 192, field-of-view (FOV) of 300 × 300 mm^2, and golden angle rotation of the trajectory every TR (42).

Simulation Experiments

Simulations were performed to investigate the feasibility of shortening the breathhold and diastolic scan window in cardiac

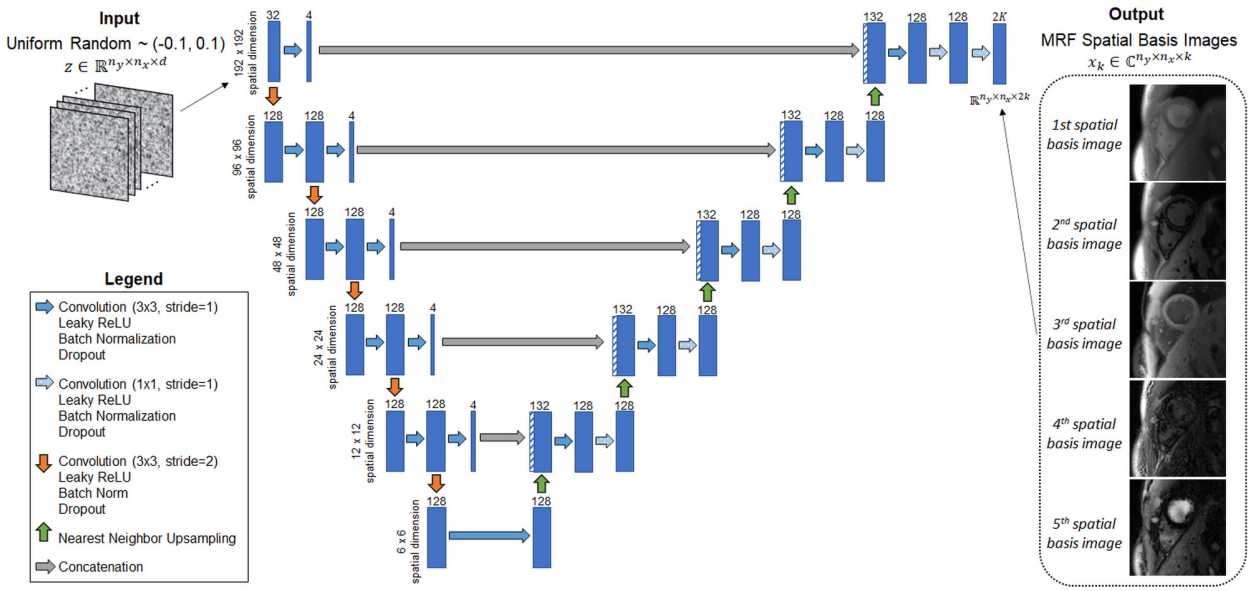

FIGURE 3 | Schematic of the image reconstruction network (IRN), which outputs MRF spatial basis images. The input, z, is a tensor of uniformly distributed random numbers between −0.1 and 0.1 that remains fixed while training the network. The network is a u-net that performs a series of 2D convolutions. It has five downsampling and upsampling paths with multiple shortcut connections. The network outputs the MRF spatial basis images—i.e., images in a low-dimensional subspace of rank k that was derived from a dictionary of simulated signal evolutions, as described in **Figure 2**. The number of 2D filters is listed above each convolutional layer (indicated by the blue rectangles).

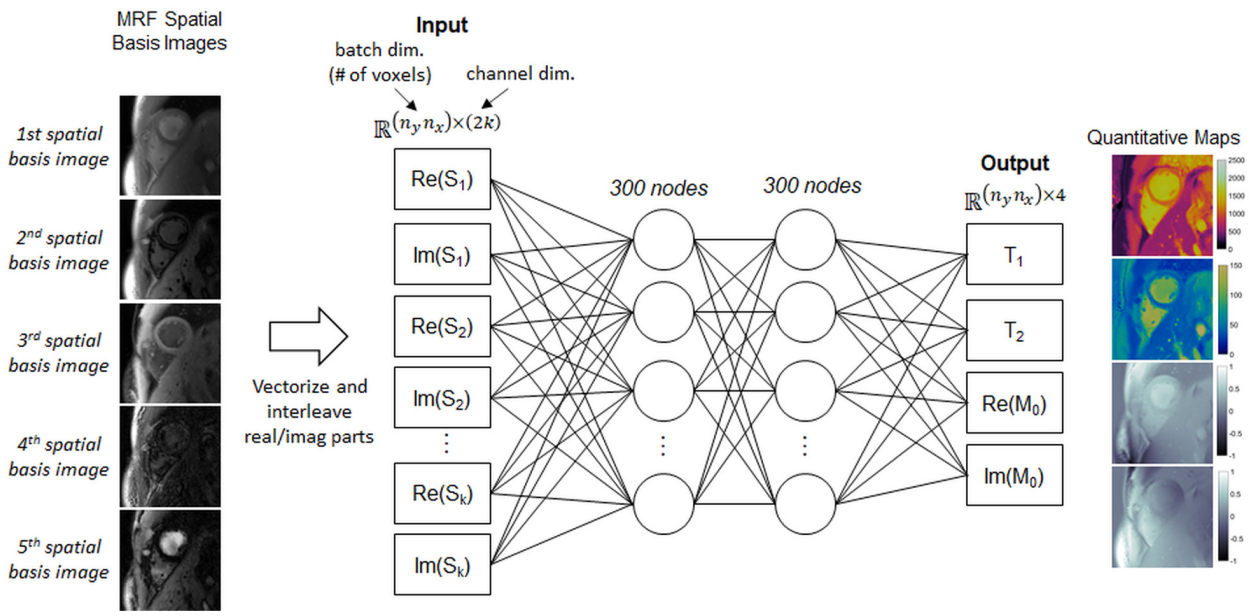

FIGURE 4 | Schematic of the parameter estimation network (PEN), which estimates quantitative maps from the spatial basis images. Before being input to the network, the spatial basis images are first vectorized to have size $n_y n_x$ (the batch dimension) by $2k$ (the channel dimension), where the channel dimension contains interleaved real and imaginary signal intensities from the k spatial basis images, and n_y and n_x are the spatial dimensions (number of voxels). The network has two hidden layers with 300 nodes per layer. The output has four channels corresponding to T_1, T_2, and the real and imaginary parts of the M_0 scaling term.

MRF. In addition to the scan with a 15HB breathhold and 254 ms acquisition window (705 total TRs), scans with a 5HB breathhold and acquisition windows of 254 ms (235 total TRs), 200 ms (185 total TRs), 150 ms (140 total TRs), 100 ms (95 total TRs), and 50 ms (45 total TRs) were simulated. The MRF data acquisition was simulated, including Bloch equation signal

simulation, coil sensitivity encoding with 8-channel sensitivity maps, and spiral k-space undersampling using the NUFFT. Complex Gaussian noise was added to the k-space data having a standard deviation of 0.1% of the maximum amplitude of the direct current (DC) signal. For each sequence variant, maps were reconstructed in three ways. In the first method (*direct matching*), one undersampled image was gridded every TR using the NUFFT, followed by dot product matching with a dictionary generated by a Bloch equation simulation to obtain T_1, T_2, and M_0 maps (13). In the second method (*SLLR-MRF*), a sparse and locally low rank MRF reconstruction was performed (34), which yielded a set of $k = 5$ spatial basis images that were matched to an SVD-compressed dictionary. Locally low rank regularization with an 8×8 patch size and l_1-wavelet regularization were used with regularization weights of $\lambda_{LLR} = 0.02$ and $\lambda_{wav} = 0.005$ relative to the maximum intensity in the basis images. The reconstruction was solved using non-linear conjugate gradient descent with 25 iterations. The third method (*DIP-MRF*) consisted of GROG preprocessing followed by the DIP-MRF reconstruction. The reconstructions were compared using the normalized root mean square error (nRMSE) relative to the ground truth T_1 and T_2 maps, computed over all non-background voxels (i.e., all voxels where the ground truth M_0 was non-zero).

A second set of simulations evaluated the robustness of DIP-MRF to noise. For the sequence with a 5HB breathhold and 150 ms acquisition window, complex Gaussian noise was added to the k-space data having standard deviations (σ_N) of 0, 0.1, 0.2, and 0.3% relative to the maximum amplitude of the DC signal. Maps were reconstructed using direct matching, SLLR-MRF, and DIP-MRF and compared in terms of nRMSE.

A third set of simulations assessed the impact of applying dropout during training (43). For the sequence with a 5HB breathhold and 150 ms acquisition window, the DIP-MRF reconstruction was repeated where different levels of dropout (0, 10, and 20%) were applied after each convolutional layer when training the IRN, and the maps were compared in terms of nRMSE.

Phantom Experiments

Experiments were performed using the ISMRM/NIST MRI system phantom (44) on a 1.5T scanner (MAGNETOM Sola, Siemens Healthineers, Erlangen, Germany). An 8 mm slice was planned through the T_2 layer of the phantom, which has 14 spheres spanning a range of physiological relaxation times with T_1 90–2,230 ms and T_2 10–750 ms. An artificial heart rate of 60 bpm was simulated on the scanner. Data were collected using two cardiac MRF sequences: a sequence with a 15HB breathhold and 254 ms acquisition window and a sequence with a 5HB breathhold and 150 ms acquisition window. Maps were reconstructed using direct matching, SLLR-MRF, and DIP-MRF. Data were also acquired with conventional cardiac mapping sequences using Siemens MyoMaps software (45). T_1 maps were collected with 5(3)3 modified look-locker inversion recovery (MOLLI) (46), and T_2 maps were collected using a 1(3)1(3)1 T_2-prepared balanced steady state free precession (bSSFP) sequence with T_2 prep times of 0, 25, and 55 ms (5). Conventional cardiac mapping scans used GRAPPA with an acceleration factor of 2 and 24 autocalibration lines, 6/8 partial Fourier, a flip angle of 35°, and a scan window of 209 ms. All scans were collected with a matrix size of 192×192 and 300 mm^2 FOV. Reference T_1 values were measured using an inversion recovery spin echo sequence with TR = 10 s, TE = 12 ms, and inversion times of 21, 100, 200, 400, 800, and 1,600 ms. Reference T_2 values were measured with a single-echo spin echo sequence with TR = 10 s and echo times of 10, 20, 40, 60, 100, 150, and 200 ms. Mean relaxation times were measured within each vial and compared to reference values using linear regression and Bland-Altman analyses (47). T_2 values above 200 ms were excluded from analysis because the cardiac MRF sequence was not designed for that regime, considering that the longest T_2 prep time was 80 ms (for completeness, measurements in all 14 vials are reported in the **Supplementary Material**).

Scans in Healthy Subjects and Patients

Eighteen healthy subjects were scanned at 1.5T after obtaining written informed consent in this IRB-approved, HIPAA-compliant study. All scans were performed during an end-expiratory breathhold at a mid-ventricular slice position. MOLLI and T_2-prep bSSFP mapping were performed in all subjects. Data were also acquired using 15HB/254 ms and 5HB/150 ms cardiac MRF acquisitions, and maps were reconstructed using direct matching, SLLR-MRF, and DIP-MRF. To study the effects of training with dropout and to determine the optimal dropout percentage, the DIP-MRF reconstruction was repeated in three subjects with 0, 5, 10, 20, and 30% dropout applied after each convolutional layer when training the IRN. Unless otherwise states, the DIP-MRF reconstruction used dropout levels of 10 and 20% for the 15HB/254 ms and 5HB/150 ms MRF acquisitions, respectively.

In addition, data were collected in ten patients referred for a clinical CMR exam due to suspected cardiomyopathy. Native T_1 and T_2 maps were collected using the same protocol as in healthy subjects. Post-contrast T_1 and T_2 maps were acquired 15–25 min after IV injection of 0.2 mmol/kg body weight gadoteridol (ProHance, Bracco Diagnostics Inc., Princeton, NJ, United States). While post-contrast MRF scans (both 15HB/254 ms and 5HB/150 ms versions) were performed in all patients, post-contrast MOLLI and T_2-prep bSSFP sequences were only collected in nine and three patients, respectively.

In vivo data were analyzed by manually segmenting the maps according to American Heart Association (AHA) guidelines (48). The mean and standard deviation for T_1 and T_2 were measured within each AHA segment and over all voxels in the myocardium. Similarly, T_1 and T_2 values were measured within the left (LV) and right ventricular (RV) blood pools after manual segmentation, taking care to avoid trabeculations and papillary muscles. Intersubject variability was quantified as the standard deviation of the mean T_1 or T_2 values over all subjects. Intrasubject variability was quantified by measuring the standard deviation in T_1 or T_2 for each subject and then calculating the mean over all subjects. T_1 and T_2 measurements using different reconstruction methods within the same subject were compared

using a within-subjects ANOVA test with a Bonferroni *post-hoc* test for multiple comparisons, with $p < 0.05$ indicating statistical significance, as well as Bland-Altman plots. T_1 and T_2 measurements between healthy subjects and patients were compared using a two-sample *t*-test.

RESULTS

Simulation Experiments

Figure 5A shows simulation results using MRF sequences with different breathhold and acquisition window lengths. In all cases, the nRMSE was highest with direct matching and lowest with DIP-MRF, and this difference was more pronounced for shorter sequence lengths. As the breathhold and acquisition window were shortened, nRMSE increased for direct matching and SLLR-MRF but remained consistently low for DIP-MRF. For the 15HB/254 ms sequence, the nRMSE was (T_1 6.5%, T_2 11.2%) for direct matching, (T_1 2.9%, T_2 4.3%) for SLLR-MRF, and (T_1 1.4%, T_2 0.7%) for DIP-MRF. For the 5HB/150 ms sequence, the nRMSE was (T_1 13.4%, T_2 20.2%) for direct matching, (T_1 6.4%, T_2 9.1%) for SLLR-MRF, and (T_1 1.2%, T_2 0.8%) for DIP-MRF. **Supplementary Figure 3** shows examples of T_1, T_2, and M_0 maps from the simulation study.

Figure 5B plots the nRMSE for the 5HB/150 ms sequence as the k-space data were corrupted with different amounts of complex Gaussian noise. The nRMSE was highest with direct matching and lowest with DIP-MRF at all noise levels. At the highest noise level tested ($\sigma_N = 0.3\%$ of the DC signal), the nRMSE was (T_1 14.9%, T_2 22.5%) for direct matching, (T_1 10.0%, T_2 14.6%) for SLLR-MRF, and (T_1 1.5%, T_2 0.9%) for DIP-MRF.

Supplementary Figure 4 demonstrates the importance of applying dropout in DIP-MRF, with simulation results shown for the 5HB/150 ms sequence. Without dropout, the nRMSE reached a minimum (T_1 1.7%, T_2 1.0%) after approximately 5,000 iterations. The nRMSE increased gradually with further training due to overfitting to noise and undersampling artifacts, reaching (T_1 2.2%, T_2 1.4%) after 30,000 iterations. Using dropout improved the reconstruction accuracy, as the minimum nRMSE was lower compared to the 0% dropout case, and it reduced overfitting, allowing the network to be trained for longer without causing the nRMSE to increase. For example, with 20% dropout, the nRMSE reached a minimum of (T_1 1.5%, T_2 0.8%) after 12,000 iterations and only increased slightly to (T_1 1.7%, T_2 1.0%) after 30,000 iterations.

Phantom Experiments

Bland-Altman plots showing the agreement between 15HB/254 ms MRF, 5HB/150 ms MRF, and conventional mapping sequences relative to reference values are shown in **Figure 6**; linear regression plots of the same data are shown in **Supplementary Figure 5**, and T_2 measurements in all 14 vials (including vials with $T_2 > 200$ ms) are given in **Supplementary Figures 6**, **7**. There were no significant differences in T_1 or T_2 relative to reference values for all MRF methods. Using DIP-MRF, the bias and 95% limits of agreement (LoA) for T_1 were 4 ms (−45, 52)ms for the 15HB/254 ms sequence and −5 ms (−61, 51) ms for the 5HB/150 ms sequence; for T_2, they were −0.9 ms (−5.5, 3.7) ms for the 15HB/254 ms sequence and 0.2 ms (−3.1, 3.4) ms for the 5HB/150 ms sequence. In general, DIP-MRF yielded narrower limits of agreement compared to direct matching and SLLR-MRF. MOLLI slightly underestimated T_1 with a bias of −39 ms and 95% LoA of (−86, 8) ms. T_2-prep bSSFP overestimated T_2 with a bias of 35.6 ms and 95% LoA of (−45.9, 117.2) ms. This overestimation was larger for vials with short T_2 values below approximately 100 ms, which is apparent on the linear regression plots (**Supplementary Figure 5**). The correlation coefficients were similar among all reconstructions for the 15HB/254 ms MRF sequence, with all $R^2 > 0.998$. For the 5HB/150 ms sequence, the correlation was slightly higher for DIP-MRF ($R^2 = 0.999$ for T_1, $R^2 = 1.000$ for T_2) compared to direct matching ($R^2 = 0.998$ for T_1, $R^2 = 0.995$ for T_2) and SLLR-MRF ($R^2 = 0.998$ for T_1, $R^2 = 0.999$ for T_2).

Scans in Healthy Subjects

Representative maps in a healthy subject using 15HB/254 ms MRF, 5HB/150 ms MRF, and conventional mapping sequences are shown in **Figure 7**. Additional examples are provided in **Supplementary Figures 8–10**. Some noise enhancement was observed with direct matching for the 15HB/254 ms MRF sequence, with better map quality using SLLR-MRF and DIP-MRF reconstructions. The improvement using DIP-MRF was especially pronounced for the 5HB/150 ms sequence; direct matching led to severe noise enhancement and aliasing artifacts, SLLR-MRF provided only moderate noise suppression, and DIP-MRF gave the best suppression of noise and aliasing artifacts while preserving high resolution details, such as the papillary muscles.

Figure 8 shows examples of spatial basis images from DIP-MRF compared to those from conventional NUFFT gridding and SLLR-MRF. Noise enhancement was observed with NUFFT gridding, especially for the 4th and 5th basis images, which was partially reduced using SLLR-MRF, with DIP-MR yielding the best image quality.

Figure 9 demonstrates the effect of training DIP-MRF with different levels of dropout, akin to the simulation results in **Supplementary Figure 4**. From a visual inspection of the maps, the dropout level that yielded the best noise suppression while preserving high resolution details was 10% for the 15HB/254 ms sequence and 20% for the 5HB/150 ms sequence, when the number of training iterations was fixed at 30,000. Noise enhancement and residual aliasing artifacts were observed at lower dropout levels, whereas overly smoothed maps with loss of fine resolution details were seen at higher dropout levels. Results in two additional subjects are shown in **Supplementary Figures 11**, **12**.

Boxplots summarizing the average relaxation times over all subjects in the myocardial septum are shown in **Figure 10**. T_1 values reported as mean ± standard deviation were: MOLLI (1,006 ± 28 ms); 15HB/254 ms MRF with direct matching (1,043 ± 36 ms), SLLR-MRF (1,064 ± 42 ms), and DIP-MRF (1,044 ± 33 ms); and 5HB/254 ms MRF with direct matching (1,065 ± 53 ms), SLLR-MRF (1,072 ± 39 ms), and DIP-MRF (1,035 ± 32 ms). T_2 values were: T_2-prep bSSFP (47.7 ± 1.6 ms);

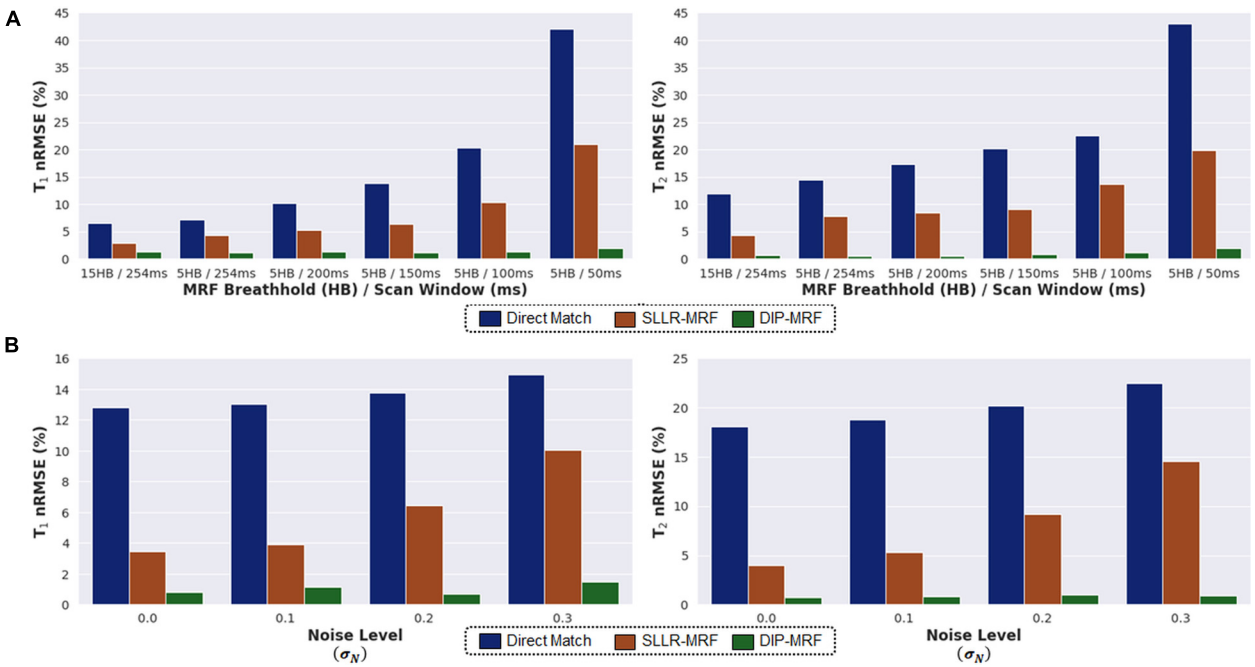

FIGURE 5 | Simulation results in the MRXCAT phantom comparing the deep image prior (DIP-MRF) to direct matching and a low-rank subspace reconstruction (SLLR-MRF). **(A)** nRMSE plots of the T_1 and T_2 maps are shown for different cardiac MRF sequence lengths. Results are shown for MRF with a 15-heartbeat breathhold and 254 ms diastolic acquisition window, as well as shortened scans with a 5-heartbeat breathhold and successively shorter acquisition windows of 254, 200, 150, 100, and 50 ms. **(B)** nRMSE plots of the T_1 and T_2 maps are shown for the 5HB/150 ms MRF scan, where different amounts of random Gaussian noise having standard deviation σ_N (expressed as a percentage of the maximum DC signal level) were added to the simulated k-space data.

15HB/254 ms MRF with direct matching (40.8 ± 3.0 ms), SLLR-MRF (42.3 ± 3.0 ms), and DIP-MRF (41.3 ± 2.9 ms); and 5HB/254 ms MRF with direct matching (46.1 ± 9.0 ms), SLLR-MRF (44.5 ± 3.9 ms), and DIP-MRF (43. ± 3.8 ms). T_1 was significantly higher with all MRF techniques compared to MOLLI. T_2 was significantly lower with all MRF techniques compared to T_2-prep bSSFP, except for the 5HB/150 ms sequence with direct matching. A similar analysis of relaxation times in LV and RV blood is given in **Supplementary Figure 14**.

The intersubject variability, quantified as the standard deviation of the mean T_1 or T_2 over all subjects, was similar among all reconstructions for the 15HB/254 ms MRF scan. For the 5HB/150 ms scan, DIP-MRF yielded a lower intersubject variability (32 ms for T_1, 3.8 ms for T_2) compared to direct matching (53 ms for T_1, 9.0 ms for T_2) and SLLR-MRF (39 ms for T_1, 3.9 ms for T_2), although still higher than conventional mapping sequences (28 ms for T_1, 1.5 ms for T_2).

Bland-Altman plots comparing relaxation times measured with 15HB/254 ms vs. 5HB/150 ms MRF scans are shown in **Figure 11** (note that a positive bias indicates higher measurements using the 5HB/150 ms scan). Both scans yielded good agreement in T_1 when using the DIP-MRF reconstruction, with a bias of −9 ms and 95% LoA (−56, 38) ms. Similar results were seen with SLLR-MRF, having a bias of 8 ms and 95% LoA (−41, 58) ms, while a larger bias (22 ms) and wider limits of agreement of (−81, 206) ms were observed with direct matching. DIP-MRF yielded the best agreement between T_2 measurements from the 15HB/254 ms and 5HB/150 ms scans, with a bias of 2.0 ms and 95% LoA (−1.9, 6.0) ms. SLLR-MRF had a similar bias (2.1 ms) but wider limits of agreement of (−3.4, 7.7) ms. Direct matching had the largest bias (5.3 ms) and widest limits of agreement (−8.7, 19.4) ms.

Figures 12A,B show the spatial distribution of T_1 and T_2 within individual myocardial segments and over the entire myocardium. Both 15HB/254 ms and 5HB/150 ms MRF scans showed some regional variability in T_1 and T_2, with higher values in the septum and lower values in the inferolateral segment. A similar but less pronounced trend was seen with MOLLI but not with T_2-prepared bSSFP. Greater regional variability was seen with direct matching compared to SLLR-MRF and DIP-MRF.

Figures 12C,D summarize the intrasubject variability for T_1 and T_2, quantified as the mean of the standard deviations over all subjects, shown within each myocardial segment and over the entire myocardium. Compared to MOLLI (57 ms), the intrasubject variability in T_1 over the entire myocardium was significantly higher using the 15HB/254 ms MRF sequence with direct matching (94 ms); this variability was reduced with SLLR-MRF (66 ms) and DIP-MRF (57 ms) and was not significantly different from MOLLI. For the 5HB/150 ms MRF sequence, the intrasubject variability was significantly higher than MOLLI when using direct matching (160 ms) and SLLR-MRF (86 ms); DIP-MRF yielded the lowest variability (61 ms) with no significant difference relative to MOLLI. Compared to T_2-prep bSSFP (4.2 ms), the intrasubject variability in T_2 over

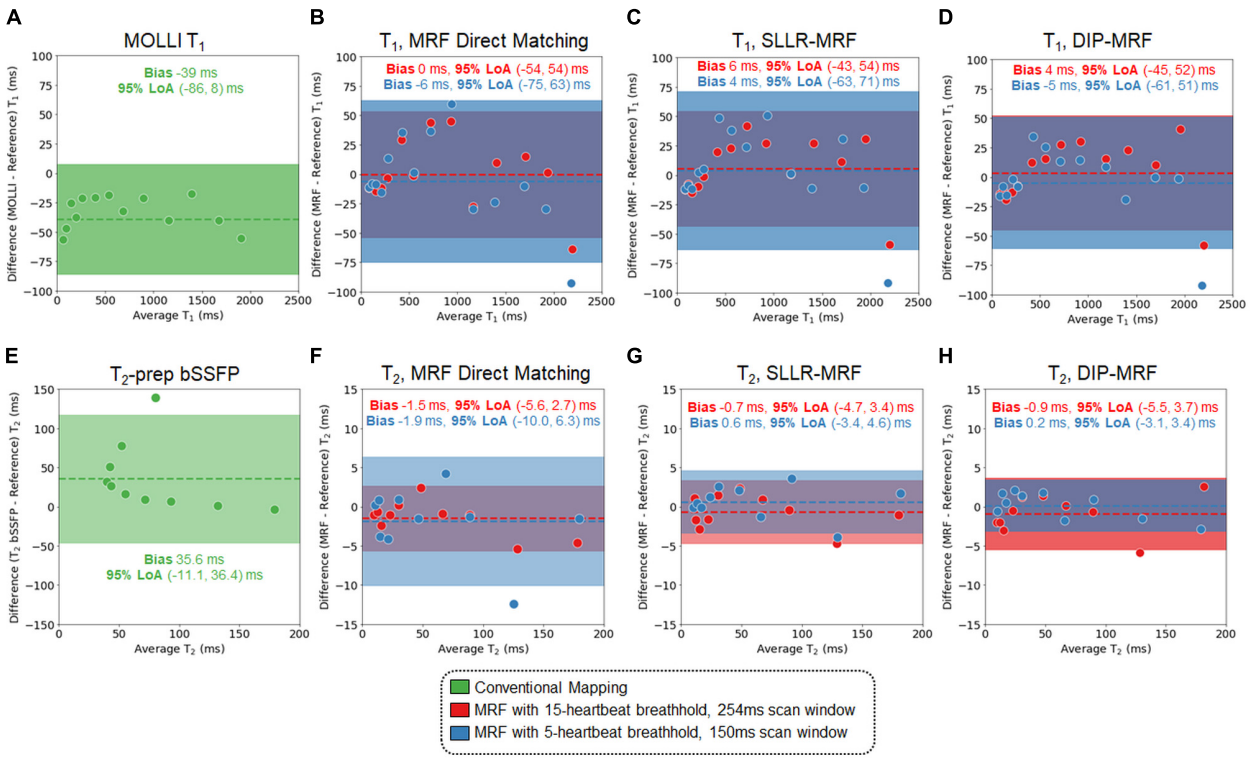

FIGURE 6 | Bland-Altman plots from the phantom study. Plots are shown for T_1 comparing **(A)** MOLLI and cardiac MRF with **(B)** direct matching, **(C)** SLLR-MRF, and **(D)** DIP-MRF reconstructions relative to gold standard measurements using an inversion recovery sequence. Similarly, plots are shown for T_2 comparing **(E)** T_2-prepared bSSFP and cardiac MRF with **(F)** direct matching, **(G)** SLLR-MRF, and **(H)** DIP-MRF reconstructions relative to gold standard measurements using a single-echo spin echo sequence. Results are shown for both 15HB/254 ms and 5HB/150 ms MRF sequences. The bias is indicated by a dotted line, and the 95% limits of agreement (LoA) are indicated by the solid colors.

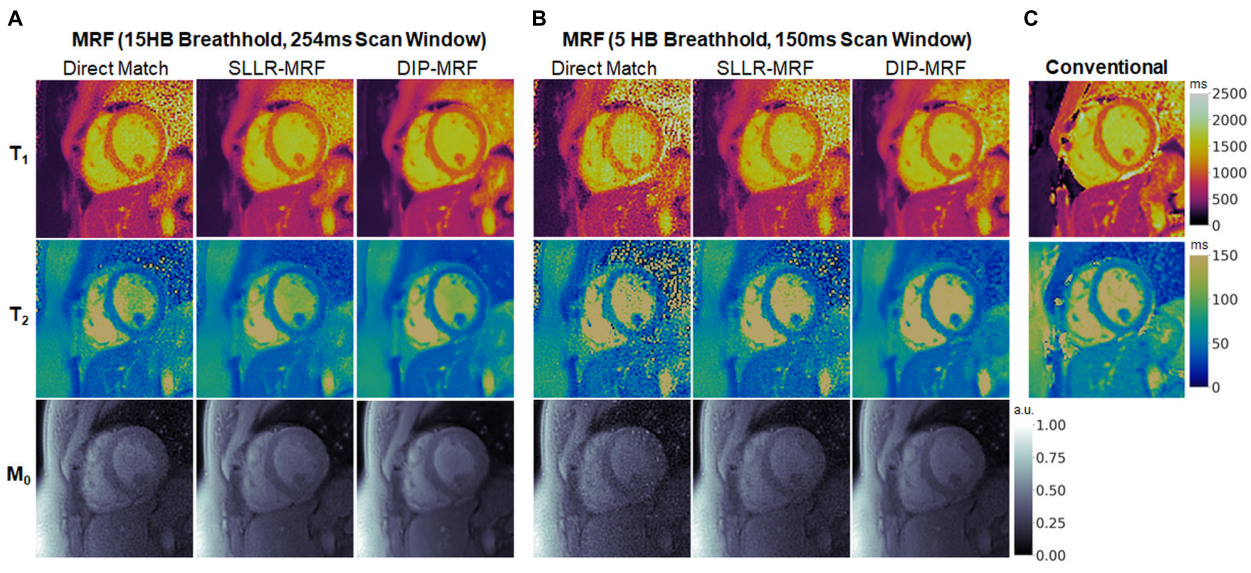

FIGURE 7 | Cardiac MRF T_1, T_2, and M_0 maps from a healthy subject. Maps reconstructed using direct matching, SLLR-MRF, and DIP-MRF are shown for **(A)** the 15HB/254 ms MRF sequence and **(B)** the 5HB/150 ms MRF sequence. **(C)** Conventional MOLLI and T_2-prepared bSSFP maps are shown for comparison. All maps were cropped to a 100 × 100 region centered over the heart.

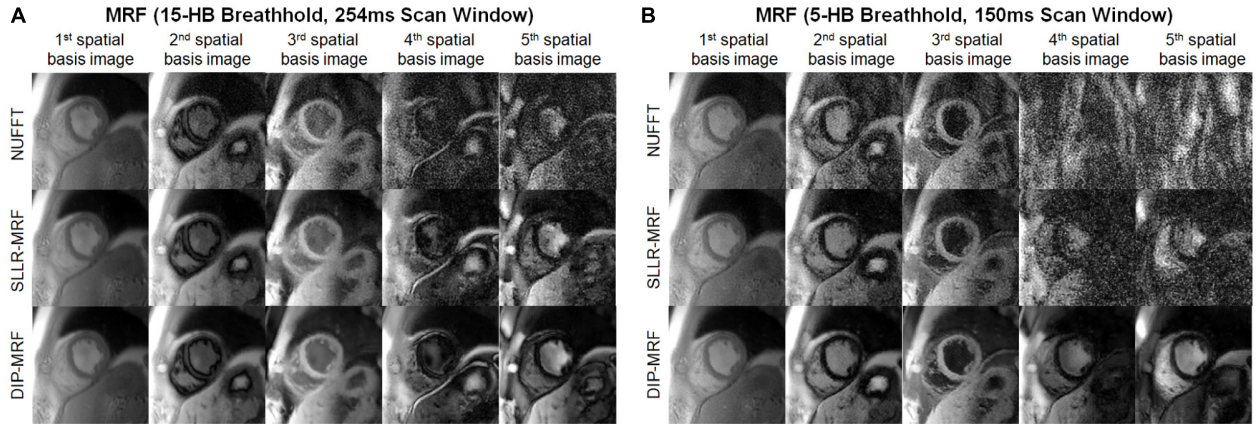

FIGURE 8 | Cardiac MRF spatial basis images from a healthy subject. Spatial basis images from **(A)** the 15HB/254 ms MRF scan and **(B)** the 5HB/150 ms MRF scan are shown, reconstructed using (top row) NUFFT gridding, (middle row) SLLR-MRF, and (bottom row) DIP-MRF. Noise enhancement was observed with NUFFT gridding and to a lesser extent SLLR-MRF, while DIP-MRF yielded the best image quality. Although they tend to look similar, the contrasts of the spatial basis images in panels **(A,B)** are not expected to be identical, as a different subspace (derived from the SVD of a dictionary of signal evolutions) is calculated separately for each scan. All images were cropped to a 100 × 100 region centered over the heart.

the entire myocardium using the 15HB/254 ms MRF sequence was significantly higher using direct matching (5.6 ms), non-significantly lower using SLLR-MRF (3.9 ms), and significantly lower using DIP-MRF (3.3 ms). For the 5HB/150 ms MRF sequence, the intrasubject variability was significantly higher than T_2-prep using direct matching (19.1 ms) and SLLR-MRF (7.1 ms); DIP-MRF yielded the lowest variability (4.1 ms) with no significant difference relative to T_2-prep bSSFP.

Patient Scans

Representative maps from a cardiomyopathy patient are shown in **Figure 13**, with additional patient examples provided in **Supplementary Figures 15**, **16**. In both native and post-contrast maps in patients, DIP-MRF yielded the best suppression of noise and aliasing artifacts, especially for the shortened 5HB/150 ms acquisition, where direct matching led to severe noise and artifacts that were only moderately improved with the SLLR-MRF reconstruction.

Figure 14 shows one example of a patient scan where the 15HB breathhold and 254 ms acquisition window resulted in motion artifacts. In this case, motion caused blurring of the myocardial wall and an artifactual increase in septal relaxation times due to partial volume effects between myocardium and blood, with DIP-MRF yielding T_1 1263 ± 48 ms and T_2 55.8 ± 6.5 ms. To confirm the presence of motion, a sliding window reconstruction was performed (window size = 48 TRs) to visualize one image per heartbeat, shown in **Supplementary Figure 17**. This analysis confirmed that the patient breathed halfway during the scan, and residual cardiac motion was apparent in the later heartbeats. Motion and partial volume effects were reduced using the shorter 5HB breathhold and 150 ms acquisition window, leading to a sharper depiction of the myocardial wall and lower septal relaxation times of T_1 1130 ± 27 ms and T_2 48.8 ± 4.1 ms (although T_1 and T_2 were still elevated compared to healthy subjects). Conventional MOLLI and T_2-prep bSSFP mapping values in this patient were T_1 = 1,122 ± 47 ms and T_2 = 50.1 ± 4.1 ms.

Boxplots summarizing the distribution of native and post-contrast relaxation times in the myocardial septum in patients are shown in **Figure 15**. Using the DIP-MRF reconstruction, both 15HB/254 ms MRF (1,079 ± 72 ms) and 5HB/150 ms MRF (1,047 ± 46 ms) acquisitions yielded higher native T_1 than MOLLI (1,033 ± 34 ms); this difference was statistically significant for 5HB/150 ms DIP-MRF. Native T_2 was non-significantly lower with both 15HB/254 ms MRF (45.2 ± 5.8 ms) and 5HB/150 ms MRF (45.7 ± 4.0 ms) compared to T_2-prep bSSFP (47.6 ± 3.9 ms). Patients had higher native T_1 than healthy subjects, but this trend was not significant for MOLLI, 15HB/254 ms MRF, or 5HB/150 ms MRF. Compared to healthy subjects (45.2 ms), native T_2 in patients was significantly lower with 15HB/254 ms MRF (41.3 ms) and non-significantly lower with 5HB/150 ms MRF (43.3 ms). No difference between patients and healthy subjects was seen with T_2-prep bSSFP (47.6 vs. 47.7 ms). There were no significant differences in post-contrast T_1 among MOLLI (417 ± 38), 15HB/254 ms MRF (409 ± 62 ms), or 5HB/150 ms MRF (397 ± 51 ms). Post-contrast myocardial T_2 was 37.9 ± 3.0 ms using 15HB/254 ms MRF and 38.7 ± 3.5 ms using 5HB/150 ms MRF (**Supplementary Figure 18**). Post-contrast T_2 bSSFP data were only acquired in a subset of three patients; a comparison of post-contrast T_2 bSSFP and MRF in these patients is provided in **Supplementary Table 1**. An analysis of native and post-contrast relaxation times in LV and RV blood in patients is given in **Supplementary Figure 19**.

DISCUSSION

This study introduced a self-supervised deep learning reconstruction for cardiac MRF, called DIP-MRF, that combines low-rank subspace modeling with the denoising

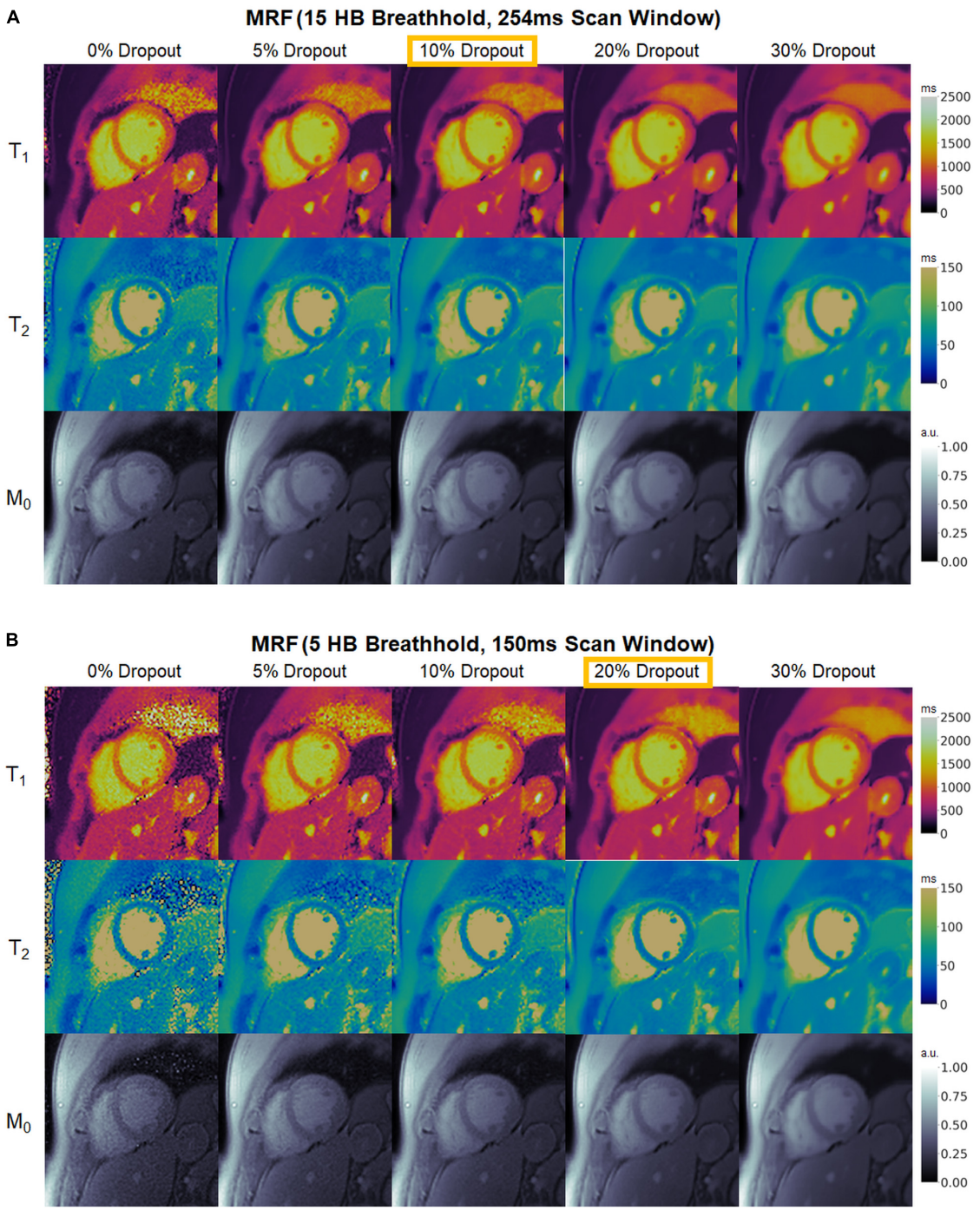

FIGURE 9 | Maps from a healthy subject using DIP-MRF with different levels of dropout during training. The best dropout percentage was determined empirically to be **(A)** 10% for the 15HB/254 ms MRF sequence and **(B)** 20% for the 5HB/150 ms MRF sequence. In all cases, the number of training iterations was fixed at 30,000. Using lower dropout led to increased noise and undersampling artifacts, while higher dropout led to overly smoothed maps with a loss of high-resolution details. All maps were cropped to a 100 × 100 region centered over the heart.

capabilities of a deep image prior. DIP-MRF was shown to reduce noise and aliasing artifacts in tissue property maps compared to conventional dictionary matching and a low-rank subspace reconstruction with spatial and locally low rank constraints (SLLR-MRF). DIP-MRF was leveraged to shorten the breathhold duration of cardiac MRF from 15 to 5 heartbeats and the diastolic acquisition from 250 to 150 ms *in vivo*, which can potentially reduce motion artifacts, especially for

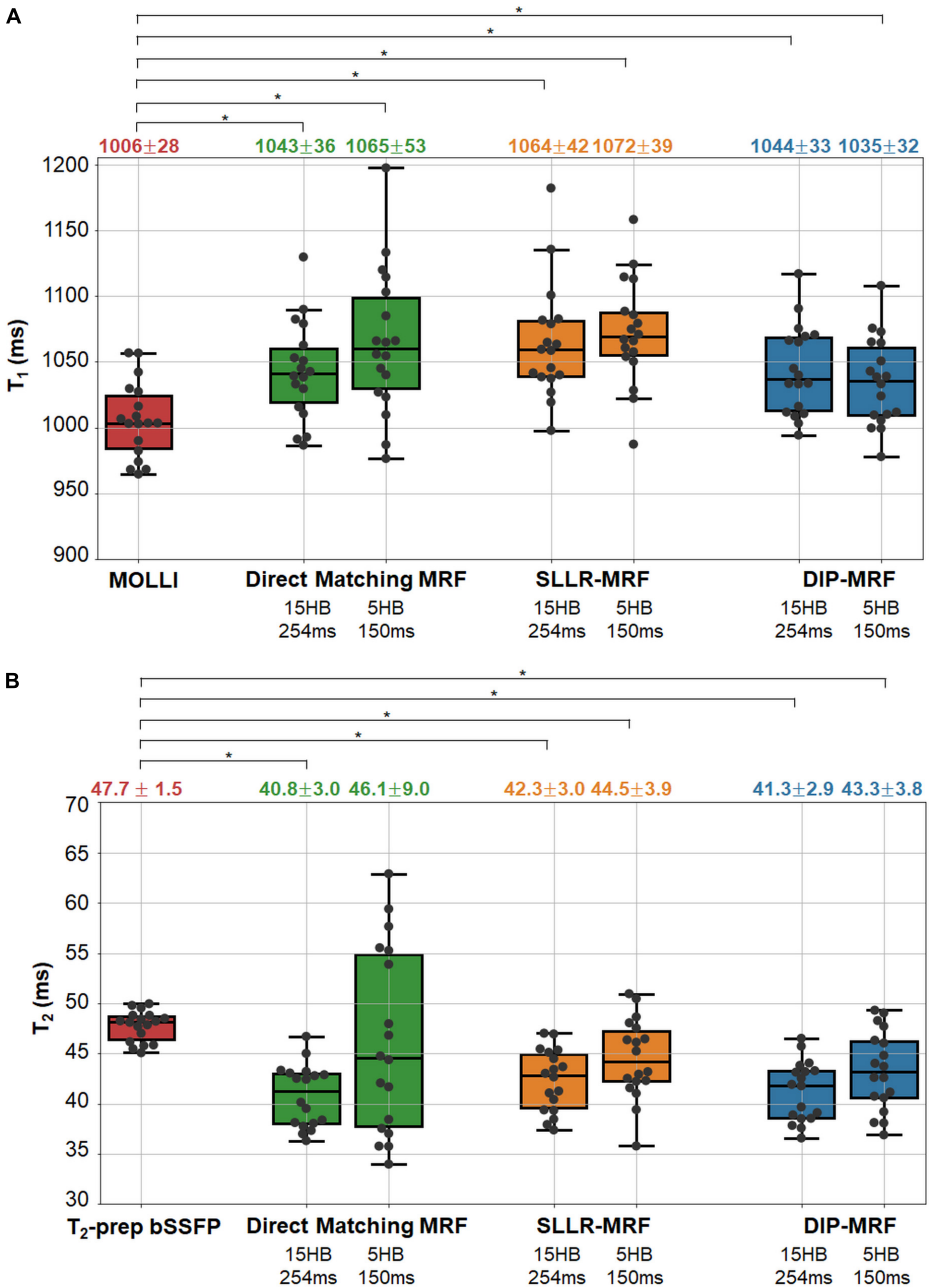

FIGURE 10 | Myocardial T_1 and T_2 in healthy subject in the left ventricular septum. The boxplots show the distribution of mean **(A)** T_1 and **(B)** T_2 values using MOLLI and T_2-prep bSSFP mapping sequences, as well as 15HB/254 ms and 5HB/150 ms MRF sequences with direct matching, SLLR-MRF, and DIP-MRF reconstructions. The top of each box indicates the upper quartile, the bottom indicates the lower quartile, and the horizontal line through the middle shows the median. The numbers above each plot indicate the mean ± standard deviation in milliseconds. Asterisks indicate a significant difference ($p < 0.05$) using a within-subjects ANOVA test with a Bonferroni *post-hoc* test for multiple comparisons.

patients who have difficulty performing long breathholds or who have elevated heart rates. By minimizing motion, the shortened acquisition may also decrease partial volume artifacts between myocardium and blood, leading to more accurate and reproducible myocardial T_1 and T_2 measurements. This effect was demonstrated in **Figure 14**, where motion resulted in an artifactual increase in myocardial T_1 and T_2 with the longer MRF scan that was mitigated by shortening the breathhold and scan window.

In most deep learning reconstructions, a neural network is pre-trained using a large number of reference images. For MRF, such training data would consist of "ground truth" tissue property maps (the network output) paired with a time series of undersampled images or k-space measurements (the network

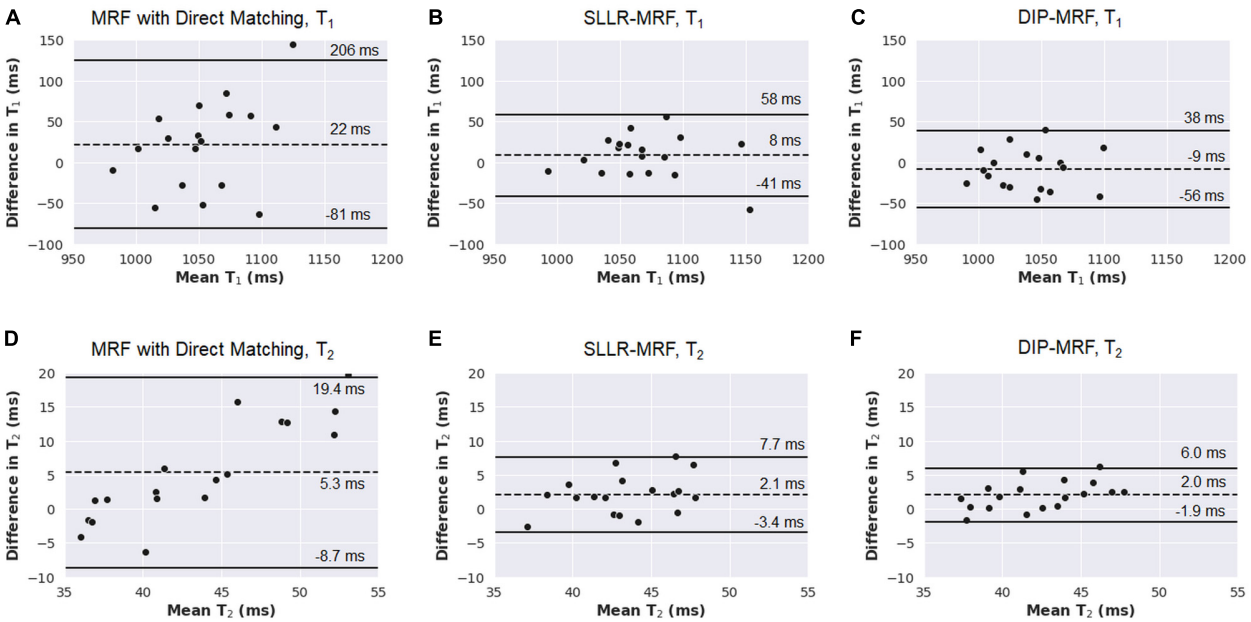

FIGURE 11 | Bland-Altman plots comparing measurements from 15HB/254 ms MRF and 5HB/150 ms MRF scans with different reconstruction methods in healthy subjects. Results are shown for T_1 using **(A)** direct matching, **(B)** SLLR-MRF, and **(C)** DIP-MRF. Similar results for T_2 are shown in panels **(D-F)**. On each plot, the bias is indicated by a dotted line, and the 95% limits of agreement are indicated by solid lines. Note that a positive bias indicates higher T_1 or T_2 measurements using 5HB/150 ms MRF compared to 15HB/254 ms MRF.

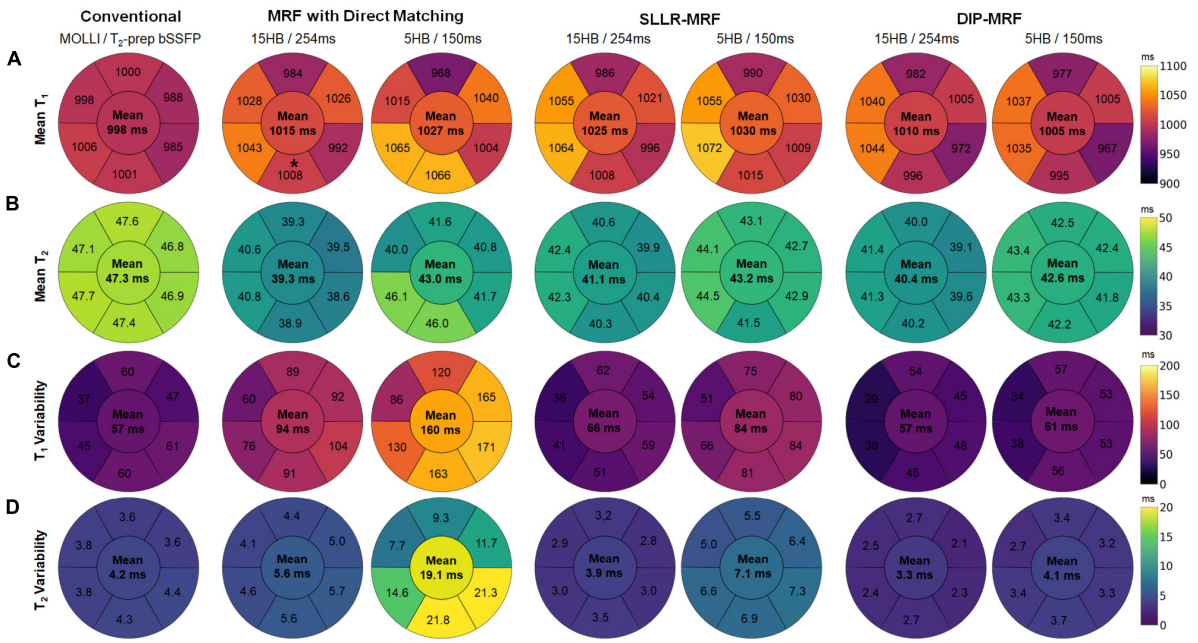

FIGURE 12 | Bullseye plots showing the spatial distribution of T_1 and T_2 in different myocardial segments of a mid-ventricular slice in healthy subjects. **(A)** Mean T_1 and **(B)** mean T_2 values are shown for mid-ventricular AHA segments, with the value in the center of the bullseye indicating the average over the entire myocardium. The spatial variability (standard deviations) for T_1 and T_2 within each segment and over the entire myocardium are shown in panels **(C,D)**, respectively.

input). While it is possible to collect such training data in stationary organs, like the brain, it is more challenging in the heart due to physiological motion and the long scan times that would be required to collect fully-sampled MRF data (on the order of several minutes). Additionally, the fingerprints in cardiac MRF are dependent on the subject's cardiac rhythm because the

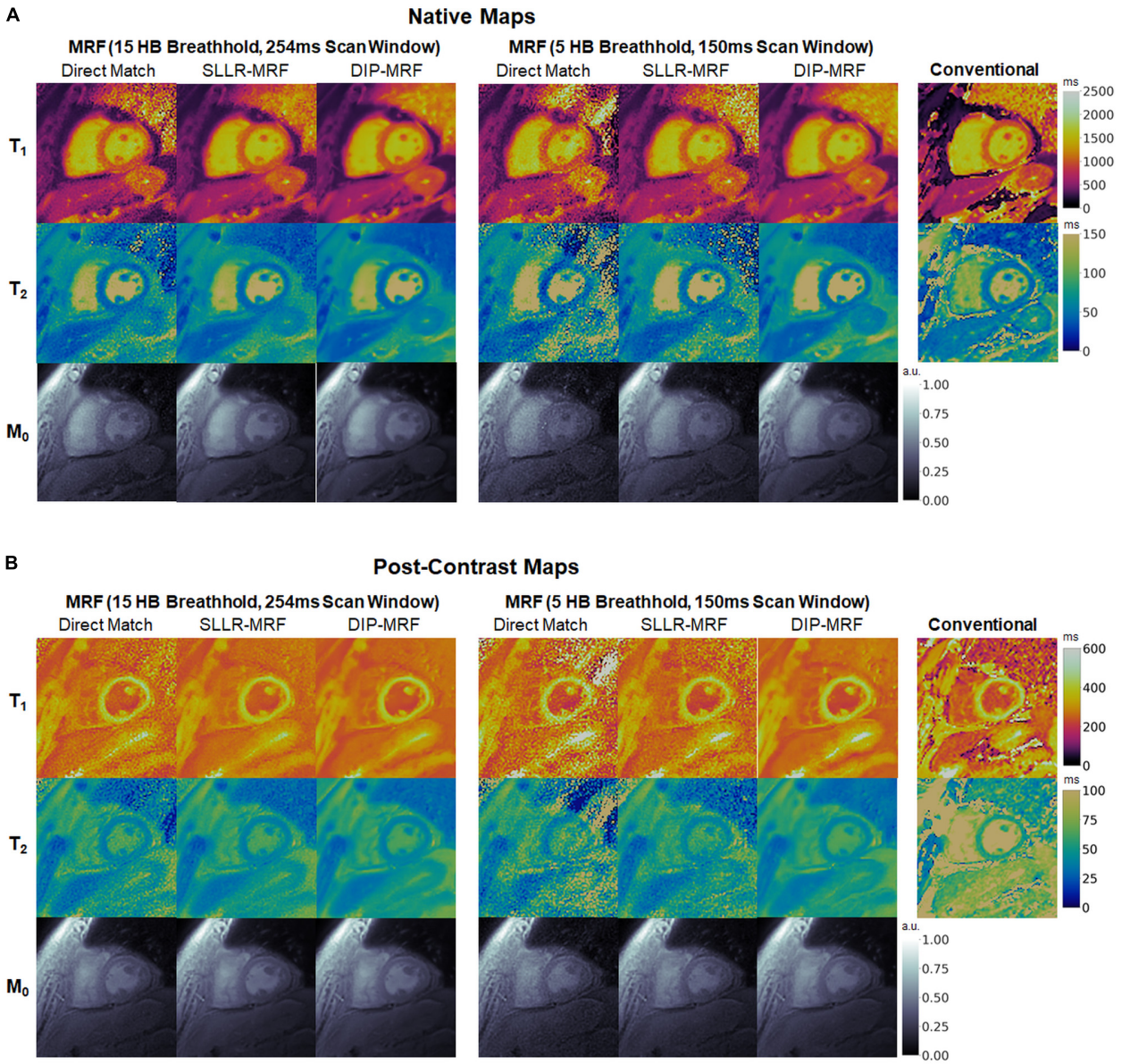

FIGURE 13 | (A) Native and **(B)** post-contrast T_1, T_2, and M_0 maps from a cardiomyopathy patient. Results are shown for conventional MOLLI and T_2-prepared bSSFP sequences, as well as 15HB/254 ms and 5HB/150 ms MRF sequences using direct matching, SLLR-MRF, and DIP-MRF reconstructions. All maps were cropped to a 100 × 100 region centered over the heart.

scan uses prospective ECG triggering, so many datasets would potentially be needed to ensure the network provides accurate tissue property estimates independent of a patient's cardiac rhythm. DIP-MRF addresses these challenges by eliminating the need for prior training. Instead, training is performed *de novo* after each MRF acquisition, and the only requirements for training data are the undersampled k-space measurements from the current scan and the patient's cardiac rhythm timings from the ECG. The self-supervised training used in DIP-MRF ensures that the reconstructed T_1, T_2, and M_0 maps and spatial basis images are consistent with the acquired k-space data and with a mathematical model of the MRF signal generation and data sampling process.

One limitation of this work is the long computation time of approximately 1.1 h, since training is performed *de novo* for each scan. Nevertheless, this work used strategies to accelerate the calculation of forward model during training. The spiral k-space data were shifted onto a Cartesian grid using GROG, which allowed use FFT rather than more time-consuming NUFFT operations during training. Without GROG pre-interpolation, the DIP-MRF reconstruction took 5.3 h. A pre-trained Fingerprint Generator Network was also used in place of

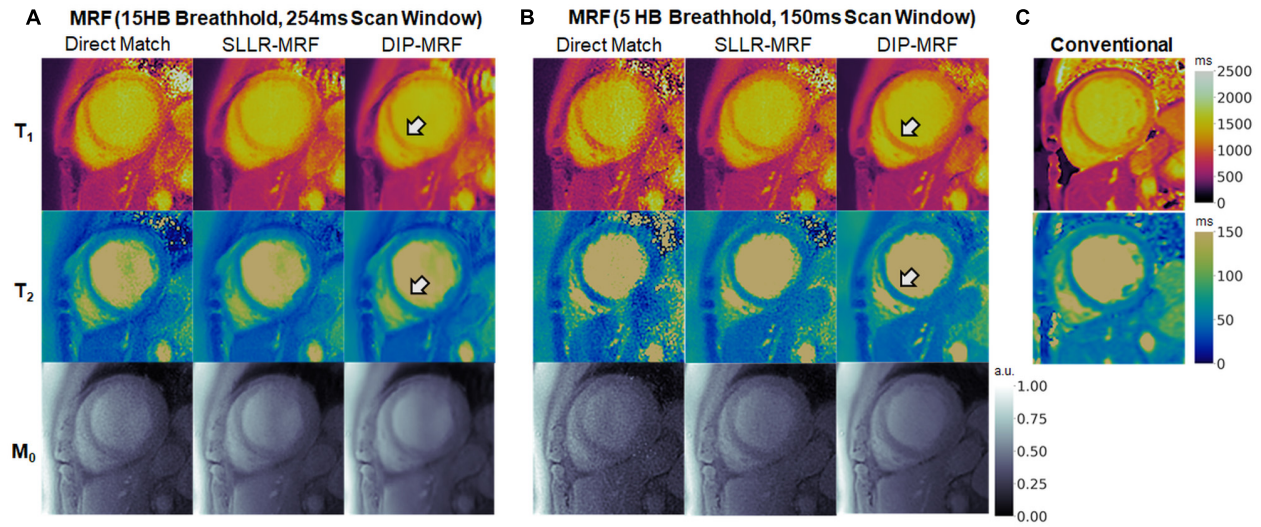

FIGURE 14 | Example of reduced motion artifacts using the shortened 5HB/150 ms MRF acquisition in a cardiomyopathy patient. **(A)** The myocardial septum (white arrow) appeared blurred using the 15HB/254 ms MRF sequence due to failed breathholding and residual cardiac motion during the acquisition window. **(B)** Motion artifacts were reduced with the shortened 5HB/150 ms MRF sequence. DIP-MRF yielded improved map quality with less noise compared to the direct matching and SLLR-MRF. **(C)** MOLLI and T_2-prepared bSSFP maps are shown for reference. All maps were cropped to a 100 × 100 region centered over the heart.

a Bloch equation simulation to rapidly generate fingerprints for arbitrary T_1, T_2, and cardiac rhythm timings. The time needed to simulate fingerprints at 192^2 voxel locations (the matrix size used for all datasets in this work) was over 8 min using a Bloch simulation (compiled MATLAB Mex code running on 12 parallel CPUs) compared to 30 ms using the Fingerprint Generator Network on a GPU. Future work will explore ways to shorten the computation time of DIP-MRF, possibly to several minutes or less. Transfer learning may be one solution (49), where DIP-MRF is pre-trained using some *in vivo* scans, and the reconstructed maps are fine-tuned based on the acquired k-space data from the current scan.

In the original DIP publication, early stopping was used to avoid overfitting to noise, and the number of training iterations was manually tuned for each application (27). This study uses dropout to reduce overfitting (43), which allowed the network to be trained for longer and placed less dependence on manually tuning the number of iterations for early stopping. Simulation results showed that dropout improved the reconstruction accuracy and slowed the rate at which overfitting occurred (**Supplementary Figure 4**). An *in vivo* dataset was also reconstructed with different dropout levels, while keeping the number of training iterations fixed at 30,000 for simplicity, to empirically determine which settings yielded the best map quality. It was found that the shortened 5HB/150 ms MRF scan benefitted from higher dropout compared to the 15HB/254 ms scan (20 vs. 10% dropout).

In the absence of motion, the 15HB/254 ms and 5HB/150 ms MRF sequences were expected to yield equivalent T_1 and T_2 measurements. However, large differences were observed using the direct matching reconstruction, which was due to the noise enhancement and aliasing artifacts in maps using the 5HB/150 ms sequence, resulting in the wide limits of agreement in the Bland-Altman plots in **Figure 11**. Similar discrepancies were seen with SLLR-MRF to a lesser extent. Due to the improved quality of the maps, DIP-MRF yielded the closest agreement in T_1 and T_2 measured by the 15HB/254 ms and 5HB/150 ms sequences. DIP-MRF also yielded better precision *in vivo* compared to direct matching and SLLR-MRF. For T_1, the intrasubject variability in healthy subjects was similar among MOLLI, 15HB/254 ms DIP-MRF, and 5HB/150 ms DIP-MRF. For T_2, the intrasubject variability was lowest for 15HB/254 ms DIP-MRF, and similar between T_2-prep bSSFP and 5HB/150 ms DIP-MRF. DIP-MRF also resulted in a lower intersubject variability for T_1 and T_2 compared to direct matching and SLLR-MRF.

Higher native T_1 and lower native T_2 were observed using MRF compared to conventional mapping sequences, which has been reported previously (50). MOLLI is known to underestimate T_1 (51), and T_2-prep bSSFP has been reported to overestimate T_2 (52), which was observed in this study in the phantom experiment (**Figure 6** and **Supplementary Figures 5–7**). The signal model in cardiac MRF accounts for slice profile imperfections and inversion pulse efficiency, which was shown to improve accuracy and lead to higher T_1 measurements (50). Lower T_2 values have been reported with FISP-based MRF sequences compared to standard techniques in other applications, which may be related to magnetization transfer (53), intravoxel dephasing (54), and motion sensitivity along the direction of the unbalanced gradient moment (i.e., slice direction).

Increased regional variability for T_1 and to a lesser degree T_2 was observed with MRF, with higher relaxation times in the septum and lower values in the inferolateral segment. Possible explanations may include susceptibility effects (especially in

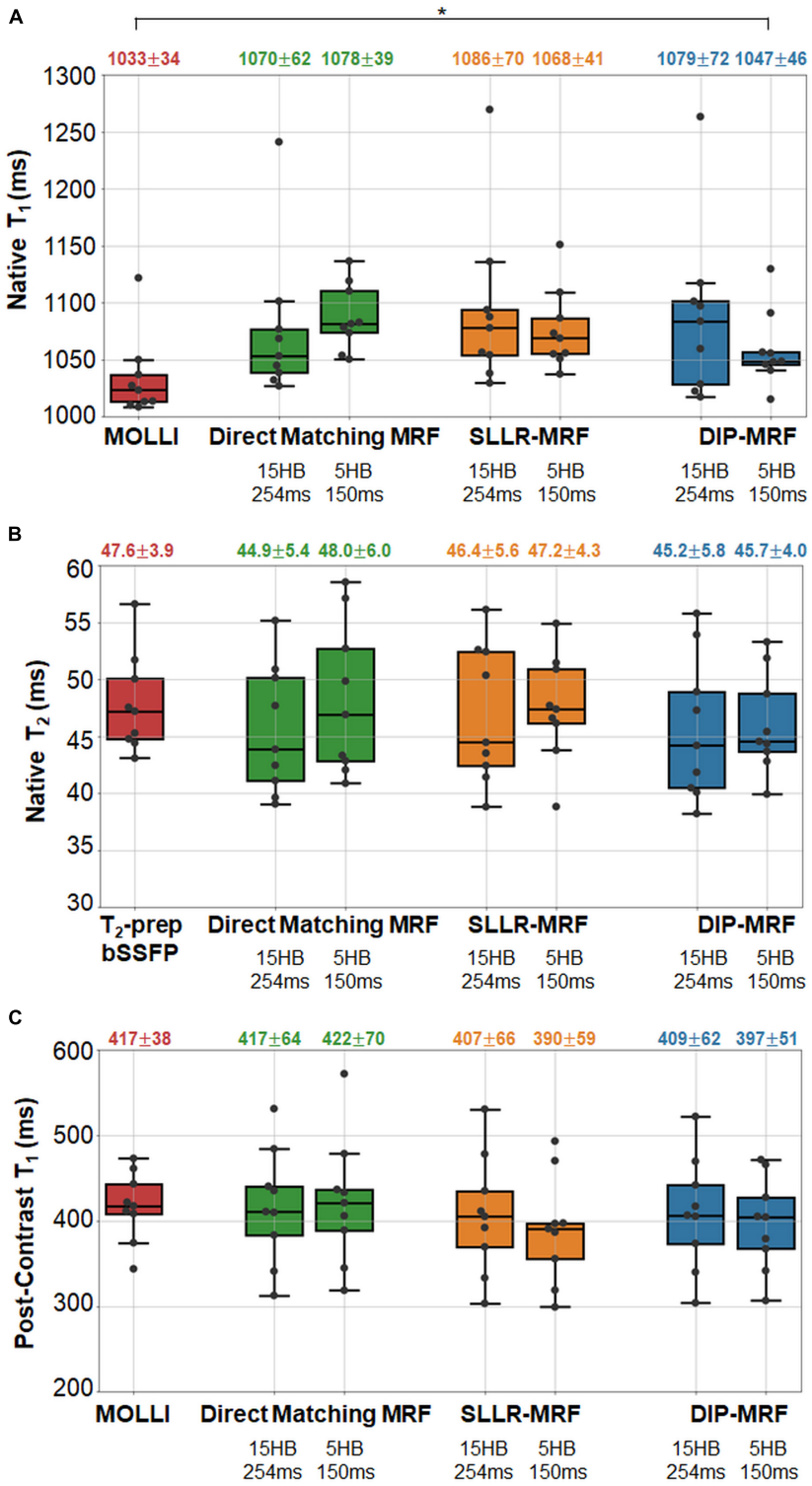

FIGURE 15 | Relaxation times in the myocardial septum in cardiomyopathy patients. The boxplots summarize the **(A)** native T_1, **(B)** native T_2, and **(C)** post-contrast T_1 using conventional mapping sequences, as well as 15HB/254 ms MRF and 5HB/150 ms MRF with direct matching, SLLR-MRF, and DIP-MRF reconstructions. The top of each box indicates the upper quartile, the bottom indicates the lower quartile, and the horizontal line through the middle shows the median. The numbers above each plot indicate the mean ± standard deviation over all patients. Asterisks indicate a significant difference ($p < 0.05$) using a within-subjects ANOVA test with a Bonferroni *post-hoc* test for multiple comparisons. Native mapping was performed in all ten patients. Post-contrast MRF was acquired in all ten patients, while post-contrast MOLLI was only collected in nine patients.

the inferolateral segment); partial volume artifacts between myocardium and epicardial fat, which could be improved with water-fat separation techniques like Dixon cardiac MRF (55) or MRF with rosette k-space sampling (56); and B_1^+ inhomogeneities, which could be addressed using B_1^+ correction (57, 58). Blood relaxation times were reported for completeness; however, blood flow into and out of the 2D imaging plane is not accounted for in the MRF signal simulation and likely affects the blood T_1 and T_2 estimates. Interestingly, higher T_1 was measured in the LV compared to the RV with both MOLLI and cardiac MRF. Higher T_2 was measured in the LV with T_2-prep bSSFP, which has been reported previously (59), but slightly lower T_2 was measured in the LV with cardiac MRF.

In summary, a DIP-MRF reconstruction that combines low-rank subspace modeling with a deep image prior was shown to reduce noise and aliasing artifacts in cardiac MRF T_1, T_2, and M_0 mapping, which does not require pre-training with *in vivo* data. This method enables a shortened breathhold duration and cardiac acquisition window in cardiac MRF, which has the potential to improve scan efficiency and reduce motion artifacts. Future work will explore extensions of DIP-MRF to motion-resolved (cine) MRF (60, 61) and 3D cardiac MRF (62).

DATA AVAILABILITY STATEMENT

The raw data supporting the conclusions of this article will be made available by the authors, without undue reservation.

ETHICS STATEMENT

The studies involving human participants were reviewed and approved by Institutional Review Boards of the University of Michigan Medical School (IRBMED). The patients/participants provided their written informed consent to participate in this study.

AUTHOR CONTRIBUTIONS

JH: study conception and design, deep learning reconstruction implementation, data collection and analysis, manuscript preparation, and approved the submitted version.

FUNDING

This work was supported by the Michigan Institute for Clinical & Health Research (MICHR) Grant UL1TR002240, Siemens Healthineers, and NIH/NHLBI R01HL163030.

SUPPLEMENTARY MATERIAL

The Supplementary Material for this article can be found online at: https://www.frontiersin.org/articles/10.3389/fcvm.2022.928546/full#supplementary-material

REFERENCES

1. Goldfarb JW, Arnold S, Han J. Recent myocardial infarction: assessment with unenhanced T1-weighted MR imaging. *Radiology.* (2007) 245:245–50. doi: 10.1148/radiol.2451061590
2. Okur A, Kantarcı M, Kızrak Y, Yıdız S, Pirimoğlu B, Karaca L, et al. Quantitative evaluation of ischemic myocardial scar tissue by unenhanced T1 mapping using 3.0 Tesla MR scanner. *Diagn Interv Radiol.* (2014) 20:407–13. doi: 10.5152/dir.2014.13520
3. Dall'Armellina E, Piechnik SK, Ferreira VM, Si QL, Robson MD, Francis JM, et al. Cardiovascular magnetic resonance by non contrast T1-mapping allows assessment of severity of injury in acute myocardial infarction. *J Cardiovasc Magn Reson.* (2012) 14:15. doi: 10.1186/1532-429X-14-15
4. Park CH, Choi E-Y, Kwon HM, Hong BK, Lee BK, Yoon YW, et al. Quantitative T2 mapping for detecting myocardial edema after reperfusion of myocardial infarction: validation and comparison with T2-weighted images. *Int J Cardiovasc Imaging.* (2013) 29:65–72. doi: 10.1007/s10554-013-0256-0
5. Giri S, Chung YC, Merchant A, Mihai G, Rajagopalan S, Raman SV, et al. T2 quantification for improved detection of myocardial edema. *J Cardiovasc Magn Reson.* (2009) 11:56. doi: 10.1186/1532-429X-11-56
6. Baggiano A, Boldrini M, Martinez-Naharro A, Kotecha T, Petrie A, Rezk T, et al. Noncontrast magnetic resonance for the diagnosis of cardiac amyloidosis. *JACC Cardiovasc Imaging.* (2020) 13:69–80. doi: 10.1016/j.jcmg.2019.03.026
7. Sado DM, White SK, Piechnik SK, Banypersad SM, Treibel T, Captur G, et al. Identification and assessment of anderson-fabry disease by cardiovascular magnetic resonance noncontrast myocardial T1 mapping. *Circ Cardiovasc Imaging.* (2013) 6:392–8. doi: 10.1161/CIRCIMAGING.112.000070
8. Messroghli DR, Walters K, Plein S, Sparrow P, Friedrich MG, Ridgway JP, et al. Myocardial T1 mapping: application to patients with acute and chronic myocardial infarction. *Magn Reson Med.* (2007) 58:34–40. doi: 10.1002/mrm.21272
9. Weingärtner S, Akçakaya M, Basha T, Kissinger KV, Goddu B, Berg S, et al. Combined saturation/inversion recovery sequences for improved evaluation of scar and diffuse fibrosis in patients with arrhythmia or heart rate variability. *Magn Reson Med.* (2014) 71:1024–34. doi: 10.1002/mrm.24761
10. Kvernby S, Warntjes MJ, Haraldsson H, Carlhall CJ, Engvall J, Ebbers T. Simultaneous three-dimensional myocardial T1 and T2 mapping in one breath hold with 3D-QALAS. *J Cardiovasc Magn Reson.* (2014) 16:102. doi: 10.1186/s12968-014-0102-0
11. Akçakaya M, Weingärtner S, Basha TA, Roujol S, Bellm S, Nezafat R. Joint myocardial T1 and T2 mapping using a combination of saturation recovery and T2-preparation. *Magn Reson Med.* (2016) 76:888–96. doi: 10.1002/mrm.25975
12. Christodoulou AG, Shaw JL, Nguyen C, Yang Q, Xie Y, Wang N, et al. Magnetic resonance multitasking for motion-resolved quantitative cardiovascular imaging. *Nat Biomed Eng.* (2018) 2:215–26. doi: 10.1038/s41551-018-0217-y
13. Ma D, Gulani V, Seiberlich N, Liu K, Sunshine JL, Duerk JL, et al. Magnetic resonance fingerprinting. *Nature.* (2013) 495:187–92. doi: 10.1038/nature11971
14. Hamilton JI, Jiang Y, Chen Y, Ma D, Lo WC, Griswold M, et al. MR fingerprinting for rapid quantification of myocardial T1, T2, and proton spin density. *Magn Reson Med.* (2017) 77:1446–58. doi: 10.1002/mrm.26216
15. Hamilton JI, Pahwa S, Adedigba J, Frankel S, O'Connor G, Thomas R, et al. Simultaneous mapping of T1 and T2 using cardiac magnetic resonance fingerprinting in a cohort of healthy subjects at 1.5T. *J Magn Reson Imaging.* (2020) 52:1044–52. doi: 10.1002/jmri.27155
16. Cavallo AU, Liu Y, Patterson A, Al-Kindi S, Hamilton J, Gilkeson R, et al. CMR fingerprinting for myocardial T1, T2, and ECV quantification in patients with nonischemic cardiomyopathy. *JACC Cardiovasc Imaging.* (2019) 12:1584–5. doi: 10.1016/j.jcmg.2019.01.034

17. Cruz G, Qi H, Jaubert O, Kuestner T, Schneider T, Botnar RM, et al. Generalized low-rank nonrigid motion-corrected reconstruction for MR fingerprinting. *Magn Reson Med.* (2022) 87:746–63. doi: 10.1002/mrm.29027
18. Pierre EY, Ma D, Chen Y, Badve C, Griswold MA. Multiscale reconstruction for MR fingerprinting. *Magn Reson Med.* (2016) 75:2481–92. doi: 10.1002/mrm.25776
19. Cline CC, Chen X, Mailhe B, Wang Q, Pfeuffer J, Nittka M, et al. AIR-MRF: accelerated iterative reconstruction for magnetic resonance fingerprinting. *Magn Reson Imaging.* (2017) 41:29–40. doi: 10.1016/j.mri.2017.07.007
20. Doneva M, Amthor T, Koken P, Sommer K, Börnert P. Matrix completion-based reconstruction for undersampled magnetic resonance fingerprinting data. *Magn Reson Imaging.* (2017) 41:41–52. doi: 10.1016/j.mri.2017.02.007
21. Zhao B, Setsompop K, Adalsteinsson E, Gagoski B, Ye H, Ma D, et al. Improved magnetic resonance fingerprinting reconstruction with low-rank and subspace modeling. *Magn Reson Med.* (2018) 79:933–42. doi: 10.1002/mrm.26701
22. Assländer J, Cloos MA, Knoll F, Sodickson DK, Hennig J, Lattanzi R. Low rank alternating direction method of multipliers reconstruction for MR fingerprinting. *Magn Reson Med.* (2018) 79:83–96. doi: 10.1002/mrm.26639
23. Cohen O, Zhu B, Rosen MS. MR fingerprinting deep reconstruction network (DRONE). *Magn Reson Med.* (2018) 80:885–94. doi: 10.1002/mrm.27198
24. Hamilton JI, Currey D, Rajagopalan S, Seiberlich N. Deep learning reconstruction for cardiac magnetic resonance fingerprinting T1 and T2 mapping. *Magn Reson Med.* (2021) 85:2127–35. doi: 10.1002/mrm.28568
25. Fang Z, Chen Y, Liu M, Lei X, Zhang Q, Wang Q, et al. Deep learning for fast and spatially-constrained tissue quantification from highly-accelerated data in magnetic resonance fingerprinting. *IEEE Trans Med Imaging.* (2019) 38:2364–74. doi: 10.1109/TMI.2019.2899328
26. Fang Z, Chen Y, Hung S, Zhang X, Lin W, Shen D. Submillimeter MR fingerprinting using deep learning–based tissue quantification. *Magn Reson Med.* (2020) 84:579–91. doi: 10.1002/mrm.28136
27. Ulyanov D, Vedaldi A, Lempitsky V. Deep image prior. *Proceedings of the IEEE Computer Society Conference on Computer Vision and Pattern Recognition*. Washington, DC: IEEE Computer Society (2018). p. 9446–54.
28. Ronneberger O, Fischer P, Brox T. U-Net: convolutional networks for biomedical image segmentation. In: Navab N, Hornegger J, Wells WM, Frangi AF editors. *Medical Image Computing and Computer-Assisted Intervention*. Berlin: Springer International Publishing (2015). p. 234–41.
29. Chakrabarty P, Maji S. The spectral bias of the deep image prior. *arXiv.* [Preprint]. (2019). Available online at: https://doi.org/10.48550/arXiv.1912.08905 (accessed March 1, 2022).
30. Baguer DO, Leuschner J, Schmidt M. Computed tomography reconstruction using deep image prior and learned reconstruction methods. *Inverse Probl.* (2020) 36:094004.
31. Gong K, Catana C, Qi J, Li Q. PET image reconstruction using deep image prior. *IEEE Trans Med Imaging.* (2019) 38:1655–65. doi: 10.1109/TMI.2018.2888491
32. Lin YC, Huang HM. Denoising of multi b-value diffusion-weighted MR images using deep image prior. *Phys Med Biol.* (2020) 65:105003. doi: 10.1088/1361-6560/ab8105
33. McGivney DF, Pierre E, Ma D, Jiang Y, Saybasili H, Gulani V, et al. SVD compression for magnetic resonance fingerprinting in the time domain. *IEEE Trans Med Imaging.* (2014) 33:2311–22. doi: 10.1109/TMI.2014.2337321
34. Lima da Cruz G, Bustin A, Jaubert O, Schneider T, Botnar RM, Prieto C. Sparsity and locally low rank regularization for MR fingerprinting. *Magn Reson Med.* (2019) 81:3530–43. doi: 10.1002/mrm.27665
35. Hamilton JI, Jiang Y, Ma D, Chen Y, Lo WC, Griswold M, et al. Simultaneous multislice cardiac magnetic resonance fingerprinting using low rank reconstruction. *NMR Biomed.* (2019) 32:e4041. doi: 10.1002/nbm.4041
36. Hamilton JI, Seiberlich N. Machine learning for rapid magnetic resonance fingerprinting tissue property quantification. *Proc IEEE Inst Electr Electron Eng.* (2020) 108:69–85. doi: 10.1109/JPROC.2019.2936998
37. Seiberlich N, Breuer FA, Blaimer M, Barkauskas K, Jakob PM, Griswold MA. Non-Cartesian data reconstruction using GRAPPA operator gridding (GROG). *Magn Reson Med.* (2007) 58:1257–65. doi: 10.1002/mrm.21435
38. Fessler J, Sutton B. Nonuniform fast fourier transforms using min-max interpolation. *IEEE Trans Signal Process.* (2003) 51:560–74.
39. Walsh D, Gmitro A, Marcellin M. Adaptive reconstruction of phased array MR imagery. *Magn Reson Med.* (2000) 43:682–90. doi: 10.1002/(sici)1522-2594(200005)43:5\<682::aid-mrm10\>3.0.co;2-g
40. Jiang Y, Ma D, Seiberlich N, Gulani V, Griswold MA. MR fingerprinting using fast imaging with steady state precession (FISP) with spiral readout. *Magn Reson Med.* (2015) 74:1621–31. doi: 10.1002/mrm.25559
41. Hargreaves B. *Variable-Density Spiral Design Functions*. (2005). Available online at: http://mrsrl.stanford.edu/~brian/vdspiral/ (accessed June 1, 2017).
42. Winkelmann S, Schaeffter T, Koehler T, Eggers H, Doessel O. An optimal radial profile order based on the golden ratio for time-resolved MRI. *IEEE Trans Med Imaging.* (2007) 26:68–76. doi: 10.1109/TMI.2006.885337
43. Srivastava N, Hinton G, Krizhevsky A, Sutskever I, Salakhutdinov R. Dropout: a simple way to prevent neural networks from overfitting. *J Mach Learn Res.* (2014) 15:1929–58.
44. Keenan KE, Stupic KF, Boss M, Russek SE, Chenevert TL, Prasad PV, et al. Comparison of T1 measurement using ISMRM/NIST system phantom. *Proceedings of the 24th Annual Meeting of ISMRM*. Concord, CA: International Society for Magnetic Resonance in Medicine (2016). p. 3290.
45. Siemens Medical Solutions [SMS]. *MyoMaps*. (2018). Available online at: https://usa.healthcare.siemens.com/magnetic-resonance-imaging/options-and-upgrades/clinical-applications/myomaps (accessed February 27, 2018).
46. Messroghli DR, Radjenovic A, Kozerke S, Higgins DM, Sivananthan MU, Ridgway JP. Modified Look-Locker inversion recovery (MOLLI) for high-resolution T1 mapping of the heart. *Magn Reson Med.* (2004) 52:141–6. doi: 10.1002/mrm.20110
47. Bland JM, Altman DG. Statistical methods for assessing agreement between two methods of clinical measurement. *Lancet.* (1986) 1:307–10.
48. Cerqueira MD. Standardized myocardial segmentation and nomenclature for tomographic imaging of the heart: a statement for healthcare professionals from the cardiac imaging committee of the council on clinical cardiology of the American heart association. *Circulation.* (2002) 105:539–42. doi: 10.1161/hc0402.102975
49. Barbano R, Leuschner J, Schmidt M, Denker A, Hauptmann A, Maaß P, et al. Is deep image prior in need of a good education? *arXiv.* [Preprint]. (2021). Available online at: https://doi.org/10.48550/arXiv.2111.11926 (accessed March 1, 2022).
50. Hamilton JI, Jiang Y, Ma D, Lo W-C, Gulani V, Griswold M, et al. Investigating and reducing the effects of confounding factors for robust T1 and T2 mapping with cardiac MR fingerprinting. *Magn Reson Imaging.* (2018) 53:40–51. doi: 10.1016/j.mri.2018.06.018
51. Kellman P, Hansen MS. T1-mapping in the heart: accuracy and precision. *J Cardiovasc Magn Reson.* (2014) 16:2. doi: 10.1186/1532-429X-16-2
52. Baeßler B, Schaarschmidt F, Stehning C, Schnackenburg B, Maintz D, Bunck AC. Cardiac T2-mapping using a fast gradient echo spin echo sequence - first in vitro and in vivo experience. *J Cardiovasc Magn Reson.* (2015) 17:67. doi: 10.1186/s12968-015-0177-2
53. Gloor M, Scheffler K, Bieri O. Quantitative magnetization transfer imaging using balanced SSFP. *Magn Reson Med.* (2008) 60:691–700. doi: 10.1002/mrm.21705
54. Assländer J, Glaser SJ, Hennig J. Pseudo steady-state free precession for MR-fingerprinting. *Magn Reson Med.* (2017) 77:1151–61. doi: 10.1002/mrm.26202
55. Jaubert O, Cruz G, Bustin A, Schneider T, Lavin B, Koken P, et al. Water–fat Dixon cardiac magnetic resonance fingerprinting. *Magn Reson Med.* (2019) 83:2107–23. doi: 10.1002/mrm.28070
56. Liu Y, Hamilton J, Eck B, Griswold M, Seiberlich N. Myocardial T1 and T2 quantification and water–fat separation using cardiac MR fingerprinting with rosette trajectories at 3T and 1.5T. *Magn Reson Med.* (2020) 85:103–19. doi: 10.1002/mrm.28404
57. Ma D, Coppo S, Chen Y, McGivney DF, Jiang Y, Pahwa S, et al. Slice profile and B1 corrections in 2D magnetic resonance fingerprinting. *Magn Reson Med.* (2017) 78:1781–9. doi: 10.1002/mrm.26580

58. Buonincontri G, Schulte RF, Cosottini M, Tosetti M. Spiral MR fingerprinting at 7T with simultaneous B1 estimation. *Magn Reson Imaging.* (2017) 41:1–6. doi: 10.1016/j.mri.2017.04.003
59. Emrich T, Bordonaro V, Schoepf UJ, Petrescu A, Young G, Halfmann M, et al. Right/left ventricular blood pool T2 ratio as an innovative cardiac MRI screening tool for the identification of left-to-right shunts in patients with right ventricular disease. *J Magn Reson Imaging.* (2022) 55:1452–8. doi: 10.1002/jmri.27881
60. Hamilton JI, Jiang Y, Eck B, Griswold M, Seiberlich N. Cardiac cine magnetic resonance fingerprinting for combined ejection fraction, T1 and T2 quantification. *NMR Biomed.* (2020) 33:e4323. doi: 10.1002/nbm.4323
61. Jaubert O, Cruz G, Bustin A, Schneider T, Koken P, Doneva M, et al. Free-running cardiac magnetic resonance fingerprinting: joint T1/T2 map and cine imaging. *Magn Reson Imaging.* (2020) 68:173–82. doi: 10.1016/j.mri.2020.02.005
62. Cruz G, Jaubert O, Qi H, Bustin A, Milotta G, Schneider T, et al. 3D free-breathing cardiac magnetic resonance fingerprinting. *NMR Biomed.* (2020) 33:e4370. doi: 10.1002/nbm.4370

Conflict of Interest: This study received funding from Siemens Healthineers (Erlangen, Germany). The funder had no involvement with any aspect of the study design, data collection, interpretation of results, or manuscript preparation.

The author declares that the research was conducted in the absence of any commercial or financial relationships that could be construed as a potential conflict of interest.

frontiers | Frontiers in Cardiovascular Medicine

PERSPECTIVE
published: 04 July 2022
doi: 10.3389/fcvm.2022.919810

Visualization and Analysis of Multidimensional Cardiovascular Magnetic Resonance Imaging: Challenges and Opportunities

Leon Axel[1]*, *Timothy S. Phan*[1] and *Dimitris N. Metaxas*[2]

[1] Department of Radiology, New York University Grossman School of Medicine, New York, NY, United States, [2] Department of Computer Science, Rutgers University, Piscataway, NJ, United States

Recent advances in magnetic resonance imaging are enabling the efficient creation of high-dimensional, multiparametric images, containing a wealth of potential information about the structure and function of many organs, including the cardiovascular system. However, the sizes of these rich data sets are so large that they are outstripping our ability to adequately visualize and analyze them, thus limiting their clinical impact. While there are some intrinsic limitations of human perception and of conventional display devices which hamper our ability to effectively use these data, newer computational methods for handling the data may aid our ability to extract and visualize the salient components of these high-dimensional data sets.

Keywords: cardiovascular, magnetic resonance imaging, MRI, multidimensional, visualization, analysis

OPEN ACCESS

Edited by:
Aleksandra Radjenovic, University of Glasgow, United Kingdom

Reviewed by:
Tim Leiner, Mayo Clinic, United States
Jeanette Schulz-Menger, Charité/Helios, Germany

***Correspondence:**
Leon Axel
leon.axel@nyumc.org

Specialty section:
This article was submitted to Cardiovascular Imaging, a section of the journal Frontiers in Cardiovascular Medicine

Received: *13 April 2022*
Accepted: *14 June 2022*
Published: *04 July 2022*

Citation:
Axel L, Phan TS and Metaxas DN (2022) Visualization and Analysis of Multidimensional Cardiovascular Magnetic Resonance Imaging: Challenges and Opportunities. Front. Cardiovasc. Med. 9:919810. doi: 10.3389/fcvm.2022.919810

INTRODUCTION

While cardiovascular magnetic resonance imaging (CMR) has become a valuable clinical tool, conventional CMR still has many limitations. Recent ongoing advances in the development of CMR imaging methods are now making possible the acquisition and reconstruction of much more comprehensive sets of imaging data on the cardiovascular system, including the creation of large-scale multidimensional and multiparametric images. However, limitations of the human perceptual system and conventional display devices make the visualization and analysis of these large and complex data sets challenging. We will briefly summarize some of the background related to the creation and potential applications of these new CMR data sets, and we will discuss some of the associated challenges involved in handling them, as well as some possible paths forward to meet these challenges.

CONVENTIONAL CARDIOVASCULAR MRI

Magnetic resonance imaging (MRI) uses the physical phenomena of nuclear magnetic resonance to create images that reflect multiple aspects of the state of the body, including the following principles: (1) Certain nuclei, including hydrogen (one of the principal constituents of the body), can become magnetized in a strong magnetic polarizing field, producing a collective bulk nuclear magnetization. (2) The orientation of the nuclear magnetization relative to the polarizing field can be changed ("excited") by applying an oscillating magnetic field at a specific resonance

frequency (proportional to the strength of the polarizing field); if the nuclear magnetization is left at an orientation inclined to the field direction, it will produce a weak, but detectable, signal at the resonance frequency. (3) Position information can be encoded in the signal, through the use of supplementary magnetic fields which vary with position in a controlled way ("gradients"), with associated changes in the local resonance frequency (1); the resulting signals are equivalent to samples of the Fourier transform of an image. A suitable set of such encoded signals can be used to reconstruct an image (2D or 3D) of the spatial distribution of the signal sources, through an inverse Fourier transform. Gradients can also be used during excitation to select a desired plane to image. Serial images over time can display motion. (4) Tissue state-dependent "relaxation times" can affect the strength of the signal; additional excitations can be used to change the local image contrast, through relaxation time-dependent effects on the signal, which can help to reveal the presence of abnormalities in the image, or to calculate the regional relaxation times or other parameters ("parameter mapping"), typically by measuring the difference in image intensity produced by the additional excitations. Such parameter mapping can potentially be used for more quantitative characterization of disease states. Contrast agents alter the image appearance by altering the local relaxation times; early and late contrast enhancement patterns provide information on perfusion and associated tissue abnormalities, which can also potentially be quantified. (5) Additional gradients can be used to sensitize the signal to motion effects, including velocity and diffusion, enabling flexible measurements of blood flow and providing an additional potential means for tissue characterization. (6) Nuclei at different positions within a molecule may have slightly different resonance frequencies, potentially providing some chemical information in the signal, e.g., distinguishing fat from water.

In applying MRI to the cardiovascular system, we have to deal with the effects of motion on the images, related to both the heart beat and breathing. If the heart beats are sufficiently similar, we can pool data from multiple heart beats, to create "cine" images at multiple relative times spanning an averaged cardiac cycle. If data acquisition times are short enough, images can be created during suspended respiration, to eliminate respiratory motion effects. In conventional clinical cardiovascular MRI, sets of relaxation time-weighted and cine images, acquired in multiple planes, are used to evaluate the local and global structure, tissue properties, and function, primarily through qualitative assessment of 2D images.

While they are clinically very useful, there are still significant limitations of conventional CMR methods. Due to breath hold limits, most imaging is 2D and acquired with separate breath-holds, leading to long imaging sessions needed to cover the heart and vessels, and potential position inconsistency between images, due to inconsistent breath-holds. Internal inconsistency of the acquired data, e.g., when patients cannot suspend respiration or have arrhythmia, can lead to image degradation. Conventional parameter mapping is time-consuming and vulnerable to motion and other artifacts, limiting its clinical use.

NEWER CMR METHODS

Various approaches have enabled the use of undersampling of the imaging data, taking advantage of the underlying correlations between pixels in medical images ("compressed sensing"), thus shortening imaging times. In addition to accelerating conventional imaging, these new methods make it possible to acquire larger image data sets in a reasonable time. In the context of CMR, considering cardiac and respiratory cycle phases as effectively being additional dimensions enables reconstruction of respiratory- and cardiac-synchronized 2D and 3D image data sets from free-breathing continuous data acquisitions (2, 3). Previously, parameter mapping required acquiring multiple images with different degrees of "steady" sensitivity to the desired tissue property, and then combining them to calculate the value of the property; however, this is a time-consuming process, and is subject to errors related to any position inconsistency between the images. Newer mapping imaging methods have taken a more efficient dynamic approach, directly incorporating the "unsteady" response of the signal to transient perturbations, such as additional excitations or contrast injections, into the data acquisition process. The resulting mixed effects on the signals can then be separated during the image reconstruction process, using mathematical tools such as "low rank" decomposition of the resulting image data set. This "multitasking" approach enables adding parameter mapping and perfusion imaging to a combined image reconstruction. Such combined multidimensional data acquisition and reconstruction imaging methods can thus enable direct joint creation of images of regional tissue properties, together with the motion, without the conventional need to separately reconstruct the properties from sets of sequential data acquisitions (which are vulnerable to problems from inconsistent tissue positions) (e.g., **Figure 1**). An alternative approach to multidimensional and multiparameter imaging is to use the evolving response of the signal to continuously varying excitation pulses and gradients ("fingerprinting"). However, all these approaches have previously required time-consuming associated iterative image reconstruction methods; machine learning (ML) methods are a promising way to speed up this up (4–10), and ML-based methods are being rapidly developed for this and many other image-related applications. Artificial intelligence (AI)-based methods can be used to help suppress artifacts that may arise from more conventional image reconstruction methods, e.g., due to motion or data undersampling. However, AI-based methods for image handling programs may be subject to instabilities. These and related methods are described in more detail and illustrated in the accompanying articles in this issue, and will not be further discussed here. We can also potentially acquire multinuclear imaging data, for an additional set of "dimensions" to display and analyze.

One thing that these methods all have in common is the ability to create very large and high-dimensional data sets; it is very challenging to visualize and analyze the wealth of data that they can potentially contain. The same underlying correlations between the images across the multiple images that make it possible to reconstruct them from undersampled data also make it possible to represent them in a correspondingly compressed

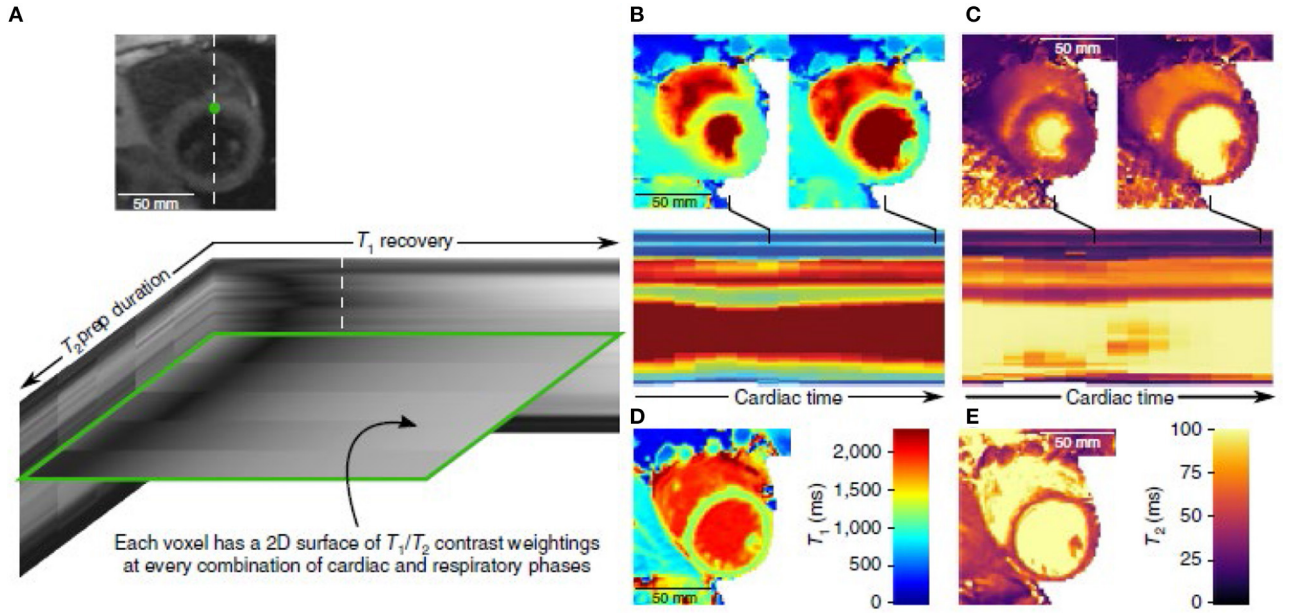

FIGURE 1 | Example of the use of multitasking imaging, with use of simultaneous T1- and T2-weighting **(A)**, to generate motion-resolved multidimensional images with parameter mapping **(B–E)** [(4) (by permission)].

form. This can make for a more compact way to store the data, and the images can then be selectively re-expanded, as needed, for displays, making for more efficient data handling. Beyond the immediate challenge of how to adequately and interactively survey the full extent of such large data sets, there are also challenging quantification issues related to associated tasks in handling the data, such as segmentation of different structures, characterization of time evolution across multiple dimensions, and identification/classification of abnormalities revealed by regional alterations in different parameters. Segmentation of cardiac structures is already challenging for conventional CMR functional analysis; segmenting cardiac structures across multiple dimensions compounds that challenge. However, being able to quantitatively assess the interactions between cardiac and respiratory cycles potentially offers new ways to characterize cardiovascular function (11, 12). One promising approach to the challenges of multidimensional image handling is the napari project, which aims to develop an open-source set of high-performing multidimensional image display and analysis tools.

HUMAN PERCEPTION LIMITATIONS

We live in a 3D dynamic world; our visual interactions with it are mediated through images projected onto effectively flat retinas. We infer relationships between 2D object features that we see in an image and the corresponding underlying 3D object surface *via* visual cues, such as shading and occlusions, and from stereo disparities of details between left- and right-eye views. However, the structures captured in our 3D (or higher dimensional) MR images may not have well-defined implicit discrete surfaces to render; this is a frequent problem with conventional 3D medical imaging methods, when trying to display such structures as 3D objects. We can explore a 3D data set by interactively scrolling through consecutive 2D sections through it, or by displaying an array of multiple such images, but it is difficult to directly compare different regions with such displays. One common way to try to effectively compress 3D data of the heart into a 2D display is to create target-like "bull's eye" plots, e.g., with concentric rings representing different short-axis locations in the ventricle walls from apex to base and a color scale linked to some mapped quantity; however, this is associated with decreased data sampling density and geometric distortion of the displayed structures.

Our eyes have perceptual limitations, including a limited dynamic range and a limited ability to discriminate similar intensities. Vision is also affected by simultaneous contrast; that is, the subjective appearance of a region can be significantly altered by changes in the brightness or color of surrounding regions. We are not good at visually judging absolute brightness. We also cannot readily attend to multiple properties and different locations at once, and thus have difficulty comparing corresponding regions between different kinds of separately displayed images. These limitations are further exacerbated when we need to compare and register motion patterns in separately displayed images of different locations. These perceptual limitations are already a problem with conventional intensity-based imaging, and they become more acute when trying to incorporate additional parameters into the images.

DISPLAY OPTIONS AND LIMITATIONS

Conventional computer displays use flat screens, which is already a significant limitation for viewing 3D data. The usual approach for interactively viewing 3D data is to use "multiplanar reformatting" (MPR) to create a virtual view of an interactively selected 2D plane from within the 3D volume; however, while MPR is very useful, it can still be difficult to build up a reliable understanding of the underlying 3D structure relationships in the imaged volume from viewing such sampled 2D slices. An alternative display approach is to use a "volume rendering technique" (VRT) approach to display a shaded rendering of implicit "surfaces" within the 3D volume; newer "cinematic" approaches to generating the shaded surface displays can help make the spatial relationships of the displayed structures clearer. However, the structures of interest in the imaged volume may not have sufficiently sharp boundaries in the intensity data to enable their use for such rendering. When extending these approaches to time-varying (e.g., real or "physiologic" time) or other multi-dimensional data, we can use interactive scrolling through or animation of a corresponding set of such displays over time or other dimensions. For images that evolve over time, e.g., images of dynamic contrast enhancement, it may be more useful to display functional images that effectively summarize the time evolution of the signal, e.g., by calculating the temporal moments or perfusion-related variables, rather than displaying the multiple underlying serial images, themselves. However, when additional dimensions are introduced into the data, we must choose which dimension to animate, as only one dimension can be mapped into the animation at a time, and we may still have difficulty exploring interactions between the different dimensions. The task of interactively exploring all potentially relevant areas of a large multidimensional data set can be daunting (like "looking for a needle in a haystack").

For display of single imaged parameters, or of scalar variables calculated from the image sets, we can use a simple color overlay with varying opacity onto the corresponding underlying intensity image data; we can interactively adjust the associated color and opacity lookup tables to qualitatively bring out structures of interest in the display. When dealing with multiparametric image data, we must choose a given property (or combination of properties) to map (using an associated color lookup table) for a given display. However, things get more difficult when we want to examine the spatial distribution of more than one scalar property at a time. Although we can try to use some sort of hue/saturation/value mapping to display multiple properties at once, these effective display "dimensions" are not very "orthogonal" to each other, and the eye's response to them is not very linear. An alternative approach to jointly evaluate images of multiple parameters is to enable interactive exploration of different combinations of the parameters. For example, we can create synthetic images reflecting the expected appearance of images that would have been acquired with different relative amounts of parameter weighting; this may be of more practical utility than simple images of the parameter values themselves. One way to approach this would be to map up to three different coregistered parameter values to be displayed in separate red, green or blue overlaid colors, with the net perceived color reflecting the relative contributions from each parameter. Alternatively, a principal component analysis approach could be used to look for ways to combine multiple parameters that would best distinguish between different particular tissue states. As an example, this approach could potentially be used to help distinguish myocardial regions of bright appearance on T1-weighted imaging that are due to late gadolinium enhancement, rather than to fat or residual contrast enhancement of the adjacent blood, which would have different chemical shift or T2 values than enhanced myocardium. Qualitative assessment of the spatial variation of such multiparametric-based displays may be more clinically useful for identifying and classifying regional abnormalities than simple local measurement of specific numerical values of parameters.

Motion and other temporally varying properties are often not readily summarized as simple scalars, although approaches such as calculation of associated temporal moments can be useful. Higher-dimensional imaged properties, such as vectors (e.g., velocity) and tensors (e.g., deformation or diffusion), can be discretely represented with arrows or glyphs at sampled locations; however, it is difficult to appreciate their 3D orientation and scales from a flat image, although "motion parallax" effects seen while interactively changing the view orientation can help. The velocity fields can also be used to generate corresponding streamlines or virtual particle traces (13). To aid the 3D representation of such higher order variables, we can let arrows or glyphs closer to the viewer progressively occlude those behind them, or create an orientation-dependent appearance for their representation, but this is inherently a difficult task. It is already challenging to work with conventionally acquired 4D (3D plus time) flow/motion data for display and analysis; adding additional effective dimensions will only compound this difficulty. While virtual reality (VR) display tools with stereoscopic capabilities have been used to augment the conventional visualization of 4D flow data, some users have found them to induce nausea, and the associated available image display resolution is still relatively limited, indicating that the virtual display technology may still need more development before it is ready for adoption for clinical use.

POTENTIAL WAYS FORWARD

Another area of similarly high information content imaging is multispectral or hyperspectral imaging, e.g., used for remote sensing of the environment or astronomy. Thus, we could potentially adapt methods used with hyperspectral imaging for handling multiparametric MR images; for example, we can seek to use linear principal component analysis or, for improved results due to the inherent non-linear nature of the problem, use machine learning (ML) approaches to combine data with different parameters for particular tissue characterization purposes.

Although they are still undergoing technical development, as described above, we can potentially adapt VR displays to enable better understanding of 3D spatial relationships within the

multidimensional CMR data. However, this still effectively only incorporates one additional dimension in the display.

We will likely need to develop and apply ML-based image analysis methods, in order to improve the automated discovery of salient regions/manifolds of the non-linear higher-dimensional "spaces" of multidimensional/multiparametric CMR, which can then be used for guided exploration of the data. As we have not previously had direct access to such kinds of high-dimensional data, developing the initial annotated data sets needed for the training of such methods will still be challenging. Thus, we will need to initially acquire and analyze such multidimensional data on a sufficient number of normal subjects to be able to establish regional normal ranges for such data, and we will need to be able to register individual patient image data sets to such normal values data. After the use of the initial supervised machine learning methods, we can use unsupervised machine learning methods for cardiac analytics which do not require data annotations, such as those recently developed by our group (14, 15); this is now an area of active research by many groups.

An advantage of these newer multidimensional CMR methods is that they can provide the data on different parameters in mutually spatially-registered ways. However, different components of some data sets are likely to still have different levels of signal-to-noise ratio (SNR) or different spatial resolutions, e.g., with multinuclear imaging. Thus, we will need to find effective ways to combine data derived from the higher SNR and resolution components of the imaging, e.g., for definition of regions of interest for quantitative analysis, with the other lower "quality" image components, for better integrated analysis of the data.

As with conventional parameter mapping, quality assurance and standardization of the data resulting from multidimensional imaging will be needed before the results can be trusted enough to be relied upon for clinical decision making. Imaging of phantoms containing material with calibrated parameter values can provide a minimum standard for such evaluation, but may not adequately test for effects on the data of *in vivo* imaging, such as due to motion. The validation of data related to motion-related analysis of multidimensional images is also necessary but challenging. Imaging of physical or numerical phantoms with known motion properties, while useful, may again not adequately assess the potential effects of *in vivo* imaging on the derived numbers. The wide range of potential approaches to the display of multidimensional data is a strength, but it will make standardization of the displays more difficult.

An "ideal" viewing/analysis user interface for the display of multidimensional/multiparametric CMR image data would provide a set of fast and flexible interactive tools for exploring the data set. These could include: (1) freely "cutting into" the different parametric components of the data with MPR, (2) the ability to freely move along or animate different time-related dimensions, (3) the ability to flexibly synthesize new combined displays from the component parameter images, (4) interactive creation of MPR and VRT images from any of these kinds of displays, and (5) options to use VR tools for an enhanced understanding of 3D spatial relationships of the displayed structures.

DISCUSSION

These new multidimensional/multiparametric CMR methods have great clinical potential, through their ability to efficiently create spatially registered images of multiple regional structure, function, and tissue properties. However, due to their large size and complexity, they also present multiple challenges related to their effective display and analysis. Limits posed by human perception, both in viewing displays and in integrating the multidimensional data, impede our ability to fully grasp the high levels of information that can potentially be contained in these new data sets. Conventional display technology methods and visualization techniques also have many limitations that can restrict our ability to interact with these data. ML-based methods are undergoing rapid development in many areas; in addition to aiding the reconstruction of these large data sets, we may be able to incorporate some aspects of their analysis directly into the reconstruction process, such as automated segmentation of cardiovascular structures and recovery of functional variables, as well as identification and classification of regional abnormalities.

There is a great potential for gaining additional clinical value from the multidimensional/multiparametric data produced with these new imaging methods, once we develop appropriate methods to handle the associated challenges of visualizing and analyzing them.

DATA AVAILABILITY STATEMENT

The original contributions presented in the study are included in the article/supplementary material, further inquiries can be directed to the corresponding author.

AUTHOR CONTRIBUTIONS

All authors have contributed to this manuscript, and they have reviewed and approved the final version of the manuscript.

FUNDING

This work was partially funded by NIH grants 1R21EB029168 and 5R01HL127661.

REFERENCES

1. Lauterbur PC. Image formation by induced local interactions - examples employing nuclear magnetic-resonance. *Nature.* (1973) 242:190–1. doi: 10.1038/242190a0

2. Feng L, Axel L, Chandarana H, Block KT, Sodickson DK, Otazo R, et al. Golden-angle radial MRI with reconstruction of extra motion-state dimensions using compressed sensing. *Magn Reson Med.* (2016) 75:775–88. doi: 10.1002/mrm.25665

3. Feng LI, Coppo S, Piccini D, Yerly J, Lim RP, Masci PG, et al. 5D whole-heart sparse MRI. *Magn Reson Med.* (2018) 79:826–38. doi: 10.1002/mrm.26745
4. Christodoulou AG, Shaw JL, Nguyen C, Yang Q, Xie Y, Wang N, et al. Magnetic resonance multitasking for motion-resolved quantitative cardiovascular imaging. *Nat Biomed Eng.* (2018) 2:215–26. doi: 10.1038/s41551-018-0217-y
5. Hammernik K, Klatzer T, Kobler E, Recht MP, Sodickson DK, Pock T, et al. Learning a variational network for reconstruction of accelerated MRI data. *Magn Reson Med.* (2018) 79:3055–71. doi: 10.1002/mrm.26977
6. Davies RH, Augusto JB, Bhuva A, Xue H, Treibel TA, Ye Y, et al. Precision measurement of cardiac structure and function in cardiovascular magnetic resonance using machine learning. *J Cardiovasc Magn Reson.* (2022) 24:16. doi: 10.1186/s12968-022-00846-4
7. Hamilton JI, Jiang Y, Chen Y, Ma D, Lo WC, Griswold M, et al. MR fingerprinting for rapid quantification of myocardial T1, T2, and proton spin density. *Magn Reson Med.* (2017) 77:1446–58. doi: 10.1002/mrm.26216
8. Lima da. Cruz GJ, Velasco C, Lavin B, Jaubert O, Botnar RM, Prieto C. Myocardial T1, T2, T2*, and fat fraction quantification via low-rank motion-corrected cardiac MR fingerprinting. *Magn Reson Med.* (2022) 87:2757–74. doi: 10.1002/mrm.29171
9. Antun V, Renna F, Poon C, Adcock B, Hansen AC. On instabilities of deep learning in image reconstruction and the potential costs of AI. *Proc Natl Acad Sci USA.* (2020) 117:30088–95. doi: 10.1073/pnas.1907377117
10. Madelin G, Regatte RR. Biomedical applications of sodium MRI *in vivo*. *J Magn Reson Imaging.* (2013) 38:511–29. doi: 10.1002/jmri.24168
11. Chitiboi T, Ramb R, Feng L, Piekarski E, Tautz L, Hennemuth A, et al. Multi-cycle reconstruction of cardiac MRI for the analysis of inter-ventricular septum motion during free breathing. *Funct Imaging Model Heart.* (2017) 10263:63–72. doi: 10.1007/978-3-319-59448-4_7
12. napari. Available from: https://napari.org/community/mission_and_values.html
13. van der Geest RJ, Garg P. Advanced analysis techniques for intra-cardiac flow evaluation from 4D flow MRI. *Curr Radiol Rep.* (2016) 4:38. doi: 10.1007/s40134-016-0167-7
14. Ye M, Kanski M, Yang D, Chang Q, Yan Z, Huang Q, et al. DeepTag: an unsupervised deep learning method for motion tracking on cardiac tagging magnetic resonance images. In: *Conference Proceedings of the IEEE/CVF Conference on Computer Vision and Pattern Recognition*. Nashville, TN (2021). p. 7261–727.
15. Wu P, Huang Q, Yi J, Qu H, Ye M, Axel L, et al. Cardiac MR image sequence segmentation with temporal motion encoding. In: *European Conference on Computer Vision*. Glasgow (2020). p. 298–309.

Conflict of Interest: The authors declare that the research was conducted in the absence of any commercial or financial relationships that could be construed as a potential conflict of interest.

Publisher's Note: All claims expressed in this article are solely those of the authors and do not necessarily represent those of their affiliated organizations, or those of the publisher, the editors and the reviewers. Any product that may be evaluated in this article, or claim that may be made by its manufacturer, is not guaranteed or endorsed by the publisher.

frontiers | Frontiers in Cardiovascular Medicine

TYPE Original Research
PUBLISHED 06 September 2022
DOI 10.3389/fcvm.2022.960403

OPEN ACCESS

EDITED BY
Aleksandra Radjenovic,
University of Glasgow, United Kingdom

REVIEWED BY
Ruud B. van Heeswijk,
Center Hospitalier Universitaire Vaudois (CHUV), Switzerland
Tamer Basha,
Cairo University, Egypt

*CORRESPONDENCE
Markus Henningsson
markus.henningsson@liu.se

†These authors have contributed equally to this work

SPECIALTY SECTION
This article was submitted to Cardiovascular Imaging, a section of the journal Frontiers in Cardiovascular Medicine

RECEIVED 02 June 2022
ACCEPTED 05 August 2022
PUBLISHED 06 September 2022

CITATION
Jarkman C, Carlhäll C-J and Henningsson M (2022) Clinical evaluation of the Multimapping technique for simultaneous myocardial T_1 and T_2 mapping. *Front. Cardiovasc. Med.* 9:960403. doi: 10.3389/fcvm.2022.960403

Clinical evaluation of the Multimapping technique for simultaneous myocardial T_1 and T_2 mapping

Charlotta Jarkman[1], Carl-Johan Carlhäll[1,2,3†] and Markus Henningsson[1,2*†]

[1]Department of Clinical Physiology in Linköping, Department of Health, Medicine and Caring Sciences, Linköping University, Linköping, Sweden, [2]Division of Diagnostics and Specialist Medicine, Department of Health, Medicine and Caring Sciences (HMV), Linköping University, Linköping, Sweden, [3]Center for Medical Image Science and Visualization (CMIV), Linköping University, Linköping, Sweden

The Multimapping technique was recently proposed for simultaneous myocardial T_1 and T_2 mapping. In this study, we evaluate its correlation with clinical reference mapping techniques in patients with a range of cardiovascular diseases (CVDs) and compare image quality and inter- and intra-observer repeatability. Multimapping consists of an ECG-triggered, 2D single-shot bSSFP readout with inversion recovery and T_2 preparation modules, acquired across 10 cardiac cycles. The sequence was implemented at 1.5T and compared to clinical reference mapping techniques, modified Look-Locker inversion recovery (MOLLI) and T_2 prepared bSSFP with four echo times (T_2bSSFP), and compared in 47 patients with CVD (of which 44 were analyzed). In diseased myocardial segments (defined as the presence of late gadolinium enhancement), there was a high correlation between Multimapping and MOLLI for native myocardium T_1 ($r^2 = 0.73$), ECV ($r^2 = 0.91$), and blood T_1 ($r^2 = 0.88$), and Multimapping and T_2bSSFP for native myocardial T_2 ($r^2 = 0.80$). In healthy myocardial segments, a bias for native T_1 (Multimapping = 1,116 ± 21 ms, MOLLI = 1,002 ± 21, $P < 0.001$), post-contrast T_1 (Multimapping = 479 ± 31 ms, MOLLI = 426 ± 27 ms, 0.001), ECV (Multimapping = 21.5 ± 1.9%, MOLLI = 23.7 ± 2.3%, $P = 0.001$), and native T_2 (Multimapping = 48.0 ± 3.0 ms, T_2bSSFP = 53.9 ± 3.5 ms, $P < 0.001$) was observed. The image quality for Multimapping was scored as higher for all mapping techniques (native T_1, post-contrast T_1, ECV, and T_2bSSFP) compared to the clinical reference techniques. The inter- and intra-observer agreements were excellent (intraclass correlation coefficient, ICC > 0.9) for most measurements, except for inter-observer repeatability of Multimapping native T_1 (ICC = 0.87), post-contrast T_1 (ICC = 0.73), and T_2bSSFP native T_2 (ICC = 0.88). Multimapping shows high correlations with clinical reference mapping techniques for T_1, T_2, and ECV in a diverse cohort of patients with different cardiovascular diseases. Multimapping enables simultaneous T_1 and T_2 mapping and can be performed in a short breath-hold, with image quality superior to that of the clinical reference techniques.

KEYWORDS

T1 mapping, T2 mapping, ECV, quantitative CMR, simultaneous multiparametric CMR

Introduction

Myocardial T_1 and/or T_2 values are altered in many cardiovascular diseases (1). T_1 and T_2 quantification, along with disease-specific patterns of regional and global distribution, can be captured with myocardial mapping techniques (2). In the last 15–20 years, a number of T_1 and T_2 mapping techniques have been published, with different strengths and weaknesses in terms of quantification accuracy, precision, scan time, spatial resolution, and coverage (3). Despite being one of the first T_1 mapping techniques, the modified Look-Locker inversion recovery (MOLLI) remains the most clinically used method due to its high precision and availability on all major scanner platforms (4, 5). However, MOLLI T_1 accuracy is relatively low, and the quantification is susceptible to confounding effects from heart rate or T_2-dependent variability, magnetization transfer effects, motion artifacts, and system imperfections (5, 6). Different T_1 mapping methods have been proposed to address these shortcomings, yet have failed to make significant inroads in the market share of clinical use (7–11). Myocardial T_2 mapping can be performed with multi-echo spin-echo or T_2-prepared balanced steady-state free precession (T_2bSSFP) techniques (12–14). The latter approach is likely the most widely used clinically due to its relative robustness to physiological motion.

In recent years, there has been a growing interest in techniques to simultaneously map T_1 and T_2 in a single scan (15–21). Advantages of this approach compared to conventional mapping, which is performed separately for T_1 and T_2, are that the images are intrinsically spatially aligned, scan time is typically shorter, and the confounding effects of T_1 or T_2 on the quantification of the opposite parameter are minimized. Despite the many theoretical advantages of simultaneous T_1 and T_2 mapping, there is a paucity of translational studies using these techniques in patients with cardiovascular disease (22, 23). This may be due to the more sophisticated acquisition, reconstruction, and mapping strategies necessary for such techniques, which pose challenges for clinical translation. Recently, a new technique for simultaneous T_1 and T_2 mapping, termed Multimapping, was proposed using a standard Cartesian trajectory and evaluated (primarily) in healthy subjects (24). Due to its simplicity, Multimapping may be readily applied in a clinical setting to enable the evaluation of simultaneous T_1 and T_2 mapping in patients with cardiovascular disease.

The primary aim of this study is to validate Multimapping T_1 and T_2 values against clinical reference techniques in patients with different cardiovascular diseases in terms of parameter quantification and image quality. The secondary aim of this study is to evaluate Multimapping intra- and inter-observer variability.

TABLE 1 Clinical characteristics.

Patients (*n*)	44
Age (years)	49 ± 20
Male sex, *n* (%)	28 (64)
BMI (kg/m2)	25 ± 4
Height (cm)	176 ± 10
Weight (kg)	78 ± 12
Heart rate (bpm)	67 ± 14
LVEF (%)	53 ± 11
LVSV (ml)	94 ± 18
LVEDV (ml)	186 ± 54

BMI, body mass index; LVEF, left ventricular ejection fraction; LVSV, left ventricular stroke volume; LVEF, left ventricular end-diastolic volume.

Materials and methods

Study population

All patients provided written informed consent prior to participation, and the study was approved by the local ethics committee (Linköping Regional Ethics Committee, 2015/396–31) and conducted according to the Declaration of Helsinki. Patients referred for CMR at Linköping University Hospital between June and November 2021 were considered for inclusion in this study. In total, 47 patients were recruited. Datasets from three patients were excluded, two because no late gadolinium enhancement (LGE) images were acquired and one due to excessive fold-over artifacts. Clinical characteristics of the remaining patients can be seen in Table 1. Of the included patients, normal cardiac MRI scan was found in 15 (34.1%) patients, myocarditis in 11 (25%) patients, dilated cardiomyopathy (DCM) in 6 (13.6%) patients, ventricular hypertrophy (hypertrophic cardiomyopathy or hypertrophy of unknown origin) in 5 (11.4%) patients, ischemic myocardial injury (acute/recent or old) in 3 (6.8%) patients, arrhythmogenic right ventricular cardiomyopathy in 2 (4.5%) patients, pericarditis in 1 (2.3%) patient, and congenital heart disease in 1 (2.3%) patient.

Data acquisition and reconstruction

All scans were performed on a 1.5T Philips clinical CMR scanner (Philips Healthcare, Best, The Netherlands) using a 28-channel torso coil. The Multimapping pulse sequence and post-processing steps are illustrated in Figure 1. Ten single-shot images are acquired across consecutive cardiac cycles using balanced steady-state free precession (bSSFP) readouts, triggered to the mid-diastolic rest period. Adiabatic inversion radiofrequency (RF) pulses with delay times of 300 ms are

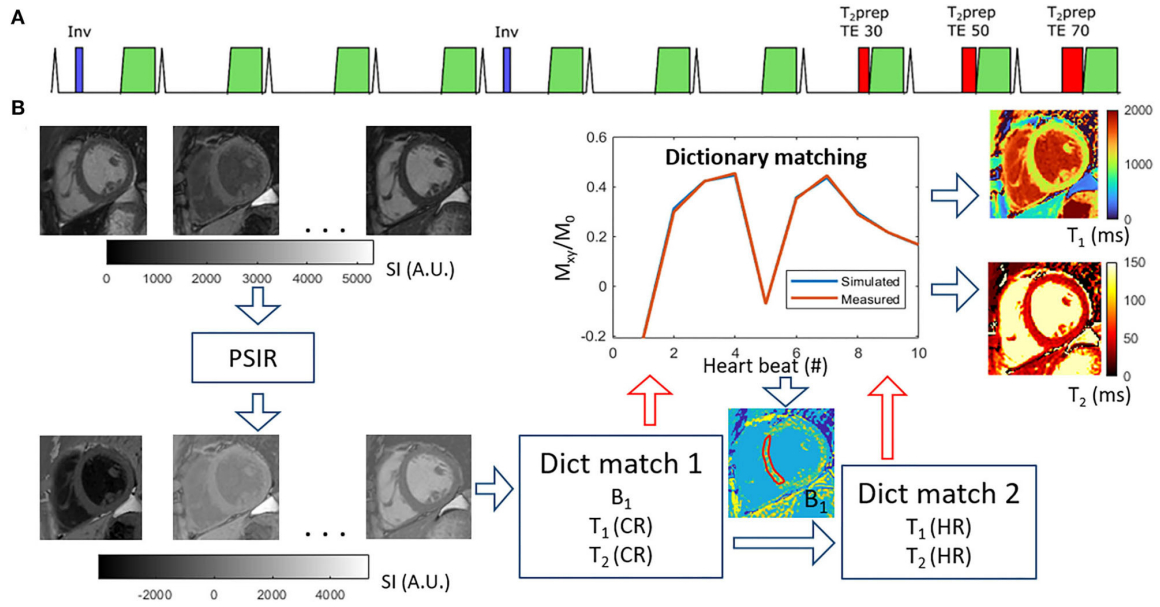

FIGURE 1
Multimapping pulse sequence **(A)** and post-processing **(B)**. The pulse sequence consists of ECG-triggered 2D single-shot acquisitions in 10 consecutive cardiac cycles, preceded by inversion pulses in cycles 1 and 5, and T_2prep with different echo times (TE) in cycles 8, 9, and 10. The post-processing involves first performing a phase-sensitive inversion recovery (PSIR) operation to restore the polarity of the signal, followed by an initial dictionary matching (Dict match 1) to estimate a global B_1 correction factor based on an ROI in the myocardial septum. The dictionary matching finds the pixel-wise closest match between acquired data and the simulated acquisition (with scan-specific delays) for different T_1, T_2, and RF scaling factor (B_1) combinations. A second dictionary matching step (Dict match 2) is then performed for only T_1 and T_2 with high temporal granularity (1 ms resolution) to generate the final T_1 and T_2 maps.

performed in the 1st and 5th cardiac cycles to improve T_1 sensitization. The inversion pulse used a hyperbolic secant shape, had a duration of 8.4 ms, and a B_1 amplitude of 13.5 μT. A previous study has shown that similar settings yield an inversion efficiency of approximately 0.89 (25), which was assumed for this study. T_2 preparation modules with hard 90° RF pulses and four adiabatic refocusing RF pulses are performed in the 8th, 9th, and 10th cardiac cycles to improve T_2 sensitization using echo times of 30, 50, and 70 ms, respectively. The Multimapping imaging parameters for all experiments are: field of view = 320×320 mm, spatial resolution = 2×2 mm, slice thickness = 10 mm, nominal flip angle = 50°, bandwidth = 1,076 Hz/pixel, TR = 2.3 ms, TE = 1.2 ms, SENSE factor = 2, linear profile order. Ten startup RF pulses are used with linearly increasing flip angles. The Multimapping scan was acquired in a mid-ventricular short-axis slice (except in one patient which was mistakenly acquired in a four-chamber view) during a breath-hold. Native Multimapping was acquired in all 47 patients, and post-contrast Multimapping was performed in 31 patients approximately 15 to 20 min after contrast agent administration (0.2 mmol/kg gadobutrol). Due to clinical prioritization, the post-contrast Multimapping was performed after the acquisition of post-contrast MOLL and LGE.

All Multimapping source images were reconstructed on the scanner and transferred to an offline workstation (Intel Core i7-8565U 1.80 GHz processor with 16Gb RAM) to generate T_1 and T_2 maps using MATLAB R2021b (The MathWorks, Natick, MA). The MATLAB code used to generate the maps, including example Multimapping source images from one subject, is available at https://github.com/Multimapping/Matlab_files. Since blood samples were not available for all patients, Multimapping synthetic ECV maps were generated using synthetic hematocrit values, based on the native MOLLI left ventricular blood pool measurements, as previously outlined (26). Image registration using a rigid body transformation was applied to spatially align the native and post-contrast T_1 maps prior to ECV calculation.

MOLLI was acquired in all 47 patients and T_2bSSFP was acquired in 45 patients, in the same slice as Multimapping and used as clinical reference techniques for T_1 and T_2 mapping, respectively. All imaging parameters for the reference techniques (field of view, spatial resolution, etc.) were the same as for Multimapping, except for the flip angle which was 35°. MOLLI was acquired with the 5 (3s) 3 scheme and used the same adiabatic inversion pulse as Multimapping. T_2bSSFP was acquired with four images at different T_2 preparation echo times (0, 23, 46, and 70 ms) and used 3 pause cardiac cycles between each image. Furthermore, T_2bSSFP used the same RF pulse types for the T_2 preparation module as Multimapping. The reference maps were reconstructed on the scanner using vendor-provided inline mapping algorithms, except for the ECV

maps which were generated offline using MATLAB. Similar to Multimapping, synthetic ECV maps were generated using a synthetic hematocrit value derived from the left ventricular blood pool T_1 measured in the native MOLLI image. As for Multimapping, image registration was applied to native and post-contrast MOLLI T_1 maps before ECV was calculated. LGE imaging parameters were TR/TE = 5.6/2.0 ms, flip angle = 25°, FOV = 350×350 mm^2, spatial resolution = 1.8×1.8 mm^2.

Image analysis

T_1 (native and post-contrast), T_2 (native), and ECV measurements were made by drawing manual regions of interest (ROIs) in all datasets. To compare Multimapping to the clinical reference techniques, two sets of myocardial measurements were performed, one targeting any diseased myocardium and one targeting healthy myocardium. For the measurements of diseased myocardium in all maps, ROIs were drawn in the area corresponding with the most prominent positive LGE findings of each patient. Since only a subset of patients had positive LGE findings in the imaged slice, this resulted in 21 measurements for native T_1 and T_2 and 12 measurements for post-contrast T_1 and ECV. For the measurements of healthy myocardium in all maps, ROIs were drawn in the area remote of any LGE abnormality and preferentially in the interventricular septum if it was free of abnormal LGE. Patients were excluded from this analysis if there were indications suggestive of global or diffuse myocardial disease. The measurements in the healthy myocardium were performed in a total of 19 patients for native T_1, 12 patients for T_1 post-contrast and ECV, and 18 patients for T_2.

Measurements were performed in all patients by one observer (CJ, 1 year of CMR experience). To allow intra-observer variability analysis, measurements were repeated in 23 patients by the same observer 2 weeks later. For inter-observer variability analysis, the same 23 patients were measured by two additional observers (MH and CJC with 14 and 21 years of CMR experience, respectively). Furthermore, to compare blood T_1 (native and post-contrast), ROIs were drawn in the left ventricular blood pool (avoiding any papillary muscles) in the Multimapping T_1 and MOLLI images.

The image quality of the acquired maps was qualitatively compared using a Likert scale as devised by Jaubert et al. (22) with the following categories: 1 = uninterpretable, 2 = poor definition of edges, significant noise and/or residual artifacts, 3 = mildly blurred edges, mild noise and/or residual artifacts, 4 = slightly blurred edges, minor residual artifacts, and 5 = negligible blurring or residual artifacts. Visual scoring was performed for T_1 (native and post-contrast), T_2 (native), and ECV separately using the different mapping techniques, and this analysis was performed in 20 patients. The visual scoring was performed by consensus of two blinded observers (CJ and CJC).

Statistical analysis

Continuous variables are expressed as mean ± SD. Categorical variables are expressed as counts and percentages. For the remote measurements, two-tailed Student's paired *t*-tests were performed to compare Multimapping to MOLLI for native T_1, post-contrast T_1, and ECV, and Multimapping and T_2bSSFP for native T_2. For the remote measurements, all parameters tested positive for normality using a Shapiro–Wilk test. Bland–Altman and correlation plots were used to evaluate the agreement and correlation, respectively, between Multimapping and the reference techniques of the measurements in diseased myocardium for native T_1, post-contrast T_1, ECV, and native T_2. To investigate any heart rate dependency for the mapping techniques, the measurements of the remote myocardium were correlated with the heart rate at the time of the scan. Similarly, dependency on T_2 for T_1 (and vice versa) was evaluated by correlating remote T_1 with T_2 for both Multimapping and the reference techniques, and testing for statistical significance. To account for multiple comparisons, Bonferroni correction was performed on the threshold for all significance tests. Since four comparisons were performed (native and post-contrast T_1, native T_2, and ECV), a threshold of 0.05/4 = 0.0125 was used. Intra-observer repeatability and inter-observer repeatability were assessed with intraclass correlation coefficient (ICC) analysis. ICC was calculated using absolute agreement two-way mixed model. Statistical analysis was performed using IBM SPSS Statistics, version 27.0.

Results

Representative parameter maps acquired with Multimapping, reference techniques, and LGE in a patient with no cardiovascular disease findings are shown in Figure 2. Parameter maps from a patient with myocarditis are shown in Figure 3, with prominently altered quantitative values seen in both Multimapping and reference techniques. The final example, in Figure 4, shows parameter maps from a patient with myocardial infarction with a clearly delineated area of infarction in the Multimaps, correlating with LGE. Multimaps for all patients can be downloaded from https://github.com/Multimapping/Patient_study/raw/main/MapReconstructions.pdf.

Comparison of Multimapping and reference techniques in remote myocardium

The Multimapping native T_1 was 1,116 ± 21 ms and for MOLLI 1,002 ± 21 ms, resulting in a statistically significant bias of 114 ms ($P < 0.001$). Multimapping post-contrast T1

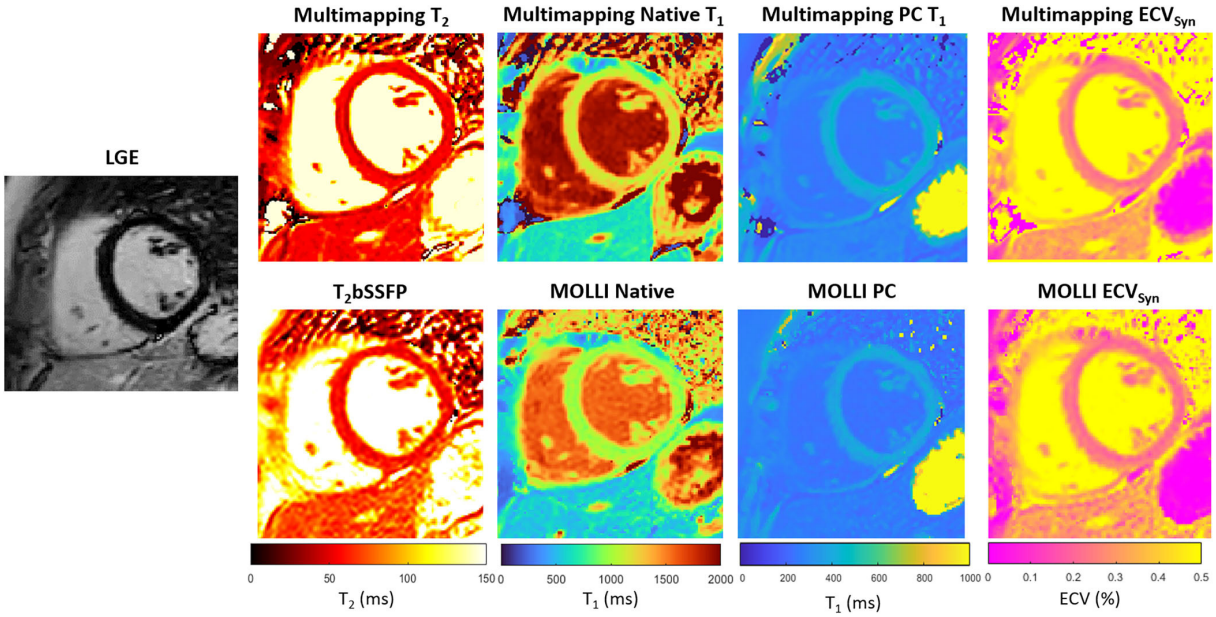

FIGURE 2
LGE and parameter maps (native T_2, native T_1, post-contrast T_1, and ECV) are shown for a patient with no cardiovascular disease findings. The parameter maps were acquired using either Multimapping (top row) or reference techniques (bottom row). Septal T_2 was 49.6 ms and 56.7 ms for Multimapping and T_2bSSFP, respectively. Septal (native/post-contrast) T_1 was 1,144/422 ms and 1,003/381 ms for Multimapping and MOLLI, respectively. Septal ECV was 24.9 and 23.8% for Multimapping and MOLLI, respectively.

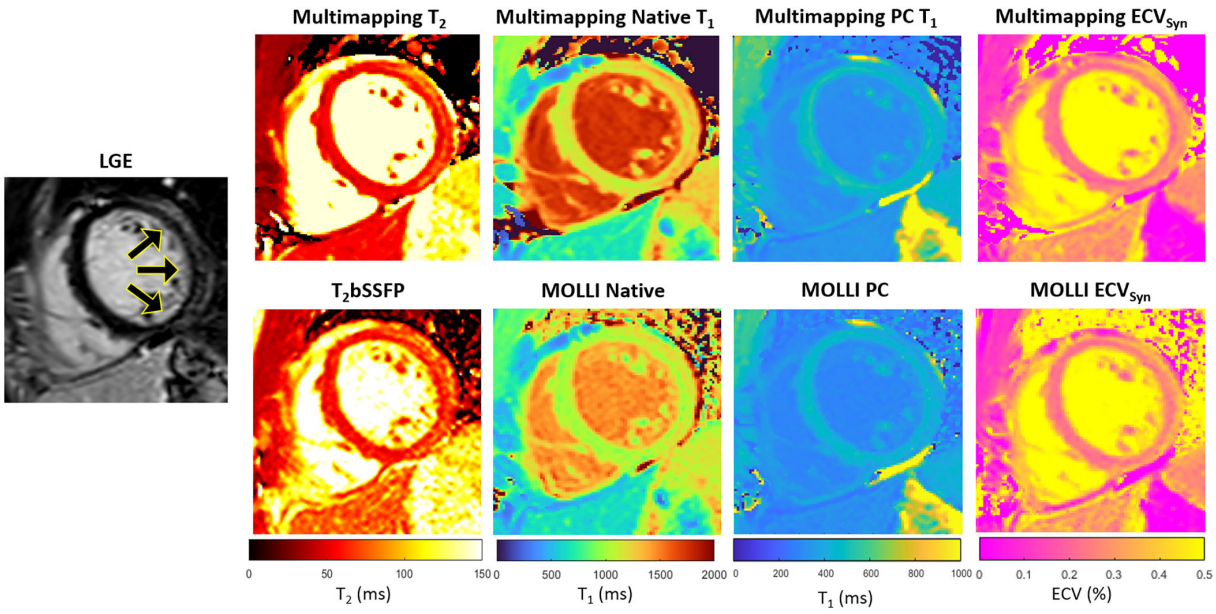

FIGURE 3
LGE and parameter maps in a patient with myocarditis, as indicated by the increased signal in the lateral wall in the LGE and also apparent as altered values in the parameter maps (Multimapping: top row, reference techniques: bottom row). Measurements in the area of enhancement (lateral wall) yielded T_2 of 65.7 ms and 62.4.6 ms for Multimapping and T_2bSSFP, respectively. T_1 values (native/post-contrast) in the same area were 1,286/446 ms and 1,111/423 ms for Multimapping and MOLLI, respectively. ECV was 26.6 and 28.3% in the enhanced area for Multimapping and MOLLI, respectively.

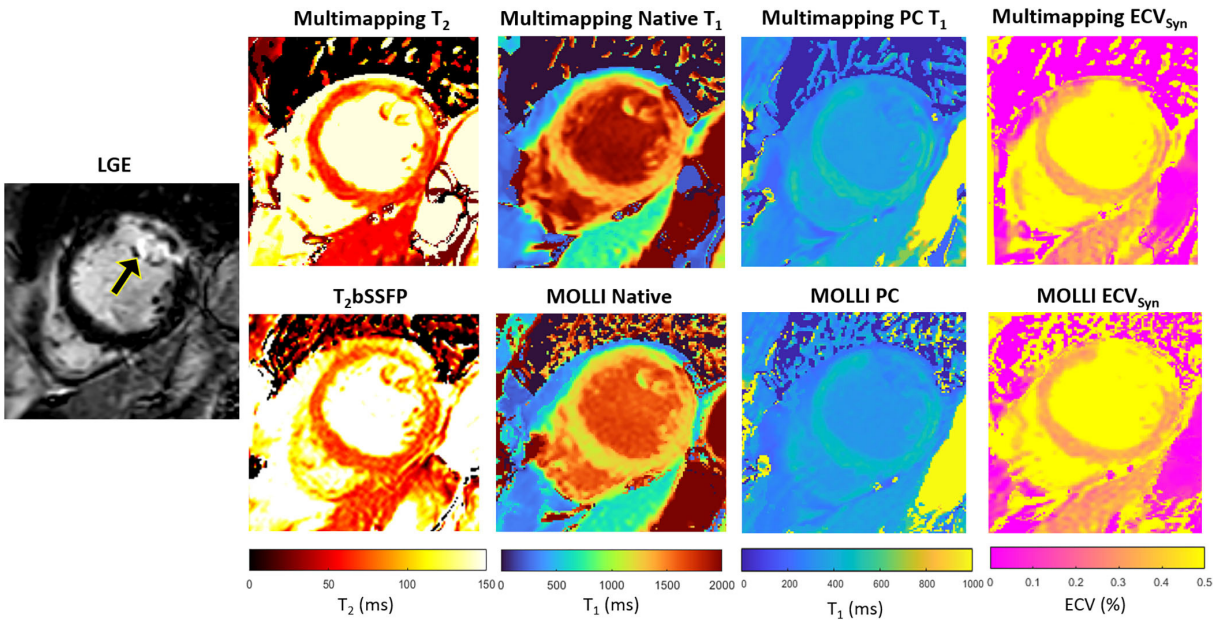

FIGURE 4
LGE and parameter maps in a patient with myocardial infarction, clearly visualized using all techniques, both native and post-contrast. Measurements in the area of enhancement (anterolateral segment) yielded T_2 of 90.5 ms and 88.6 ms for Multimapping and T_2bSSFP, respectively. T_1 values (native/post-contrast) in the same area were 1,516/355 ms and 1,440/338 ms for Multimapping and MOLLI, respectively. ECV was 33.3% and 33% in the enhanced area for Multimapping and MOLLI, respectively.

was 479 ± 31 ms and for MOLLI 426 ± 27 ms, yielding a bias of 53 ms which was statistically significant ($P < 0.001$). Multimapping ECV was 21.5 ± 1.9%, and MOLLI ECV was 23.7 ± 2.3%, resulting in a bias of −2.2% which was statistically significant ($P = 0.001$). Multimapping native T_2 was 48.0 ± 3.0 ms while T_2bSSFP was 53.9 ± 3.5 ms, a statistically significant bias of −9 ms ($P < 0.001$) (Figure 5).

There was no correlation between native T_1 and T_2 for neither Multimapping nor MOLLI and T_2bSSFP. Multimapping T_1 (native and post-contrast), T_2, or ECV and MOLLI T_1 (native and post-contrast) or ECV did not correlate with heart rate either. However, T_2bSSFP showed a correlation with heart rate ($P < 0.001$) (Figure 5).

Comparison of Multimapping and reference techniques for diseased myocardium

In general, the correlation between Multimapping and the clinical reference techniques was very strong ($r^2 > 0.7$) for most variables (Figure 6). A strong correlation coefficient ($r^2 > 0.5$) was found between Multimapping and MOLLI for myocardial T_1 post-contrast ($r^2 = 0.66$) and blood T_1 post-contrast ($r^2 = 0.53$).

Inter- and intra-observer variability

The myocardial measurements and measurements of the left ventricular blood pool for intra-repeatability assessment showed excellent repeatability (myocardial ICC > 0.97, LV blood pool ICC = 1.00) (Table 2). The myocardial measurements for inter-repeatability showed moderate to excellent repeatability (ICC > 0.73) for all mapping techniques. The native and post-contrast T_1 measurements of the blood pool for inter-repeatability showed good to excellent repeatability (ICC > 0.92).

Image quality assessment

The image quality was scored significantly higher for Multimapping compared to T_2bSSFP ($P < 0.001$), MOLLI native T_1 ($P = 0.007$), MOLLI post-contrast T_1 ($P < 0.001$), and MOLLI ECV ($P < 0.001$) (Figure 7).

Discussion

In this study, a new method for simultaneous T_1 and T_2 mapping was compared to the clinical reference mapping technique in a cohort of patients with cardiovascular disease. We found a strong to very strong correlation between the methods for all measured parameters (native T_1, post-contrast

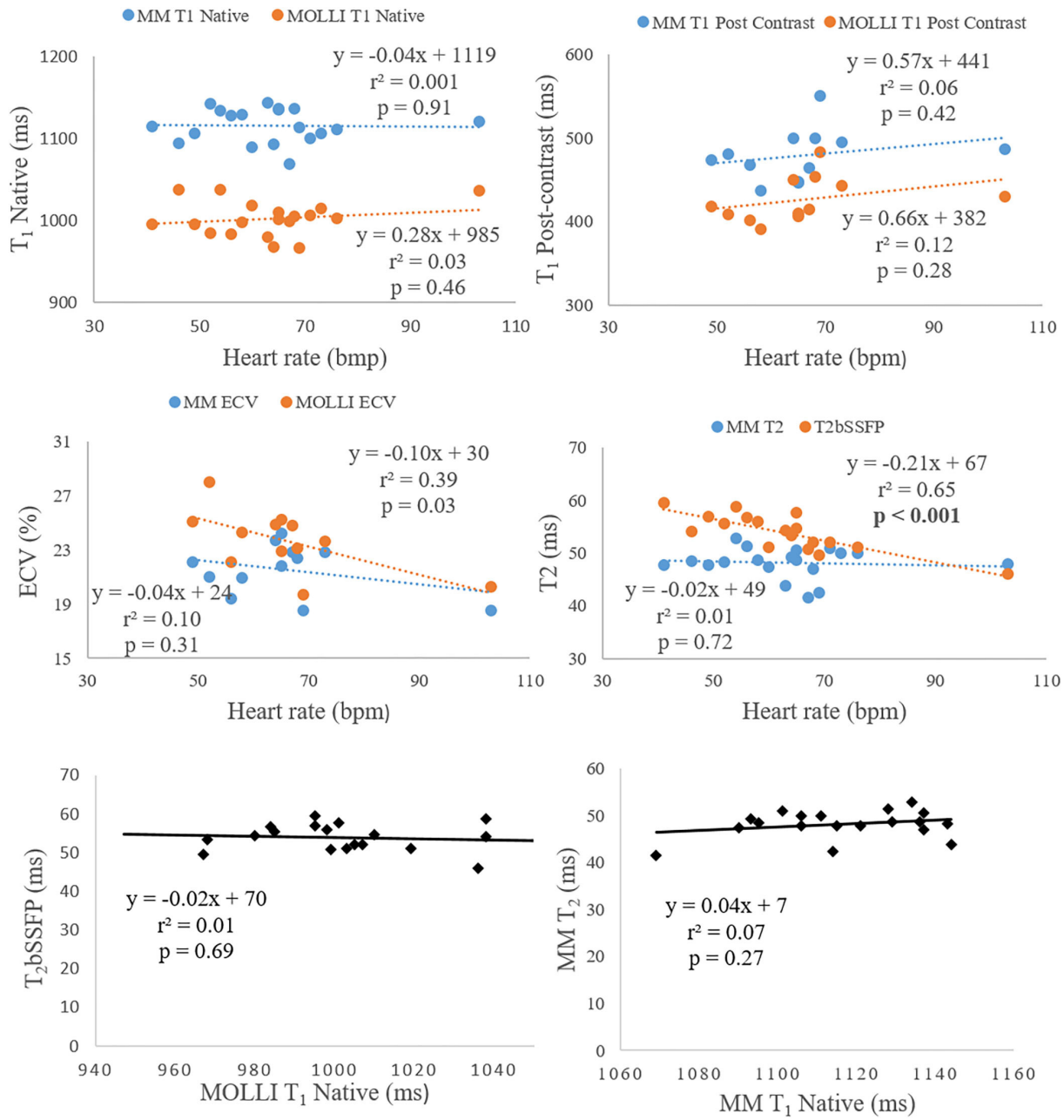

FIGURE 5
The two top rows show the correlation analysis of heart rate dependency to T_1 (native and post-contrast), ECV, and T_2. The bottom row shows the correlation analysis between native T_1 and T_2.

T_1, ECV, and native T_2), while the image quality was considered better using the proposed Multimapping technique compared to the reference methods. Furthermore, intra- and inter-observer variability of Multimapping parameter measurements were in general low and similar to those obtained with the clinical reference techniques.

In segments of healthy/remote myocardium, we measured a mean native T_1 of 1116 ms using Multimapping, more than 100 ms higher than for MOLLI. However, MOLLI is known to significantly underestimate T_1 when compared to more accurate methods such as SASHA (5), which typically yields native T_1 of around 1,200 ms at 1.5T (7, 27). The native T_1 Multimapping values are also in line with the previous study using this technique in healthy volunteers which measured 1,114 ms (24). For post-contrast T_1 mapping, there was also a significantly longer T_1 using Multimapping (479 ms) compared

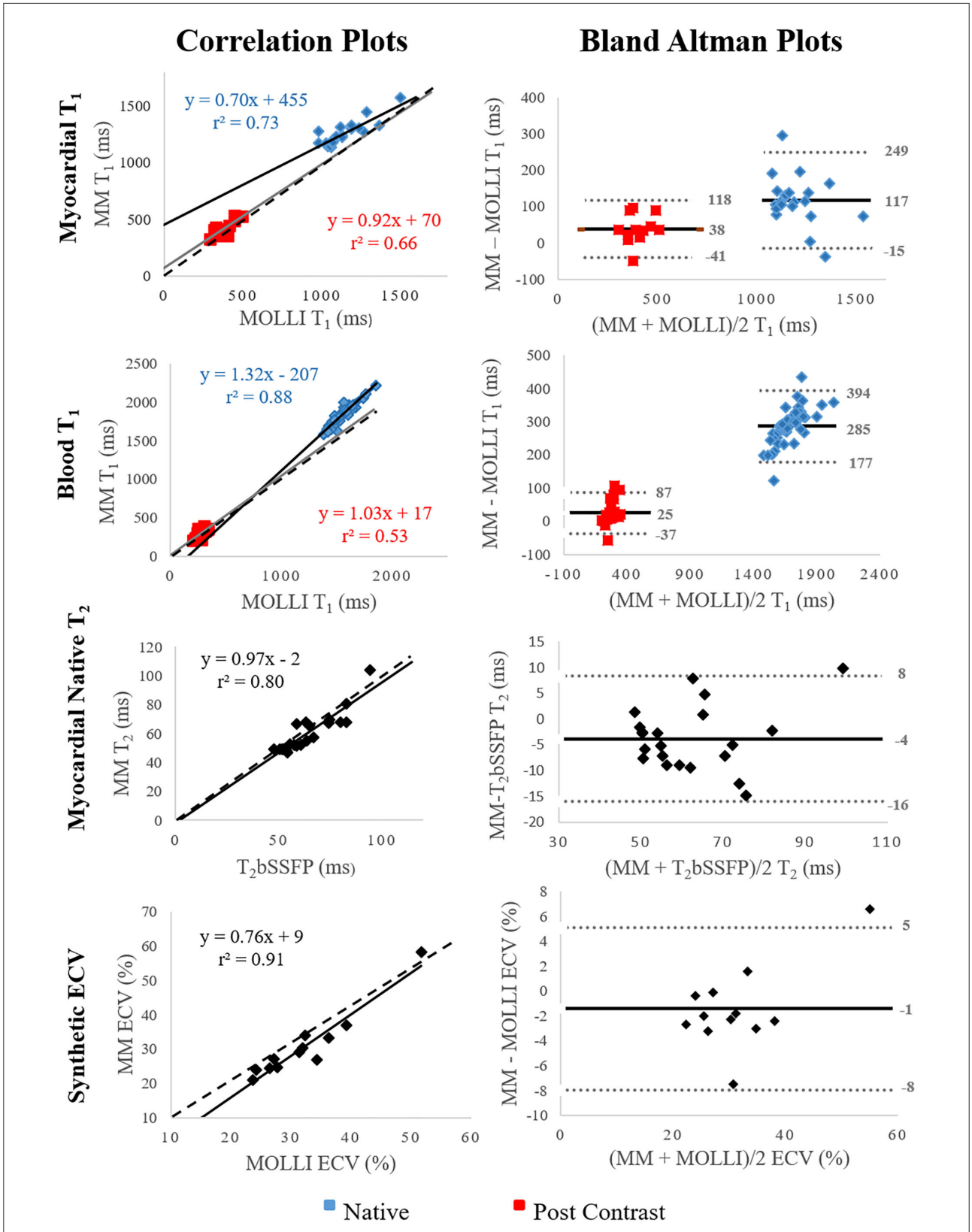

FIGURE 6
Correlation and Bland–Altman plots comparing Multimapping (MM) to MOLLI and T_2bSSFP. For the correlation plots, black and gray lines indicate line of best fit, and the dotted lines show the identity lines. The black lines indicate bias in the Bland–Altman plots. Correlation coefficient (r^2) is reported in the correlation plots and mean difference, and lower and upper limits of agreement (1.96 SD) in the Bland–Altman plots.

to MOLLI (427 ms). Although post-contrast T_1 values are more difficult to compare between studies due to differences in contrast agents and the timing of acquisition after injection, previous studies have shown underestimation of post-contrast T_1 for MOLLI compared to more accurate techniques such as SASHA (28, 29). The study by Nordlund et al. (29) also demonstrated that MOLLI overestimates ECV by approximately 4% in healthy volunteers compared to SASHA, the latter technique correlating more closely with radioisotopes in pigs. This suggests that the significantly lower ECV measured in this study with Multimapping (22%) may be more accurate compared to MOLLI (24%). However, the conversion from T_1 to hematocrit was based on the relationship established for MOLLI in a previous study, which may bias measurements if applied to Multimapping synthetic ECV. For Multimapping synthetic ECV to be used independently of MOLLI, then the relationship between Multimapping blood T_1 and hematocrit should be established. Alternatively, the hematocrit could be directly measured to calculate Multimapping ECV without the need for a MOLLI acquisition. Correlation of T_1 and T_2 values with potential confounding variables such as heart rate or the opposite (T_2 or T_1) parameter did not show any particular dependency for Multimapping in this regard. However, T_2bSSFP appeared to be inversely correlated with heart rate. This suggests additional delayed cardiac cycles may be required to yield less biased T_2 values for high heart rates. Conversely, Multimapping may be a more robust approach for T_1 and T_2 mapping at higher heart rates as no additional modification of the pulse sequence is required.

In the measurements of myocardial segments with disease, we found a high correlation between Multimapping and the clinical reference techniques for native T_1 (blood and myocardium), T_2, and ECV. While correlations for post-contrast T_1 (blood and myocardium) were more moderate, this may be explained by the confounding factor of time after injection, which affect the T_1 measurements. Furthermore, measured post-contrast T_1 in this study had a narrower range for both Multimapping and MOLLI compared to native T_1 which can contribute to a weaker correlation between techniques. Nevertheless, a very strong correlation between Multimapping and reference techniques for native T_1, T_2, and ECV indicates that Multimapping is a useful technique that can be used to detect disease.

Dictionary-based mapping techniques such as Multimapping typically assume that there is no through-plane motion, which is not the case for flowing blood. Such through-plane motion leads to T_1 overestimation as inflowing spins have seen fewer RF pulses and are therefore less saturated. This can explain the observed overestimation of blood (particularly native) T_1 relative to MOLLI. However, it should also be noted that, due to the strong correlation for native blood T_1 blood between Multimapping and MOLLI, the Multimapping technique can likely still capture variability in blood T_1 (due to, e.g., different hematocrit levels) with a similar sensitivity as MOLLI.

The image quality was superior using Multimapping compared to all clinical reference techniques. This could be due to the higher flip angle of 50° using Multimapping, compared to MOLLI and T_2bSSFP which both use a flip angle 35°, with otherwise identical imaging parameters to Multimapping. A higher flip angle for bSSFP-based mapping techniques leads to a higher signal-to-noise ratio which typically contributes to improved image quality. The shorter duration of Multimapping (10 beats) compared to both MOLLI (11 beats) and T_2bSSFP (16 beats) means that Multimapping is less prone to respiratory motion-induced misalignment, which may also contribute to a better image quality. While the Multimapping and MOLLI pulse sequences are very similar (both inversion recovery with bSSFP readouts), Multimapping benefits from phase-sensitive inversion recovery post-processing step which has been shown to improve T_1 map image quality compared to fitting with magnitude images (30), used in the vendor-provided fitting algorithm for MOLLI. Compared to Multimapping, T_2bSSFP uses significantly fewer source images for T_2 mapping, and while only three T_2 preparation modules are included in the Multimapping pulse sequence, the bSSFP readout is intrinsically T_2/T_1 weighted which contributes to the T_2 sensitivity and may explain the improved image quality.

The intra- and inter-observer repeatability analysis showed an excellent repeatability for most measurements using both Multimapping and reference techniques. While Multimapping post-contrast myocardial T_1 inter-observer ICC of 0.73 was relatively low compared to that of MOLLI (ICC = 0.95), post-contrast T_1 mapping is primarily used to generate ECV maps, and here, Multimapping and MOLLI yielded near identical ICC values of 0.94 and 0.93, respectively.

Comparison with other simultaneous T_1 and T_2 mapping techniques

Several simultaneous T_1 and T_2 mapping techniques have been proposed over the last years, comparable to Multimapping. Published studies using similar methods in healthy volunteers are summarized in Table 3, including Multimapping (24). Multimapping has a shorter scan duration than nearly all other simultaneous T_1 and T_2 mapping techniques, requiring 10 beats, which is also shorter than both MOLLI and T_2bSSFP. As many patients with cardiovascular diseases struggle to hold their breath for an extended period, reducing the scan time of mapping techniques is important and has been the focus of several studies (11, 38). This is also in line with the endeavor of utilizing less time-consuming CMR protocols in order to improve the adoption of CMR in routine cardiovascular practice. Inversion recovery magnetization preparation pulses

10.3389/fcvm.2022.960403

TABLE 2 Inter- and intra-observer ICC (95% confidence interval).

	Myocardium		Blood pool	
	Intra-repeatability	Inter-repeatability	Intra-repeatability	Inter-repeatability
MM T_1 native	0.99 (0.97–1.00)	0.87 (0.76–0.94)	1.00 (1.00–1.00)	0.92 (0.85–0.96)
MOLLI T_1 native	0.99 (0.97–0.99)	0.93 (0.88–0.97)	1.00 (1.00–1.00)	0.97 (1.00–1.00)
MM T_1 PC	0.99 (0.98–1.00)	0.73 (0.54–0.86)	1.00 (1.00–1.00)	1.00 (1.00–1.00)
MOLLI T_1 PC	0.97 (0.93–0.99)	0.95 (0.90–0.98)	1.00 (1.00–1.00)	1.00 (1.00–1.00)
MM ECV	0.99 (0.98–1.00)	0.94 (0.89–0.97)		
MOLLI ECV	0.99 (0.97–0.99)	0.93 (0.87–0.97)		
MM T_2	0.99 (0.96–0.99)	0.91 (0.82–0.95)		
T_2bSSFP	0.98 (0.94–0.99)	0.88 (0.78–0.95)		

MM, Multimapping; ECV, extracellular volume fraction; MOLLI, modified Look-Locker inversion recovery; T_2bSSFP, T_2-prepared balanced steady-state free precession.

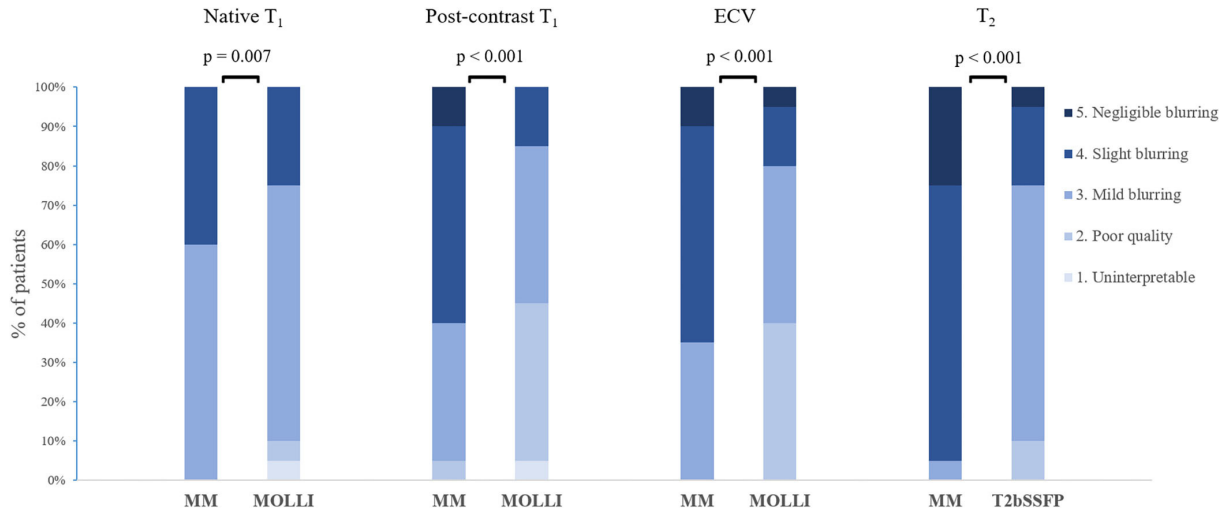

FIGURE 7
Distribution of image quality scores for Multimapping (MM) and *in vivo* reference techniques.

are often used for myocardial T_1 mapping as they increase quantification precision compared to saturation recovery (5), using the full dynamic range of the longitudinal magnetization, at the expense of accuracy as inversion pulses are more sensitive to confounding elements such as magnetization transfer and transverse relaxation during the pulses, which reduce their efficiency (6, 25, 39). Therefore, saturation recovery technique measurements are generally considered to be closer to the "true" *in vivo* T_1 times, typically several 100 ms higher than MOLLI on either 1.5T and 3T scanners. In this regard, Multimapping, which uses inversion recovery, generates T_1 values in healthy/remote myocardium of 1,116 ms, which is closer to the saturation recovery-based techniques (of approximately 1,200 ms) than MOLLI (approximately 1,000 ms) or the most comparable simultaneous T_1 and T_2 mapping studies, Blume et al. (15) and Jaubert et al. (33), which report a myocardial T_1 of 1,017 ms and 1,045 ms, respectively. This may be due to the assumed lower inversion efficiency of 0.89 for the inversion pulses, incorporated into the Multimapping signal model, which is likely closer to the true inversion efficiency than assuming perfect efficiency. However, the inversion efficiency potentially varies between field strengths and vendors, or even spatially across an image due to B_0 and B_1 inhomogeneity. Furthermore, the current Multimapping technique does not consider magnetization transfer. To yield more accurate T_1 values, reproducible across scanner platforms, these confounding effects should be included in the Multimapping signal model, preferably on a pixel-wise basis, although this will likely negatively impact the precision.

It can be difficult to precisely pinpoint the sources of differences in T_1 and T_2 values for the different techniques outlined in Table 3, particularly as many techniques rely on the unconventional acquisition, reconstruction, and mapping strategies. These include, for example, non-Cartesian

TABLE 3 Comparable published simultaneous T_1 and T_2 mapping techniques.

Study	Scan time	FB/BH	IR/SR	Readout	Subjects	Additional mapping	Field strength	Native T1 (ms)	Native T2 (ms)
Blume et al. (15)	Around 3 min	FB	IR	2D cartesian bSSFP	19 HV	-	1.5T	1,017 ± 91	50 ± 4
Kvernby et al. (17)	15 beats	BH	IR	3D Cartesian GRE	10 HV	-	3T	1,083 ± 43	50.4 ± 3.6
Akçakaya et al. (18)	13 beats	BH	SR	2D cartesian bSSFP	10 HV	-	1.5T	1,210 ± 24	48.2 ± 2.8
Santini et al. (31)	8 beats	BH	IR	2D cartesian bSSFP	5 HV	-	3T	1,227 ± 68	37.9 ± 2.4
Hamilton et al. (32)	15 beats	BH	IR	2D spiral GRE	11 HV	-	3T	1,235, range 1,199 −1,316	38, range 32–43
Jaubert et al. (33)	15 beats	BH	IR	2D radial ME-GRE	10 HV	PDFF	1.5T	1,045 ± 32	42.8 ± 2.6
Christodoulou et al. (19)	88 s	FB	IR	2D radial GRE	10 HV	Cardiac motion	3T	1,216 ± 67	47.8 ± 4.9
Shao et al. (34)	11 beats	BH	IR	2D radial GRE	10 HV	-	3T	1,366 ± 31	37.4 ± 0.9
Guo et al. (35)	1.4 ± 0.3 min (WH)	FB	SR	M2D Cartesian bSSFP	13 HV	-	3T	1,373 ± 50	48.7 ± 2.5
Hermann et al. (36)	18.5 s (+resp gating)	FB	SR	2D cartesian ME-GRE	10 HV	T2*	3T	1,573 ± 86	33.2 ± 3.6
Chow et al. (37)	11 beats	BH	SR	2D cartesian bSSFP	10 HV	-	3T	1,523 ± 18	36.7 ± 1.1
Jarkman et al.	10 beats	BH	IR	2D cartesian bSSFP	Remote myocardium 19 patients	-	1.5T	1,116 ± 21	48.0 ± 3.0

WH, whole heart; FB, free breathing; BH, breath-hold; IR, inversion recovery; SR, saturation recovery; bSSFP, balanced steady-state free precession; GRE, spoiled gradient echo; ME-GRE, multi-echo spoiled gradient echo; M2D, multi-slice 2D; HV, healthy volunteer; PDFF, proton density fat fraction.

(radial or spiral) trajectories with iterative reconstruction algorithm, coupled with sophisticated and advanced mapping techniques which may be difficult to reproduce. In contrast, the Multimapping pulse sequence consists of a MOLLI-like acquisition scheme (inversion recovery with Cartesian single-shot 2D bSSFP readout) which are available on all major vendor platforms, with the addition of T_2prep modules which have also been implemented on all vendor platforms. For transparency, the Multimapping parameter mapping method using dictionary matching has been provided open source to enable reproduction of this technique by other investigators which may also enable direct comparison of Multimapping with other simultaneous T_1 and T_2 mapping techniques.

Limitations

This study has several limitations: no respiratory motion correction was performed. Correcting for respiratory-induced image misalignment is important even for breath-held scans and can be achieved using image registration (40). Although image registration could be readily applied to Multimapping source image to this end, this was not performed in order to have a fair comparison with MOLLI and T_2bSSFP maps which were generated using inline vendor algorithm without motion correction. A second technical limitation of Multimapping is that manual interaction is required to define an ROI in the myocardial septum for the B_1 estimation. However, this is a relatively simple step, comparable to the input required to define ROIs for ECV maps. Further work is required to automatize this step or to incorporate B_1 in the high-resolution T_1 and T_2 dictionary matching, which would obviate the need for any manual interaction but with a potential penalty to the precision. A study limitation is that the patient cohort consisted of a small, heterogeneous population of patients with various cardiovascular diseases and performed on a single 1.5T Philips scanner. Further studies are required to evaluate the performance of Multimapping at 3T and using

other vendors. The evaluation of heart rate dependence of the mapping techniques was limited by the relatively narrow heart rates of nearly all patients (only one with heart rate over 100 bpm).

Conclusions

Multimapping T_1 and T_2 values show high correlations with clinical reference mapping techniques in a diverse cohort of patients with different cardiovascular diseases. Multimapping enables simultaneous T_1 and T_2 mapping and can be performed in a short (10 cardiac beats) breath-hold, with image quality superior to that of the clinical reference techniques.

Data availability statement

The dataset presented in this study can be found in online at: https://github.com/Multimapping/Patient_study/raw/main/MapReconstructions.pdf.

Ethics statement

The studies involving human participants were reviewed and approved by Linköping Regional Ethics Committee. The patients/participants provided their written informed consent to participate in this study. Written informed consent was obtained from the individual(s) for the publication of any potentially identifiable images or data included in this article.

Author contributions

MH and C-JC conceived of the study. MH developed the methods, acquired the data, and performed image reconstruction and processing. MH, CJ, and C-JC analyzed the data. All authors participated in revising the manuscript, read, and approved the final manuscript.

Funding

The research leading to these results has received funding from the Swedish Medical Research Council [2018-02779], the Swedish Heart and Lung Foundation [20170440], ALF Grants Region Östergötland [LIO-797721], and the Swedish Research Council [2018-04164].

Conflict of interest

The authors declare that the research was conducted in the absence of any commercial or financial relationships that could be construed as a potential conflict of interest.

Publisher's note

All claims expressed in this article are solely those of the authors and do not necessarily represent those of their affiliated organizations, or those of the publisher, the editors and the reviewers. Any product that may be evaluated in this article, or claim that may be made by its manufacturer, is not guaranteed or endorsed by the publisher.

References

1. Messroghli DR, Moon JC, Ferreira VM, Grosse-Wortmann L, He T, Kellman P, et al. Clinical recommendations for cardiovascular magnetic resonance mapping of T1, T2, T2 and extracellular volume: a consensus statement by the Society for Cardiovascular Magnetic Resonance (SCMR) endorsed by the European association for cardiovascular imagin. *J Cardiovasc Magn Reson.* (2017) 19:75. doi: 10.1186/s12968-017-0389-8

2. Kim PK, Hong YJ, Im DJ, Suh YJ, Park CH, Kim JY, et al. Myocardial T1 and T2 mapping: techniques and clinical applications. *Korean J Radiol.* (2017) 18:113–31. doi: 10.3348/kjr.2017.18.1.113

3. Ogier AC, Bustin A, Cochet H, Schwitter J, van Heeswijk RB. The road toward reproducibility of parametric mapping of the heart: a technical review. *Front Cardiovasc Med.* (2022) 9:876475. doi: 10.3389/fcvm.2022.876475

4. Messroghli DR, Radjenovic A, Kozerke S, Higgins DM, Sivananthan MU, Ridgway JP. Modified look-locker inversion recovery (MOLLI) for high-resolution T1 mapping of the heart. *Magn Reson Med.* (2004) 52:141–6. doi: 10.1002/mrm.20110

5. Kellman P, Hansen MS. T1-mapping in the heart: accuracy and precision. *J Cardiovasc Magn Reson.* (2014) 16:2. doi: 10.1186/1532-429X-16-2

6. Robson MD, Piechnik SK, Tunnicliffe EM, Neubauer S. T1 measurements in the human myocardium: The effects of magnetization transfer on the SASHA and MOLLI sequences. *Magn Reson Med.* (2013) 70:664–70. doi: 10.1002/mrm.24867

7. Chow K, Flewitt JA, Green JD, Pagano JJ, Friedrich MG, Thompson RB. Saturation recovery single-shot acquisition (SASHA) for myocardial T1 mapping. *Magn Reson Med.* (2014) 71:2082–95. doi: 10.1002/mrm.24878

8. Weingärtner S, Akçakaya M, Basha T, Kissinger K V, Goddu B, Berg S, et al. Combined saturation/inversion recovery sequences for improved evaluation of scar and diffuse fibrosis in patients with arrhythmia or heart rate variability. *Magn Reson Med.* (2014) 71:1024–34. doi: 10.1002/mrm.24761

9. Weingärtner S, Roujol S, Akçakaya M, Basha TA, Nezafat R. Free-breathing multislice native myocardial T1 mapping using the slice-interleaved T1 (STONE) sequence. *Magn Reson Med.* (2015) 74:115–24. doi: 10.1002/mrm.25387

10. Marty B, Coppa B, Carlier PG. Fast, precise, and accurate myocardial T1 mapping using a radial MOLLI sequence with FLASH readout. *Magn Reson Med.* (2018) 79:1387–98. doi: 10.1002/mrm.26795

11. Piechnik SK, Ferreira VM, Dall'Armellina E, Cochlin LE, Greiser A, Neubauer S, et al. Shortened Modified Look-Locker Inversion recovery (ShMOLLI) for clinical myocardial T1-mapping at 1.5 and 3 T within a 9 heartbeat breathhold. *J Cardiovasc Magn Reson.* (2010) 12:69. doi: 10.1186/1532-429X-12-69

12. Baeßler B, Schaarschmidt F, Stehning C, Schnackenburg B, Maintz D, Bunck AC. Cardiac T2-mapping using a fast gradient echo spin echo sequence - First *in vitro* and *in vivo* experience. *J Cardiovasc Magn Reson.* (2015) 17:67. doi: 10.1186/s12968-015-0177-2

13. Ding H, Fernandez-De-Manuel L, Schär M, Schuleri KH, Halperin H, He L, et al. Three-dimensional whole-heart T2 mapping at 3T. *Magn Reson Med.* (2015) 74:803–16. doi: 10.1002/mrm.25458

14. Sprinkart AM, Luetkens JA, Träber F, Doerner J, Gieseke J, Schnackenburg B, et al. Gradient Spin Echo (GraSE) imaging for fast myocardial T2 mapping. *J Cardiovasc Magn Reson.* (2015) 17:12. doi: 10.1186/s12968-015-0127-z

15. Blume U, Lockie T, Stehning C, Sinclair S, Uribe S, Razavi R, et al. Interleaved T1 and T2 relaxation time mapping for cardiac applications. *J Magn Reson Imaging.* (2009) 29:480–7. doi: 10.1002/jmri.21652

16. Shao J, Zhou Z, Nguyen KL, Finn JP, Hu P. Accurate, precise, simultaneous myocardial T1 and T2 mapping using a radial sequence with inversion recovery and T2 preparation. *NMR Biomed.* (2019) 32:e4165. doi: 10.1002/nbm.4165

17. Kvernby S, Warntjes MJ a. B, Haraldsson H, Carlhäll CJ, Engvall J, Ebbers T. Simultaneous three-dimensional myocardial T1 and T2 mapping in one breath hold with 3D-QALAS. *J Cardiovasc Magn Reson.* (2014) 16:102. doi: 10.1186/s12968-014-0102-0

18. Akçakaya M, Weingärtner S, Basha TA, Roujol S, Bellm S, Nezafat R. Joint myocardial T1 and T2 mapping using a combination of saturation recovery and T2-preparation. *Magn Reson Med.* (2016) 76:888–96. doi: 10.1002/mrm.25975

19. Christodoulou AG, Shaw JL, Nguyen C, Yang Q, Xie Y, Wang N, et al. Magnetic resonance multitasking for motion-resolved quantitative cardiovascular imaging. *Nat Biomed Eng.* (2018) 2:215–26. doi: 10.1038/s41551-018-0217-y

20. Milotta G, Bustin A, Jaubert O, Neji R, Prieto C, Botnar RM. 3D whole-heart isotropic-resolution motion-compensated joint T1/T2 mapping and water/fat imaging. *Magn Reson Med.* (2020) 84:3009–26. doi: 10.1002/mrm.28330

21. Mao X, Lee H-L, Hu Z, Cao T, Han F, Ma S, et al. Simultaneous multi-slice cardiac MR multitasking for motion-resolved, non-ECG, free-breathing T1–T2 mapping. *Front Cardiovasc Med.* (2022) 9:833257. doi: 10.3389/fcvm.2022.833257

22. Jaubert O, Cruz G, Bustin A, Hajhosseiny R, Nazir S, Schneider T, et al. T1, T2, and fat fraction cardiac MR fingerprinting: preliminary clinical evaluation. *J Magn Reson Imaging.* (2021) 53:1253–65. doi: 10.1002/jmri.27415

23. Cavallo AU, Liu Y, Patterson A, Al-Kindi S, Hamilton J, Gilkeson R, et al. CMR Fingerprinting for Myocardial T1, T2, and ECV quantification in patients with nonischemic cardiomyopathy. *JACC Cardiovasc Imaging.* (2019) 12:1584–5. doi: 10.1016/j.jcmg.2019.01.034

24. Henningsson M. Cartesian dictionary-based native T1 and T2 mapping of the myocardium. *Magn Reson Med.* (2022) 87:2347–62. doi: 10.1002/mrm.29143

25. Kellman P, Herzka DA, Hansen MS. Adiabatic inversion pulses for myocardial T1 mapping. *Magn Reson Med.* (2014) 71:1428–34. doi: 10.1002/mrm.24793

26. Fent GJ, Garg P, Foley JRJ, Swoboda PP, Dobson LE, Erhayiem B, et al. Synthetic Myocardial Extracellular Volume Fraction. *JACC Cardiovasc Imaging.* (2017) 10:1402–4. doi: 10.1016/j.jcmg.2016.12.007

27. Roujol S, Weingärtner S, Foppa M, Chow K, Kawaji K, Ngo LH, et al. Accuracy, precision, and reproducibility of four T1 mapping sequences: a head-to-head comparison of MOLLI, ShMOLLI, SASHA, and SAPPHIRE. *Radiology.* (2014) 272:683–9. doi: 10.1148/radiol.14140296

28. Weingärtner S, Meßner NM, Budjan J, Loßnitzer D, Mattler U, Papavassiliu T, et al. Myocardial T1-mapping at 3T using saturation-recovery: reference values, precision and comparison with MOLLI. *J Cardiovasc Magn Reson.* (2016) 18:84. doi: 10.1186/s12968-016-0302-x

29. Nordlund D, Xanthis C, Bidhult S, Jablonowski R, Kanski M, Kopic S, et al. Measuring extracellular volume fraction by MRI: first verification of values given by clinical sequences. *Magn Reson Med.* (2020) 83:662–72. doi: 10.1002/mrm.27938

30. Xue H, Greiser A, Zuehlsdorff S, Jolly MP, Guehring J, Arai AE, et al. Phase-sensitive inversion recovery for myocardial T1 mapping with motion correction and parametric fitting. *Magn Reson Med.* (2013) 69:1408–20. doi: 10.1002/mrm.24385

31. Santini F, Kawel-Boehm N, Greiser A, Bremerich J, Bieri O. Simultaneous T1 and T2 quantification of the myocardium using Cardiac Balanced-SSFP Inversion Recovery with Interleaved Sampling Acquisition (CABIRIA). *Magn Reson Med.* (2015) 74:365–71. doi: 10.1002/mrm.25402

32. Hamilton JI, Jiang Y, Chen Y, Ma D, Lo WC, Griswold M, et al. MR fingerprinting for rapid quantification of myocardial T1, T2, and proton spin density. *Magn Reson Med.* (2017) 77:1446–58. doi: 10.1002/mrm.26216

33. Jaubert O, Cruz G, Bustin A, Schneider T, Lavin B, Koken P, et al. Water–fat Dixon cardiac magnetic resonance fingerprinting. *Magn Reson Med.* (2020) 83:2107–23. doi: 10.1002/mrm.28070

34. Shao J, Ghodrati V, Nguyen KL, Hu P. Fast and accurate calculation of myocardial T1 and T2 values using deep learning Bloch equation simulations (DeepBLESS). *Magn Reson Med.* (2020) 84:2831–45. doi: 10.1002/mrm.28321

35. Guo R, Cai X, Kucukseymen S, Rodriguez J, Paskavitz A, Pierce P, et al. Free-breathing simultaneous myocardial T1 and T2 mapping with whole left ventricle coverage. *Magn Reson Med.* (2021) 85:1308–21. doi: 10.1002/mrm.28506

36. Hermann I, Kellman P, Demirel OB, Akçakaya M, Schad LR, Weingärtner S. Free-breathing simultaneous T1, T2, and T2∗ quantification in the myocardium. *Magn Reson Med.* (2021) 86:1226–40. doi: 10.1002/mrm.28753

37. Chow K, Hayes G, Flewitt JA, Feuchter P, Lydell C, Howarth A, et al. Improved accuracy and precision with three-parameter simultaneous myocardial T1 and T2 mapping using multiparametric SASHA. *Magn Reson Med.* (2022) 87:2775–91. doi: 10.1002/mrm.29170

38. Guo R, El-Rewaidy H, Assana S, Cai X, Amyar A, Chow K, et al. Accelerated cardiac T1 mapping in four heartbeats with inline MyoMapNet: a deep learning-based T1 estimation approach. *J Cardiovasc Magn Reson.* (2022) 24:6. doi: 10.1186/s12968-021-00834-0

39. Chow K, Kellman P, Spottiswoode BS, Nielles-Vallespin S, Arai AE, Salerno M, et al. Saturation pulse design for quantitative myocardial T1 mapping. *J Cardiovasc Magn Reson.* (2015) 17:84. doi: 10.1186/s12968-015-0187-0

40. Roujol S, Foppa M, Weingärtner S, Manning WJ, Nezafat R. Adaptive registration of varying contrast-weighted images for improved tissue characterization (ARCTIC): application to T1 mapping. *Magn Reson Med.* (2015) 73:1469–82. doi: 10.1002/mrm.25270

frontiers | Frontiers in Cardiovascular Medicine

TYPE Review
PUBLISHED 20 September 2022
DOI 10.3389/fcvm.2022.1009131

OPEN ACCESS

EDITED BY
Anthony G. Christodoulou,
Cedars-Sinai Medical Center,
United States

REVIEWED BY
Jesse Hamilton,
University of Michigan, United States
Xianglun Mao,
GE Healthcare, United States

*CORRESPONDENCE
Carlos Velasco
carlos.velasco@kcl.ac.uk

†These authors have contributed equally to this work and share first authorship

SPECIALTY SECTION
This article was submitted to Cardiovascular Imaging, a section of the journal Frontiers in Cardiovascular Medicine

RECEIVED 01 August 2022
ACCEPTED 30 August 2022
PUBLISHED 20 September 2022

CITATION
Velasco C, Fletcher TJ, Botnar RM and Prieto C (2022) Artificial intelligence in cardiac magnetic resonance fingerprinting.
Front. Cardiovasc. Med. 9:1009131.
doi: 10.3389/fcvm.2022.1009131

Artificial intelligence in cardiac magnetic resonance fingerprinting

Carlos Velasco[1*†], Thomas J. Fletcher[1†], René M. Botnar[1,2,3] and Claudia Prieto[1,2,3]

[1]School of Biomedical Engineering and Imaging Sciences, King's College London, London, United Kingdom, [2]Institute for Biological and Medical Engineering, Pontificia Universidad Católica de Chile, Santiago, Chile, [3]Millennium Institute for Intelligent Healthcare Engineering, Santiago, Chile

Magnetic resonance fingerprinting (MRF) is a fast MRI-based technique that allows for multiparametric quantitative characterization of the tissues of interest in a single acquisition. In particular, it has gained attention in the field of cardiac imaging due to its ability to provide simultaneous and co-registered myocardial T_1 and T_2 mapping in a single breath-held cardiac MRF scan, in addition to other parameters. Initial results in small healthy subject groups and clinical studies have demonstrated the feasibility and potential of MRF imaging. Ongoing research is being conducted to improve the accuracy, efficiency, and robustness of cardiac MRF. However, these improvements usually increase the complexity of image reconstruction and dictionary generation and introduce the need for sequence optimization. Each of these steps increase the computational demand and processing time of MRF. The latest advances in artificial intelligence (AI), including progress in deep learning and the development of neural networks for MRI, now present an opportunity to efficiently address these issues. Artificial intelligence can be used to optimize candidate sequences and reduce the memory demand and computational time required for reconstruction and post-processing. Recently, proposed machine learning-based approaches have been shown to reduce dictionary generation and reconstruction times by several orders of magnitude. Such applications of AI should help to remove these bottlenecks and speed up cardiac MRF, improving its practical utility and allowing for its potential inclusion in clinical routine. This review aims to summarize the latest developments in artificial intelligence applied to cardiac MRF. Particularly, we focus on the application of machine learning at different steps of the MRF process, such as sequence optimization, dictionary generation and image reconstruction.

KEYWORDS

magnetic resonance fingerprinting (MRF), artificial intelligence (AI), cardiac MRF, multiparametric imaging, cardiac magnetic resonance (CMR)

Introduction

Cardiac magnetic resonance fingerprinting

Cardiac Magnetic Resonance (CMR) imaging is widely accepted as a key non-invasive imaging technique for the evaluation of cardiovascular diseases (1). CMR enables comprehensive myocardial tissue characterization, evaluating specific parameters such as T_1, T_2 and $T_{1\rho}$, relaxation times and extracellular volume (2–5). Hence, quantitative mapping of these parameters of interest has become a primary tool for diagnosis of cardiomyopathies. Conventionally, several MRI scans using different protocols are acquired sequentially to provide multiparametric quantification by encoding one parameter at a time. However, this methodology is time consuming and leads to long scan times, patient discomfort, and mis-registered parameter maps. In contrast, simultaneous quantification of multiple parameters would address several of these issues, making multiparametric quantitative CMR appealing for widespread use in the clinical routine.

Many simultaneous multiparametric approaches have recently been proposed to address these issues and provide co-registered multiparametric quantification, including Multitasking (6, 7), steady-state techniques with multiparametric encoding (8, 9), other free-running approaches (10, 11) and Magnetic Resonance Fingerprinting (MRF), (12). MRF has the potential to provide not only multiple co-registered parametric maps in a time-efficient manner but can also include additional model corrections [e.g., B_0 (12), B_1 (13), slice profile (14)]. Underlying MRF is the concept that each tissue has unique properties (such as T_1 and T_2) and thus unique signal evolutions for a given sequence. By varying several sequence parameters (such as flip angle, repetition time or magnetization preparation pulses) throughout the acquisition (see Figures 1A1,A2), unique signal evolutions (or "fingerprints") for each combination of parameters of interest are created. Beforehand, a large dictionary (lookup table) of usually 10^4 to 10^8 parameter combinations and signal evolutions can be pre-calculated (Figure 1C), knowing the sequence details [using, for example Bloch simulations (15) or Extended Phase Graphs (EPG) (16)], and reutilized for the subsequent scans provided that the acquisition parameters remain unchanged. The measured signal evolution is then compared against the expected signal behavior *via* dictionary matching to simultaneously estimate the parametric maps in a voxel-wise basis, [respectively Figures 1D,E, (10)].

Although the original MRF work was proposed on brain MRI, the technique was rapidly implemented for other anatomic regions, including cardiac MRF (17). Compared to conventional MRF, cardiac MRF faces two main challenges derived for the inevitable heart motion that occurs during a scan. Firstly, since the heart is beating while the scan is being performed, the acquisition needs to be ECG-triggered, so that the acquisition window is always in the same cardiac phase. However, since the cardiac wave cannot be predicted, the dictionary must be specifically calculated for each subject once the acquisition has been performed to include the exact cardiac rhythm measured by the ECG. Secondly, cardiac and respiratory motions may affect MR image quality considerably. Therefore, scans are usually performed under breath-hold and on a short cardiac acquisition window (usually at mid-diastole), limiting the feasible scan time to the breath-hold duration and resulting in very highly undersampled data.

Despite these challenges, the field of cardiac MRF has experienced rapid growth. Many efforts have focused on improving its diagnostic potential by; extending the number of encoded parameters beyond just T_1 and T_2 [e.g., fat fraction (18), T_2^* (19), $T_{1\rho}$ (20)], optimizing sequence design (21), fast and robust dictionary generation (22–25) and advanced undersampled image reconstruction (26–28) among others. However, most of these techniques are computationally expensive using conventional methods, limiting their practical utility. There is still much room for improvement, and the integration of state-of-the-art developments in Artificial Intelligence (AI) and Deep Learning (DL) could help solve these and other challenges in cardiac MRF.

Artificial intelligence and deep learning

Artificial Intelligence refers to the ability of machines or computer algorithms to perform tasks that would typically require human intelligence (Figure 2). Machine learning (ML) is a subfield of AI where a model learns how to make predictions for a specific problem using relevant training data. In this way, the features of the model are learnt from relevant training examples without the need of explicitly pre-programmed rules, allowing the model to generalize and make predictions for unseen examples. The most advanced form of ML is DL, that uses multi-layered artificial Neural Networks (NNs) consisting of artificial neurons, inspired by biological neural networks. NNs are universal approximators (29), in theory able to approximate any Borel measurable function with a finite number of neurons. Thus, NNs can offer a more compact representation of complicated functions allowing for more efficient calculation. They are therefore ideal for cardiac MRF that involves complex acquisition strategies, scan-specific information, multi-dimensional image data dominated by noise, complicated reconstruction steps and computationally expensive calculations using conventional methods. Indeed, the ability of ML and DL has already been proven to be of great value in many domains of CMR imaging (30, 31), from image reconstruction (32–34) to diagnosis of cardiomyopathies (35, 36), reporting of cardiac function (37, 38), segmentation of cardiac CINE imaging (39, 40) and quantification of tissue parameters (41).

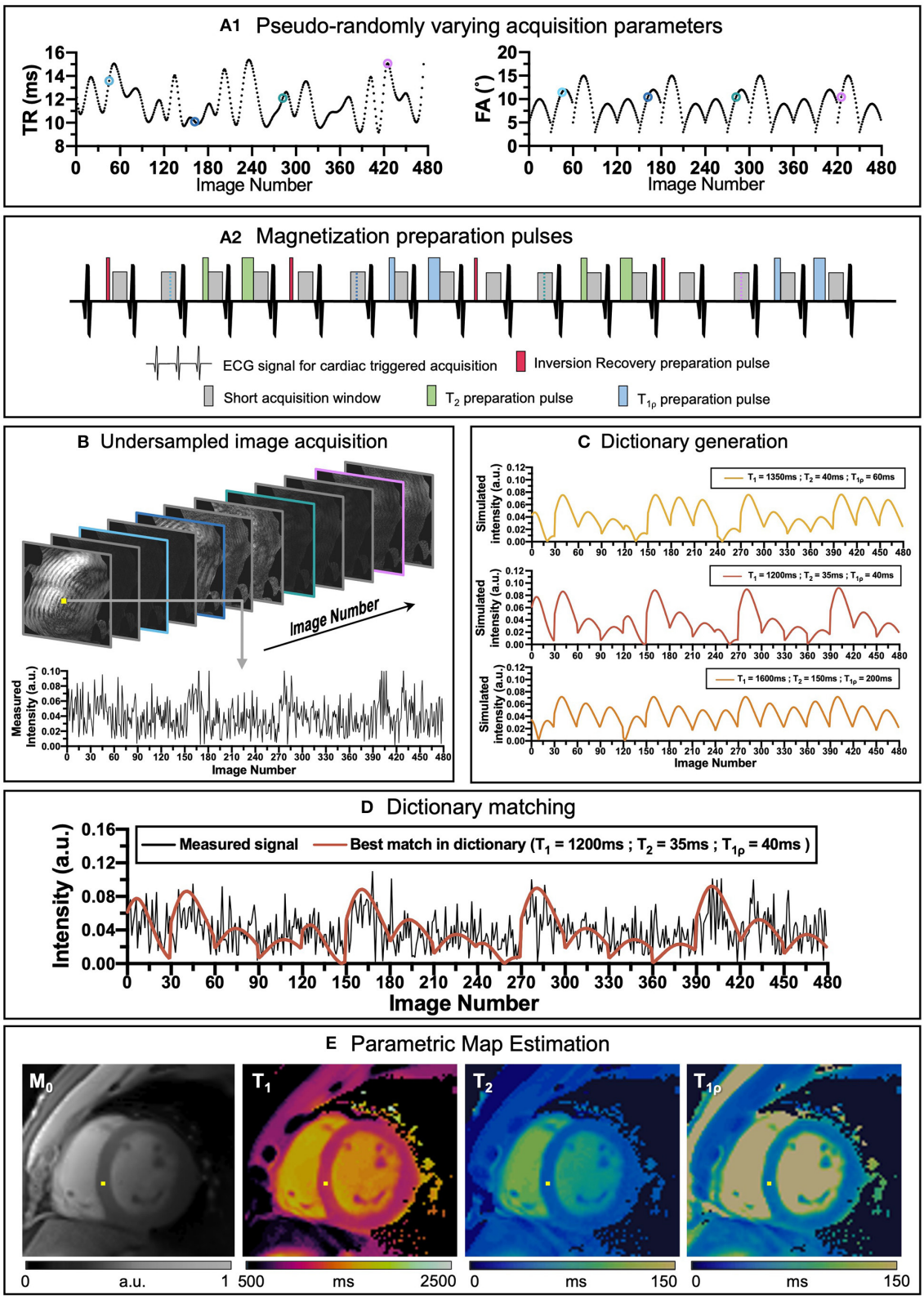

FIGURE 1
An overview of cardiac MRF framework. **(A1)** Repetition time (TR) and variable flip angles (FA) may be pseudo-randomly varied throughout acquisition. **(A2)** Magnetization preparation pulses are introduced to increment contrast weighing on the desired parameters (in this example Inversion Recovery, (IR pulses, in red), T_2 preparation, (T_2 prep pulses in green) and $T_{1\rho}$ preparation, ($T_{1\rho}$ prep pulses in blue) are included to

(Continued)

FIGURE 1 (Continued)
encode T_1 and T_2 contrasts before some heartbeats). **(B)** Highly undersampled images are obtained, and **(C)** a subject-specific dictionary due to the unique cardiac rhythm during the scan is calculated in parallel. **(D)** Matching the temporal evolution of the signal measured with the dictionary will provide **(E)** inherently co-registered parametric maps of the scanned region. The different colored dots in **(A1)** correspond to different timepoints and contrasts **(B)** during the sequence.

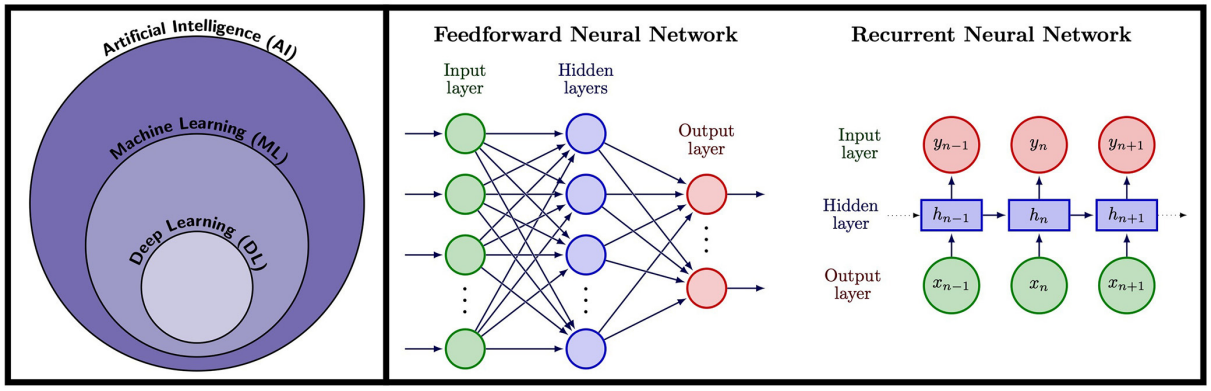

FIGURE 2
Left: Artificial Intelligence (AI) encompasses tasks performed by machines and computers that would normally require human intelligence. A subfield of AI is Machine Learning (ML), a technique whereby computer algorithms learn to perform a task from training data rather than requiring explicitly pre-programmed rules, allowing them to provide predictions for unseen examples. Deep Learning (DL) is a subfield of ML that uses artificial Neural Networks (NNs), modeled on neurons in the human brain, trained using data to provide predictions. **Right:** NN architectures used in cardiac MRF. Feedforward neural networks consist of an input later which could be for example a fingerprint in MRF, followed by a series of hidden layers, followed by a final output later that could output for example tissue parameters. RNNs are ideal for sequence data and take an input timepoint, along with an internal hidden state that encodes information from previous data in the sequence, thus incorporating memory of previous patterns in the sequence.

In traditional ML, measurable properties known as features are first extracted from relevant data. These features are then input into the model as training data, training the model parameters so that the model can find and generate accurate predictions of general underlying patterns using an optimization algorithm. The optimization algorithm measures the accuracy of these predictions using some quality measure, for example, the mean absolute error calculating the mean difference between predicted and ground truth values. The ability of the model to generalize is measured on a separate validation dataset. The accuracy of the predictions from the validation dataset are then used to optimize model parameters and prevent over-fitting to the training data. Finally, the model is evaluated on a separate held-out test dataset to simulate how the model will perform on unseen data. In medical imaging, models are often trained using supervised learning, where data is accompanied with ground truth labels. An example in cardiac MRF would be predicting signal evolutions labeled with ground truth parameter combinations and RR intervals (the time between successive R peaks determined from ECG data which itself is used to trigger the acquisitions in cardiac MRF). Models can also be trained in an unsupervised manner, where no labels are given. Autoencoders are one example, where a sparse representation of the data is learnt from unlabeled data and then this encoding is used to regenerate the input data, which can be useful for denoising applications. Self-supervised learning is a subset of unsupervised learning where supervisory signals are obtained from the data itself. For example, a cardiac motion algorithm can be trained without labels by using the motion estimation predictions to warp one cardiac phase to another and a loss term calculated between the now-similar images. Typically, there are a large number of features that the algorithm can use, and the accuracy of the model increases when more relevant features are used. The art of designing the optimal combination of features is called feature engineering but this can be a difficult task, usually requiring an experienced user and even so, the optimal features for a certain dataset are unlikely to be optimal for a slightly different one.

DL (42, 43) algorithms can learn features automatically from the dataset by themselves, removing the need to extract and select relevant features. NNs consist of multiple layers of connected nodes, called neurons, mimicking the behavior of the nervous system in humans. Each neuron is a mathematical function that takes one or more inputs and sums them with weights learnt during training, this is then passed through a non-linear activation function to produce an output. The NN is made up of layers of neurons with the outputs of one layer

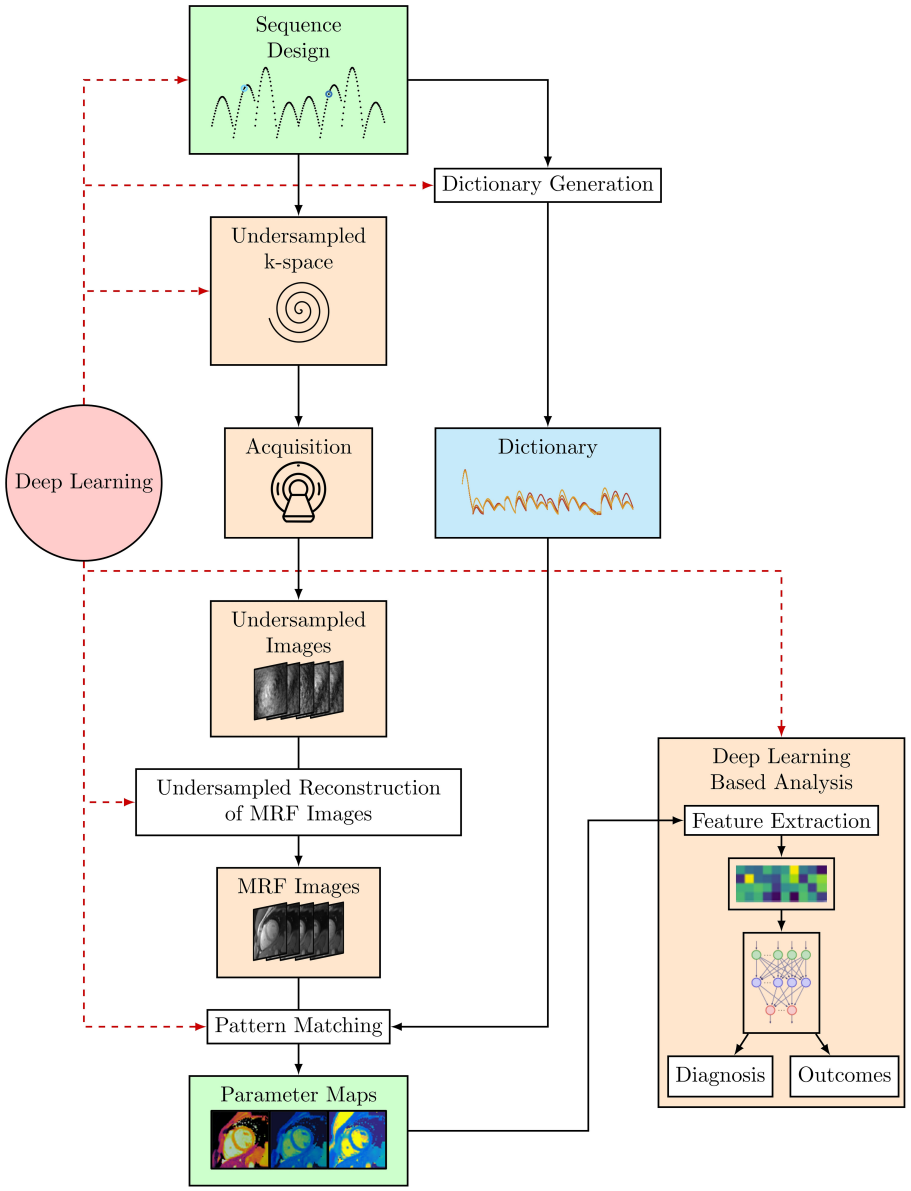

FIGURE 3
The cardiac MRF workflow from sequence design and optimization through to parameter map estimation and potential uses of cardiac MRF data, where DL-based analyses such as Radiomics can be used to provide a diagnosis or predict outcomes. Black arrows indicate the flow of steps taken in the cardiac MRF workflow. The red dashed arrows indicate steps where DL methods have or could be applied within this workflow.

forming the inputs for the next layer and the depth of the network is given by the number of layers contained within the model. Recently, rapid advances in DL have been made due to the combination of the availability of large high-quality training datasets and tweaks to the architecture of NNs capable of extracting features. Alongside this, advances in GPUs for parallel computation and open-source libraries to construct and train DL algorithms have aided its adoption. There are a broad range of concepts and types of models within the field of DL, and a full description of them is outside the scope of this review. Thus, here only a small selection of terms of interest relevant to DL applications in CMR and more specifically in cardiac MRF will be briefly introduced.

Deep learning in cardiac MR

In DL for medical imaging and in particular for CMR imaging, input data is typically information obtained from the scanner, such as signal evolutions, k-space data or reconstructed images. The type of NN model these data are input into

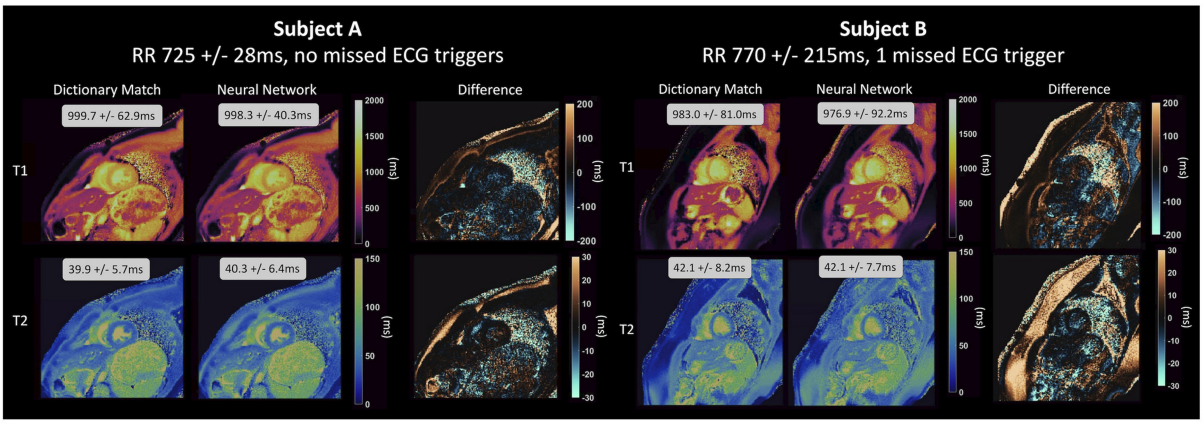

FIGURE 4
Parameter maps generated by a NN for cardiac MRF from Hamilton et al. (82) for two healthy subjects and compared to maps generated using dictionary matching. The feedforward network with skip connections that was used takes the real and imaginary components of the fingerprint and the RR intervals as input and outputs parameter estimates for T_1 and T_2 on a fingerprint-wise basis. The network produces accurate parameter estimations for different cardiac rhythms, even for subject B, with a variable heart rate and 1 missed ECG-trigger.

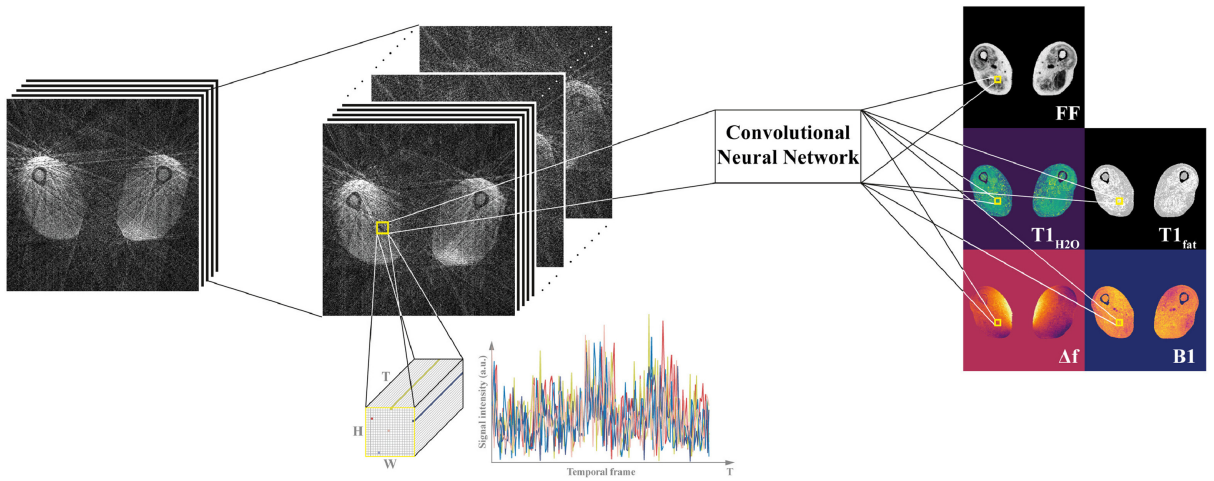

FIGURE 5
Spatially-regularized convolutional neural network from Balsiger et al. (90). In addition to the temporal information from each fingerprint, for each voxel a HxWxT patch of undersampled image data is used to calculate the parameter maps [in their work, Balsiger et al. (90) employ a patch size of H = W = 15]. The network achieves improved accuracy by incorporating spatial regularization in the map generation process from undersampled image data.

will affect the predicted outputs and the overall accuracy of the trained network. Hence, different types of network architecture are more suited to different types of data and problems. As an example, an image can be made up of patches of highly correlated data that form specific patterns or features such as edges, corners, ridges and blobs. A discrete convolution, a mathematical operation, can be used to filter these patches, hence a stack of convolutions can extract complex information and features from an image. Convolutional Neural Networks (CNNs) have been proven to be a powerful tool when working with imaging data and are widely applied in CMR. However, if the input is a set of temporal signal evolutions measured from a scan, a CNN may be less efficient than other types of networks better suited for long sequential datasets. Instead, recurrent neural networks (RNNs) such as long short-term memory (LSTM) networks can be used. These networks can track dependencies over a large number of time steps and remember previous inputs, making them more suitable for time-series predictions.

A good understanding of the type of input data and the nature of the problem is important to properly exploit AI for medical imaging. Accelerated (i.e., undersampled) CMR acquisitions lead to ill-posed inverse reconstruction problems. Many techniques, such as compressed sensing (44, 45) or low-rank-based reconstructions (26, 28), have been proposed to tackle these undersampled problems. However, the non-linear nature of the problems to be solved leads to long reconstruction times, in addition to the parameter tuning required for an optimal regularization. Several DL-based alternatives have been proposed to overcome these limitations and enable not only highly accelerated acquisitions in short reconstruction times (32, 33, 46–51), but also a wide range or AI-aided solutions for CMR segmentation (40) and analysis or outcome prediction (52, 53) among others.

Beyond quantitative CMR, many of the ideas in these studies have been successfully applied in MRF with the potential to be employed in cardiac MRF. Some of the most interesting ideas in AI along with their potential use in cardiac MRF are presented in the following sections.

Artificial intelligence in cardiac MRF

Conventional cardiac MRF is a powerful technique for quantitative parameter estimation. However, the computational burden of dictionary generation and pattern matching grows exponentially with the number of parameters considered. Dictionary generation and pattern matching is especially challenging for cardiac MRF as it must incorporate information about subject-specific heart rate variability throughout the scan. In addition, the short acquisition times required for a cardiac MRF sequence to be feasible within a breath-hold means high acceleration factors must be used, leading to very highly undersampled k-space that must be reconstructed. Furthermore, since cardiac MRF sequences are frequently designed heuristically, it may be possible to further optimize sequence design to both shorten scan times and provide better discrimination between the parameters of interest. ML offers the ability to solve these problems and it has been or has the potential to be applied to each of these problems, to both speed up acquisition and reconstruction and optimize MRF sequences (see Figure 3).

Dictionary generation

Dictionaries are conventionally generated using Bloch equation simulations or EPG calculations (16). The size of a dictionary and thus the time required to generate it scales with the sequence length (number of TRs) and the number of unique parameter combinations considered. Indeed, the size and thus time taken to simulate a dictionary grows exponentially with the number of tissue properties considered. For example, the dictionary for a 15 heartbeat T_1, T_2 cardiac MRF sequence contained 26,680 parameter combinations with 750 TRs and took 2.2 min to generate (54). However, the dictionary for a 16 heartbeat T_1, T_2, $T_{1\rho}$ cardiac MRF scan contained signal evolutions for 253,000 parameter combinations with 480 time points (20) and can take ∼15 min to generate using EPG simulations on a standard multicore CPU-based workstation.

As mentioned above, cardiac MRF differs from regular MRF as it uses ECG triggering to acquire signals during the same cardiac phase, across different heartbeats, to reduce artifacts from cardiac motion. This introduces a dependency of the measured signal evolutions on the subject-specific cardiac rhythm. Unlike MRF, where the pulse sequence is fixed and dictionaries can be generated ahead of time and used for all future scans, dictionaries for cardiac MRF must be calculated for each new scan using the measured RR intervals derived from ECG data recorded during the scan. This problem is further complicated when a more granular dictionary is required to reduce quantization errors, or as the number of modeled or encoded parameters is increased. This significant bottleneck presents a barrier to clinical adoption where long computation times for short scans hamper online parameter map generation in a fast-paced clinical workflow.

ML offers the promise of learning a surrogate model that can approximate the Bloch equations, turning dictionary generation into a straightforward pass through a NN. This provides the possibility of rapidly generating dictionaries in real-time, crucial for subject-specific cardiac MRF scans. Furthermore, rapid dictionary generation using ML makes it possible to quickly simulate dictionaries that consider larger numbers of parameters as well as aiding in applications such as sequence optimization where many different dictionaries must be generated. In the following sections we will explore in more detail studies where ML has been applied to the problem of dictionary generation in cardiac and non-cardiac MRF.

Fully connected feedforward neural network

A fully connected neural network has been proposed for generating dictionaries for a 16 heartbeat T_1 and T_2 cardiac MRF sequence (55). The network takes as input a 17-element vector consisting of T_1 and T_2 parameters plus 15 RR intervals. The input data, passes to two fully connected layers of 300 neurons, each followed by batch normalization and a ReLU activation function. The final output layer consists of 1,536 outputs corresponding to the real and imaginary components of the signal evolution of 768 TRs.

To model heart rate variability, the network was trained with dictionaries corresponding to 1,020 different cardiac rhythms. The mean of the RRs for each dictionary was varied from 40 to 120 beats per min (bpm) with a step size of 5 bpm. Noise was added to these RRs to simulate heart rate variability, with noise

of standard deviation ranging from 0% to 50% of the mean RRs for a given dictionary. In total 4,392 T_1 and T_2 combinations were simulated for each dictionary resulting in ∼4.5 million signal evolutions for training. In addition, missed ECG triggers were modeled with a 5% chance of each beat being a missed trigger, doubling the RR.

The network provided a significant time saving, generating a dictionary of 26,680 T_1 and T_2 combinations in just 0.8 s compared to 158 s using Bloch equations. Monte Carlo simulations were performed for a range of cardiac rhythms where for each rhythm, 500 dictionaries were generated using the network and the best-matching entry was found for a ground truth signal representative of healthy myocardium. The root mean square error (RMSE) for T_1 and T_2 for these simulations was found to be 2% or lower except for low heart rates with high variability. Further simulations, modeling up to 8 ECG missed trigger events showed the RMSE values to always be below 3%. The NN-generated dictionaries were also validated using phantoms and on *in vivo* cardiac mapping in healthy subjects. Maps constructed using the NN generated dictionaries appeared similar to those generated with dictionaries from Bloch equations, and there was 6.1 ms bias for T_1 and 0.2 ms bias for T_2.

Significantly, this network focused on cardiac MRF, considered a wide range of cardiac rhythms, mis-triggering events, and evaluated the generated dictionaries on phantom and *in vivo* data. However, the network only considered sequences encoding T_1 and T_2. Further improvements could extend this work to sequences encoding additional parameters. Furthermore, rather than training the network solely on simulated data, actual ECG data could be incorporated, thus exposing the network to cardiac rhythms and parameter combinations that may exist in real scans but may not be fully represented in simulated training data.

Generative adversarial networks

A different approach using generative adversarial networks (GANs) (56) has been applied to the problem of generating T_1 and T_2 dictionaries for MRF in the brain (57). This approach consists of a generative network that is given T_1 and T_2 tissue parameters, sequence parameters and pure random noise signals. It consists of 3 hidden layers of 128 neurons each followed by ReLU activation functions and an output layer with a hyperbolic tangent activation function with 1,000 output elements, mimicking a fingerprint. The discriminator network takes as input MR fingerprints, either generated by Bloch simulations or the generator network. It has a similar internal structure as the generative network, but it has an output layer with a sigmoid activation function, that represents a probability that the input fingerprint was simulated by Bloch equation simulations. The two networks are trained together, acting as two players in a min-max game, with the generator mimicking fingerprints to fool the discriminator and the discriminator improving such that it can distinguish between generated and ground truth fingerprints.

Fingerprints for a total of 5,970 T_1 and T_2 combinations were calculated using Bloch equations, each with 1,000 TRs. A 60:20:20 training, validation, test split was used to train and evaluate the model.

The GAN-MRF model introduced in Yang et al. (57) could generate a dictionary in 0.3 seconds with Python and Tensorflow, compared to several hours using Bloch simulations in MATLAB. Fingerprints synthesized by the GAN-MRF model were compared to those from Bloch equation simulations for white and gray matter and cerebrospinal fluid and provided a good match. A dictionary generated using the GAN-MRF model was used to reconstruct *in vivo* T_1 and T_2 maps and compared to benchmark maps reconstructed using a dictionary from Bloch equation simulations. The maps showed little difference, with RMSE of 0.55 and 2.66%, respectively for T_1 and T_2 maps, respectively. Additionally, the scalability of this method was tested by using coarser and finer dictionaries, compared to the grid of parameter combinations used in training, to reconstruct the *in vivo* maps. Again, good results were found with 1.69% and 6.39% RMSE, respectively for T_1 and T_2 maps for the coarse dictionary.

While the GAN-MRF model was only evaluated on brain MRF sequences, a similar model could be trained for cardiac MRF. However, GANs can be difficult to train due to the non-convex nature of the min-max problem and mode collapse, where the generator can learn a single pattern that seems the most plausible to the discriminator, thus fooling it. This is especially true when GANs are required to generate a wide variety of outputs, as is the case in MRF dictionary generation. Yang et al. (57) use regularization and a modified loss function to counter these affects. However, this requires a model-specific regularization parameter to be chosen. Also, convergence of the GAN during training will likely be more elusive for cardiac MRF due to increased variety in the fingerprints introduced by many additional degrees of freedom as a result of cardiac rhythm dependence.

Invertible neural networks

Invertible neural networks (INNs) (58) have also been employed to generate fingerprints from parameters in addition to predicting parameters from signal evolutions (59). Truly INNs such as NICE (60) and RealNVP (61) (the latter based upon real valued non-volume preserving transformations) are constructed of coupling layers, are invertible by design and have tractable Jacobian determinants and can thus easily be trained. Ardizzone et al. extended the RealNVP architecture to calculate posteriors for real-world inverse problems in natural sciences (58). Using this framework, an INN based upon a

RealNVP (61) architecture, with two reversible blocks and two permutation layers, was trained on a T_1 and fat fraction (T_1-FF) MRF sequence (62) for diseased skeletal muscle with 175 TRs. Within each invertible block, two fully connected layers were used with 128 neurons, each followed by a ReLU and linear activation function. Dictionaries encoding Fat fraction, $T_{1,H2O}$, $T_{1,fat}$ and B_1 were simulated with 396,000, 6,720 and 26,880 entries used, respectively for training, validation and testing. As well as providing good results for parameter matching when the INN is evaluated in the backwards direction (see Section Pattern matching), the estimated fingerprints were very accurate, with inner products between predicted and reference fingerprints > 0.997 for the majority of parameter combinations.

However, this INN was trained for a non-cardiac musculoskeletal sequence. Thus, it does not encode the additional degrees of freedom due to heart rate variability that is seen in cardiac sequences. Additionally, as with most inverse problems, while there is a direct mapping from physical parameters to signal evolutions, some information is lost in this forwards process. Thus, the backwards process (estimating tissue parameters from MRF signals) is often ambiguous, and a single fingerprint could correspond to a range of parameter combinations. Due to the cyclic nature of the INN and the fact no latent space was used to encode this information that is lost, large errors in this often-ambiguous backwards process can result in larger errors in the well-defined forwards process, hampering dictionary generation for some tissue combinations. Finally, dictionaries generated using this INN for non-cardiac MRF were not used to reconstruct *in vivo* data, nor was the parameter estimation part of the network evaluated on *in vivo* data.

Recurrent neural networks

RNNs, (see Figure 2) are capable of memorizing temporal structures within sequences and are therefore good candidates for dictionary generation in MRF. For instance, Liu et al. (63) propose a RNN as a surrogate model for dictionary generation for non-cardiac MRF. A novel feature of this network is that it is capable of modeling MRF signal evolutions resulting from different sequence parameters, in addition to encoding dependencies on tissue parameters. To achieve this, their RNN takes both tissue parameters and sequence parameters (such as repetition times, flip angles and sequence length) as inputs, and outputs MRF signal evolutions. Their RNN architecture consists of three stacked gated recurrent units (GRUs) and a linear layer, to generate the transversal magnetization and its derivates for every nth echo. This RNN can generate a dictionary three orders of magnitude faster than the snapMRF (25) GPU-accelerated EPG simulation package. As the RNN can rapidly generate both signal evolutions and derivative signals with respect to tissue parameters it is an ideal candidate for sequence optimization based upon Cramer-Rao lower bound (CRLB, see Section Sequence optimization). Liu et al. demonstrate that by using their RNN to optimize an MRF sequence, they improve the relative error in reconstructed *in vivo* brain T_2 maps from 12.75 to 3.63%. The key advantage of this RNN is that it can generalize to predict fingerprints and their derivatives for different sequence parameters, compared to most networks that are trained for a specific sequence. However, the RNN was ∼24 times slower generating dictionaries than the network proposed by Hamilton et al. (55). Extending the RNN to encode cardiac rhythm dependence for cardiac MRF would likely require significantly more training data, longer training times and a model with more layers and parameters.

Undersampled reconstruction of time-series MRF images

The next significant step in the MRF framework is the reconstruction of acquired undersampled data. In the case of cardiac MRF, there is a need to execute the sequence in a short time (so it can be run within a breath-hold) and within short acquisition windows (so there is minimal corruption by cardiac motion). This usually translates into elevated acceleration factors, which leads to very highly undersampled k-space data of the order of 10x-10^2x and produces severely aliased images at each timepoint. This can be alleviated by exploiting redundancy in the acquired data, as in Cruz et al. (64, 65), where a regularized low-rank high-dimensional patch-based tensor is used to improve the reconstructed image quality noticeably despite high undersampling factors, although this adds computational expense.

Cardiac MRF could benefit from recent advances in Deep MR quantitative imaging where end-to-end DL-based approaches (66–71), reconstructing images and maps from k-space data, have been explored. Although the literature on this topic is vast, there are reviews that summarize much of this work (41, 72). Some of the most relevant studies are mentioned here.

For instance, Jeelani et al. (73) propose a CNN, where spatial and temporal information is exploited for fast end-to-end myocardial T1 mapping, using MOLLI weighted images as the network's input. Cheng et al. (74) propose an unsupervised end-to-end network for $T_{1?}$ mapping of knee cartilage. The network has a compressed sensing loss function and an unrolled approach with two chained networks, one to generate reconstructed contrast-weighted images and another for map generation. Their approach generates both maps and contrast-weighted images from undersampled k-space data and incorporates data consistency, the sparse prior of the image and prior information provided by the signal model. By using a compressed sensing loss function and training in an unsupervised manner, their network eliminates the need for fully sampled training data needed for supervised approaches, as is

the case for MANTIS (67). A similar approach could be used for cardiac MRF by replacing the map generation network with one that incorporates cardiac rhythm dependencies.

The reconstruction process within cardiac MRF could also benefit from the advances in dynamic MR reconstruction. For instance, Qin et al. (75) propose a 3D Convolutional recurrent neural network (CRNN) able to faithfully produce CINE image reconstructions from 9x undersampled data, by learning from information propagated along time dimension and also through iterations.

A large number of scans are usually required for optimal training of a NN, especially in multiparametric CMR reconstruction with its dependency on subject-specific cardiac rhythms during acquisition. Ulyanov et al. (76) propose Deep Image Priors, a possible solution to this drawback. In their work, they show that the structure of deep convolutional generator networks can sufficiently capture enough image statistics prior to any learning. Hence, inverse problems such as MR reconstruction can be solved by randomly initializing a NN's parameters and searching for the optimal parameters to accurately reconstruct an image from a single degraded input image on an image-by-image basis. As a result, this eliminates the requirement for a large number of scans for training data. This method has already been successfully applied to dynamic MR reconstruction (77) and T_2 mapping from undersampled data (78). Recently, low-rank subspace modeling has been combined with a deep image prior for a cardiac MRF sequence in a self-supervised framework (79). This results in improved quality of reconstructed maps, reduced noise and aliasing artifacts, enabling the sequence to be modified to both improve scan efficiency and reduce motion artifacts.

Pattern matching

Conventionally, pattern matching or template matching for MRF involves an exhaustive search of the dictionary receiving as input the reconstructed time-series MRF images. For a given voxel, the dot product between the measured signal and each of the dictionary entries is calculated. In this way, a measured fingerprint is matched to the most similar signal evolution in the dictionary, and the voxel is assigned the parameter combination corresponding to that entry. While this method can find the globally optimal match from all simulated fingerprints, in the case of cardiac MRF it first requires a subject-specific dictionary to be generated which can require large amounts of storage. Also, both the dictionary generation and dot product matching become prohibitively computationally expensive as the size of the dictionary grows with the number of parameters encoded in the sequence or as the sampling along each dictionary dimension becomes more granular. Dot product matching can also result in quantization errors as parameter estimation is limited by the discrete step sizes used in simulating the dictionary.

Improvements to conventional pattern matching have been proposed. One approach, tested for dictionary sizes of 10^4 to 10^5, snapMRF (25), parallelizes dictionary generation and pattern matching on the GPU and results in 10–100 times speed-up for pattern matching compared to other open-source packages. Singular value decomposition (SVD), where the dictionary and observed signals are compressed in the time domain and matching is then performed in the compressed space, without sacrificing signal-to-noise ratio (SNR), has been proposed. Accelerated dictionary search methods, including fast group matching (80) and the Fast Library for Approximate Nearest Neighbors (FLANN) (81), first group similar dictionary entries and compare measured signals to representative signals for these groups, which are successively pruned. In this way only a portion of the total dictionary entries are searched over, and fast dictionary matching proves to be almost two orders of magnitude faster than an exhaustive search of the dictionary. Similarly MRF-ZOOM (23), iteratively refines its parameter estimation by searching over a more coarse version of the dictionary.

However, in the case of cardiac MRF, these methods still require a subject-specific dictionary to be generated, which itself is a significant computational bottleneck. Further to this, SVD requires the dictionary to be compressed and accelerated dictionary matching techniques require some grouping of dictionary entries, both of which must be repeated with each new scan and thus dictionary for cardiac MRF. Finally, all these methods depend on a dictionary and as a result they are limited by the discrete sampling used when generating the dictionary.

DL-based methods additionally offer the promise of completely bypassing the dictionary generation step, and to generate MRF parametric maps in real time with continuous variables. A NN can be trained as a surrogate model to learn the mapping from measured signals to tissue properties. These methods can transform the pattern matching step from an optimization-based problem, the complexity of which grows exponentially with the number of parameters modeled, to a much faster forward pass through a network. DL methods either work on a fingerprint-wise basis, reconstructing individual fingerprints, or on a spatially regularized basis, reconstructing a small patch of data and leveraging information from neighboring fingerprints that is likely correlated. They are typically trained on noiseless data from dictionaries or acquired *in vivo* data where it is also possible for NNs to reduce the amount of noise and aliasing in reconstructed maps compared to conventional dictionary matching. In the following sections we will discuss some of these different approaches for cardiac MRF and non-cardiac MRF.

Fully connected networks

Fully connected neural networks (FCNN) have been proposed to perform pattern matching on a voxel-wise basis

for cardiac MRF (82), as well as brain, liver and prostate MRF (83, 84) for T_1 and T_2 mapping. The network architectures for all these approaches have an input layer consisting of either the magnitude fingerprints or concatenating the real and imaginary components of the fingerprint. These are followed by a series of hidden layers, each with activation layers and a final output layer with sigmoid activations for the regression outputs, corresponding to the parameter values. The DRONE (83) network for brain MRF and the network for brain, liver and prostate (84) (hereafter referred to FCNN2) have just 2 and 3 hidden layers, respectively (300 and 256 neurons each layer, respectively). However, the FCNN for cardiac MRF (82) must also take as input 10 RR intervals, to model the dependency of the measured sequence on the subject's cardiac rhythm during the acquisition. As a result, the network is much deeper consisting of 18 hidden layers (300 neurons each) with skip connections every 4 layers, beginning after the first hidden layer, to prevent vanishing gradients during training.

The DRONE network was trained with 69,000 EPG-generated signals with Gaussian noise added to the simulated signals to promote robust learning. It was evaluated on *in vivo* data reconstructed using a sliding-window approach (85), which removes most of the artifacts due to the spiral undersampling used. Other studies focus on directly training on signals that include artifacts due to the non-Cartesian undersampling artifacts from spiral trajectories used in cardiac MRF. In an attempt to make more realistic training data in a scalable manner, without acquiring *in vivo* data, the cardiac MRF FCNN (82) used pseudo-noise from a pre-computed library generated before training. The pseudo-noise library was generated by simulating the data acquisition of random maps using a spiral k-space trajectory and subtracting fully sampled reference images from the undersampled images. The noise patterns were then randomly scaled, phase shifted and added to the simulated signals with no noise which were also randomly phase shifted, resulting in simulated signals with pseudo-noise. In total, 8 million signal evolutions were simulated across 4,000 different cardiac rhythms, and these were combined with 1.8 million pseudo-noise samples. A similar approach for generating pseudo-noise for artifact patterns was used to generate training data for the FCNN2 (84), making it possible for both of these networks to take MRF images with undersampling artifacts as input.

The DRONE network achieved relative errors of $< 3\%$ when evaluated on simulated data with no noise but this increased significantly in Monte Carlo experiments where the SNR was varied, climbing to ∼15% and ∼48%, respectively for T_1 and T_2 at the lowest SNR. For the models trained on undersampled data, FCNN2 performed much better when trained using pseudo-noise and achieved $R^2 \geq 0.98$ in phantom experiments and good results on *in vivo* data >200 times faster than conventional dictionary matching. Equally, as is shown in Figure 4, the cardiac MRF FCNN achieved good results, with $R^2 = 0.93$ for T_1 and $R^2 = 0.95$ for T_2 and could quantify gridded sections of images in < 400 ms compared to 10 s with conventional methods and without the need of a subject-specific dictionary that typically takes 4 min to generate.

Convolutional neural networks

As mentioned before, CNNs are commonly used in image and pattern recognition and work by performing convolutions using filters learnt during training. Therefore, they are excellent candidates for MRF pattern recognition, where fingerprints have repeating patterns and shapes encoding tissue parameters, and fingerprints are spatially correlated due to tissue structure and undersampling patterns in k-space.

One-dimensional CNNs have been proposed for brain MRF (86, 87). A 1D residual CNN (87) was proposed consisting of two 1D convolutional layers followed by 4 residual blocks, with 1D CNN architecture and short-cuts, followed by a max-pooling layer and two fully connected layers to give the parameter outputs. The advantage of this network is that the CNN architecture can learn patterns in the input signals, while residual blocks allow the model to avoid vanishing gradient problems as the model becomes sufficiently deep to effectively learn the mapping from measured signals to parameters. The network is trained using dictionary generated sequences and a low-rank prior is exploited for signature restoration of *in vivo* data before it is input into the network. The network outperforms dictionary matching on synthetic maps without undersampling as well as maps with 15% undersampling, where it provides comparable results to a conventional low-rank method (88). Importantly, the network produces T_1 and T_2 maps in 1.6 seconds, 56 times faster than dot product dictionary matching.

A further refinement of this method, HYbrid Deep magnetic ResonAnce fingerprinting (HYDRA) (86) inspired by self-attention and non-local NNs, modifies the architecture of the previous network to include non-local operations. The non-local operations capture long-range dependencies of the signal in the temporal dimension, thus extracting global features which would not be captured by convolutions alone that process one local neighborhood at a time. Importantly, parameter estimation for HYDRA is continuous and errors for predicted T_1 and T_2 are as small as ∼0.2 ms, compared to errors of up to 4.5 ms due to discrete sampling every 10 ms in the case of dictionary matching. Song et al. demonstrate for noise-free synthetic data that HYDRA outperforms dictionary matching and continuous methods including the DRONE FCNN (83) and a standard 1D CNN, with HYDRA having the smallest deviations and bias. When applied to *in vivo* data where signature restoration using a low-rank prior is performed, HYDRA outperforms dictionary matching and other DL based methods for fully sampled, 15% undersampled and especially for 9% undersampled data with variable density spiral trajectories. For undersampled data,

HYDRA is also 4.8 times faster than a competing low-rank method for parameter map generation (88).

Spatially regularized or spatiotemporal CNNs have also been proposed for MRF (89, 90). These networks are motivated by noisy reconstructions arising from fingerprint-wise reconstructions, the fact that neighboring tissue properties are likely correlated and that undersampling in k-space leads to the signal from one pixel being distributed to several other pixels. To determine parameter values at each voxel, these networks take MRF image patches as input, a square grid of fingerprints centered on the voxel. Initially, a spatiotemporal CNN using 5x5xT image patches (5x5 image patches in image dimension and length T corresponding to the size of the fingerprints in the temporal dimension) was explored for T_1 and T_2 brain MRF (89). The approach in training and evaluation of this network differed from most studies, in this case ground truth maps derived from separate T_1 and T_2 scans were used instead of deriving these maps from dictionary matching using the MRF scans. A sliding-window reconstruction (85) was used to partially reconstruct the data and to obtain MRF images for input into the network. Applying this method demonstrated that the spatiotemporal CNN outperformed the DRONE (FCNN) (83), a 1D CNN and spatiotemporal dictionary matching (91), achieving the lowest RMSE and producing less noisy maps than the fingerprint-wise networks.

This spatially-regularized network was extended by Balsiger et al. (90), this time with a HxWxT image patch (see Figure 5) using a database of 164 MRF scans for a T_1-FF sequence (62) that gives 5 parametric maps. A non-uniform fast Fourier transform (NUFFT) (92) was used to transform the data to image space which led to some undersampling artifacts in the input data to the network. This CNN achieved the best reconstruction compared to dictionary matching, a fingerprint-wise RNN (93) and a spatially regularized network (94) without introducing artifacts. Additionally, this method generalized to anatomical regions not previously seen during training.

A network combining residual channel attention blocks (RCABs) and a U-Net (RCA-U-Net) has been also investigated for brain MRF (95). The network improves upon U-Net architectures by including RCABs at each layer of the U-Net. These include channel attention blocks to focus on the most informative features for parameter quantification, and residual skip connections to allow more efficient flows of information within the network. The U-Net itself includes 3 down-sampling and 3 up-sampling layers to extract spatial information at different scales. The network is trained on undersampled *in vivo* brain scans. Training data input into the network are first head-masked and then passed through a compression network for feature extraction and dimensionality reduction. The performance of the RCA-U-Net was compared to conventional dictionary matching, SVD matching (22), a 1D-CNN (96) and spatially-constrained quantification network (94). For the high acceleration rates used (8x and 16x), the RCA-U-Net achieves improved accuracy compared to all the other state-of-the-art methods with relative errors of <2%. In particular, the RCA-U-Net provides accurate T_2 estimation (1.4% error) for standard scans with an acceleration factor of 16 when compared to conventional dictionary matching (6.2% relative error).

Recurrent neural networks

RNNs, with their ability to memorize temporal structures, have also been employed for pattern matching for brain T_1 and T_2 MRF sequences (93, 97) where signal evolutions evolve continuously, there is redundant information and patterns are repeated. Both Oksuz et al. and Hoppe et al. use Long Short-Term Memory (LSTM) RNNs followed by fully connected layers which lead to outputs for the parameter values on a voxel-wise basis. Oksuz et al. also use GRUs equivalent to RNNs. The RNNs provided good results, with the LSTM from Hoppe et al. (97) outperforming a comparable CNN (96) method on *in vivo* data and the networks in Oksuz et al. providing lower mean absolute errors than the DRONE FCNN (83), a 1D CNN and conventional inner product matching on EPG generated signals.

Invertible neural networks

INNs have been proposed for a wide range of inverse problems in natural science (58). Inverse problems, such as cardiac MRF parametric mapping generation, typically involve determining physical parameters (x) from a set of measurements (y). While the forward process from parameters to measurements (Bloch equation simulations) is well understood, the backward process, or inverse problem, from measurements to parameters (parametric mapping generation) is often ambiguous. Ideally, cardiac MRF sequence design would make the inverse problem as unambiguous as possible, but this becomes more challenging due to artifact noise from undersampling and as the number of encoded parameters increases. INNs are unique in that they jointly optimize the well-defined forward problem and the ambiguous inverse problem using the same network and weights. During training, a latent space (z) is introduced that encodes information lost in the forwards process, which then aids the network in the inverse process, where the latent space is sampled over ($[[y, z] \rightarrow x]$), allowing it to disentangle ambiguous cases. It has been demonstrated by Ardizzone et al. (58) that for INNs, learning the forwards process and latent space dramatically improves the accuracy of parameter estimation, compared to learning the backward process alone.

Balsiger et al. (59) implemented an INN to perform both dictionary generation and pattern matching on a voxel-wise basis for musculoskeletal MRF sequences. In their implementation training data simulated using the Bloch

equations was augmented with Gaussian noise and no latent space was used in the network. The INN consisted of two reversible blocks, each followed by permutation layers, with each reversible block using fully connected layers with 128 neurons each. Their INN accurately generated fingerprints (inner product > 0.995) and significantly outperformed non-invertible networks (83, 86, 93, 97) for the pattern matching step, achieving mean relative errors for parameter estimation ranging from 2 to 8%. Inferring parameter values for 1,000 fingerprints took just 50 ms with the INN, comparable to other ML based methods.

INNs offer multiple avenues for improvement which could aid in using them for parametric mapping generation for cardiac MRF. Conditional INNs could be used for cardiac MRF where both the forward and backward processes in the INN could be conditioned on subject-specific RRs. Additionally, the invertible blocks within INNs can consist of any network architecture and can therefore be adapted to use convolutional networks to operate on image patches rather than on individual voxels. Finally, by sampling the latent space, INNs can provide marginal posterior distributions $p(x|y, z)$ for each parameter of interest. This could give insight into the uncertainty of parameter estimation for cardiac MRF, the correlation between marginal posterior distributions across parameters and innately measure whether the signal from certain regions is multi-modal, due to combinations of different tissues.

Complex-valued neural networks

Typically, the real and imaginary components of complex-valued MRF signals are concatenated or input as 2-channels into real-valued NNs. However, this approach neglects the phase information and may lead to poorer reconstructions had the phase been considered. To rectify this problem, Virtue et al. (98) proposed a complex-valued NN for parameter estimation in MRF that includes a complex cardioid activation function sensitive to the input phase rather than the input magnitude. Using a numerical brain phantom, they show that complex-valued NNs outperform 2-channel real valued networks in the majority of their experiments, suggesting the inclusion of phase information aids in the reconstruction. Complex-valued NNs have not been trialed for cardiac MRF and the adaptation of previous methods to include complex-values could lead to better pattern matching algorithms for cardiac MRF where data is highly undersampled.

While each of the networks architectures shown here have promising features that could be employed in cardiac MRF pattern matching, most of these networks, with the exception of the work from Hamilton et al. (82), are for non-cardiac MRF sequences. Further work is needed to extend these networks to cardiac MRF where the additional dependence of measured fingerprints on the subject's cardiac rhythm during the scan must be considered. Additionally, many studies did not evaluate their networks on *in-vivo* data but instead on simulated signals (59, 93, 98), while some networks depended upon partially reconstructed data for their inputs (83, 86, 87, 89), others took data corrupted by undersampling artifacts (82, 84, 90, 95). Furthermore, most networks focused on fingerprint-wise reconstruction (59, 82–84, 86, 87, 93, 97, 98), only a few of the studies took advantage of the fact signals from neighboring tissues are correlated due to undersampling by using spatial-temporal networks (89, 90, 95). These points, combined with the fact that each study considered a different sequence, makes it hard to compare the performance of the different networks. Ideally a standardized MRF-specific dataset could be used for comparison across models.

Sequence optimization

AI has already been used in different stages of sequence optimization in MRI, such as automatic generation of sequences (99, 100), or in the search of more efficient sampling patterns (101–104). In the field of MRF, due to the inherent flexibility of its sequence design, there are essentially infinite combinations of parameters such as flip angle trains, TR, TE, number of RF shots, position and duration of magnetization preparation pulses, and strength and waveform of gradients. As a result, most of the cardiac MRF sequences proposed so far have been designed heuristically.

An MRF sequence can be optimized in search of different goals, such as better encoding power, higher accuracy, or shorter scan times (i.e., higher efficiency). To quantify the performance of a certain sequence on these areas, different specific cost functions may be employed. The goal of a sequence optimization strategy would then be the minimization of the chosen cost function.

Given that parametric mapping in MRF is widely achieved by pattern matching between the undersampled fingerprint and the predicted dictionary, most optimization strategies have focused on the minimization of the inner product between these two signals (i.e., maximization of the encoding capability of the sequence). Cohen et al. (105) explore four different optimization algorithms to optimize the pattern of short TR and FA trains in a constrained range. Sommer et al. (106) also investigate the encoding capability of MRF sequences by inner product minimization and a Monte Carlo simulation that tries to consider the aliasing noise present in pattern matching by adding Gaussian noise to the fingerprints. Noise and aliasing artifacts were also taken into consideration in the optimization approach proposed by Kara et al. (107).

MRF sequence performance can be analyzed in terms of a cost function based on CRLB. This statistical tool looks for the lower bound of the variance of unbiased estimators and has been already utilized by MRF community to optimize FA and TR patterns for optimal sequence design (108–111). Apart

from statistical-based optimizers, physics knowledge could be also included in the model, as in Jordan et al. (112).

All these algorithms work on the premise of a cost function or optimizer that is iteratively minimized. However, this is a computationally expensive task, and AI offers the ability of speeding up this process. The RNN proposed by Liu et at. (63) for dictionary generation is also employed to develop a computationally efficient method to solve the CRLB optimization. In their work, they optimize a flip angle train of an MRF sequence given two target tissues by computing the 14,000 necessary magnetization signals and their derivatives with their proposed RNN in ∼10s, a reduction of two orders of magnitude in runtime. NNs and supervised learning have also been proposed for use in the joint sequence optimization and image reconstruction frame for MRI [Loktyushin et al. (113)]. However, most of these works have been proposed on phantom and *in vivo* brain MRF studies. Although efforts have been made to optimize a 2D cardiac MRF acquisition pattern (21) from a large number of simulated sequences, AI is yet to be fully exploited for sequence optimization in cardiac MRF. Particular problems within cardiac MRF sequence optimization, like RR interval dependance or short acquisition windows, are potential issues to be addressed with NN-based sequence optimization algorithms and further investigation is required for this purpose.

Discussion

Current limitations

The possibilities and promising results shown in recent years demonstrate that current advances in AI could become part of the cardiac MRF workflow in the near future and help its potential clinical adoption. However, there are still several remaining challenges and limitations that need to be addressed and understood before widespread implementation.

Data availability

The main obstacle that DL-derived techniques face in medical imaging in general is data availability. The accuracy of DL alg orithms heavily relies on the amount of data used to train and validate these algorithms. Whereas, very large databases (in some cases, containing millions of samples) can be generated in other fields in AI, the amount of trainable data available in CMR is several orders of magnitude smaller. Huge efforts are underway to generate large databases of CMR datasets, for example UK biobank or other open-source datasets (114). However, libraries of multiparametric co-registered scans (including k-space data) such as those that could be obtained with MRF are yet to be constructed, especially since multiparametric quantitative MR is not routinely carried out in a clinical environment and k-space data is not conventionally stored. Still, for AI applications to be of help in the clinical routine, training databases should include not only healthy subject data, but also incorporate multiparametric maps corresponding to different pathologies. Currently, most cardiac MRF studies in the literature are evaluated against healthy subjects or a reduced cohort of patients, although Hamilton et al. (115) recently presented results clinically evaluating a specific T_1 and T_2 cardiac MRF sequence. Nonetheless, this study was carried out on a relatively small number of subjects ($n = 68$) within a reduced age range. Cardiac MRF is further complicated by its dependence on subject-specific cardiac rhythms during the scan. This introduces an additional requirement for training data to either sample a wide range of heart rates and variabilities or the use of methods that rely on additional simulated data across this parameter space. Crucially, further studies are needed to generate larger clinical datasets.

The training dataset must not only be generalizable against different diagnoses but must also be unbiased. Recent studies have shown that the existence of imbalanced data may lead to inaccuracies and underperformance over different population groups, such as gender or race (116). Future studies such as that of Puyol-Anton et al. (117) should be conducted to further investigate the impact of biases and potential strategies to address this so-called "fairness", or lack thereof, in DL.

In addition to data availability and the issue of balanced multicenter multiparametric training data, anonymization and data protection are required conditions for the use of medical data in research. These necessary privacy requirements hinder sharing of locally generated data between different medical institutions, leading to data silos. Model-sharing alternatives like the distributed DL techniques proposed by Chang et al. (118) and federated learning (118, 119), where algorithms are trained without exchanging training data from different centers, need to be explored further.

Reconstruction quality and fidelity

Given the lack of data availability, it is currently inevitable that many DL-MRF reconstruction approaches are based on simulated datasets. Nevertheless, for some applications, such as DL for dictionary generation (where data can be generated by EPG calculations or Bloch equations) this may be adequate. In such cases, close attention needs to be paid to the accuracy of the generated data, and its similarity to real data. The simulated data should ideally include all sort of possible imperfections that could be present in a real MRF acquisition. This implies approximations such as perfect slice profile, field homogeneity or hard RF excitation pulse should be disregarded, and instead all the possible corrections should be included, even at the cost of longer simulation times. Moreover, cardiac MRF-specific features such as cardiac and respiratory motion, mis-triggering, and an essentially infinite number of heart rate possibilities must be taken into account in the simulations. In any case, as in any other AI-based solution proposed for CMR, the algorithms need

to be generalizable in different clinical settings such as vendors or field strengths, and for this to happen wide multi-vendor involvement is required.

Interpretability

Although novel DL algorithms have been shown to outperform non-AI-based techniques, and results may be more accurate in terms of quantitative metrics, it is often difficult to understand how these predictions have been made and where they come from. There are efforts to improve interpretability, such as *explainable AI* (120), which tries to generate solutions that can be more easily understood by the end user. However, this so-called black-box problem (121) still needs to be addressed so that the community can better comprehend what factors contribute to the decision-making of a ML model in order to better interpret its outputs.

Future perspective

In addition to the MRF-specific solutions that the presented NNs offer, the advances in other more "traditional" directions need to also be integrated in the cardiac MRF framework. In this way, DL-based approaches for motion correction or fast CMR acquisition and reconstruction, along with the inherent versatility of cardiac MRF, would enable the extension of cardiac MRF in the spatial (from 2D to 3D), temporal (from ECG-triggered to motion-corrected free-running) and contrast (other parametric maps apart from T_1 and T_2) dimensions.

In addition to the usual symbiosis between cardiac MRF and ML, where ML is used as a tool to address problems faced in cardiac MRF, such as sequence optimization and reconstruction, this synergy can also be flipped and cardiac MRF could be used as a tool in a ML-based field. There has been growing interest in the use of multiparametric MRI to generate ML-based risk prediction or stratification. Radiomics is an example in this field (122), an approach where a set of medical images are used as input to extract quantitative information by means of a set of well-defined mathematical operations that are performed to extract information of the distribution and neighborhood relations of each pixel in the image of interest. These relations, or features, can be used to feed an ML algorithm and provide a quantitative analysis. Radiomics is a well stablished technique in some medical imaging fields like oncology, and it has started showing its potential for MRI and particularly CMR application in the recent years (123), however reproducibility is still limited.

Conventionally, the input datasets used for CMR radiomics are Late-Gadolinium Enhanced (LGE), CINE or contrast-weighted semi-quantitative images (124–128). However, in recent years quantitative information given by parametric maps such as T_1 and T_2 have been employed, showing a great potential (129–133). In most of these studies, only one type of relaxation parameter is used for radiomics analysis. Nevertheless, as in conventional quantitative CMR, stacking multiparametric information could increase the diagnostic power of radiomics, as shown by Baessler et al. (129, 130). However, an accurate and robust multiparametric radiomics analysis can only be performed when the different parametric maps are perfectly aligned. This is where the multiparametric information provided by cardiac MRF could become a more robust input for radiomics applications, due to its inherent spatial and temporal co-registration. Consequently, cardiac MRF presents the potential to generate a multidimensional dataset that may serve as an input to improve diagnostic capacity of radiomics or other DL approaches for diagnosis in CMR.

Conclusion

Cardiac magnetic resonance fingerprinting is increasingly proven in its potential as a valuable tool for multiparametric quantification on CMR. Its scalable ability to generate several parametric maps within the same acquisition usually comes, however, at the cost of sequence complexity and increased reconstruction and dictionary generation times. This is further aggravated by the CMR-specific problems, such as unpredictable heart rate and cardiac motion. Nevertheless, recent advances in AI applied to medical imaging have shown that, with the correct understanding of the type of network required for the specific problem and a sufficient amount of training data, NNs are capable of solving many of these problems, much more rapidly and to comparable accuracy as conventional methods. Thus, the field of AI, which has experienced a rapid growth in recent years, is expected to become part of cardiac MRF at every step of its framework (sequence optimization, dictionary generation, image reconstruction, parametric estimation and analysis) and greatly contribute to the potential inclusion of cardiac MRF in the clinical routine. Nonetheless, special care needs to be taken to overcome the limitations that may hinder this goal; aspects such as algorithm interpretability and most importantly data availability need to be enforced to ensure AI is used at its full capacity in cardiac magnetic resonance fingerprinting.

Author contributions

CV and TF devised and wrote the manuscript. RB and CP reviewed the manuscript. All authors contributed to the article and approved the submitted version.

Funding

The authors acknowledge financial support from the BHF PG/18/59/33955 and RG/20/1/34802, EPSRC EP/V044087/1, EP/P001009, EP/P032311/1, EP/P007619, Wellcome EPSRC Center for Medical Engineering (NS/A000049/1), Millennium Institute for Intelligent Healthcare Engineering ICN2021_004, FONDECYT 1210637 and 1210638, ANID - Basal FB210024, Millenium Nucleus NCN19_161, and the Department of health *via* the National Institute for Health Research (NIHR) comprehensive Biomedical Research Center award to Guy's and St. Thomas' NHS Foundation Trust.

Conflict of interest

The authors declare that the research was conducted in the absence of any commercial or financial relationships that could be construed as a potential conflict of interest.

Publisher's note

All claims expressed in this article are solely those of the authors and do not necessarily represent those of their affiliated organizations, or those of the publisher, the editors and the reviewers. Any product that may be evaluated in this article, or claim that may be made by its manufacturer, is not guaranteed or endorsed by the publisher.

Author disclaimer

The views expressed are those of the authors and not necessarily those of the NHS, the NIHR, or the Department of Health.

References

1. Messroghli DR, Moon JC, Ferreira VM, Grosse-Wortmann L, He T, Kellman P, et al. Clinical recommendations for cardiovascular magnetic resonance mapping of T1, T2, T2* and extracellular volume: a consensus statement by the Society for Cardiovascular Magnetic Resonance (SCMR) endorsed by the European Association for Cardiovascular Imaging (EACVI). *J Cardiovasc Magn Reson.* (2017) 19:75. doi: 10.1186/s12968-017-0389-8

2. Haaf P, Garg P, Messroghli DR, Broadbent DA, Greenwood JP, Plein S. Cardiac T1 Mapping and Extracellular Volume (ECV) in clinical practice: a comprehensive review. *J Cardiovasc Magn Reson.* (2016) 18:89. doi: 10.1186/s12968-016-0308-4

3. Tahir E, Sinn M, Bohnen S, Avanesov M, Saring D, Stehning C, et al. Acute vs. chronic myocardial infarction: diagnostic accuracy of quantitative native T1 and T2 mapping vs. assessment of edema on standard T2-weighted cardiovascular MR images for differentiation. *Radiology.* (2017) 285:83–91. doi: 10.1148/radiol.2017162338

4. Giri S, Chung YC, Merchant A, Mihai G, Rajagopalan S, Raman SV, et al. T2 quantification for improved detection of myocardial edema. *J Cardiovasc Magn Reson.* (2009) 11:56. doi: 10.1186/1532-429X-11-56

5. van Oorschot JW, El Aidi H. Jansen of Lorkeers SJ, Gho JM, Froeling M, Visser F, et al. Endogenous assessment of chronic myocardial infarction with T(1rho)-mapping in patients. *J Cardiovasc Magn Reson.* (2014) 16:104. doi: 10.1186/s12968-014-0104-y

6. Christodoulou AG, Shaw JL, Nguyen C, Yang Q, Xie Y, Wang N, et al. Magnetic resonance multitasking for motion-resolved quantitative cardiovascular imaging. *Nat Biomed Eng.* (2018) 2:215–26. doi: 10.1038/s41551-018-0217-y

7. Mao X, Lee HL, Hu Z, Cao T, Han F, Ma S, et al. Simultaneous multi-slice cardiac mr multitasking for motion-resolved, non-ECG, free-breathing T1-T2 mapping. *Front Cardiovasc Med.* (2022) 9:833257. doi: 10.3389/fcvm.2022.833257

8. Milotta G, Bustin A, Jaubert O, Neji R, Prieto C, Botnar RM. 3D whole-heart isotropic-resolution motion-compensated joint T1 /T2 mapping and water/fat imaging. *Magn Reson Med.* (2020) 84:3009–26. doi: 10.1002/mrm.28330

9. Santini F, Kawel-Boehm N, Greiser A, Bremerich J, Bieri O. Simultaneous T1 and T2 quantification of the myocardium using cardiac balanced-SSFP inversion recovery with interleaved sampling acquisition (CABIRIA). *Magn Reson Med.* (2015) 74:365–71. doi: 10.1002/mrm.25402

10. Qi H, Bustin A, Cruz G, Jaubert O, Chen H, Botnar RM, et al. Free-running simultaneous myocardial T1/T2 mapping and cine imaging with 3D whole-heart coverage and isotropic spatial resolution. *Magn Reson Imaging.* (2019) 63:159–69. doi: 10.1016/j.mri.2019.08.008

11. Guo R, Chen Z, Herzka DA, Luo J, Ding H. A three-dimensional free-breathing sequence for simultaneous myocardial T1 and T2 mapping. *Magn Reson Med.* (2019) 81:1031–43. doi: 10.1002/mrm.27466

12. Ma D, Gulani V, Seiberlich N, Liu K, Sunshine JL, Duerk JL, et al. Magnetic resonance fingerprinting. *Nature.* (2013) 495:187–92. doi: 10.1038/nature11971

13. Buonincontri G, Sawiak SJ, MR. fingerprinting with simultaneous B1 estimation. *Magn Reson Med.* (2016) 76:1127–35. doi: 10.1002/mrm.26009

14. Ma D, Coppo S, Chen Y, McGivney DF, Jiang Y, Pahwa S, et al. Slice profile and B1 corrections in 2D magnetic resonance fingerprinting. *Magn Reson Med.* (2017) 78:1781–9. doi: 10.1002/mrm.26580

15. Bloch F. Nuclear induction. *Physical Review.* (1946) 70:460–74. doi: 10.1103/PhysRev.70.460

16. Weigel M. Extended phase graphs: dephasing, RF pulses, and echoes - pure and simple. *J Magn Reson Imaging.* (2015) 41:266–95. doi: 10.1002/jmri.24619

17. Hamilton JI, Jiang Y, Chen Y, Ma D, Lo WC, Griswold M, et al. MR fingerprinting for rapid quantification of myocardial T1, T2, and proton spin density. *Magn Reson Med.* (2017) 77:1446–58. doi: 10.1002/mrm.26216

18. Jaubert O, Cruz G, Bustin A, Schneider T, Lavin B, Koken P, et al. Water–fat Dixon cardiac magnetic resonance fingerprinting. *Magn Reson Med.* (2020) 83:2107–23. doi: 10.1002/mrm.28070

19. Jaubert O, Cruz G, Bustin A, Hajhosseiny R, Nazir S, Schneider T, et al. T1, T2, and fat fraction cardiac MR fingerprinting: preliminary clinical evaluation. *J Magn Reson Imaging.* (2021) 53:1253–65. doi: 10.1002/jmri.27415

20. Velasco C, Cruz G, Lavin B, Hua A, Fotaki A, Botnar RM, et al. Simultaneous T1, T2, and T1rho cardiac magnetic resonance fingerprinting for contrast agent-free myocardial tissue characterization. *Magn Reson Med.* (2021) 87:1992–2002. doi: 10.1002/mrm.29091

21. Hamilton JI, Jiang Y, Ma D, Lo WC, Gulani V, Griswold M, et al. Investigating and reducing the effects of confounding factors for robust T1 and T2 mapping with cardiac MR fingerprinting. *Magn Reson Imaging.* (2018) 53:40–51. doi: 10.1016/j.mri.2018.06.018

22. McGivney DF, Pierre E, Ma D, Jiang Y, Saybasili H, Gulani V, et al. SVD compression for magnetic resonance fingerprinting in the time domain. *IEEE Trans Med Imaging.* (2014) 33:2311–22. doi: 10.1109/TMI.2014.2337321

23. Ze W, Jian Z, Di C, Jun X, Mengye L, Hui ES, et al. Magnetic resonance fingerprinting using a fast dictionary searching algorithm: MRF-ZOOM. *IEEE Trans Biomed Eng.* (2019) 66:1526–35. doi: 10.1109/TBME.2018.2874992

24. Boux F, Forbes F, Arbel J, Lemasson B, Barbier EL. Bayesian inverse regression for vascular magnetic resonance fingerprinting. *IEEE Trans Med Imaging.* (2021) 40:1827–37. doi: 10.1109/TMI.2021.3066781

25. Wang D, Ostenson J, Smith DS. snapMRF: GPU-accelerated magnetic resonance fingerprinting dictionary generation and matching

using extended phase graphs. *Magn Reson Imaging.* (2020) 66:248–56. doi: 10.1016/j.mri.2019.11.015

26. Asslander J, Cloos MA, Knoll F, Sodickson DK, Hennig J, Lattanzi R. Low rank alternating direction method of multipliers reconstruction for MR fingerprinting. *Magn Reson Med.* (2018) 79:83–96. doi: 10.1002/mrm.26639

27. Zhao B, Setsompop K, Adalsteinsson E, Gagoski B, Ye H, Ma D, et al. Improved magnetic resonance fingerprinting reconstruction with low-rank and subspace modeling. *Magn Reson Med.* (2018) 79:933–42. doi: 10.1002/mrm.26701

28. Lima da. Cruz G, Bustin A, Jaubert O, Schneider T, Botnar RM, Prieto C. Sparsity and locally low rank regularization for MR fingerprinting. *Magn Reson Med.* (2019) 81:3530–43. doi: 10.1002/mrm.27665

29. Hornik K, Stinchcombe M, White H. Multilayer feedforward networks are universal approximators. *Neural Netw.* (1989) 2:359–66. doi: 10.1016/0893-6080(89)90020-8

30. Leiner T, Rueckert D, Suinesiaputra A, Baessler B, Nezafat R, Isgum I, et al. Machine learning in cardiovascular magnetic resonance: basic concepts and applications. *J Cardiovasc Magn Reson.* (2019) 21:61. doi: 10.1186/s12968-019-0575-y

31. Hagiwara A, Fujita S, Ohno Y, Aoki S. Variability and standardization of quantitative imaging: monoparametric to multiparametric quantification, radiomics, and artificial intelligence. *Invest Radiol.* (2020) 55:601–16. doi: 10.1097/RLI.0000000000000666

32. Schlemper J, Caballero J, Hajnal JV, Price AN, Rueckert D, A. Deep cascade of convolutional neural networks for dynamic mr image reconstruction. *IEEE Trans Med Imaging.* (2018) 37:491–503. doi: 10.1109/TMI.2017.2760978

33. Hammernik K, Klatzer T, Kobler E, Recht MP, Sodickson DK, Pock T, et al. Learning a variational network for reconstruction of accelerated MRI data. *Magn Reson Med.* (2018) 79:3055–71. doi: 10.1002/mrm.26977

34. Bustin A, Fuin N, Botnar RM, Prieto C. From compressed-sensing to artificial intelligence-based cardiac MRI reconstruction. *Front Cardiovasc Med.* (2020) 7:17. doi: 10.3389/fcvm.2020.00017

35. Martin-Isla C, Campello VM, Izquierdo C, Raisi-Estabragh Z, Baessler B, Petersen SE, et al. Image-based cardiac diagnosis with machine learning: a review. *Front Cardiovasc Med.* (2020) 7:1. doi: 10.3389/fcvm.2020.00001

36. Martini N, Aimo A, Barison A, Della Latta D, Vergaro G, Aquaro GD, et al. Deep learning to diagnose cardiac amyloidosis from cardiovascular magnetic resonance. *J Cardiovasc Magn Reson.* (2020) 22:84. doi: 10.1186/s12968-020-00690-4

37. Vergani V, Razavi R, Puyol-Anton E, Ruijsink B. Deep learning for classification and selection of cine CMR images to achieve fully automated quality-controlled CMR analysis from scanner to report. *Front Cardiovasc Med.* (2021) 8:742640. doi: 10.3389/fcvm.2021.742640

38. Ruijsink B, Puyol-Anton E, Oksuz I, Sinclair M, Bai W, Schnabel JA, et al. Fully automated, quality-controlled cardiac analysis from CMR: validation and large-scale application to characterize cardiac function. *JACC Cardiovasc Imaging.* (2020) 13:684–95. doi: 10.1016/j.jcmg.2019.05.030

39. Bernard O, Lalande A, Zotti C, Cervenansky F, Yang X, Heng PA, et al. Deep learning techniques for automatic MRI cardiac multi-structures segmentation and diagnosis: is the problem solved? *IEEE Trans Med Imaging.* (2018) 37:2514–25. doi: 10.1109/TMI.2018.2837502

40. Chen C, Qin C, Qiu H, Tarroni G, Duan J, Bai W, et al. Deep learning for cardiac image segmentation: a review. *Front Cardiovasc Med.* (2020) 7:25. doi: 10.3389/fcvm.2020.00025

41. Feng L, Ma D, Liu F. Rapid MR relaxometry using deep learning: an overview of current techniques and emerging trends. *NMR Biomed.* (2020) 35:e4416. doi: 10.1002/nbm.4416

42. Schmidhuber J. Deep learning in neural networks: an overview. *Neural Netw.* (2015) 61:85–117. doi: 10.1016/j.neunet.2014.09.003

43. LeCun Y, Bengio Y, Hinton G. Deep learning. *Nature.* (2015) 521:436–44. doi: 10.1038/nature14539

44. Vincenti G, Monney P, Chaptinel J, Rutz T, Coppo S, Zenge MO, et al. Compressed sensing single-breath-hold CMR for fast quantification of LV function, volumes, and mass. *JACC Cardiovasc Imaging.* (2014) 7:882–92. doi: 10.1016/j.jcmg.2014.04.016

45. Kido T, Kido T, Nakamura M, Watanabe K, Schmidt M, Forman C, et al. Compressed sensing real-time cine cardiovascular magnetic resonance: accurate assessment of left ventricular function in a single-breath-hold. *J Cardiovasc Magn Reson.* (2016) 18:50. doi: 10.1186/s12968-016-0271-0

46. Kustner T, Fuin N, Hammernik K, Bustin A, Qi H, Hajhosseiny R, et al. CINENet: deep learning-based 3D cardiac CINE MRI reconstruction with multi-coil complex-valued 4D spatio-temporal convolutions. *Sci Rep.* (2020) 10:13710. doi: 10.1038/s41598-020-70551-8

47. Fuin N, Bustin A, Kustner T, Oksuz I, Clough J, King AP, et al. A multi-scale variational neural network for accelerating motion-compensated whole-heart 3D coronary MR angiography. *Magn Reson Imaging.* (2020) 70:155–67. doi: 10.1016/j.mri.2020.04.007

48. Steeden JA, Quail M, Gotschy A, Mortensen KH, Hauptmann A, Arridge S, et al. Rapid whole-heart CMR with single volume super-resolution. *J Cardiovasc Magn Reson.* (2020) 22:56. doi: 10.1186/s12968-020-00651-x

49. Sandino CM, Lai P, Vasanawala SS, Cheng JY. Accelerating cardiac cine MRI using a deep learning-based ESPIRiT reconstruction. *Magn Reson Med.* (2021) 85:152–67. doi: 10.1002/mrm.28420

50. Qi H, Hajhosseiny R, Cruz G, Kuestner T, Kunze K, Neji R, et al. End-to-end deep learning nonrigid motion-corrected reconstruction for highly accelerated free-breathing coronary MRA. *Magn Reson Med.* (2021) 86:1983–96. doi: 10.1002/mrm.28851

51. Kustner T, Munoz C, Psenicny A, Bustin A, Fuin N, Qi H, et al. Deep-learning based super-resolution for 3D isotropic coronary MR angiography in less than a minute. *Magn Reson Med.* (2021) 86:2837–52. doi: 10.1002/mrm.28911

52. Dawes TJW, de Marvao A, Shi W, Fletcher T, Watson GMJ, Wharton J, et al. Machine learning of three-dimensional right ventricular motion enables outcome prediction in pulmonary hypertension: a cardiac MR imaging study. *Radiology.* (2017) 283:381–90. doi: 10.1148/radiol.2016161315

53. Bello GA, Dawes TJW, Duan J, Biffi C, de Marvao A, Howard L, et al. Deep learning cardiac motion analysis for human survival prediction. *Nat Mach Intell.* (2019) 1:95–104. doi: 10.1038/s42256-019-0019-2

54. Hamilton JI, Jiang Y, Ma D, Chen Y, Lo WC, Griswold M, et al. Simultaneous multislice cardiac magnetic resonance fingerprinting using low rank reconstruction. *NMR Biomed.* (2019) 32:e4041. doi: 10.1002/nbm.4041

55. Hamilton JI, Seiberlich N. Machine learning for rapid magnetic resonance fingerprinting tissue property quantification. *Proc IEEE Inst Electr Electron Eng.* (2020) 108:69–85. doi: 10.1109/JPROC.2019.2936998

56. Goodfellow I, Pouget-Abadie J, Mirza M, Xu B, Warde-Farley D, Ozair S, et al. *Generative Adversarial Networks.* (2014). Available online at: https://arxiv.org/abs/1406.2661 (accessed December, 2021).

57. Yang M, Jiang Y, Ma D, Mehta BB, Griswold MA. *Game of Learning Bloch Equation Simulations for MR Fingerprinting.* (2020). Available online at: https://arxiv.org/abs/2004.02270 (accessed November, 2021).

58. Ardizzone Lynton, Kruse Jakob, Wirkert Sebastian, Rahner Daniel, Pellegrini Eric W., Klessen Ralf S., et al. *Analyzing Inverse Problems with Invertible Neural Networks.* (2019). Available online at: https://arxiv.org/abs/1808.04730 (accessed November, 2021).

59. Balsiger F, Jungo A, Scheidegger O, Marty B, Reyes M. *Learning Bloch Simulations for MR Fingerprinting by Invertible Neural Networks*. Lima: Springer International Publishing (2020). p. 60–9.

60. Dinh L, Krueger D, Bengio Y. *Nice: Non-Linear Independent Components Estimation.* (2014). Available online at: https://arxiv.org/abs/1410.8516 (accessed December, 2021).

61. Dinh L, Sohl-Dickstein J, Bengio S. *Density Estimation Using Real NVP.* (2016). Available oline at: https://arxiv.org/abs/1605.08803 (accessed December, 2021).

62. Marty B, Carlier PG. MR fingerprinting for water T1 and fat fraction quantification in fat infiltrated skeletal muscles. *Magn Reson Med.* (2020) 83:621–34. doi: 10.1002/mrm.27960

63. Liu H, Heide O, Berg CAT, Sbrizzi A. Fast and accurate modeling of transient-state, gradient-spoiled sequences by recurrent neural networks. *NMR Biomed.* (2021) 34:e4527. doi: 10.1002/nbm.4527

64. Cruz G, Qi H, Jaubert O, Kuestner T, Schneider T, Botnar RM, et al. Generalized low-rank non-rigid motion-corrected reconstruction for MR fingerprinting. *Magn Reson Med.* (2022) 87:746–63. doi: 10.1002/mrm.29027

65. Lima da. Cruz GJ, Velasco C, Lavin B, Jaubert O, Botnar RM, Prieto C. Myocardial T1, T2, T2*, and fat fraction quantification *via* low-rank motion-corrected cardiac MR fingerprinting. *Magn Reson Med.* (2022) 87:2757–74. doi: 10.1002/mrm.29171

66. Cai C, Wang C, Zeng Y, Cai S, Liang D, Wu Y, et al. Single-shot T2 mapping using overlapping-echo detachment planar imaging and a deep convolutional neural network. *Magn Reson Med.* (2018) 80:2202–14. doi: 10.1002/mrm.27205

67. Liu F, Feng L, Kijowski R, MANTIS. Model-Augmented Neural neTwork with Incoherent k-space Sampling for efficient MR parameter mapping. *Magn Reson Med.* (2019) 82:174–88. doi: 10.1002/mrm.27707

68. Liu F, Kijowski R, Feng L, El Fakhri G. High-performance rapid MR parameter mapping using model-based deep adversarial learning. *Magn Reson Imaging.* (2020) 74:152–60. doi: 10.1016/j.mri.2020.09.021

69. Li Y, Wang Y, Qi H, Hu Z, Chen Z, Yang R, et al. Deep learning-enhanced T1 mapping with spatial-temporal and physical constraint. *Magn Reson Med.* (2021) 86:1647–61. doi: 10.1002/mrm.28793

70. Liu F, Kijowski R, El Fakhri G, Feng L. Magnetic resonance parameter mapping using model-guided self-supervised deep learning. *Magn Reson Med.* (2021) 85:3211–26. doi: 10.1002/mrm.28659

71. Jun Y, Shin H, Eo T, Kim T, Hwang D. Deep model-based magnetic resonance parameter mapping network (DOPAMINE) for fast T1 mapping using variable flip angle method. *Med Image Anal.* (2021) 70:102017. doi: 10.1016/j.media.2021.102017

72. Liang D, Cheng J, Ke Z, Ying L. Deep magnetic resonance image reconstruction: inverse problems meet neural networks. *IEEE Signal Process Mag.* (2020) 37:141–51. doi: 10.1109/MSP.2019.2950557

73. Jeelani H, Yang Y, Zhou R, Kramer CM, Salerno M, Weller DS, et al. Myocardial T1-mapping framework with recurrent and U-Net convolutional neural networks. *IEEE Int Symposium Biomed Imaging.* (2020) 1941–4. doi: 10.1109/ISBI45749.2020.9098459

74. Cheng J, Liu Y, Zhu Y, Liang D. DEMO: deep MR parametric mapping with unsupervised multi-tasking framework. *Invest Magn Reson Imaging.*(2021) 25:300. doi: 10.13104/imri.2021.25.4.300

75. Qin C, Schlemper J, Caballero J, Price AN, Hajnal JV, Rueckert D. Convolutional recurrent neural networks for dynamic MR image reconstruction. *IEEE Trans Med Imaging.* (2019) 38:280–90. doi: 10.1109/TMI.2018.2863670

76. Ulyanov D, Vedaldi A, Lempitsky V. Deep image prior. *Int J Comput Vis.* (2020) 128:1867–88. doi: 10.1007/s11263-020-01303-4

77. Yoo J, Jin KH, Gupta H, Yerly J, Stuber M, Unser M. Time-dependent deep image prior for dynamic MRI. *IEEE Trans Med Imaging.* (2021) 40:3337–48. doi: 10.1109/TMI.2021.3084288

78. Meng Z, Guo R, Li Y, Guan Y, Wang T, Zhao Y, et al. Accelerating T2 mapping of the brain by integrating deep learning priors with low-rank and sparse modeling. *Magn Reson Med.* (2021) 85:1455–67. doi: 10.1002/mrm.28526

79. Hamilton JI. A self-supervised deep learning reconstruction for shortening the breathhold and acquisition window in cardiac magnetic resonance fingerprinting. *Front Cardiovasc Med.* (2022) 9:928546. doi: 10.3389/fcvm.2022.928546

80. Cauley SF, Setsompop K, Ma D, Jiang Y, Ye H, Adalsteinsson E, et al. Fast group matching for MR fingerprinting reconstruction. *Magn Reson Med.* (2015) 74:523–8. doi: 10.1002/mrm.25439

81. Cline CC, Chen X, Mailhe B, Wang Q, Pfeuffer J, Nittka M, et al. AIR-MRF: accelerated iterative reconstruction for magnetic resonance fingerprinting. *Magn Reson Imaging.* (2017) 41:29–40. doi: 10.1016/j.mri.2017.07.007

82. Hamilton JI, Currey D, Rajagopalan S, Seiberlich N. Deep learning reconstruction for cardiac magnetic resonance fingerprinting T 1 and T 2 mapping. *Magn Reson Med.* (2021) 85:2127–35. doi: 10.1002/mrm.28568

83. Cohen O, Zhu B, Rosen MS. MR fingerprinting Deep RecOnstruction NEtwork (DRONE). *Magn Reson Med.* (2018) 80:885–94. doi: 10.1002/mrm.27198

84. Cao P, Cui D, Vardhanabhuti V, Hui ES. Development of fast deep learning quantification for magnetic resonance fingerprinting *in vivo*. *Magn Reson Imaging.* (2020) 70:81–90. doi: 10.1016/j.mri.2020.03.009

85. Cao X, Liao C, Wang Z, Chen Y, Ye H, He H, et al. Robust sliding-window reconstruction for accelerating the acquisition of MR fingerprinting. *Magn Reson Med.* (2017) 78:1579–88. doi: 10.1002/mrm.26521

86. Song P, Eldar YC, Mazor G, Rodrigues MRD, HYDRA. Hybrid deep magnetic resonance fingerprinting. *Med Phys.* (2019) 46:4951–69. doi: 10.1002/mp.13727

87. Song P, Eldar YC, Mazor G, Rodrigues MRD. Magnetic resonance fingerprinting using a residual convolutional neural network. In: *ICASSP 2019 - 2019 IEEE International Conference on Acoustics, Speech and Signal Processing (ICASSP)*. Brighton (2019).

88. Mazor G, Weizman L, Tal A, Eldar YC. Low-rank magnetic resonance fingerprinting. *Med Phys.* (2018) 45:4066–84. doi: 10.1002/mp.13078

89. Balsiger F, Shridhar Konar A, Chikop S, Chandran V, Scheidegger O, Geethanath S, et al. *Magnetic Resonance Fingerprinting Reconstruction via Spatiotemporal Convolutional Neural Networks*. Springer International Publishing (2018). p. 39–46.

90. Balsiger F, Jungo A, Scheidegger O, Carlier PG, Reyes M, Marty B. Spatially regularized parametric map reconstruction for fast magnetic resonance fingerprinting. *Med Image Anal.* (2020) 64:101741. doi: 10.1016/j.media.2020.101741

91. Gómez PA, Molina-Romero M, Ulas C, Bounincontri G, Sperl JI, Jones DK, et al. *Simultaneous Parameter Mapping, Modality Synthesis, and Anatomical Labeling of the Brain with MR Fingerprinting*. Medical Image Computing and Computer-Assisted Intervention - MICCAI 2016(2016).

92. Fessler JA, Sutton BP. Nonuniform fast fourier transforms using min-max interpolation. *IEEE Trans Signal Process.* (2003) 51:560–74. doi: 10.1109/TSP.2002.807005

93. Oksuz I, Cruz G, Clough J, Bustin A, Fuin N, Botnar RM, et al. Magnetic resonance fingerprinting using recurrent neural networks. In: *2019 IEEE 16th International Symposium on Biomedical Imaging (ISBI 2019)* (2019).

94. Fang Z, Chen Y, Liu M, Xiang L, Zhang Q, Wang Q, et al. Deep learning for fast and spatially constrained tissue quantification from highly accelerated data in magnetic resonance fingerprinting. *IEEE Trans Med Imaging.* (2019) 38:2364–74. doi: 10.1109/TMI.2019.2899328

95. Fang Z, Chen Y, Nie D, Lin W, Shen D. RCA-U-Net: Residual channel attention U-net for fast tissue quantification in magnetic resonance fingerprinting. *Med Image Comput Comput Assist Interv.* (2019) 11766:101–9. doi: 10.1007/978-3-030-32248-9_12

96. Hoppe E, Körzdörfer G, Nittka M, Würr T, Wetzl J, Lugauer F, et al. Deep learning for magnetic resonance fingerprinting: accelerating the reconstruction of quantitative relaxation maps. In: *Proceedings of the 26th Annual Meeting of ISMRM.* Paris (2018).

97. Hoppe E, Thamm F, Korzdorfer G, Syben C, Schirrmacher F, Nittka M, et al. Magnetic resonance fingerprinting reconstruction using recurrent neural networks. *Stud Health Technol Inform.* (2019) 267:126–33. doi: 10.3233/SHTI190816

98. Virtue P, Yu Stella X, Michael L. Better than real: complex-valued neural nets for MRI fingerprinting. In: *2017 IEEE International Conference on Image Processing (ICIP)*. Beijing (2017).

99. Zhu B, Liu J, Koonjoo N, Rosen B, Rosen MS. AUTOmated pulse SEQuence generation (AUTOSEQ) using Bayesian reinforcement learning in an MRI physics simulation environment. In: *Proceedings 26th Annual Meeting ISMRM.* Paris (2018).

100. Zhu B, Liu J, Koonjoo N, Rosen B, Rosen M. AUTOmated pulse SEQuence generation (AUTOSEQ) and neural network decoding for fast quantitative MR parameter measuremente using continuous and simultaneous RF transmit and receive. In: *Proceedings 27th Annual Meeting ISMRM*. Montreal, QC (2019).

101. Bahadir C, AV. D, Sabuncu M. *Learning-Based Optimization of the Undersampling Pattern in MRI.* (2019). Available online at: https://arxiv.org/abs/1901.01960 (accessed December, 2021).

102. Jin K, Unser M, Yi K. *Self-Supervised Deep Active Accelerated MRI.* (2019). Available online at: https://arxiv.org/abs/1901.04547 (accessed December, 2021).

103. Sherry F, Benning M, de los Reyes J, Graves M, Maierhofer G, Williams G, et al. *Learning the Sampling Pattern for MRI.* (2020). Available online at: https://arxiv.org/abs/1906.08754 (accessed December, 2021).

104. Weiss T, Senouf O, Vedula S, Michailovich O, Zibulevsky M, Bronstein A. *PILOT: Physics-Informed Learned Optimized Trajectories for Accelerated MRI.* (2021). Available online at: https://arxiv.org/abs/1909.05773

105. Cohen O, Rosen MS. Algorithm comparison for schedule optimization in MR fingerprinting. *Magn Reson Imaging.* (2017) 41:15–21. doi: 10.1016/j.mri.2017.02.010

106. Sommer K, Amthor T, Doneva M, Koken P, Meineke J, Bornert P. Towards predicting the encoding capability of MR fingerprinting sequences. *Magn Reson Imaging.* (2017) 41:7–14. doi: 10.1016/j.mri.2017.06.015

107. Kara D, Fan M, Hamilton J, Griswold M, Seiberlich N, Brown R. Parameter map error due to normal noise and aliasing artifacts in MR fingerprinting. *Magn Reson Med.* (2019) 81:3108–23. doi: 10.1002/mrm.27638

108. Asslander J, Lattanzi R, Sodickson DK, Cloos MA. Optimized quantification of spin relaxation times in the hybrid state. *Magn Reson Med.* (2019) 82:1385–97. doi: 10.1002/mrm.27819

109. Zhao B, Haldar JP, Congyu L, Dan M, Yun J, Griswold MA, et al. Optimal experiment design for magnetic resonance fingerprinting: cramer-rao bound meets spin dynamics. *IEEE Trans Med Imaging.* (2019) 38:844–61. doi: 10.1109/TMI.2018.2873704

110. van Riel MHC. *Optimization of MR Fingerprinting for Free-Breathing Quantitative Abdominal Imaging.* (2020). Available online at: https://arxiv.org/abs/2006.02928

111. Lee PK, Watkins LE, Anderson TI, Buonincontri G, Hargreaves BA. Flexible and efficient optimization of quantitative sequences using automatic differentiation of Bloch simulations. *Magn Reson Med.* (2019) 82:1438–51. doi: 10.1002/mrm.27832

112. Jordan SP, Hu S, Rozada I, McGivney DF, Boyacioglu R, Jacob DC, et al. Automated design of pulse sequences for magnetic resonance fingerprinting using physics-inspired optimization. *Proc Nat Acad Sci.* (2021) 118:e2020516118. doi: 10.1073/pnas.2020516118

113. Loktyushin A, Herz K, Dang N, Glang F, Deshmane A, Weinmuller S, et al. MRzero - Automated discovery of MRI sequences using supervised learning. *Magn Reson Med.* (2021) 86:709–24. doi: 10.1002/mrm.28727

114. Lundervold AS, Lundervold A. An overview of deep learning in medical imaging focusing on MRI. *Z Med Phys.* (2019) 29:102–27. doi: 10.1016/j.zemedi.2018.11.002

115. Hamilton JI, Pahwa S, Adedigba J, Frankel S, O'Connor G, Thomas R. et al. Simultaneous Mapping of T1 and T2 Using Cardiac Magnetic Resonance Fingerprinting in a Cohort of Healthy Subjects at 15T J. *Magn Reson Imaging.* (2020) 52:1044–52. doi: 10.1002/jmri.27155

116. Larrazabal AJ, Nieto N, Peterson V, Milone DH, Ferrante E. Gender imbalance in medical imaging datasets produces biased classifiers for computer-aided diagnosis. *Proc Natl Acad Sci U S A.* (2020) 117:12592–4. doi: 10.1073/pnas.1919012117

117. Puyol-Anton E, Ruijsink B, Piechnik SK, Neubauer S, Petersen S, Razavi R, et al. *Fairness in Cardiac MR Image Analysis: An Investigation of Bias Due to Data Imbalance in Deep Learning Based Segmentation.* (2021). Available online at: https://arxiv.org/abs/2106.12387

118. Chang K, Balachandar N, Lam C, Yi D, Brown J, Beers A, et al. Distributed deep learning networks among institutions for medical imaging. *J Am Med Inform Assoc.* (2018) 25:945–54. doi: 10.1093/jamia/ocy017

119. Rieke N, Hancox J, Li W, Milletari F, Roth HR, Albarqouni S, et al. The future of digital health with federated learning. *NPJ Digit Med.* (2020) 3:119. doi: 10.1038/s41746-020-00323-1

120. Singh A, Sengupta S, Lakshminarayanan V. Explainable deep learning models in medical image analysis. *J Imaging.* (2020) 6:52. doi: 10.3390/jimaging6060052

121. Castelvecchi D. Can we open the black box of AI? *Nature.* (2016) 538:20–3. doi: 10.1038/538020a

122. Gillies RJ, Kinahan PE, Hricak H. Radiomics: images are more than pictures, they are data. *Radiology.* (2016) 278:563–77. doi: 10.1148/radiol.2015151169

123. Raisi-Estabragh Z, Izquierdo C, Campello VM, Martin-Isla C, Jaggi A, Harvey NC, et al. Cardiac magnetic resonance radiomics: basic principles and clinical perspectives. *Eur Heart J Cardiovasc Imaging.* (2020) 21:349–56. doi: 10.1093/ehjci/jeaa028

124. Larroza A, Materka A, Lopez-Lereu MP, Monmeneu JV, Bodi V, Moratal D. Differentiation between acute and chronic myocardial infarction by means of texture analysis of late gadolinium enhancement and cine cardiac magnetic resonance imaging. *Eur J Radiol.* (2017) 92:78–83. doi: 10.1016/j.ejrad.2017.04.024

125. Kotu LP, Engan K, Borhani R, Katsaggelos AK, Orn S, Woie L, et al. Cardiac magnetic resonance image-based classification of the risk of arrhythmias in post-myocardial infarction patients. *Artif Intell Med.* (2015) 64:205–15. doi: 10.1016/j.artmed.2015.06.001

126. Gibbs T, Villa ADM, Sammut E, Jeyabraba S, Carr-White G, Ismail TF, et al. Quantitative assessment of myocardial scar heterogeneity using cardiovascular magnetic resonance texture analysis to risk stratify patients post-myocardial infarction. *Clin Radiol.* (2018) 73:1059 e17–e26. doi: 10.1016/j.crad.2018.08.012

127. Baessler B, Mannil M, Maintz D, Alkadhi H, Manka R. Texture analysis and machine learning of non-contrast T1-weighted MR images in patients with hypertrophic cardiomyopathy-preliminary results. *Eur J Radiol.* (2018) 102:61–7. doi: 10.1016/j.ejrad.2018.03.013

128. Baessler B, Mannil M, Oebel S, Maintz D, Alkadhi H, Manka R. Subacute and chronic left ventricular myocardial scar: accuracy of texture analysis on nonenhanced cine MR images. *Radiology.* (2018) 286:103–12. doi: 10.1148/radiol.2017170213

129. Baessler B, Luecke C, Lurz J, Klingel K, von Roeder M, de Waha S, et al. Cardiac MRI texture analysis of T1 and T2 maps in patients with infarctlike acute myocarditis. *Radiology.* (2018) 289:357–65. doi: 10.1148/radiol.2018180411

130. Baessler B, Luecke C, Lurz J, Klingel K, Das A, von Roeder M, et al. Cardiac MRI and texture analysis of myocardial T1 and T2 maps in myocarditis with acute versus chronic symptoms of heart failure. *Radiology.* (2019) 292:608–17. doi: 10.1148/radiol.2019190101

131. Neisius U, El-Rewaidy H, Nakamori S, Rodriguez J, Manning WJ, Nezafat R. Radiomic analysis of myocardial native T1 imaging discriminates between hypertensive heart disease and hypertrophic cardiomyopathy. *JACC Cardiovasc Imaging.* (2019) 12:1946–54. doi: 10.1016/j.jcmg.2018.11.024

132. El-Rewaidy H, Neisius U, Nakamori S, Ngo L, Rodriguez J, Manning WJ, et al. Characterization of interstitial diffuse fibrosis patterns using texture analysis of myocardial native T1 mapping. *PLoS ONE.* (2020) 15:e0233694. doi: 10.1371/journal.pone.0233694

133. Antonopoulos AS, Boutsikou M, Simantiris S, Angelopoulos A, Lazaros G, Panagiotopoulos I, et al. Machine learning of native T1 mapping radiomics for classification of hypertrophic cardiomyopathy phenotypes. *Sci Rep.* (2021) 11:23596. doi: 10.1038/s41598-021-02971-z

frontiers | Frontiers in Cardiovascular Medicine

TYPE Original Research
PUBLISHED 20 September 2022
DOI 10.3389/fcvm.2022.977603

OPEN ACCESS

EDITED BY
Christopher T. Nguyen,
Cleveland Clinic, United States

REVIEWED BY
Stanislas Rapacchi,
UMR7339 Centre de Résonance Magnétique Biologique et Médicale (CRMBM), France
Andrew Scott,
Royal Brompton Hospital, United Kingdom

*CORRESPONDENCE
Yuchi Liu
yuchiliu@med.umich.edu

SPECIALTY SECTION
This article was submitted to Cardiovascular Imaging, a section of the journal Frontiers in Cardiovascular Medicine

RECEIVED 24 June 2022
ACCEPTED 25 August 2022
PUBLISHED 20 September 2022

CITATION
Liu Y, Hamilton J, Jiang Y and Seiberlich N (2022) Cardiac MRF using rosette trajectories for simultaneous myocardial T_1, T_2, and proton density fat fraction mapping. *Front. Cardiovasc. Med.* 9:977603. doi: 10.3389/fcvm.2022.977603

Cardiac MRF using rosette trajectories for simultaneous myocardial T_1, T_2, and proton density fat fraction mapping

Yuchi Liu[1]*, Jesse Hamilton[1,2], Yun Jiang[1,2] and Nicole Seiberlich[1,2]

[1]Department of Radiology, University of Michigan, Ann Arbor, MI, United States, [2]Department of Biomedical Engineering, University of Michigan, Ann Arbor, MI, United States

The goal of this work is to extend prior work on cardiac MR Fingerprinting (cMRF) using rosette k-space trajectories to enable simultaneous T_1, T_2, and proton density fat fraction (PDFF) mapping in the heart. A rosette trajectory designed for water-fat separation at 1.5T was used in a 2D ECG-triggered 15-heartbeat cMRF sequence. Water and fat specific T_1 and T_2 maps were generated from the cMRF data. A PDFF map was also retrieved using Hierarchical IDEAL by segmenting the rosette cMRF data into multiple echoes. The accuracy of rosette cMRF in T_1, T_2, and PDFF quantification was validated in the ISMRM/NIST phantom and an in-house built fat fraction phantom, respectively. The proposed method was also applied for myocardial tissue mapping of healthy subjects and cardiac patients at 1.5T. T_1, T_2, and PDFF values measured using rosette cMRF in the ISMRM/NIST phantom and the fat fraction phantom agreed well with the reference values. In 16 healthy subjects, rosette cMRF yielded T_1 values which were 80∼90 ms higher than spiral cMRF and MOLLI. T_2 values obtained using rosette cMRF were ∼3 ms higher than spiral cMRF and ∼5 ms lower than conventional T_2-prep bSSFP method. Rosette cMRF was also able to detect abnormal T_1 and T_2 values in cardiomyopathy patients and may provide more accurate maps due to effective fat suppression. In conclusion, this study shows that rosette cMRF has the potential for efficient cardiac tissue characterization through simultaneous quantification of myocardial T_1, T_2, and PDFF.

KEYWORDS

cardiac MRF, T_1 mapping, T_2 mapping, PDFF, rosette trajectory

Introduction

Quantitative cardiac MRI is a powerful tool which can enable comprehensive tissue characterization for cardiac disease diagnosis. In particular, T_1 and T_2 mapping in the heart have been shown to be more sensitive to pathological changes than traditional T_1- and T_2-weighted images, including in cases of myocardial inflammation, fibrosis, myocarditis, infarcts, and edema, etc., (1–3). In addition, elimination of fat signals can reduce errors in these quantitative maps caused by water-fat partial volume effects,

and quantitative proton density fat fraction (PDFF) mapping may provide additional value in diagnosing diseases like intramyocardial fat infiltration (4, 5). Recently, studies have shown that epicardial adipose tissue may play a role in COVID-19 myocardial inflammation, and quantification of epicardial fat volume may potentially aid evaluating this risk factor for COVID-19 complications (6).

When collected as part of the clinical routine, T_1 and T_2 mapping and fat imaging in the myocardium are often performed in separate scans and thus require long scan times with multiple breath holds. Multi-parametric mapping methods such as cardiac Magnetic Resonance Fingerprinting (cMRF) (7) are potentially more efficient because they can provide multiple quantitative measurements in a single scan. Previously, the Dixon method has been incorporated in the cMRF framework using multi-echo radial acquisitions to enable T_1, T_2, and PDFF quantification (8). Alternatively, rosette trajectories have also been used in the cMRF sequence to achieve water-fat separation along with myocardial T_1 and T_2 mapping (9). Rosette trajectories can be designed to sample the center of k-space multiple times during one readout, resulting in the suppression of signals at certain off-resonance frequencies due to dephasing. In other words, rosette trajectories can be used to generate a "pass band" and "null band" in the spectral dimension. This feature has been used for water-fat separation (10), chemical shift encoding (11, 12), and simultaneous multi-slice imaging (13). While the previous rosette cMRF work achieved water-fat separation, quantification of fat fraction was found unreliable due to the nature of the proton density estimates generated by pattern matching (9). The goal of this work is to extend rosette cMRF to enable quantitative PDFF measurements using Hierarchical IDEAL along with myocardial T_1 and T_2 mapping from a single scan.

Materials and methods

Pulse sequence design

A rosette trajectory with eight lobes and a readout duration of 7.7 ms (Figure 1A) was designed to suppress signals at −220 Hz (the main resonance frequency of fat at 1.5T). The time optimal gradient design software package developed by Vaziri and Lustig (14, 15) was used for the gradient waveform design according to the following criteria: maximum gradient amplitude 23 mT/m, maximum slew rate 145 T/m/s, FOV 300 × 300 mm^2, matrix size 192×192, in-plane resolution 1.56 × 1.56 mm^2. Simulation studies show that this trajectory suppresses 94.7% of the signal at−220 Hz (Figure 1B). This readout trajectory was incorporated into a previously reported 15-heartbeat ECG-triggered cMRF sequence structure (9) with flip angles ranging from 4 to 25 degrees. A constant TR of 9.7 ms and TE of 1.39 ms were used. A total of 26 repetitions of this acquisition were collected at late diastole during each heartbeat, resulting in an acquisition window of ∼250 ms per heartbeat and a total of 390 highly undersampled images (one image per TR) over 15 heartbeats. The rosette trajectory was rotated by the golden angle (111°) between TRs. A slice thickness of 8 mm was employed in all phantom and *in vivo* experiments. All data were acquired at the resonance frequency of water.

Dictionary generation and image reconstruction

An individual dictionary was simulated for each subject that models the subject's cardiac rhythm (7) and includes corrections for slice profile and preparation pulse efficiency (16). The dictionary resolution, denoted by min:step:max, was (10:10:2000, 2050:50:3000 3200:200:4000 4500 5000) ms for T_1 in the heart; (10:10:90, 100:20:1000, 1040:40:2000, 2050:50:3000) ms for T_1 in phantoms; (4:2:80, 85:5:120, 130:10:300, 350:50:500) ms for T_2 in the heart; (2:2:8, 10:5:100, 110:10:300, 350:50:1100) ms for T_2 in phantoms. The dictionary was compressed along the time dimension using singular value decomposition (SVD) (17). A threshold was set to preserve 99.9% of the signal energy, resulting in the first six singular values retained.

The cMRF k-space data were first compressed along the coil dimension using SVD to preserve 98% of the signal energy. Then the k-space data were projected to the subspace derived from the SVD of the dictionary as described above, resulting in six "coefficient images" by applying the NUFFT (18). These six coefficient images correspond to the six largest singular values and aliasing artifacts are greatly reduced in them. When rosette data are collected at the resonance frequency of water (as described above), water signal is preserved, but signal from fat is suppressed, resulting in images which depict water but not fat. As in previous work (9), fat images were generated by demodulating the acquired data at the resonance frequency of fat with a single-peak fat model and then reapplying the projection and NUFFT to the k-space data.

Additionally, a B_0 map was computed by generating two images with different echo times by gridding the first and second halves of the readout (lobes 1–4 for echo 1 and lobes 5–8 for echo 2) and calculating the phase difference of these two images (9). B_0 correction was performed on both the water and fat coefficient images by demodulating the k-space data at a series of frequencies from−150 Hz to 150 Hz with a step size of 5 Hz. The final B_0 corrected image combines pixels demodulated at the true resonance frequency according to the B_0 map. The two sets of B_0 corrected coefficient images, one for water and one for fat, were then matched to the compressed dictionary using direct pattern match to generate the final T_1 and T_2 maps, and proton density images for water and fat, respectively. For spiral

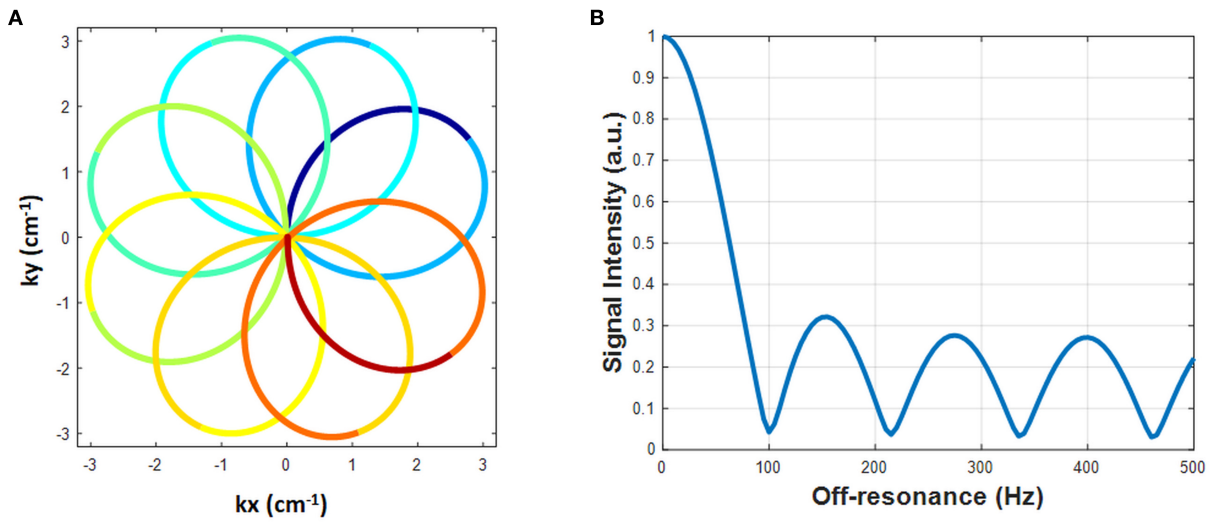

FIGURE 1
The designed rosette trajectory and its spectral response. **(A)** The rosette trajectory used in this work, where the segments used to generate images at different echo times are indicated by different colors. **(B)** Spectral response of the trajectory. Fat signals at −220 Hz are suppressed to 5.3%.

cMRF data, similar dictionary generation and pattern matching processes were performed without B_0 correction due to the lack of a co-registered B_0 map.

To generate quantitative PDFF maps, the data were processed as multi-echo acquisitions using Hierarchical IDEAL (19) in a separate process from MRF reconstruction (pattern matching was not involved). The 8-lobe trajectory was divided into nine segments (Figure 1A). The first and the last segment were half lobes going from the center to the edge of k-space and rewinding from the edge of k-space back to the center, respectively. The other seven segments started and ended at the edge of k-space with a zero-crossing in the middle. Because the images generated from single segments were highly undersampled, an SVD was performed along the time dimension to reduce aliasing artifacts. Data from each segment were projected onto a low-dimensional subspace of rank six derived from the SVD of the dictionary as described above. Subspace images corresponding to the first singular value from each of the nine rosette segments served as multi-echo images. TE of each echo was defined as the time of the zero-crossing of each segment; the TEs of the nine echoes were: 1.39, 2.46, 3.4, 4.34, 5.28, 6.22, 7.16, 8.1, and 9.2 ms. These multi-echo images and their corresponding TEs served as the inputs to the Hierarchical IDEAL toolbox. Note that B_0 correction was not performed on these multi-echo images prior to the IDEAL processing because B_0 fitting was already embedded in the IDEAL algorithm. A six-peak fat model was used in the Hierarchical IDEAL algorithm and outputs of the toolbox were a water image and a fat image. A PDFF map was calculated from the water and fat images using a noise correction method (20) to reduce bias in the regions where either water or fat image has low SNR according to the following equation:

$$PDFF = \begin{cases} \dfrac{\left|M_0^{fat}\right|}{\left|M_0^{fat} + M_0^{water}\right|} & if \ \left|M_0^{fat}\right| > \left|M_0^{water}\right| \\ 1 - \dfrac{\left|M_0^{water}\right|}{\left|M_0^{fat} + M_0^{water}\right|} & if \ \left|M_0^{water}\right| > \left|M_0^{fat}\right| \end{cases} \quad (1)$$

where M_0^{water} and M_0^{fat} are pixel-wise signal intensities of the water and fat images generated from Hierarchical IDEAL, respectively.

Phantom experiments

All experiments were performed on a 1.5T scanner (Siemens Sola, Erlangen, Germany). Rosette cMRF data were collected in the T_2 layer of the ISMRM/NIST MRI system phantom (21, 22) to validate the accuracy of water T_1 and T_2 quantification. The mean and standard deviation of the T_1 and T_2 values within a physiological range obtained using rosette cMRF were compared with gold standard values measured using inversion recovery and single echo spin echo methods.

The accuracy of rosette cMRF in PDFF quantification was validated using an in-house developed fat fraction phantom (23). This phantom had one vial filled with peanut oil, one vial filled with water solution, and the rest of the five vials filled with a mixture of peanut oil and water solution to target a range of PDFF values from 10% to 50%. The water solution contained 43 mM sodium dodecyl sulfate, 43 mM sodium

chloride, 3.75 mM sodium azide, and 0.3 mM gadolinium. For all vials except for the one with pure peanut oil, agar (2% w/v) was added over heat and the vials formed a solid gel after cooling to room temperature. Note that super-paramagnetic iron oxide was not added in this phantom compared to the original recipe in (23). Considering imperfect operations which might cause water solution and/or peanut oil losses in transfer, the actual PDFF values were measured using a three-point GRE sequence with optimal echo times at 1.5T (1.9/3.4/4.9 ms). The three-point GRE data were processed using the Hierarchical IDEAL toolbox in the same way as for rosette cMRF 9-echo data, and the results were used as the gold-standard PDFF values.

Both phantoms were scanned in an axial orientation using a 20-channel head coil with simulated ECG signals at 60 bpm. For both phantoms, ROIs in each vial were drawn manually. The mean and standard deviation in T_1 and T_2 values in the ISMRM/NIST phantom and PDFF values in the fat fraction phantom for each ROI were compared to reference values using a linear regression test.

In vivo experiments

Sixteen healthy subjects and two patients with suspected cardiomyopathy were scanned after written informed consent in this IRB-approved study. Mid-ventricular level short axis slices in the heart were acquired using the proposed rosette cMRF sequence and the original spiral 15-heartbeat cMRF sequence with the same flip angle pattern and acquisition window (9). Conventional T_1 and T_2 maps (MOLLI and T_2-prepared bSSFP) were also collected in twelve of the healthy subjects and patients. The conventional scans are part of the Siemens MyoMaps product and used the following parameters: FOV 300 × 300 mm^2, matrix size 192 × 192, GRAPPA R = 2 and 6/8 Partial Fourier acquisition. The 5(3)3 version of MOLLI was used with an acquisition window of 285.2 ms. The conventional T_2 mapping scan used a 1(3)1(3)1 acquisition scheme with T_2 preparation times of 0, 25, 55 ms and an acquisition window of 242 ms. Shimming was performed over the volume of the heart instead of the entire FOV to achieve better B_0 field homogeneity. For patient scans, rosette cMRF, spiral cMRF and MOLLI were also performed ∼10 min after contrast agent injection.

ROIs over the myocardial wall were drawn manually in segments 7–12 of the standardized AHA model. The mean and standard deviation in T_1 and T_2 values of each ROI as well as over the entire myocardium were calculated. In healthy subjects, a student's *t*-test was used to compare T_1 and T_2 measurements using rosette cMRF, spiral cMRF, and conventional T_1/T_2 mapping sequences. Significant difference was considered with $P < 0.05$.

To further investigate the effects of fat suppression on T_1 and T_2 measurements using rosette cMRF *in vivo*, a water-fat "unseparated" situation was mimicked by combining the water and fat information from the rosette trajectory. To this end, using rosette cMRF data in all healthy subjects, the k-space data demodulated at the fat frequency (fat signals with water suppression) were added to the original acquired k-space data (water signals with fat suppression). Then image reconstruction and pattern matching were performed in the same way as for spiral cMRF data. The mean and standard deviation in T_1 and T_2 values of the ROIs described above were calculated and compared with rosette and spiral cMRF measurements.

Results

Phantom data

In the ISMRM/NIST system phantom, T_1 and T_2 measurements using rosette cMRF are in excellent agreement with the reference values (Supplementary Figure 1) (slope of best-fit line 1.02/1.01 for T_1/T_2, R^2 >0.99). In the fat fraction phantom, water and fat specific T_1 and T_2 maps, proton density images, and the PDFF map generated by Hierarchical IDEAL using the rosette cMRF data are shown in Figure 2. PDFF measurements using rosette cMRF agree well with 3-point GRE measurements (Figure 2B) (slope of best-fit line 1.07, R^2 > 0.99). The water and fat specific T_1 and T_2 measurements in the fat fraction phantom are shown in Supplementary Figure 2. T_1 and T_2 measurements are consistent across the vials regardless of PDFF values (except in the high/low PDFF vials which have too little signal for either water or fat).

Healthy subjects

Representative maps and images from one healthy subject are shown in Figure 3. The averaged T_1 and T_2 values of all subjects in each segment as well as in the entire myocardium are shown in Figure 4. Over the entire myocardium, spiral cMRF yielded similar T_1 values (1,002 ± 50.6 ms) compared with MOLLI (996.5 ± 20.1 ms) while rosette cMRF generated significantly higher T_1 values (1,081.1 ± 31.8 ms). Both spiral and rosette cMRF yielded significantly lower T_2 values (spiral 37.4 ± 2.8 ms; rosette 40.5 ± 1.4 ms) compared with the conventional method (45.7 ± 2.2 ms) over the entire myocardium., and rosette cMRF generated significantly higher T_2 values than spiral cMRF. Averaged PDFF over the myocardium was 0.4% among all subjects (ranging from −4.5% to 5.7%). Individual PDFF of the sixteen healthy subjects are shown in Figure 5.

In most of the individual segments (AHA segments 8-12), T_1 and T_2 values measured by the three methods show similar trends as in the entire slice. Spiral cMRF generated similar T_1 values compared with MOLLI except for segment 7 and 8;

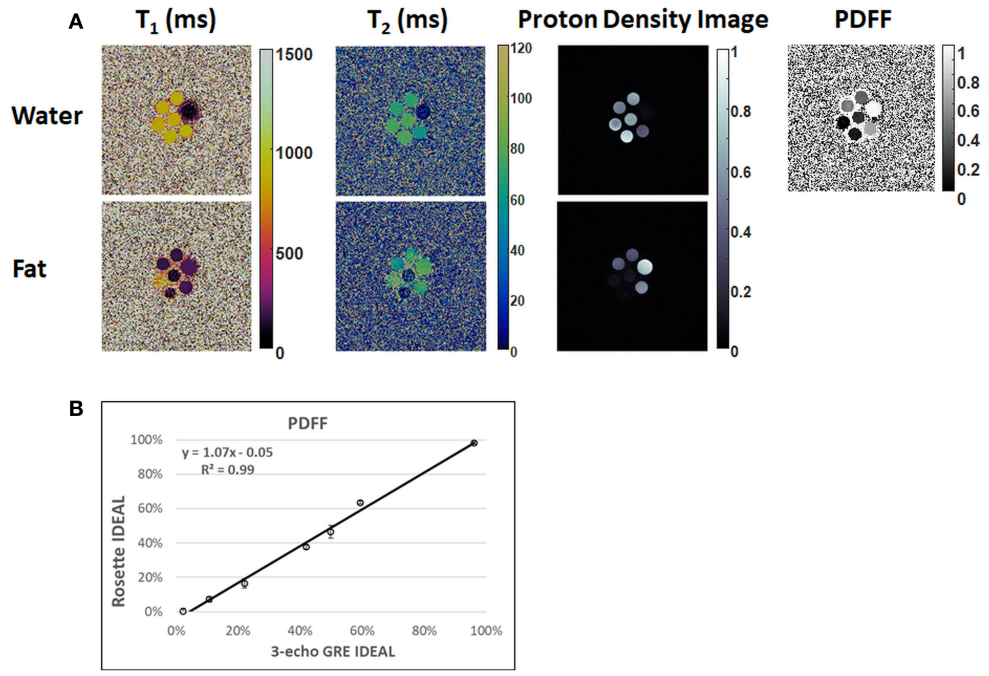

FIGURE 2
Results in the fat fraction phantom. **(A)** Water and fat specific T_1 and T_2 maps, proton density images, and the PDFF map generated by Hierarchical IDEAL using the rosette cMRF data. **(B)** PDFF measurements using rosette cMRF compared with reference values.

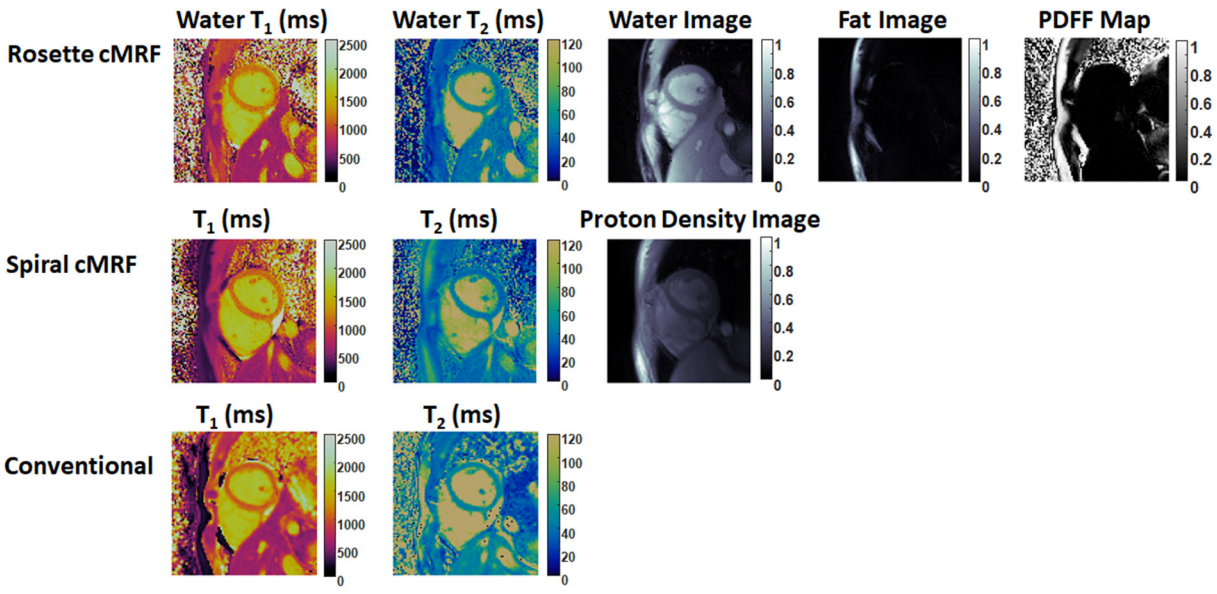

FIGURE 3
Representative T_1 map, T_2 map, water image, fat image, and PDFF maps in a healthy subject. T_1 and T_2 maps measured by spiral cMRF and conventional methods are shown for comparison. The field-of-view has been cropped to 150 × 150 mm^2 to better visualize the heart.

rosette cMRF generated significantly higher T_1 values compared with both MOLLI and spiral cMRF throughout all segments. Both spiral and rosette cMRF yielded significantly lower T_2 values compared with conventional method throughout all segments. Rosette cMRF generated significantly higher T_2 values than spiral cMRF in all segments except for segment

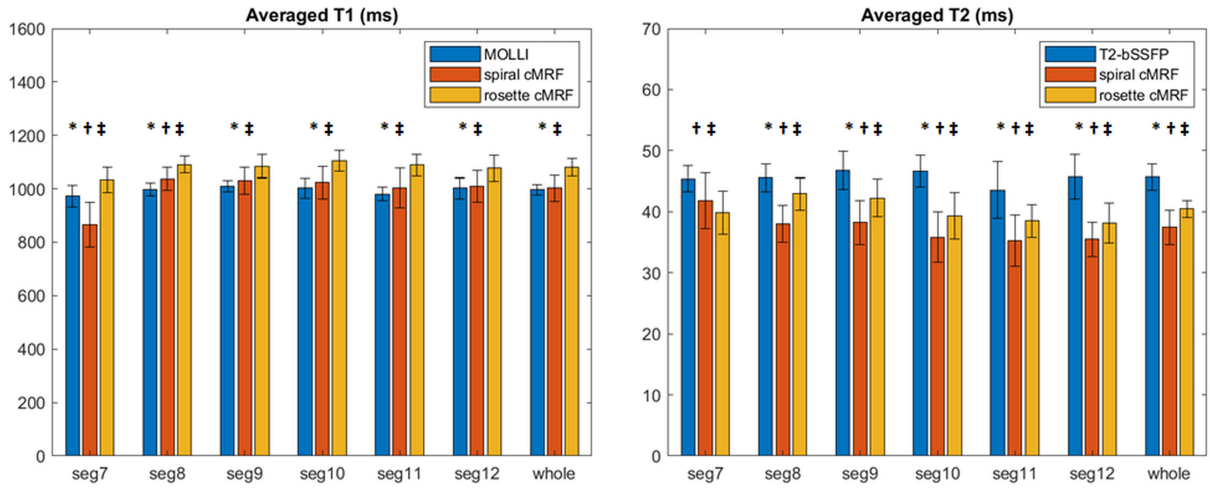

FIGURE 4
T_1 and T_2 values in 16 healthy subjects measured using conventional methods, spiral cMRF, and rosette cMRF. Measurements in segment 7–12 as well as over the entire myocardium are shown. *Significant difference between spiral and rosette cMRF. †Significant difference between conventional method and spiral cMRF. ‡Significant difference between conventional method and rosette cMRF.

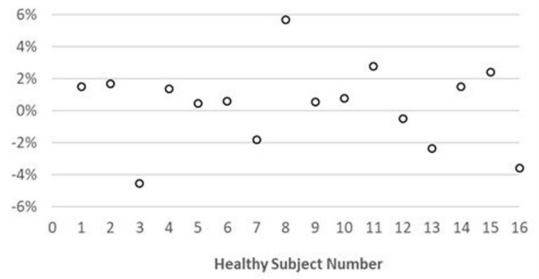

FIGURE 5
Individual PDFF over the myocardium measured using rosette cMRF in 16 healthy subjects.

7. A cyclic pattern was noted in T_1 and T_2 measurements across the segments using all three methods, with lateral T_1 and T_2 slightly lower than septal ones. Variations in T_1 and T_2 across the segments are most pronounced in spiral cMRF (T_1 ~170 ms; T_2 ~6.6 ms), but smaller in rosette cMRF (T_1 ~70 ms; T_2 ~4.4 ms) and conventional methods (T_1 ~38 ms; T_2 ~3.2 ms).

With fat signals added back, the averaged rosette cMRF T_1 measurements in segment 7 in all healthy subjects decreased from 1033.6 ± 48.4 ms to 1016 ± 85 ms; averaged T_2 increased from 39.8 ± 3.6 ms to 43.5 ± 4.6 ms. A comparison of T_1 and T_2 measurements in all segments as well as the entire slice between spiral cMRF, rosette cMRF (with fat suppression), and rosette cMRF with fat signals added back is shown in Supplementary Figure 3.

cMRF maps in patients

Figures 6, 7 show the pre- and post-contrast maps and images from one patient with cardiomyopathy, respectively. Elevated native T_1 and T_2 were observed using all three methods. PDFF over the myocardium measured by rosette cMRF pre- and post-contrast are 2.7 and 1.3%, respectively. Pre- and post-contrast results for the second patient are shown in Figures 8, 9. Myocardial PDFF measured by rosette cMRF pre- and post-contrast are 4.2 and 2.9%, respectively. Spiral cMRF maps exhibit blurring, especially in the T_2 maps, caused by epicardial fat; rosette cMRF was able to achieve much clearer boundaries of the myocardium due to fat signal suppression.

Discussion

The current study is an extension of previous work which used rosette cMRF for water-fat separation in addition to T_1 and T_2 mapping. The rosette trajectory originally designed for water-fat separation at 1.5T was optimized to improve off-resonance fat signal suppression from 86.5 to 94.7%. Note that the rosette trajectory was redesigned for PDFF measurement as compared to the trajectory used in (9), and thus all phantom and *in vivo* results presented here have no overlap with those reported in the previous work. A segmentation strategy was used to generate nine single echo images from each rosette readout, which could be used in conjunction with the Hierarchical IDEAL algorithm to enable PDFF quantification with no penalty in acquisition time. The first SVD coefficient images were used as the inputs to IDEAL in this work. Even though additional T_1 and/or

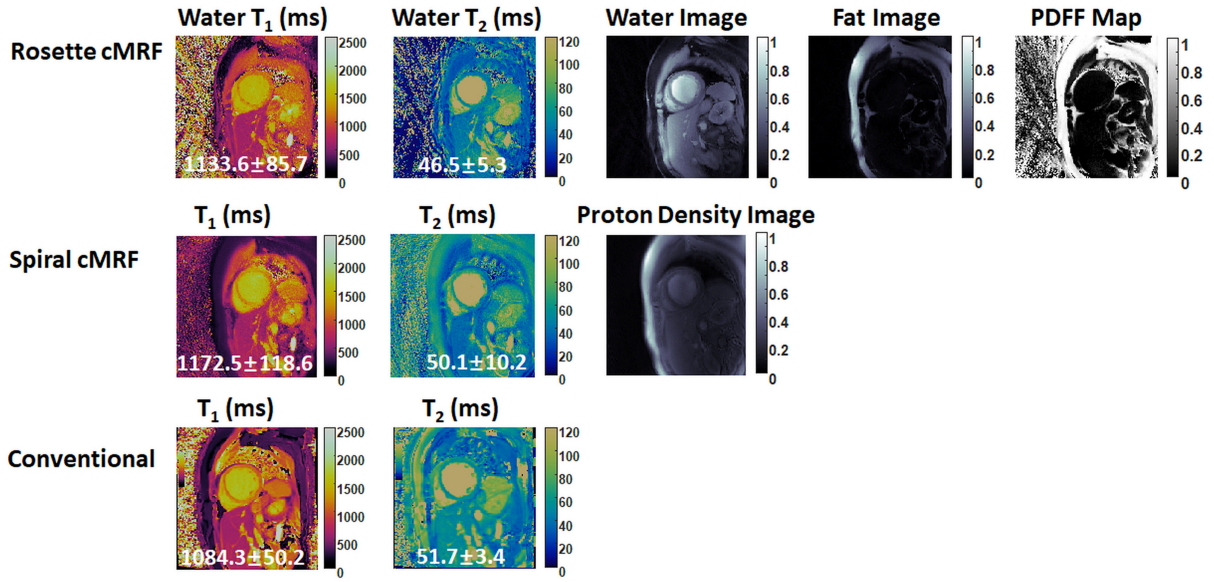

FIGURE 6
Pre-contrast results in the first cardiomyopathy patient acquired using rosette cMRF, spiral cMRF, and conventional methods. T_1 and T_2 values over the entire myocardium are shown in the maps.

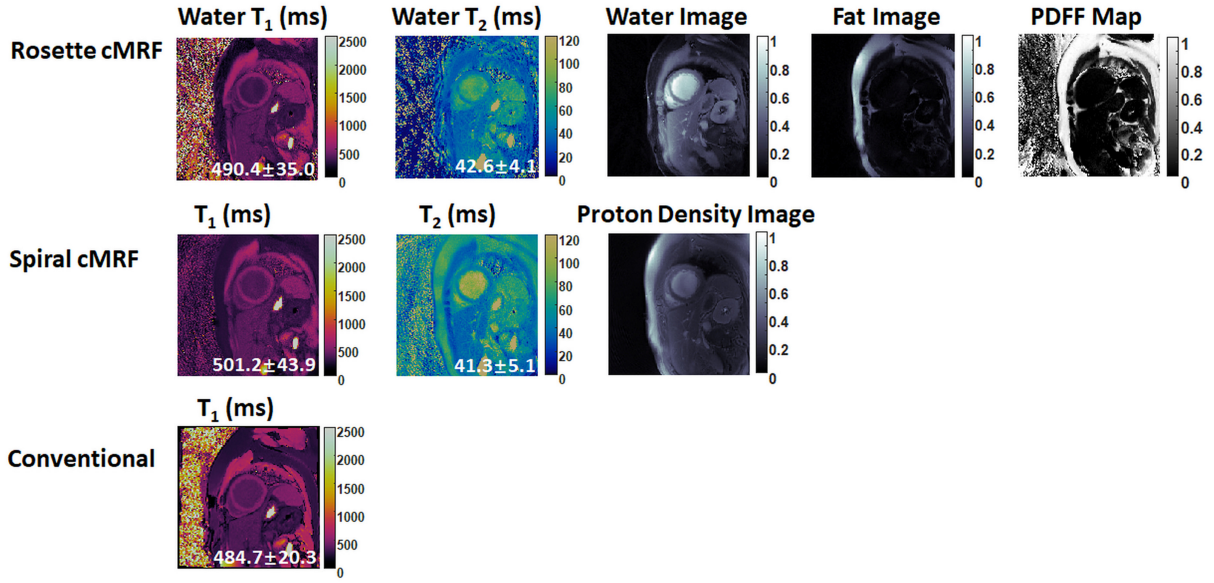

FIGURE 7
Post-contrast results in the first cardiomyopathy patient acquired using rosette cMRF, spiral cMRF, and conventional methods. T_1 and T_2 values over the entire myocardium are shown in the maps.

T_2 corrections to these images were not found necessary for the specific sequence used in this study, potential T_1 and T_2 weighting of these images depending on the specific sequence structure (e.g. flip angles, magnetization preparation modules) might cause inaccuracy in PDFF quantification especially for low or high T_1 (or T_2) values. In contrast, the previous work was able to generate qualitative water and fat images but not quantitative PDFF maps; while the attempt was made to calculate PDFF maps from the water and fat proton density images generated by pattern matching, these values were found to be inaccurate,

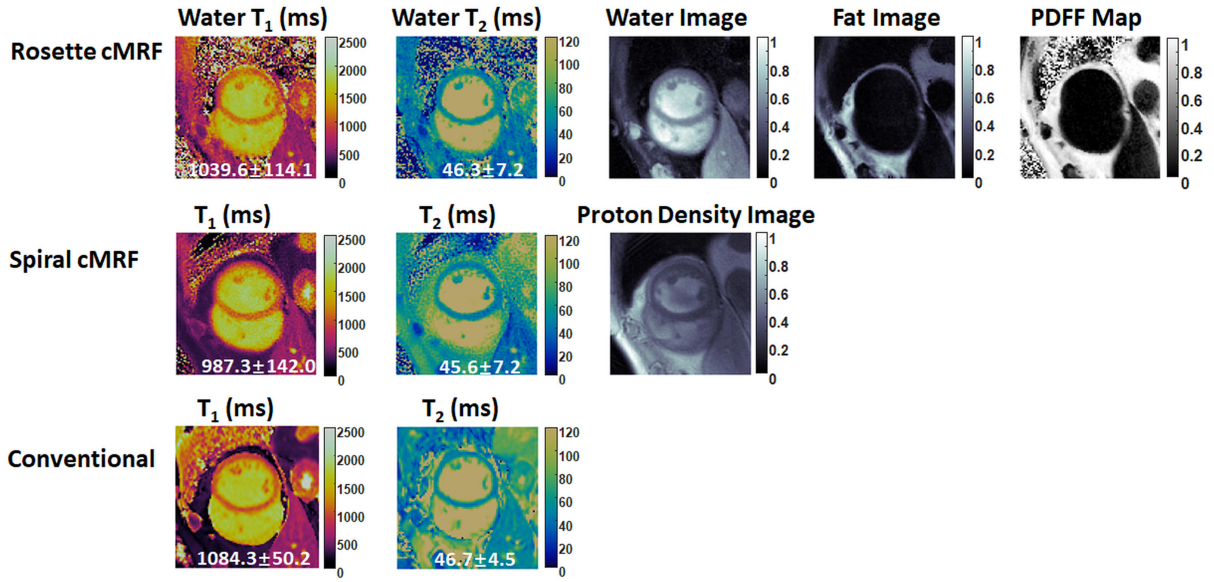

FIGURE 8
Pre-contrast results in the second cardiomyopathy patient acquired using rosette cMRF, spiral cMRF, and conventional methods. T_1 and T_2 values over the entire myocardium are shown in the maps. The field-of-view has been cropped to 150 × 150 mm^2 to better visualize the heart.

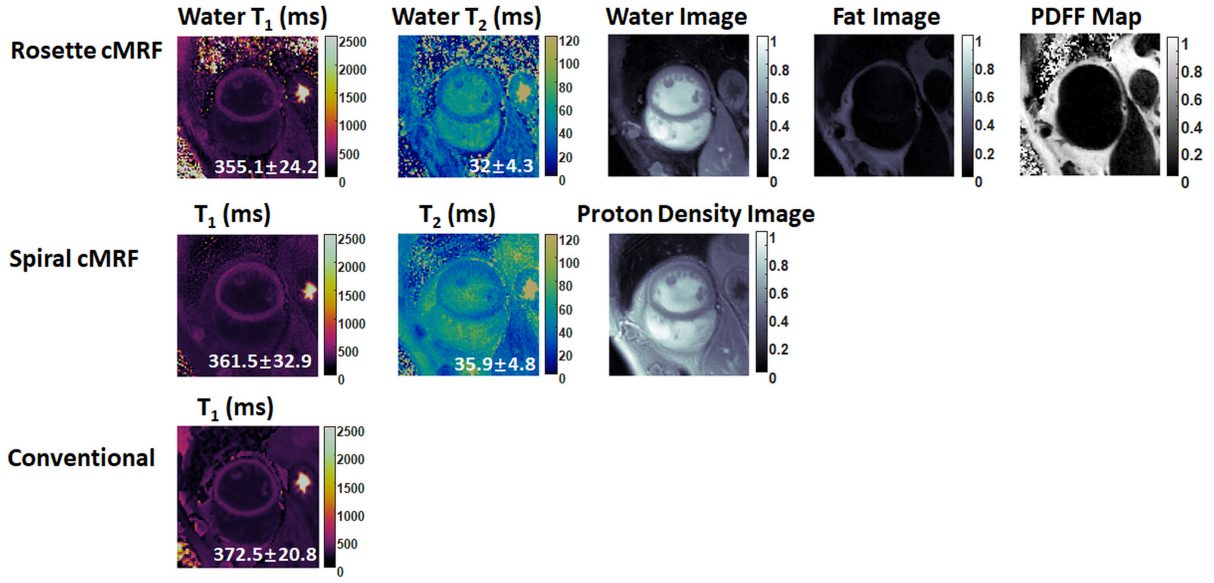

FIGURE 9
Post-contrast results in the second cardiomyopathy patient acquired using rosette cMRF, spiral cMRF, and conventional methods. T_1 and T_2 values over the entire myocardium are shown in the maps. The field-of-view has been cropped to 150 × 150 mm^2 to better visualize the heart.

as these proton density images derived from the scaling factors between the signal time courses and the dictionary entries are not quantitative maps of proton density. In this work, a similar calculation relying on proton density images for PDFF using the newly designed rosette trajectory again resulted in inaccurate values (Supplementary Figure 4).

Other studies have explored water-fat separation and PDFF quantification using the MRF framework in static organs (24–28) and in the heart. For example, Dixon-cMRF using multi-echo radial readout has been proposed to quantify T_1, T_2, and PDFF simultaneously in the heart (8, 29). Compared to rosette cMRF, Dixon-cMRF generated comparable myocardial

T_1 (1032 ms) and T_2 (42.1 ms) in healthy subjects in a similar acquisition time (~15 s) with slightly larger voxel size (2 × 2 × 8 mm^3 in healthy subjects and 1.8 × 1.8 × 8 mm^3 in patients). While Dixon-cMRF employed a different water-fat separation algorithm (graph cut) for PDFF quantification compared to the current study that used Hierarchical IDEAL, similar PDFF values were observed in healthy subjects (1.3% in the septum). Negative PDFF values were observed in the myocardium (Figure 5) due to the noise correction method performed in this study (20). When used in tissues with no fat content, this correction results in mean PDFF values of zero (with both positive and negative values possible). Unlike other MRF studies including Dixon-cMRF, advanced reconstruction methods such as low-rank reconstruction were not used in the current study to avoid long computation times with B_0 correction. In this work, direct pattern match with SVD along the time dimension in conjunction with rosette MRF yields good image and map quality without the need for advanced reconstruction techniques. Incorporating low-rank reconstruction yields slightly smaller standard deviations in the T_1 and T_2 measurements with almost identical mean values and image quality at a price of much longer computing time (data not shown here).

T_1 and T_2 values measured by spiral cMRF and conventional methods in a large cohort of healthy subjects ($n = 58$) at 1.5T have been reported previously (30). Over the entire mid-ventricular slice, the current study found T_1 values very close to the previous report and T_2 values slightly lower in both spiral cMRF and conventional measurements. The trend that spiral cMRF with confounding factor corrections yielded higher T_1 values than MOLLI and lower T_2 values than T_2-prep bSSFP method is also consistent with previous reports (16, 30). Similar to the previous rosette cMRF work (9), the current study found that rosette cMRF yielded ~3 ms higher T_2 values than spiral cMRF over the entire myocardium. However, the significant difference between rosette and spiral cMRF T_1 measurements observed in the current study was not found previously, possibly due to a much smaller number of subjects in the previous work (9).

While the previous rosette cMRF work only reported T_1 and T_2 values over the entire myocardium, the current study also examined each AHA segment of the mid-ventricular slice. Interestingly, segment 7 shows more pronounced difference in T_1 measurements and an opposite trend in T_2 measurements compared to the other segments regarding the comparison between spiral and rosette cMRF. Given that segment 7 (anterior wall) is surrounded by more epicardial fat than the other segments in the healthy subjects, and fat has T_1 of 300~370 ms (lower than myocardium) and T_2 of ~53 ms (higher than myocardium) at 1.5T (31), the higher T_1 and lower T_2 measured by rosette cMRF are possibly due to reduced fat contamination and may potentially be more accurate compared to spiral cMRF measurements. This hypothesis was also verified by the fact that T_1 in segment 7 was decreased and T_2 was increased when fat signals were added back to rosette cMRF data retrospectively (Supplementary Figure 3). The fact that rosette cMRF yielded smaller variations in T_1 and T_2 across cardiac segments compared to spiral cMRF (Figure 4) could also be evidence of effective fat signal suppression and more reliable T_1 and T_2 mapping. Note that difference between spiral and rosette cMRF measurements was still observed after fat signals were added back to the rosette data, indicating fat is not the only factor causing the difference. B_0 field inhomogeneity, which was not modeled in this simulation, might play a role because it causes blurring in spiral images but signal loss in rosette images. Spiral and rosette trajectories may also react to flow differently due to their different gradient waveforms and gradient moments, resulting in variations in T_1 and T_2 measurements.

Preliminary results from cardiomyopathy patients are shown in this study. Both spiral and rosette cMRF were able to detect abnormal T_1 and T_2 values, while rosette cMRF potentially provided better image quality by suppressing fat signals in the water T_1 and T_2 maps. Studies with a larger cohort of cardiac patients are on-going to validate the proposed method in a variety of cardiac diseases.

In addition to T_1 and T_2, T_2^* is also an important tissue property reflecting iron load in the myocardium (32). Given the multi-echo acquisition nature of rosette trajectories, T_2^* quantification in the heart and liver has been shown feasible using rosette trajectories (33). Even though the current study did not aim at T_2^* quantification and thus used a relatively short rosette readout, future work will explore the quantification of T_1, T_2, T_2^* and PDFF simultaneously using either a long rosette readout (34) or multi-echo radial readout (35) in the MRF framework.

There are a few limitations of the current study. First, even though the accuracy of PDFF quantification was validated in fat fraction phantoms, *in vivo* validation of PDFF measurements was not performed due to unavailability of the clinical PDFF mapping sequences. Second, repeatability of rosette cMRF was not tested in healthy subjects. Third, the image quality in patient data was not assessed by cardiologists using a systematic approach such as a Likert scale. Future studies will aim to address these aspects.

Conclusion

In conclusion, rosette cMRF is a promising method for efficient cardiac tissue characterization through the simultaneous quantification of myocardial T_1, T_2, and PDFF.

Data availability statement

The original contributions presented in the study are included in the article/Supplementary material, further inquiries can be directed to the corresponding author.

Ethics statement

The studies involving human participants were reviewed and approved by Institutional Review Boards of the University of Michigan Medical Campus. The patients/participants provided their written informed consent to participate in this study.

Author contributions

YL and JH contributed to pulse sequence development and data acquisition. YL performed data reconstruction, statistical analysis, wrote the draft of the manuscript, and created figures. All authors contributed to conception of the study, manuscript revision, and approved the submitted version.

Funding

JH is supported by NIH/NHLBI R01HL163030. This work was supported by NSF/CBET 1553441, NIH/NHLBI R01HL094557, and Siemens Healthineers (Erlangen, Germany). Siemens Healthineers was not involved in the study design, collection, analysis, interpretation of data, the writing of this article or the decision to submit it for publication.

Conflict of interest

The authors declare that the research was conducted in the absence of any commercial or financial relationships that could be construed as a potential conflict of interest.

Publisher's note

All claims expressed in this article are solely those of the authors and do not necessarily represent those of their affiliated organizations, or those of the publisher, the editors and the reviewers. Any product that may be evaluated in this article, or claim that may be made by its manufacturer, is not guaranteed or endorsed by the publisher.

Supplementary material

The Supplementary Material for this article can be found online at: https://www.frontiersin.org/articles/10.3389/fcvm.2022.977603/full#supplementary-material

References

1. Puntmann VO, Nagel E. T1 and T2 mapping in nonischemic cardiomyopathies and agreement with endomyocardial biopsy. *J Am Coll Cardiol.* (2016) 68:1923–4. doi: 10.1016/j.jacc.2016.06.075

2. Patel AR, Kramer CM. Role of cardiac magnetic resonance in the diagnosis and prognosis of nonischemic cardiomyopathy. *JACC Cardiovasc Imaging.* (2017) 10:1180–93. doi: 10.1016/j.jcmg.2017.08.005

3. Hamlin SA, Henry TS, Little BP, Lerakis S, Stillman AE. Mapping the future of cardiac MR imaging: case-based review of T1 and T2 mapping techniques. *RadioGraphics.* (2014) 34:1594–611. doi: 10.1148/rg.346140030

4. Farrelly C, Shah S, Davarpanah A, Keeling AN, Carr JC. ECG-gated multiecho Dixon fat-water separation in cardiac MRI: advantages over conventional fat-saturated imaging. *Am J Roentgenol.* (2012) 199W74–83. doi: 10.2214/AJR.11.7759

5. Kellman P, Hernando D, Shah S, Zuehlsdorff S, Jerecic R, Mancini C, et al. Multiecho dixon fat and water separation method for detecting fibrofatty infiltration in the myocardium. *Magn Reson Med.* (2008) 61:215–21. doi: 10.1002/mrm.21657

6. Iacobellis G, Secchi F, Capitanio G, Basilico S, Schiaffino S, Boveri S, et al. Epicardial fat inflammation in severe COVID-19. *Obesity.* (2020) 28:2260–2. doi: 10.1002/oby.23019

7. Hamilton JI, Jiang Y, Chen Y, Ma D, Lo WC, Griswold M, et al. MR fingerprinting for rapid quantification of myocardial T1, T2, and proton spin density. *Magn Reson Med.* (2017) 77:1446–58. doi: 10.1002/mrm.26216

8. Jaubert O, Cruz G, Bustin A, Schneider T, Lavin B, Koken P, et al. Water–fat Dixon cardiac magnetic resonance fingerprinting. *Magn Reson Med.* (2019) 00:1–17. doi: 10.1002/mrm.28070

9. Liu Y, Hamilton J, Eck B, Griswold M, Seiberlich N. Myocardial T1 and T2 quantification and water–fat separation using cardiac MR fingerprinting with rosette trajectories at 3T and 1.5T. *Magn Reson Med.* (2021) 85:103–19. doi: 10.1002/mrm.28404

10. Noll DC. Multishot rosette trajectories for spectrally selective MR imaging. *IEEE Trans Med Imaging.* (1997) 16:372–7. doi: 10.1109/42.611345

11. Schirda C V, Tanase C, Boada FE. Rosette spectroscopic imaging: optimal parameters for alias-free, high sensitivity spectroscopic imaging. *J Magn Reson Imaging.* (2009) 29:1375–85. doi: 10.1002/jmri.21760

12. Schirda C V, Zhao T, Andronesi OC, Lee Y, Pan JW, Mountz JM, et al. *In vivo* brain rosette spectroscopic imaging (RSI) with LASER excitation, constant gradient strength readout, and automated LCModel quantification for all voxels. *Magn Reson Med.* (2016) 76:380–90. doi: 10.1002/mrm.25896

13. Noll DC, Peltier SJ, Boada FE. Simultaneous multislice acquisition using rosette trajectories (SMART): a new imaging method for functional MRI. *Magn Reson Med.* (1998) 39:709–16. doi: 10.1002/mrm.1910390507

14. Lustig M, Kim SJ, Pauly JM. A fast method for designing time-optimal gradient waveforms for arbitrary k-space trajectories. *IEEE Trans Med Imaging.* (2008) 27:866–73. doi: 10.1109/TMI.2008.922699

15. Vaziri S, Lustig M. The fastest arbitrary k-space trajectories. *Proc Intl Soc Mag Reson Med.* (2012) 20:2284.

16. Hamilton JI, Jiang Y, Ma D, Lo W-C, Gulani V, Griswold M, et al. Investigating and reducing the effects of confounding factors for robust T1 and T2 mapping with cardiac MR fingerprinting. *Magn Reson Imaging.* (2018) 53:40–51. doi: 10.1016/j.mri.2018.06.018

17. McGivney DF, Pierre E, Ma D, Jiang Y, Saybasili H, Gulani V, et al. SVD compression for magnetic resonance fingerprinting in the time domain. *IEEE Trans Med Imaging.* (2014) 33:2311–22. doi: 10.1109/TMI.2014.2337321

18. Fessler JA. On NUFFT-based gridding for non-Cartesian MRI. *J Magn Reson.* (2007) 188:191–5. doi: 10.1016/j.jmr.2007.06.012

19. Tsao J, Jiang Y. Hierarchical IDEAL: Fast, robust, and multiresolution separation of multiple chemical species from multiple echo times. *Magn Reson Med.* (2013) 70:155–9. doi: 10.1002/mrm.24441

20. Liu CY, McKenzie CA Yu H, Brittain JH, Reeder SB. Fat quantification with IDEAL gradient echo imaging: Correction of bias from T1 and noise. *Magn Reson Med.* (2007) (58):354–64. doi: 10.1002/mrm.21301

21. Keenan K, Stupic K, Russek S, Chenevert T, Prasad P, Reddick W, et al. Multi–site, multi–vendor comparison of T1 measurement using ISMRM/NIST system phantom. *Proc Int Soc Magn Reson Med.* (2016) 24:3290.

22. Russek S, Boss M, Jackson E, Jennings D, Eveloch J, Gunter J, et al. Characterization of NIST/ISMRM MRI system phantom. *Proc Int Soc Magn Reson Med.*(2012) 20:2456.

23. Hines CDG Yu H, Shimakawa A, McKenzie CA, Brittain JH, Reeder SB. T1 independent, T2* corrected MRI with accurate spectral modeling for quantification of fat: Validation in a fat-water-SPIO phantom. *J Magn Reson Imaging.* (2009) 30:1215–22. doi: 10.1002/jmri.21957

24. Cencini M, Biagi L, Kaggie JD, Schulte RF, Tosetti M, Buonincontri G. Magnetic resonance fingerprinting with dictionary - based fat and water separation (DBFW MRF): a multi - component approach. *Magn Reson Med.* (2019) 81:3032–45. doi: 10.1002/mrm.27628

25. Koolstra K, Webb AG, Veeger TTJ, Kan HE, Koken P, Börnert P. Water–fat separation in spiral magnetic resonance fingerprinting for high temporal resolution tissue relaxation time quantification in muscle. *Magn Reson Med.* (2020) 84:646–62. doi: 10.1002/mrm.28143

26. Nolte T, Gross-Weege N, Doneva M, Koken P, Elevelt A, Truhn D, et al. Spiral blurring correction with water–fat separation for magnetic resonance fingerprinting in the breast. *Magn Reson Med.* (2020) 83:1192–207. doi: 10.1002/mrm.27994

27. Ostenson J, Damon BM, Welch EB. MR fingerprinting with simultaneous T1, T2, and fat signal fraction estimation with integrated B0 correction reduces bias in water T1 and T2 estimates. *Magn Reson Imaging.* (2019) 60:7–19. doi: 10.1016/j.mri.2019.03.017

28. Marty B, Carlier PG. MR fingerprinting for water T1 and fat fraction quantification in fat infiltrated skeletal muscles. *Magn Reson Med.* (2019) 83:621–34. doi: 10.1002/mrm.27960

29. Jaubert O, Cruz G, Bustin A, Hajhosseiny R, Nazir S, Schneider T, et al. T1, T2, and fat fraction cardiac MR fingerprinting: preliminary clinical evaluation. *J Magn Reson Imaging.* (2020) 53:1253–65. doi: 10.1002/jmri.27415

30. Hamilton JI, Pahwa S, Adedigba J, Frankel S, O'Connor G, Thomas R, et al. Simultaneous mapping of T1 and T2 using cardiac magnetic resonance fingerprinting in a cohort of healthy subjects at 1.5T. *J Magn Reson Imaging.* (2020) 52:1044–52. doi: 10.1002/jmri.27155

31. Rakow-Penner R, Daniel B, Yu H, Sawyer-Glover A, Glover GH. Relaxation times of breast tissue at 1.5T and 3T measured using IDEAL. *J Magn Reson Imaging.* (2006) 23:87–91. doi: 10.1002/jmri.20469

32. Anderson LJ, Holden S, Davis B, Prescott E, Charrier CC, Bunce NH, et al. Cardiovascular T2-star (T2*) magnetic resonance for the early diagnosis of myocardial iron overload. *Eur Heart J.* (2001) 22:2171–9. doi: 10.1053/euhj.2001.2822

33. Bush AM, Sandino CM, Ramachandran S, Ong F, Dwork N, Zucker EJ, et al. Rosette trajectories enable ungated, motion-robust, simultaneous cardiac and liver T_2 * iron assessment. *J Magn Reson Imaging.* (2020) 52:1688–98. doi: 10.1002/jmri.27196

34. Cummings E, Liu Y, Jiang Y, Ropella-Panagis K, Hamilton J, Seiberlich N. Simultaneous mapping of T1, T2, T2*, and fat fraction at 0.55T with rosette MRF. In: *Proceedings of the Low Field Workshop, International Society for Magnetic Resonance in Medicine, virtual.* (2022).

35. Lima da Cruz GJ, Velasco C, Lavin B, Jaubert O, Botnar RM, Prieto C. Myocardial T1, T2, T2*, and fat fraction quantification via low-rank motion-corrected cardiac MR fingerprinting. *Magn Reson Med.* (2022) 87:2757–74. doi: 10.1002/mrm.29171

frontiers | Frontiers in Cardiovascular Medicine

TYPE Original Research
PUBLISHED 29 September 2022
DOI 10.3389/fcvm.2022.917180

OPEN ACCESS

EDITED BY
Anthony G. Christodoulou,
Cedars-Sinai Medical Center,
United States

REVIEWED BY
Sen Ma,
Q Bio, Inc., United States
Aurelien Bustin,
INSERM Institut de Rythmologie et Modélisation Cardiaque (IHU-Liryc), France

*CORRESPONDENCE
Sebastian Weingärtner
S.Weingartner@tudelft.nl

SPECIALTY SECTION
This article was submitted to Cardiovascular Imaging, a section of the journal Frontiers in Cardiovascular Medicine

RECEIVED 10 April 2022
ACCEPTED 13 September 2022
PUBLISHED 29 September 2022

CITATION
Weingärtner S, Demirel Ö, Gama F, Pierce I, Treibel TA, Schulz-Menger J and Akçakaya M (2022) Cardiac phase-resolved late gadolinium enhancement imaging.
Front. Cardiovasc. Med. 9:917180.
doi: 10.3389/fcvm.2022.917180

Cardiac phase-resolved late gadolinium enhancement imaging

Sebastian Weingärtner[1]*, Ömer B. Demirel[2,3], Francisco Gama[4], Iain Pierce[4], Thomas A. Treibel[4,5], Jeanette Schulz-Menger[6,7] and Mehmet Akçakaya[2,3]

[1]Department of Imaging Physics, Delft University of Technology, Delft, Netherlands, [2]Department of Electrical and Computer Engineering, University of Minnesota, Minneapolis, MN, United States, [3]Center for Magnetic Resonance Research, University of Minnesota, Minneapolis, MN, United States, [4]Bart's Heart Centre, St. Bartholomew's Hospital, London, United Kingdom, [5]Institute of Cardiovascular Science, University College London, London, United Kingdom, [6]Working Group on Cardiovascular Magnetic Resonance Imaging, Experimental and Clinical Research Center, Joint Cooperation of the Max-Delbrück-Centrum and Charite-Medical University Berlin, Berlin, Germany, [7]Department of Cardiology and Nephrology, HELIOS Klinikum Berlin-Buch and DZHK, Berlin, Germany

Late gadolinium enhancement (LGE) with cardiac magnetic resonance (CMR) imaging is the clinical reference for assessment of myocardial scar and focal fibrosis. However, current LGE techniques are confined to imaging of a single cardiac phase, which hampers assessment of scar motility and does not allow cross-comparison between multiple phases. In this work, we investigate a three step approach to obtain cardiac phase-resolved LGE images: (1) Acquisition of cardiac phase-resolved imaging data with varying $\mathbf{T_1}$ weighting. (2) Generation of semi-quantitative $\mathbf{T_1^*}$ maps for each cardiac phase. (3) Synthetization of LGE contrast to obtain functional LGE images. The proposed method is evaluated in phantom imaging, six healthy subjects at 3T and 20 patients at 1.5T. Phantom imaging at 3T demonstrates consistent contrast throughout the cardiac cycle with a coefficient of variation of 2.55 ± 0.42%. *In-vivo* results show reliable LGE contrast with thorough suppression of the myocardial tissue is healthy subjects. The contrast between blood and myocardium showed moderate variation throughout the cardiac cycle in healthy subjects (coefficient of variation 18.2 ± 3.51%). Images were acquired at 40–60 ms and 80 ms temporal resolution, at 3T and 1.5, respectively. Functional LGE images acquired in patients with myocardial scar visualized scar tissue throughout the cardiac cycle, albeit at noticeably lower imaging resolution and noise resilience than the reference technique. The proposed technique bears the promise of integrating the advantages of phase-resolved CMR with LGE imaging, but further improvements in the acquisition quality are warranted for clinical use.

KEYWORDS

cardiac magnetic resonance (CMR), T1 mapping, LGE imaging, myocardial tissue characterization, magnetic resonance imaging, MRI sequence development

1. Introduction

Late gadolinium enhancement (LGE) is the clinical gold standard for assessment of myocardial viability (1, 2) forming an integral part of clinical work up for a wide range of ischemic and non-ischemic cardiomyopathies (3). LGE imaging enables the depiction of myocardial scar by visualizing the retention of a gadolinium based contrast agent. Imaging is performed 10-to-20 min after contrast injection and data is typically acquired during the diastolic quiescence to minimize motion artifacts. In LGE imaging, an inversion recovery sequence is used, where the inversion time is selected to null the signal from the healthy myocardium. This facilitates high contrast of scar tissue as hyper-enhancement against a dark background.

In addition to LGE imaging, most routine clinical cardiac MRI protocols comprise the acquisition of CINE MRI (4, 5). In these scans, data is sampled throughout the cardiac cycle and either prospectively or retrospectively binned into different cardiac phases (6). This allows for reconstruction of phase-resolved images throughout the cardiac cycle. Thus, cine images enable the detailed depiction of cardiac motion, allowing for the quantification of functional parameters and visual assessment of wall motion abnormalities (7).

Thus, LGE and CINE imaging acquisitions differ in terms of their timing and contrast requirements. While CINE imaging is acquired through the cardiac cycle with a steady-state contrast, LGE imaging aims for a particular inversion contrast which is typically specified to coincide with an imaging window in diastole. Nonetheless, acquisition of LGE images at cardiac phases other than end-diastole has proven to be advantageous under certain conditions, as it offers the potential to more clearly depict concealed scar tissue (8, 9). However, due to the use of inversion recovery in traditional LGE imaging, scans are restricted to a single cardiac phase to provide the desired imaging contrast. This inherent limitation prevents joint evaluation of scar and wall motion with traditional LGE sequences. Thus, even though CINE and LGE imaging are the cornerstones of CMR and routinely evaluated alongside each other (3), separate scans are required to comprehensively characterize the myocardium. This not only leads to long scan protocols but also impedes evaluation: Information needs to be fused from separate scans in order to evaluate functional and viability information together. Obtaining phase-resolved LGE images on the other hand has been a long standing aim in cardiac MRI (10, 11) as it may allow for joint evaluation of wall motion abnormalities and viability in a single scan. However, the need for consistent LGE contrast throughout the cardiac cycle has prevented its implementation so far.

Myocardial T_1 mapping was introduced as an alternative for myocardial tissue characterization (12, 13). While sensitivity to ischemic scar remains a subject of ongoing debate (14), native T_1 mapping was demonstrated to provide clinical value in numerous cardiomyopathies (15). Advanced sequence developments have most recently enabled the quantification of myocardial T_1 throughout the cardiac cycle (16–19). Multiple methods have been proposed, including Temporally resolved parametric assessment of Z-magnetization recovery (TOPAZ) (16), phase-resolved cardiac magnetic resonance fingerprinting (MRF) (17, 19), cardiac magnetic resonance multi-tasking (20), and multi-contrast CINE MRI (18). Furthermore, utility of quantitative or semi-quantitative T_1 relaxation information to synthesize LGE imaging contrast has also been explored, showing that synthetic LGE can circumvent the sensitivity to a predefined inversion time that may lead to residual myocardial signal and hamper identification of scar (21–24).

The aim of this study is to integrate these recent developments and enable cardiac phase-resolved LGE imaging with consistent contrast throughout the cardiac cycle. Three steps are proposed to provide phase-resolved viability information in a single scan: First, multiple images with different T_1 weighting are acquired for each cardiac phase, extending on our previously developed TOPAZ technique. Second, semi-quantitative phase-resolved T_1 maps are obtained from this multi-contrast CINE data. Finally, images with the desired LGE imaging contrast are retrospectively synthesized for each cardiac phase, in such a way that the scar is depicted as hyper-enhancement against a dark background of healthy myocardium. Phantom measurements are performed to validate the technique, and image quality is tested in several healthy volunteers and patients at 3T and 1.5T, respectively.

2. Materials and methods

2.1. Sequence

Figure 1 depicts the sequence diagram of the proposed acquisition scheme, which builds on our recently developed TOPAZ technique (16). In the proposed sequence, the following steps are implemented: (1) The magnetization is driven to pulsed steady-state with continuous FLASH acquisitions. (2) Magnetization inversion is performed. (3) FLASH images are acquired continuously throughout the inversion recovery until pulsed steady-state is re-reached. The magnetization inversion and the imaging readout are prospectively triggered to the R-wave of the ECG to obtain Look-Locker experiments. Low imaging flip angles are used to ensure that the recovery to the steady-state spans two heart beats. In turn, this leads to two points on the inversion curve, separated by an R-R interval, for each inversion pulse. The same Look-Locker experiment is then repeated multiple times, to fill the acquisition k-spaces of all cardiac phases. To ensure an uninterrupted pulsed recovery curve, dummy pulses with no associated imaging readout are performed after the acquisition window. The dummy pulses are played until the R-wave is detected, to ensure there is no gap in pulses before the acquisition window. In the presence of R-R

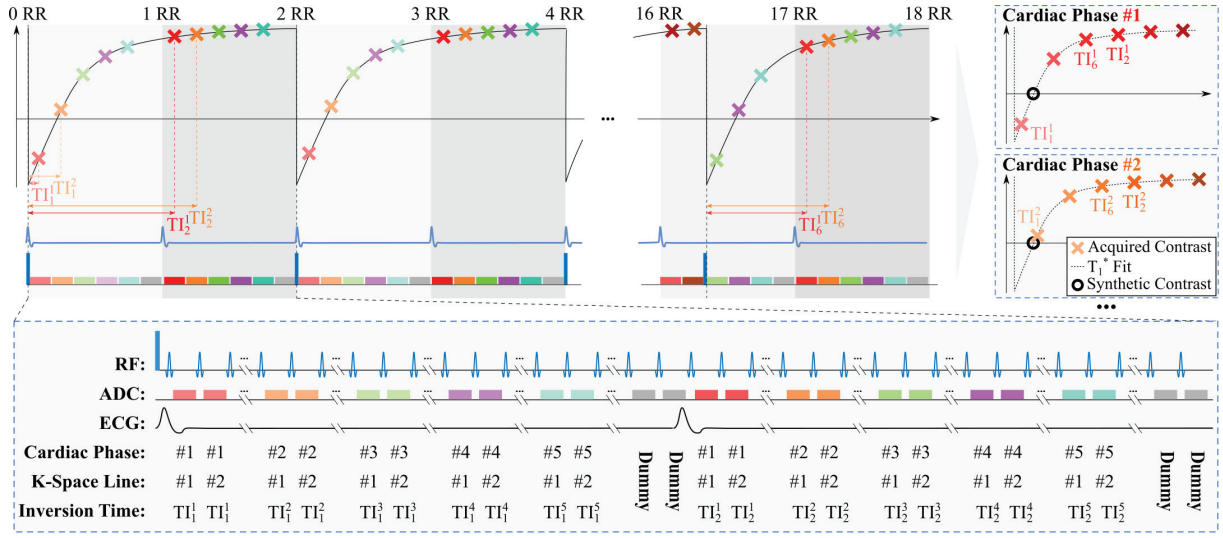

FIGURE 1
Sequence diagram of the proposed functional LGE sequence. Prior to the inversion pulses shown, magnetization is driven to pulsed steady-state *via* repeated FLASH pulses. Subsequently, an adiabatic pulse is performed to invert the magnetization. Then, contiguous FLASH imaging pulses are played to read out the magnetization during its re-recovery to the pulsed-steady state. The acquisition is segmented, thus, multiple inversion pulses are required to fill the k-space for each cardiac phase. In order to ensure a dense sampling of the inversion recovery curve for each cardiac phase, the Look-Locker experiment is then repeated multiple times with varying inversion pulse offset with respect to the R-wave. As the recovery to the pulsed-steady state spans across two RR-intervals, for each cardiac phase i two inversion times TI_j^i are acquired per inversion pulse offset. Thus, a total of $1 \leq j \leq 6$ inversion times, are acquired per cardiac phase for three inversion pulse offsets. Due to the limited number of inversion pulse offsets, a different sampling of the inversion recovery curve is realized for each cardiac phase, as indicated in the top right panels. Following the acquisition, a semi-quantitative inversion recovery model is fit on these multiple inversion points per cardiac phase to synthesize LGE contrast with suppression of the healthy myocardial tissue.

variability, this leads to a variable number of dummy pulses. This way no deviation from the pulsed recovery model occurs and the magnetization is consistently driven to a pulsed steady state, even in the presence of variable R-R durations. The acquisition window, i.e., the time window during an R-R interval in which the prospective data acquisition is performed, is specified to a fixed duration when planning the sequence. Typically the acquisition window duration was chosen around 90% of the R-R interval. (4) The overall experiment is further repeated multiple times while varying the position of the inversion pulse relative to the R-wave. Changing this inversion pulse offset, i.e., the time period between the detection of the R-wave and the application of the inversion pulse, leads to a different time between any given cardiac phase and the preceding inversion pulse. Thus, it enables the acquisition of multiple points on the inversion recovery curve. In the proposed sequence three inversion pulse offsets are acquired. Sampling the inversion recovery curve for each cardiac phase, in turn, allows for semi-quantitative assessment of the longitudinal recovery time and generating synthetic LGE images, as explained below.

For accurate T_1 mapping in the TOPAZ sequence, a three-parameter fit model had to be used to correct for B_1^+-dependent attenuation during the Look-Locker readout. However, in the proposed functional LGE imaging technique, absolute quantification of T_1 or an accurate estimation of B_1^+ are not required, to achieve qualitative LGE contrast after synthetization. Thus, a two-parameter fit model can be employed under the assumption of complete magnetization inversion:

$$S(T_I) = A\left(1 - 2e^{-\frac{T_I}{T_1^*}}\right), \quad (1)$$

where $S(T_I)$ is the voxel intensity at inversion time T_I, and A and T_1^* are model fit parameters, with the latter denoting the apparent T_1 time. Fitting has been performed in a custom tool implemented in C using a Levenberg-Marquardt algorithm from the levmar toolbox for non-linear least-squares fits (25).

Following the fitting procedure, the synthetic LGE image is then generated by applying the following equation voxel-by-voxel:

$$S_{syn}(T_{syn}) = A\left(1 - 2e^{-\frac{T_{syn}}{T_1^*}}\right), \quad (2)$$

where S_{syn} is the synthesized signal, and A and T_1^* are the parameters as obtained from the voxel-wise model fit in Equation (1). T_{syn} is the synthetic inversion time that is retrospectively chosen to null the signal of the healthy myocardium. A single virtual inversion time is used for all cardiac phases in order to provide consistent LGE contrast and enable cross comparison among the phases.

TABLE 1 Sequence parameters of the proposed functional LGE sequence at 1.5T and 3T.

	Functional LGE		Conventional LGE	
	1.5T	3T	1.5T	3T
Sequence type	FLASH	FLASH	FLASH	bSSFP
TE (ms)	3.2	2.6	4.9	1.1
TR (ms)	6.7	5.0	10.0	2.6–2.8
Flip angle	6°	3°	30°	50°
GRAPPA	2	2	1	2
Partial fourier	6/8	6/8	1	1
Averages	1	1	1	8
In-plane resolution (mm^2)	2.1 × 2.1	1.9 × 1.9	2.1 × 2.1	1.6 × 1.6
Slice thickness (mm)	10.0	10.0	10	8.0
Temporal resolution (ms)	80	40–60	N/A	N/A
Number of inversion times	6	6	1	1
Field of view (mm^2)	225 × 300	225 × 300	300 × 300	270 × 360
Number of heart beats	18	18	12	16
Breath-hold duration (s)	15–18	17–19	10–12	14–16
Time between inversion pulses (heart beats)	2	2	2 (PSIR)	2 (PSIR)

N/A indicates not applicable.

2.2. Simulations

Numerical simulations have been performed to assess the noise resilience at different cardiac phases acquired with the proposed method. Noisy Bloch simulations were performed with a simulated heart rate of 60 bpm. The post-contrast myocardial T_1 time was simulated between 350 and 650 ms. The remaining sequence parameters were chosen to match the phantom and *in vivo* experiments at 3T (Table 1). The noise level was chosen to simulate a baseline SNR of 20 and N = 1,000 repetitions were performed. The coefficient of variability was assessed as the standard deviation of the obtained, apparent T_1^* over its mean.

2.3. Phantom experiments

Phantom experiments were conducted on a 3T Siemens Magnetom Prisma (Siemens Healthcare, Erlangen, Germany) scanner. Imaging was performed with a 30-channel receiver array. The imaging parameters for the functional LGE sequence are listed in Table 1. As previously proposed for TOPAZ (16), flip-angle and TR were chosen using numerical optimizations to obtain an ideal trade-off between signal strength and relaxation rate of the pulsed recovery curve. Two sets of phantom experiments were performed, to study the CNR across the cardiac cycle, and to investigate the effect of different heart rates, respectively.

For the first set of phantom experiments two spheres filled with Gadolinium-doped agarose gel were used. The spheres were constructed to be approximately representative of post-contrast T_1 times in the blood pool and the healthy myocardium [T_1 = 489 ms, 910 ms, respectively, (26)]. The synthetic inversion time was set to T_{syn} = 567 ms in order to null the signal in the sphere representative of the myocardium. Imaging was performed with a simulated ECG at 60 bpm. Ten repetitions of the functional LGE sequence were acquired in the phantom setting. The contrast-to-noise ratio (CNR) was assessed between manually drawn ROIs in the two spheres. Due to the non-linear processing, noise was defined as pixel wise variability across the ten repetitions. The contrast homogeneity was quantified by analyzing the coefficient of variance (CoV) of the CNR throughout the simulated cardiac cycle.

In the second set of experiments, a bottle phantom was imaged at various simulated heart rates. T_{syn} was chosen to null the compartment with the longer T_1 time. Heart rates between 50 and 90 bpm were simulated and five repetitions were acquired for each heart rate. The signal in the other phantom compartment was compared across the different heart rates.

2.4. *In-vivo* experiments

The imaging protocols were approved by the respective local institutional review boards. Written informed consent was obtained from each subject prior to examination.

Three *in vivo* cohorts have been scanned in this study. First, six healthy subjects (4 male, 2 female, 40 ± 19 years old) have been scanned at 3T (Magnetom Prisma, Siemens Healthineers, Erlangen, Germany). Second, 20 patients (13 male, 7 female, 50 ± 16 years old) were imaged on a 1.5T scanner (Avanto Fit, Siemens Healthineers, Erlangen, Germany). In this

cohort patients with suspected or confirmed coronary artery disease who were scheduled to be scanned on one of the three selected scan days have been included. Finally, four patients (1 male, 4 female, 66 ± 7 years old) have been scanned at 3T (Magnetom Prisma, Siemens Healthineers, Erlangen, Germany). Two of those patients have been referred to CMR for potential myocarditis, one for evaluation of coronary artery disease, and one for follow-up of dilated cardiomyopathy.

The differences in scanner hardware, field strength and consequently different required adoption of the imaging parameters. The full set of imaging parameters is provided in Table 1. Additionally, phase-sensitive inversion recovery (27) LGE imaging was performed as reference. The corresponding sequence parameters can be found in Table 1. All LGE imaging was performed 10–20 min after injection of 0.2 mmol/kg gadobutrol (Gadovist, Bayer, Leverkusen, Germany) or 0.1 mmol/kg gadoterate meglumine (Dotarem, Guerbet, Villepinte, France) contrast agent.

Contrast was quantitatively analyzed in all healthy subjects. ROIs were manually drawn in the septum and the left-ventricular blood-pool. Apparent *in-vivo* CNR was defined as follows:

$$\mathrm{aCNR} = \frac{\left|\mu_{Myo} - \mu_{Blood}\right|}{\sqrt{\left(\sigma^2_{Myo} + \sigma^2_{Blood}\right)/2}}, \qquad (3)$$

where μ_{Myo}, μ_{Blood} describe the average signal in the ROI drawn in the myocardium and the blood pool, respectively. σ_{Myo} and σ_{Blood} describe the spatial standard deviation across the ROIs.

In healthy subjects ROIs were drawn for all cardiac phases individually. As the temporal resolution was fixed, a different number of acquisition cardiac phases is acquired for different heart rates. In order to compare the aCNR for subjects with different heart rates, the acquired number of cardiac phases (10–18) was interpolated to 20 reconstruction phases, using linear interpolation. The CoV of the aCNR was assessed throughout the cardiac cycle as a measure of contrast homogeneity.

In the patient cohorts, ROIs were drawn for one diastolic and one systolic phase. The aCNR was then quantitatively compared among the cohorts for both phases. ANOVA was performed to find statistical differences among the aCNR of the groups, and $p < 0.05$ was considered significant.

3. Results

3.1. Simulations

The results of the numerical simulations are displayed in Supplementary Figure 1. A marked difference in noise resilience is observed across the cardiac cycle. Cardiac phases with minimal TIs close to the nulling point of the simulated T_1, suffer from the most noise variability. Additionally, increasing simulated T_1 times, leads to an overall increase in noise susceptibility, as observed in the coefficient of variability.

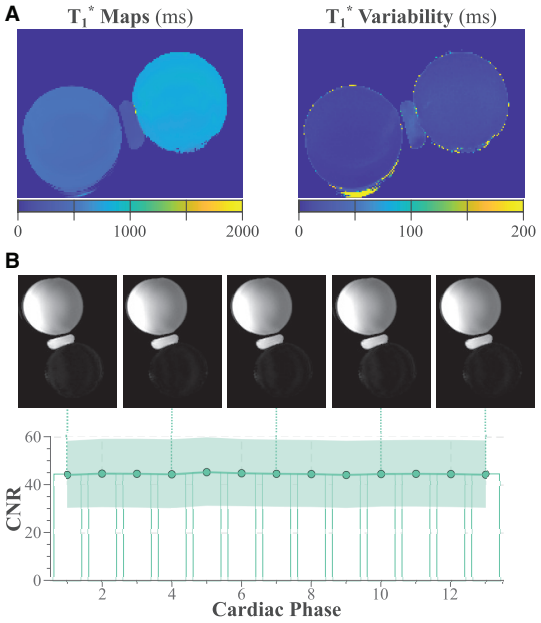

FIGURE 2
(A) T_1^* acquired in phantom with the proposed functional LGE sequence. The left panel shows the maps averaged across the simulated cardiac cycle, while the right panel displays the variability throughout the cardiac cycle. **(B)** Phantom functional LGE images with the synthetic inversion time chosen to null the myocardial (lower) sphere. The contrast to noise ratio between the two spheres is plotted throughout the simulated cardiac cycle. Shading indicates the spatial variability across the manually drawn ROIs.

3.2. Phantom experiments

Semi-quantitative T_1^* maps acquired with the proposed functional LGE sequence are displayed in Figure 2A. The maps display the average and variability of the T_1^* time throughout the cardiac cycle. The CoV of the T_1^* time was 1.31 ± 0.19 and 1.89 ± 0.23% for the blood and the myocardial sphere, respectively. Figure 2B shows functional LGE images acquired in the phantom throughout the simulated cardiac cycle. The images depict thorough nulling of the myocardial sphere. The CNR is largely constant throughout the simulated cardiac cycle, resulting in a CoV of 2.55 ± 0.42%.

Additionally, only minor variation of the functional LGE signal was observed for different heart rates (Supplementary Figure 2). The CoV of the signal when varying the simulated heart rate from 50 to 90 bpm, was 2.03 ± 0.81%, with no significant trend ($R^2 = 0.0013, p = 0.865$).

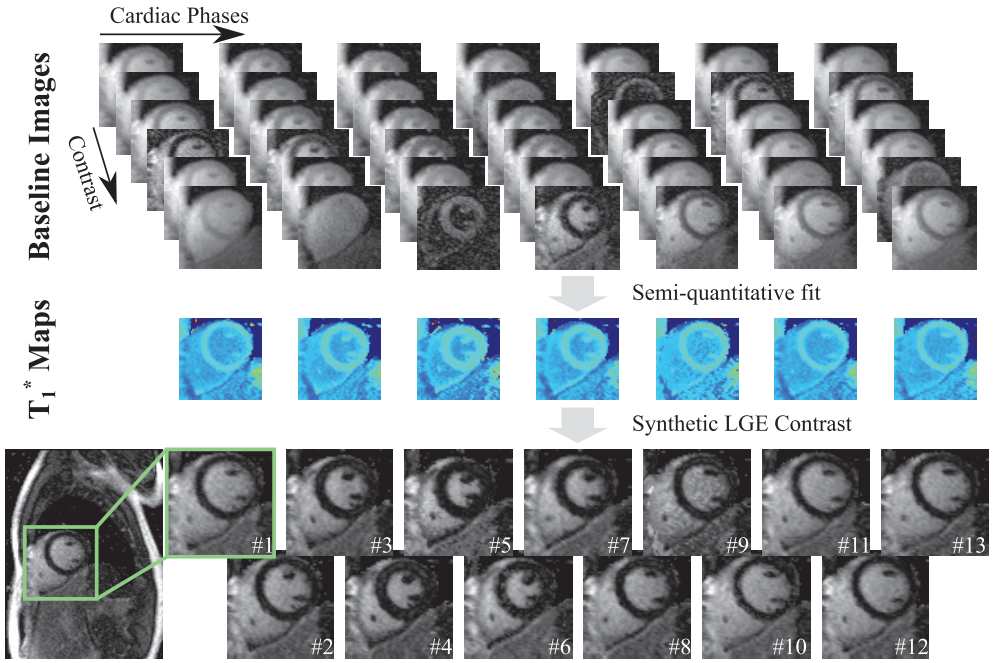

FIGURE 3
The post-processing pipeline for generating the proposed functional LGE images from the acquired T_1-weighted data. For each cardiac phase, the proposed sequence acquires multiple images with different T_1 weighting, denoted as Baseline Images. A two-parameter fit is performed on these images to obtain semi-quantitative T_1^* maps for each cardiac phase. Finally, a virtual inversion time is retrospectively chosen to synthesize functional LGE images for all cardiac phases.

3.3. *In-vivo* experiments

Figure 3 depicts an example of the processing pipeline used to obtain functional LGE images in a healthy subject scanned at 3T and 40 ms temporal resolution. Six baseline images with different T_1 weighting are acquired for each cardiac cycle and used to generate the apparent T_1^* maps. The T_1^* maps depict visually high image quality with homogeneous T_1^* times throughout the myocardium and across cardiac cycles. Accordingly, the resulting synthetic functional LGE images depict thorough suppression of the healthy myocardial signal at each phase of the cardiac cycle. Furthermore, clear delineation with respect to the blood pool is visually apparent.

Figure 4 depicts further examples acquired in two healthy subjects at 3T. Consistent nulling of the myocardium is obtained in both healthy subjects. Furthermore, homogeneous contrast with clear depiction of the blood-myocardium contrast is visible throughout the entire cardiac cycle (Supplementary Video 1). Quantitative analysis of the aCNR between the myocardium and the blood pool is depicted in Figure 4C. Moderate variation of the aCNR across the cardiac cycle was observed, amounting to a CoV of 18.2 ± 3.51%.

Patient images obtained at 1.5T are shown in Figure 5. Both of these patients were LGE negative. Although the myocardial signal is visually suppressed in all cardiac phases, noise variability appears visually higher in some cardiac phases (e.g., phase 3 for both patients). A cinematographic view of all cardiac phases can be found in Supplementary Video 2.

Figure 6A shows images acquired in a patient with a history of myocarditis and CAD. Antero-lateral scar is visible in the LGE reference scan. The scar is also visually apparent in all phases acquired with the proposed method. Better resolution of the scar structure is achieved with the reference method, and the reference scan appears markedly less noisy. Two cardiac phases (3 and 6) present patch-like artifacts in the blood pools, as a result of the contrast synthetization. Scar motility and contrast throughout the cardiac cycle can be visualized using a cinematographic view of the cardiac phases, as shown in Supplementary Video 3.

Figure 6B depicts a second CAD patient imaged at 1.5T with 80 ms temporal resolution. Both conventional and the proposed functional LGE methods display scar in the lateral segment. Scar tissue can be visually discerned in all cardiac phases of the functional LGE scan. Thus, scar motility is captured and the displacement can be tracked throughout the heart-beat (Supplementary Video 3). However, a noticeably higher level of imaging noise is observed compared with the clinical reference LGE scan. Furthermore, the noise level appears visually exacerbated in later cardiac phases.

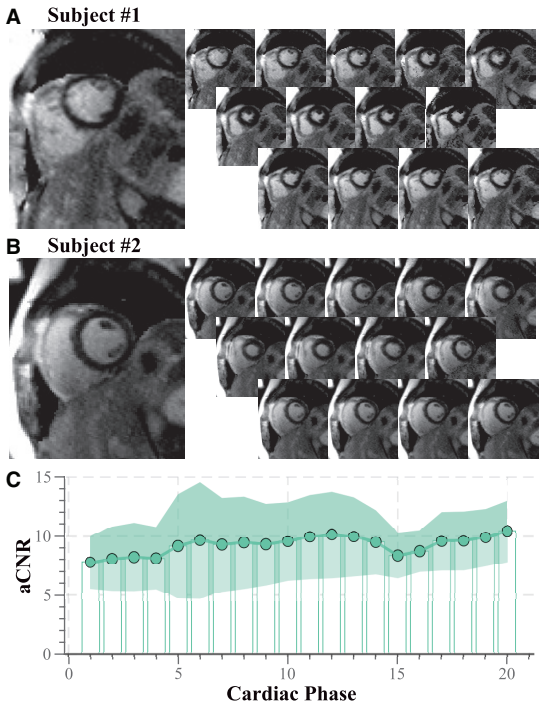

FIGURE 4
Representative functional LGE images acquired in healthy volunteers at 3T. **(A)** Subject #1 with heart rate 57 bpm, number of acquisition phases 13, **(B)** subject #2 heart rate 57 bpm, number of acquisition phases 13. Thorough suppression of the healthy myocardial tissue with sharp delineation against the blood pools is visible for both subjects. **(C)** Quantitative analysis of aCNR throughout the cardiac cycle across the six healthy volunteers. Moderate variation of the aCNR is obtained across the cardiac phases.

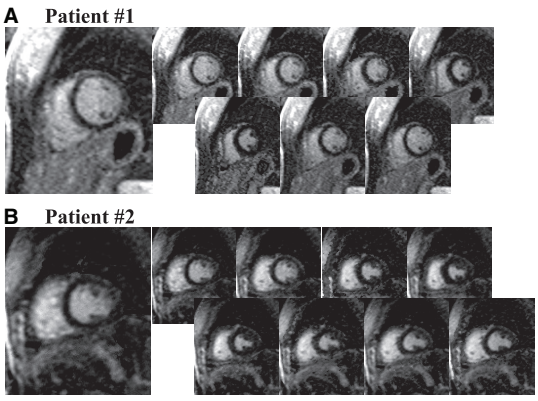

FIGURE 5
Functional LGE images acquired in LGE negative patients at 1.5T with 80 ms temporal resolution. Compared with 3T visually increased noise is depicted in the 1.5T images due to reduced baseline SNR at this lower field strength, and later acquisition time after contrast injection. While, consistent nulling of the myocardium is achieved and the blood-pools remain clearly depicted. **(A)** Seven cardiac phases were obtained in this patient with a heart rate of 73 bpm. **(B)** Eight cardiac phases were acquired in this subject with 77 bpm heart rate.

Figure 7 shows images acquired in two patients 3T with 60 ms temporal resolution. In the first subject (Figure 7A) lateral scar is visually apparent in functional LGE images. However, the scar depiction in the high-resolution reference scan is visually superior and the structure of the scar tissue can be better delineated. Additionally, the functional LGE scan shows elevated noise variability in some cardiac phases (6 and 11). A two chamber view in the second patient (Figure 7A) reveals a subendocardial scar, which is not easily discerned from the blood pool. However, in systolic cardiac phases the scar tissue is well-separated spatially and in terms of contrast, aiding the identification in the functional LGE images.

Figure 8 depicts the quantitative comparison of the aCNR across the different cohorts. No significant difference was found for the diastolic phase among the different cohorts ($p = 0.90$). However, the patient cohorts suffer from substantially lower aCNR in the systolic phase, as compared with the healthy subject data ($p < 0.037$), suggesting larger variability in the aCNR throughout the cardiac cycle.

4. Discussion

In this study, we proposed a method for augmenting LGE imaging with a functional acquisition. Cardiac phase-resolved LGE images are obtained with consistent contrast throughout the cardiac cycle. In this study, we demonstrated the feasibility of obtaining cardiac phase-resolved images with LGE contrast. Semi-quantitative T_1^* maps were acquired in a cardiac phase-resolved manner. Subsequently, synthetic image generation was used to obtain the clinical LGE contrast that nulls the healthy myocardium for all cardiac phases. Phantom imaging showed consistent contrast with thorough nulling of the desired signal using the proposed method. Initial *in-vivo* results at 3T demonstrate promising image quality with a temporal resolution of up to 40 ms in healthy subjects. However, initial clinical data at both 1.5T and 3T shows substantially higher noise levels and reduced imaging resolution compared to clinical reference LGE images.

Noise susceptibility and imaging resolution remained a challenge in the clinical cohorts in this study. The drop in image quality in the patient cohort compared to healthy subjects was likely primarily driven by the much later acquisition time after contrast injection, as clinical reference LGE scans were always acquired first. Acquisitions late after contrast injection lead to longer post-contrast T_1 times, due to contrast washout. Our simulation results show that this leads to an overall increase in noise variability with the proposed technique. While imaging contrast was observed to be largely constant, noise susceptibility showed major variations throughout the cardiac cycle. Due to

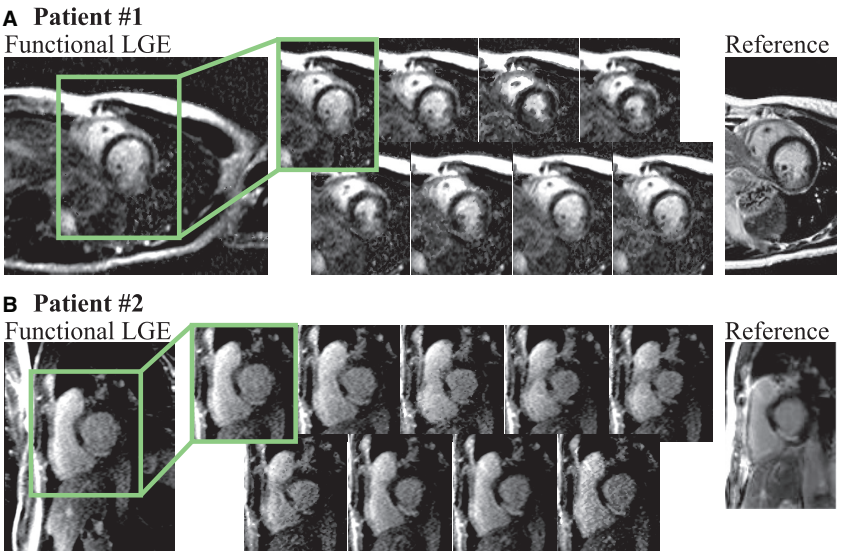

FIGURE 6
(A) Functional LGE images acquired in a 41 year old female patient with known history of CAD and myocarditis in comparison to a reference LGE acquisition (heart rate 80 bpm, acquisition phases 8). The patient displays a large antero-lateral scar that is visible with the proposed technique throughout all cardiac phases. Retrospective choice of the inversion time enables bright scar hyper-enhancement delineated against the remote myocardium. However, compared to the reference scan, decreased imaging resolution hampers depiction of the scar structure. **(B)** Functional LGE images acquired in a patient suffering from CAD and displaying scar in the lateral segment (heart rate 72 bpm, acquisition phases 9). Clear depiction of the scar tissue is achieved in all cardiac phases, albeit at higher noise levels compared with the clinical reference scan.

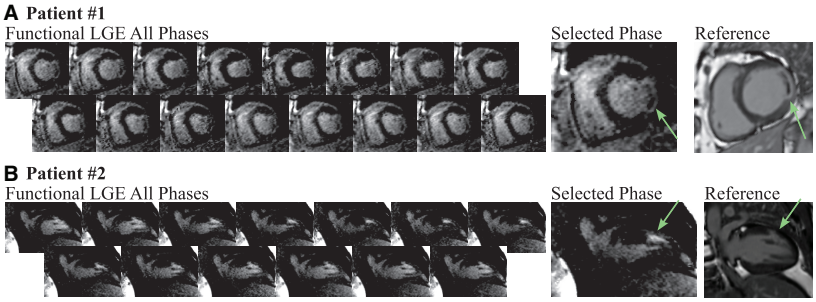

FIGURE 7
Functional LGE images acquired in two patients at 3T compared to high-resolution reference LGE images. **(A)** Lateral scar (green arrows) is observed in a 73 old woman (heart rate 57 bpm, acquisition phases 16), referred to CMR for evaluation of myocarditis and perfusion defects. The scar tissue is visible in all cardiac phases of the functional LGE scan acquired at 60 ms temporal resolution, albeit variations in the noise levels across the cardiac cycle can be observed. In comparison, the high-resolution reference LGE scan displays much better noise resilience and a finer depiction of the scar structure. **(B)** Two chamber acquisition in a 58 year-old man (heart rate 64 bpm, acquisition phases 13) referred to CMR for evaluation of coronary artery disease. The subendocardial scar (green arrows) can be seen in both the reference and the functional LGE images. Systolic phases of the latter visualize spatially and contrast the separation of the scar tissue from the nearby blood pool.

the sequence design, each cardiac phase realizes a different sampling of the inversion recovery curve. Simulation results show that cardiac phases, where the minimal TI is close to the null point of the inversion recovery curve, lead to the highest noise variability. Accordingly, in the patient cohorts, cardiac phases where the first point on the inversion recovery curve is relatively late, appear visually most susceptible to noise. In the present method, the signal polarity is restored prior to fitting using the approach proposed by Messroghli et al. (12). However, it has been previously reported that this can lead to additional noise variability if an inversion time near the zero crossing of the inversion recovery curve is sampled (28). Accordingly, due to inadvertent sampling of the inversion recovery curve, salt-and-pepper-like noise and patchy appearance can be observed in these phases. Using the signal phase to restore the polarity has been proposed as a way to mitigate those sampling-related artifacts. Incorporating this method into the proposed technique bears promise to

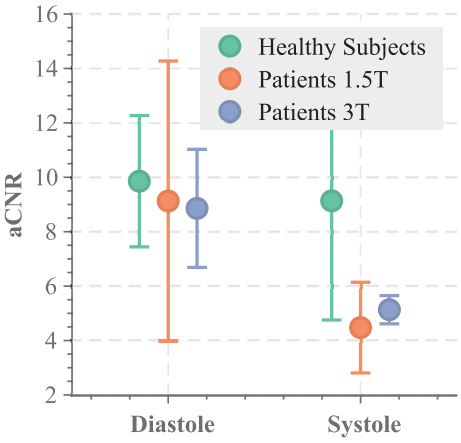

FIGURE 8
aCNR across the different cohorts, analyzed for a diastolic and systolic phase of the functional LGE scans.

enable more homogeneous noise resilience across the cardiac cycle and warrants further investigation. While the image quality can still be sufficient to track large areas of hyper-enhancement throughout the cardiac cycle, improvements in the trade-off between spatiotemporal resolution and noise resilience and needed to match reference LGE image quality. An increasing number of methods have emerged that also enable cardiac phase-resolved T_1 mapping, including methods based on cardiac MRF (29) and cardiac multi-tasking (20). These methods attain better baseline map quality by means of regularized or model-based reconstructions. Similarly, regularization approaches have recently been demonstrated to substantially improve noise resilience in TOPAZ (30, 31). Thus, future work is warranted that integrates regularized reconstruction schemes, as proposed for TOPAZ or other phase resolved cardiac T_1 mapping techniques, to enhance noise resilience and spatiotemporal resolution.

Functional LGE imaging has the premise of depicting scar at multiple cardiac phases. Thus, the images allow for cross-comparison of scar signal throughout the cardiac cycle. This may increase diagnostic certainty if ambiguous enhancement is observed, for example in the vicinity of the left-ventricular blood pool or close to fatty tissue. Furthermore, the proposed functional LGE imaging sequence achieved substantially higher temporal resolution than conventional LGE imaging. In standard clinical LGE imaging, diastolic triggering is used, requiring careful manual timing to place the acquisition window (~100–250 ms) into the diastolic quiescence. This temporal resolution might not be ideal when highly mobile structures, such as the papillary muscles, are to be assessed (32). Functional LGE imaging can potentially improve upon these points as a temporal resolution as low as 40–80 ms was achieved. Additionally, since synthetic LGE images are available throughout the cardiac cycle, potentially detrimental imaging artifacts due to incorrect placement of the acquisition window are eliminated. Instead phase-resolved imaging ensures that LGE images are provided at the desired cardiac phase with no need for manual timing. However, additional improvements in image quality may be required to fully replace the reference LGE scan at least at 1.5T.

The most recent recommendations for clinical CMR include CINE MRI of the left ventricle and LGE for almost all ischemic and non-ischemic cardiomyopathies (5). More specifically, when revascularization is considered, for example, only the joint evaluation of cardiac function and viability is considered to offer sufficient information for clinical decision making (3). Together, LGE imaging and CINE MRI, enable the assessment of functional impairment of the scar region and potential links to any wall motion abnormalities. However, as these scans are commonly acquired with two separate sequences, cross evaluation can only be performed subjectively. This hampers the fusion of data and complicates the reading of images. Cardiac phase-resolved LGE images on the other hand, inherently allow for joint assessment of myocardial function and viability in scar and surrounding tissue. Furthermore, previous studies have indicated value of obtaining viability information in parts of the cardiac cycle other than diastole (22, 24, 33). Specifically, it has been shown that this may ease the assessment of scar transmurality (21). Thus, depiction in multiple cardiac phases as achieved with the proposed method bears promise for improved clinical certainty in assessing myocardial scar and warrants further investigation for its prognostic value in the clinical setting. This, however, was beyond the scope of the current work.

Apparent CNR in functional LGE images between myocardium and blood pool was found to be moderately variable throughout the cardiac cycle. This is in-line with previous reports indicating differences in T_1 times at different the cardiac phases (33, 34) and might be explained with differences in the blood-myocardium volume fraction. Due to the non-linear processing of the functional LGE images, noise variability cannot be obtained from background intensity, but was instead defined as the spatial standard deviation within the regions of interest. Thus, variability of physiological and system parameters within the ROI will compromise the reported aCNR values. While the reported aCNR is useful as a metric to compare contrast throughout the cardiac cycle, it should be noted that this hampers comparability of the reported aCNR to literature values of CNR.

The phase-resolved images in this study were acquired with prospective ECG triggering. Prospective and retrospective triggering has a different spectrum of advantages and disadvantages for cardiac phase-resolved imaging. Prospectively triggered image acquisitions have been recognized to be resilient against variabilities in the RR interval, as the duration of the systolic phase commonly remains relatively constant (35). On the other hand, a prospectively defined acquisition window is

commonly defined to only cover 80–90% of the cardiac cycle. Thus, the end-diastolic phase may be partially missed, and peak diastolic filling may be underestimated. For those reasons retrospective CINE is commonly preferred for quantification of cardiac function and is most commonly used in clinical practice (5). An increasing number of techniques enabling cardiac phase-resolved quantification of the longitudinal relaxation time have recently been proposed (20). Those methods can be used in combination with retrospective cardiac gating, and may therefore warrant investigation in combination with the proposed approach if the extraction of quantitative cardiac function is desired.

Imaging in this study was performed in a single mid-ventricular slice only. Thus, the functional LGE images obtained in this study have not been evaluated for cardiac volumetry. However, at 3T a temporal resolution up to 40 ms was obtained. This is comparable to the temporal resolution used for 2D CINE MRI in clinical routine (5, 36). At this temporal resolution blurring due to cardiac motion is considered to be minimal (37–39), making CINE MRI suitable for accurate assessment of cardiac function. Hence, functional LGE images may be suitable for quantification of cardiac function, albeit being subject to the specific drawbacks of prospectively triggered CINE with the current sequence implementation, as reported for certain patient groups (40). Alternatively, retrospective ECG gating can be employed in the present sequence design. However, the inversion pulse timing would need to be adapted in real time to ensure the desired semi-quantitative imaging information. Thus, further improvements to tailor the proposed approach for functional volumetry remain a subject of future work.

The proposed method synthesizes LGE contrast based on a range of different inversion contrasts for each cardiac phase. The fusion of multiple data points potentially makes this approach susceptible to residual motion, for example, due to incomplete breath-holds. While this has not been observed to be an issue in the present data set, this issue may be exacerbated in some clinical cohorts. Other previously proposed cardiac phase-resolved T_1 mapping techniques have been proposed as a free-breathing acquisition based on self-gating signals (17, 18, 20). A similar approach could be employed in this sequence to mitigate the need for long breath-holds, avoid susceptibility to incomplete breath-holds, and enable increased sequence durations. Additionally, a range of motion correction techniques has been proposed and successfully applied to quantitative cardiac MRI (41–43). Using these techniques in the proposed method on a phase-by-phase basis to alleviate residual motion, warrants further investigation.

The proposed functional LGE method relies on selection of a synthetic inversion time to achieve LGE imaging contrast. In this study, the remote myocardium that needed to be nulled was visually identified, from which the synthetic inversion time was generated. Recent advances in machine learning have enabled improved tools for automatic identification of such tissues. Specifically for cardiac MRI, numerous methods have been developed to achieve highly accurate segmentation of the cardiac anatomy (44–47). Such methods can be used to automatically delineate the tissue that is to be nulled. Thus, future work will explore the integration of deep-learning based segmentation to enable automatic selection of the synthetic inversion time. This would facilitate LGE scanning without the need for manual timing selection, neither prospectively in the protocol nor retrospectively in the reconstruction.

Black-blood LGE imaging has recently been developed, based on a combination of T_1 and T_2 contrast sensitization (48, 49). The black-blood contrast bears promise for improved depiction of sub-endocardial scar neighboring the blood-pool (50). Combined methods for simultaneous quantification of myocardial T_1 and T_2 times have also been explored (17, 19, 51, 52). By exploiting phase-resolved T_1 and T_2 quantification the proposed method can potentially be extended for the generation of functional black-blood LGE images. This combination remains subject of future work.

The present study and the proposed functional LGE imaging method are subject to several limitations. In this study, only a small number of healthy volunteers was scanned at 3T and no comparison to healthy subjects at 1.5T has been performed, to minimize the use of gadolinium contrast agents in a healthy population. Furthermore, the method was evaluated in a general patient cohort, providing representative examples of feasibility and image quality as encountered in clinical use. However, more specific and larger patient cohorts with LGE need to be assessed in order to evaluate prognostic and diagnostic value of functional LGE as compared to conventional LGE and CINE imaging. In this study only a single mid-ventricular slice was acquired with proposed functional LGE method. Whole heart coverage requires repeated breath-holds, which hampers integration in the existing clinical workflow. Simultaneous-multi slice (SMS) imaging has recently been evaluated for improved spatial coverage in quantitative mapping of the heart (53–55). In functional LGE imaging SMS can facilitate improved coverage in fewer breath-holds for the benefit of easing clinical translation. Future studies will evaluate the use of SMS accelerated scans to obtain whole heart coverage in functional LGE imaging.

5. Conclusion

We have demonstrated the feasibility of generating functional LGE imaging with temporal resolution of up to 40 ms. The proposed functional LGE images allowed consistent contrast, nulling the healthy myocardium throughout the cardiac cycle, as well as clear delineation of the myocardium against the blood-pool in healthy subjects at 3T. Initial patient images demonstrate the feasibility of our functional LGE approach to visualize scar motility across multiple cardiac phases. However, spatial resolution and imaging

noise were markedly worse in the patient cohort, and further improvements are warranted to match reference LGE image quality. Nonetheless, the proposed technique bears the promise to offer additional insights by enabling a direct depiction of scar tissue motility.

Data availability statement

The raw data supporting the conclusions of this article will be made available by the authors, without undue reservation.

Ethics statement

The studies involving human participants were reviewed and approved by the Ethics Committees of the University of Minnesota, HELIOS Klinikum Berlin-Buch, and the Barts Heart Centre. The patients/participants provided their written informed consent to participate in this study.

Author contributions

SW and MA: study conception and design, analysis and interpretation of results, and draft manuscript preparation. SW: pulse sequence development. SW, ÖD, JS-M, FG, IP, and TT: data collection. All authors reviewed the results and approved the final version of the manuscript.

Funding

This work was supported in part by the 4TU federation, a NWO Start-up grant STU.019.024, ZonMW Off-Road 04510011910073, NIH R01HL153146, NIH R21EB028369, NIH P41EB027061, and NSF CAREER CCF-1651825. ÖD was partially supported by an AHA Predoctoral Fellowship. TT was funded by a BHF Intermediate Research Fellowship (FS/19/35/34374) and directly and indirectly supported by the UCLH NIHR Biomedical Research Centre and Biomedical Research Unit at UCLH and Barts, respectively.

Acknowledgments

The authors thank Bianca Linssen, Rick Voncken, and SCANNEXUS for their resources and support with the phantom experiment.

Conflict of interest

The authors declare that the research was conducted in the absence of any commercial or financial relationships that could be construed as a potential conflict of interest.

Publisher's note

All claims expressed in this article are solely those of the authors and do not necessarily represent those of their affiliated organizations, or those of the publisher, the editors and the reviewers. Any product that may be evaluated in this article, or claim that may be made by its manufacturer, is not guaranteed or endorsed by the publisher.

Supplementary material

The Supplementary Material for this article can be found online at: https://www.frontiersin.org/articles/10.3389/fcvm.2022.917180/full#supplementary-material

References

1. Kim RJ, Wu E, Rafael A, Chen EL, Parker MA, Simonetti O, et al. The use of contrast-enhanced magnetic resonance imaging to identify reversible myocardial dysfunction. *N Engl J Med*. (2000) 343:1445–53. doi: 10.1056/NEJM200011163432003

2. Kim Raymond J, Fieno David S, Parrish Todd B, Kathleen H, Enn-Ling C, Orlando S, et al. Relationship of MRI delayed contrast enhancement to irreversible injury, infarct age, and contractile function. *Circulation*. (1999) 100:1992–2002. doi: 10.1161/01.CIR.100.19.1992

3. Judd RM, Wagner A, Rehwald WG, Albert T, Kim RJ. Technology Insight: Assessment of myocardial viability by delayed-enhancement magnetic resonance imaging. *Nat Clin Pract Card*. (2005) 2:150. doi: 10.1038/ncpcardio0134

4. Kramer CM, Barkhausen J, Flamm SD, Kim RJ, Nagel E, for Cardiovascular Magnetic Resonance S, et al. Standardized cardiovascular magnetic resonance (CMR) protocols 2013 update. *J Cardiovasc Magn Reson*. (2013) 15:91. doi: 10.1186/1532-429X-15-91

5. Kramer CM, Barkhausen J, Bucciarelli-Ducci C, Flamm SD, Kim RJ, Nagel E. Standardized cardiovascular magnetic resonance imaging (CMR) protocols: 2020 update. *J Cardiovasc Magn Reson*. (2020) 22:17. doi: 10.1186/s12968-020-00607-1

6. Atkinson DJ, Edelman RR. Cineangiography of the heart in a single breath hold with a segmented turboFLASH sequence. *Radiology*. (1991) 178:357–360. doi: 10.1148/radiology.178.2.1987592

7. Patel MR, White RD, Abbara S, Bluemke DA, Herfkens RJ, Picard M, et al. 2013 ACCF/ACR/ASE/ASNC/SCCT/SCMR appropriate utilization of cardiovascular imaging in heart failure. *J Am Coll Cardiol*. (2013) 61:2207–31. doi: 10.1016/j.jacc.2013.02.005

8. Matsumoto H, Matsuda T, Miyamoto K, Shimada T, Hayashi A, Mikuri M, et al. Late gadolinium-enhanced cardiovascular MRI at end-systole: feasibility study. *Am J Roentgenol*. (2010) 195:1088–94. doi: 10.2214/AJR.09.3860

9. Schuster A, Chiribiri A, Ishida M, Morton G, Paul M, Hussain S, et al. End-systolic versus end-diastolic late gadolinium enhanced imaging for the

assessment of scar transmurality. *Int J Cardiovas Imaging*. (2012) 28:773–81. doi: 10.1007/s10554-011-9877-3

10. Connelly KA, Detsky JS, Graham JJ, Paul G, Vijayaragavan R, Dick AJ, et al. Multicontrast late gadolinium enhancement imaging enables viability and wall motion assessment in a single acquisition with reduced scan times. *J Magn Reson Imaging*. (2009) 30:771–7. doi: 10.1002/jmri.21907

11. Ferrari Victor A, Witschey Walter RT, Rong Z. Cardiac magnetic resonance assessment of myocardial fibrosis. *Circ-Cardiovasc Imaging*. (2011) 4:604–6. doi: 10.1161/CIRCIMAGING.111.969204

12. Messroghli DR, Radjenovic A, Kozerke S, Higgins DM, Sivananthan MU, Ridgway JP. Modified Look-Locker inversion recovery (MOLLI) for high-resolution T1 mapping of the heart. *Magn Reson Med*. (2004) 52:141–6. doi: 10.1002/mrm.20110

13. Kellman P, Hansen MS. T1-mapping in the heart: accuracy and precision. *J Cardiovasc Magn Reson*. (2014) 16:2. doi: 10.1186/1532-429X-16-2

14. Hamdy A, Kitagawa K, Ishida M, Sakuma H. Native myocardial T1 mapping, are we there yet? *Int Heart J*. (2016) 57:400–7. doi: 10.1536/ihj.16-169

15. Radenkovic D, Weingärtner S, Ricketts L, Moon JC, Captur G. T1 mapping in cardiac MRI. *Heart Fail Rev*. (2017) 22:415–30. doi: 10.1007/s10741-017-9627-2

16. Weingärtner S, Shenoy C, Rieger B, Schad LR, Schulz-Menger J, Akçakaya M. TempOrally-resolved parametric assessment of Z-magnetization recovery (TOPAZ): dynamic myocardial T1 mapping using a cine steady-state look-locker approach. *Magn Reson Med*. (2017) 79:2087–100. doi: 10.1002/mrm.26887

17. Jaubert O, Cruz G, Bustin A, Schneider T, Koken P, Doneva M, et al. Free-running cardiac magnetic resonance fingerprinting: Joint T1/T2 map and Cine imaging. *Magn Reson Imaging*. (2020) 68:173–82. doi: 10.1016/j.mri.2020.02.005

18. Becker KM, Schulz-Menger J, Schaeffter T, Kolbitsch C. Simultaneous high-resolution cardiac T1 mapping and cine imaging using model-based iterative image reconstruction. *Magn Reson Med*. (2019) 81:1080–91. doi: 10.1002/mrm.27474

19. Hamilton JI, Jiang Y, Eck B, Griswold M, Seiberlich N. Cardiac cine magnetic resonance fingerprinting for combined ejection fraction, T1 and T2 quantification. *NMR Biomed*. (2020) 33:e4323. doi: 10.1002/nbm.4323

20. Christodoulou AG, Shaw JL, Nguyen C, Yang Q, Xie Y, Wang N, et al. Magnetic resonance multitasking for motion-resolved quantitative cardiovascular imaging. *Nat Biomed Eng*. (2018) 2:215–26. doi: 10.1038/s41551-018-0217-y

21. Varga-Szemes A, van der Geest RJ, Spottiswoode BS, Suranyi P, Ruzsics B, De Cecco CN, et al. Myocardial late gadolinium enhancement: accuracy of T1 mapping-based synthetic inversion-recovery imaging. *Radiology*. (2016) 278:374–82. doi: 10.1148/radiol.2015150162

22. Varga-Szemes A, van der Geest RJ, Schoepf UJ, Spottiswoode BS, De Cecco CN, Muscogiuri G, et al. Effect of inversion time on the precision of myocardial late gadolinium enhancement quantification evaluated with synthetic inversion recovery MR imaging. *Eur Radiol*. (2017) 27:3235–43. doi: 10.1007/s00330-016-4665-z

23. Abdula G, Nickander J, Sörensson P, Lundin M, Kellman P, Sigfridsson A, et al. Synthetic late gadolinium enhancement cardiac magnetic resonance for diagnosing myocardial scar. *Scand Cardiovasc J*. (2018) 52:127–32. doi: 10.1080/14017431.2018.1449960

24. van Dijk R, Kuijpers D, Kaandorp TAM, van Dijkman PRM, Vliegenthart R, van der Harst P, et al. Accurate late gadolinium enhancement prediction by early T1-based quantitative synthetic mapping. *Eur Radiol*. (2018) 28:844–50. doi: 10.1007/s00330-017-5018-2

25. Lourakis MIA. *levmar: Levenberg-Marquardt Nonlinear Least Squares Algorithms in C/C++* (2004). Available online at: `http://www.ics.forth.gr/ lourakis/levmar/` (accessed January 31, 2005).

26. Weingärtner S, Meßner NM, Budjan J, Loänitzer D, Papavassiliu T, Zöllner FG, et al. Myocardial T1-mapping at 3T using saturation-recovery: reference values, precision and comparison with MOLLI. *J Cardiov Magn Reson*. (2016) 18:84. doi: 10.1186/s12968-016-0302-x

27. Kellman P, Arai AE, McVeigh ER, Aletras AH. Phase-sensitive inversion recovery for detecting myocardial infarction using gadolinium-delayed hyperenhancement†. *Magn Reson Med*. (2002) 47:372–83. doi: 10.1002/mrm.10051

28. Xue H, Greiser A, Zuehlsdorff S, Jolly MP, Guehring J, Arai AE, et al. Phase-sensitive inversion recovery for myocardial T1 mapping with motion correction and parametric fitting. *Magn Reson Med*. (2013) 69:1408–20. doi: 10.1002/mrm.24385

29. Hamilton JI, Jiang Y, Chen Y, Ma D, Lo WC, Griswold M, et al. MR fingerprinting for rapid quantification of myocardial T1, T2, and proton spin density. *Magn Reson Med*. (2017) 77:1446–58. doi: 10.1002/mrm.26216

30. Moeller S, Weingärtner S, Akçakaya M. Multi-scale locally low-rank noise reduction for high-resolution dynamic quantitative cardiac MRI. In: *Proc IEEE EMBC*. Jeju Island: IEEE (2017). p. 1473–1476. doi: 10.1109/EMBC.2017.8037113

31. Yaman B, Weingärtner S, Kargas N, Sidiropoulos ND, Akçakaya M. Low-rank tensor models for improved multidimensional MRI: application to dynamic cardiac T_1 mapping. *IEEE Trans Med Imaging*. (2020) 6:194–207. doi: 10.1109/TCI.2019.2940916

32. Ferreira PF, Gatehouse PD, Mohiaddin RH, Firmin DN. Cardiovascular magnetic resonance artefacts. *J Cardiovasc Magn Reson*. (2013) 15:41. doi: 10.1186/1532-429X-15-41

33. Reiter U, Reiter G, Dorr K, Greiser A, Maderthaner R, Fuchsjäger M. Normal diastolic and systolic myocardial T1 values at 1.5-T MR imaging: correlations and blood normalization. *Radiology*. (2014) 271:365–72. doi: 10.1148/radiol.13131225

34. Meßner NM, Budjan J, Loßnitzer D, Papavassiliu T, Schad LR, Weingärtner S, et al. Saturation-recovery myocardial T1-mapping during systole: accurate and robust quantification in the presence of arrhythmia. *Sci Rep*. (2018) 8:5251. doi: 10.1038/s41598-018-23506-z

35. Bluemke DA, Boxerman JL, Atalar E, McVeigh ER. Segmented K-space cine breath-hold cardiovascular MR imaging: Part 1. Principles and technique. *Am J Roentgenol*. (1997) 169:395–400. doi: 10.2214/ajr.169.2.9242742

36. Epstein FH. MRI of left ventricular function. *J Nucl Cardiol*. (2007) 14:729–44. doi: 10.1016/j.nuclcard.2007.07.006

37. Usman M, Ruijsink B, Nazir MS, Cruz G, Prieto C. Free breathing whole-heart 3D CINE MRI with self-gated Cartesian trajectory. *Magn Reson Imaging*. (2017) 38:129–37. doi: 10.1016/j.mri.2016.12.021

38. Metze P, Li H, Speidel T, Buckert D, Rottbauer W, Rasche V. Sliding window reduced FOV reconstruction for real-time cardiac Imaging. *Z Med Phys*. (2020) 30:236–44. doi: 10.1016/j.zemedi.2020.01.001

39. Moghari MH, Barthur A, Amaral ME, Geva T, Powell AJ. Free-breathing whole-heart 3D cine magnetic resonance imaging with prospective respiratory motion compensation. *Magn Reson Med*. (2018) 80:181–9. doi: 10.1002/mrm.27021

40. Menchón-Lara RM, Simmross-Wattenberg F, Casaseca-de-la Higuera P, Martín-Fernández M, Alberola-López C. Reconstruction techniques for cardiac cine MRI. *Insights Imaging*. (2019) 10:100. doi: 10.1186/s13244-019-0754-2

41. Xue H, Shah S, Greiser A, Guetter C, Littmann A, Jolly MP, et al. Motion correction for myocardial T1 mapping using image registration with synthetic image estimation. *Magn Reson Med*. (2012) 67:1644–55. doi: 10.1002/mrm.23153

42. Roujol S, Foppa M, Weingärtner S, Manning WJ, Nezafat R. Adaptive registration of varying contrast-weighted images for improved tissue characterization (ARCTIC): application to T1 mapping. *Magn Reson Med*. (2015) 73:1469–82. doi: 10.1002/mrm.25270

43. Tao Q, van der Tol P, Berendsen FF, Paiman EHM, Lamb HJ, van der Geest RJ. Robust motion correction for myocardial T(1) and extracellular volume mapping by principle component analysis-based groupwise image registration. *J Magn Reson Imaging*. (2018) 47:1397–405. doi: 10.1002/jmri.25863

44. Chen C, Qin C, Qiu H, Tarroni G, Duan J, Bai W, et al. Deep learning for cardiac image segmentation: a review. *Front Cardiovasc Med*. (2020) 7:25. doi: 10.3389/fcvm.2020.00025

45. Tao Q, Yan W, Wang Y, Paiman EHM, Shamonin DP, Garg P, et al. Deep learning-based method for fully Automatic Quantification of left ventricle function from cine MR images: a multivendor, multicenter study. *Radiology*. (2019) 290:81–8. doi: 10.1148/radiol.2018180513

46. Zhang L, Karanikolas GV, Akçakaya M, Giannakis GB. Fully automatic segmentation of the right ventricle via multi-task deep neural networks. In: *2018 IEEE International Conference on Acoustics, Speech and Signal Processing (ICASSP)*. (2018). p. 6677–81. doi: 10.1109/ICASSP.2018.8461556

47. Yue Q, Luo X, Ye Q, Xu L, Zhuang X. Cardiac segmentation from LGE MRI using deep neural network incorporating shape and spatial priors. In: *Medical Image Computing and Computer Assisted Intervention-MICCAI 2019*. Shenzhen; Cham (2019). p. 559–67. doi: 10.1007/978-3-030-32245-8_62

48. Basha TA, Tang MC, Tsao C, Tschabrunn CM, Anter E, Manning WJ, et al. Improved dark blood late gadolinium enhancement (DB-LGE) imaging using an optimized joint inversion preparation and T2 magnetization preparation. *Magn Reson Med*. (2018) 79:351–60. doi: 10.1002/mrm.26692

49. Kellman P, Xue H, Olivieri LJ, Cross RR, Grant EK, Fontana M, et al. Dark blood late enhancement imaging. *J Cardiovasc Magn Reson*. (2016) 18:77. doi: 10.1186/1532-429X-18-S1-P211

50. Kellman P. Dark-blood late–enhancement imaging–improves detection of myocardial infarction. *Cardiovasc Imag*. (2018) 11:1770. doi: 10.1016/j.jcmg.2017.10.014

51. Akçakaya M, Weingärtner S, Basha T, Roujol S, Bellm S, Nezafat R. Joint myocardial T1 and T2 mapping using a combination of saturation recovery and T2-preparation. *Magn Reson Med*. (2015) 76:888–96. doi: 10.1002/mrm.25975

52. Hermann I, Kellman P, Demirel OB, Akçakaya M, Schad LR, Weingärtner S. Free-breathing simultaneous T1, T2, and T2* quantification in the myocardium. *Magn Reson Med*. (2021) 86:1226–40. doi: 10.1002/mrm.28753

53. Weingärtner S, Schmitter S, Auerbach E, Kellman P, Shenoy C, Akçakaya M. Simultaneous multi slice imaging for myocardial T1 mapping: 16-segment coverage in a single breath-hold. *Magn Reson Med*. (2017) 78:462–71. doi: 10.1002/mrm.26770

54. Bentatou Z, Troalen T, Bernard M, Guye M, Pini L, Bartoli A, et al. Simultaneous multi-slice T1 mapping using MOLLI with blipped CAIPIRINHA bSSFP. *Magn Reson Imaging*. (2020). doi: 10.1016/j.mri.2020.03.006

55. Huang L, Neji R, Nazir MS, Whitaker J, Duong P, Reid F, et al. FASt single-breathhold 2D multislice myocardial T1 mapping (FAST1) at 1.5T for full left ventricular coverage in three breathholds. *J Magn Reson Imaging*. (2020) 51:492–504. doi: 10.1002/jmri.26869

frontiers | Frontiers in Cardiovascular Medicine

TYPE Review
PUBLISHED 06 October 2022
DOI 10.3389/fcvm.2022.953823

OPEN ACCESS

EDITED BY
Aleksandra Radjenovic,
University of Glasgow, United Kingdom

REVIEWED BY
Yuchi Liu,
University of Michigan, United States
Gastao Cruz,
King's College London,
United Kingdom

*CORRESPONDENCE
Katerina Eyre
katerina.eyre@muhc.mcgill.ca

SPECIALTY SECTION
This article was submitted to Cardiovascular Imaging, a section of the journal Frontiers in Cardiovascular Medicine

RECEIVED 26 May 2022
ACCEPTED 22 September 2022
PUBLISHED 06 October 2022

CITATION
Eyre K, Lindsay K, Razzaq S, Chetrit M and Friedrich M (2022) Simultaneous multi-parametric acquisition and reconstruction techniques in cardiac magnetic resonance imaging: Basic concepts and status of clinical development. *Front. Cardiovasc. Med.* 9:953823. doi: 10.3389/fcvm.2022.953823

Simultaneous multi-parametric acquisition and reconstruction techniques in cardiac magnetic resonance imaging: Basic concepts and status of clinical development

Katerina Eyre[1,2]*, Katherine Lindsay[1,2], Saad Razzaq[2], Michael Chetrit[1,2] and Matthias Friedrich[1,2]

[1]McGill University Health Centre, Montreal, QC, Canada, [2]Department of Experimental Medicine, McGill University, Montreal, QC, Canada

Simultaneous multi-parametric acquisition and reconstruction techniques (SMART) are gaining attention for their potential to overcome some of cardiovascular magnetic resonance imaging's (CMR) clinical limitations. The major advantages of SMART lie within their ability to simultaneously capture multiple "features" such as cardiac motion, respiratory motion, T1/T2 relaxation. This review aims to summarize the overarching theory of SMART, describing key concepts that many of these techniques share to produce co-registered, high quality CMR images in less time and with less requirements for specialized personnel. Further, this review provides an overview of the recent developments in the field of SMART by describing how they work, the parameters they can acquire, their status of clinical testing and validation, and by providing examples for how their use can improve the current state of clinical CMR workflows. Many of the SMART are in early phases of development and testing, thus larger scale, controlled trials are needed to evaluate their use in clinical setting and with different cardiac pathologies.

KEYWORDS

cardiac MRI (CMR), undersampled acquisition, fast cardiac imaging, multiparametric cardiovascular magnetic resonance imaging, sub-Nyquist sampling

Introduction

Cardiovascular magnetic resonance imaging (CMR) is a versatile imaging modality that allows a quantitative assessment of cardiac function, morphology, blood flow, and tissue composition (1). A major advantage of CMR is its ability to directly characterize myocardial tissue without the need for invasive procedures or ionizing radiation (1, 2).

While contrast agents are still frequently used, more and more techniques are now available that use native contrast mechanisms. The contrast in MR images arises primarily from variability in the proton density as well as longitudinal (T1) and transverse (T2) magnetic relaxation times of the tissue, which can be used to determine tissue composition based on quantitative T1 and T2 values (2). Since T1 and T2 values differ between different tissues and change with tissue pathologies such as inflammation or infiltration, T1 and T2 quantification strongly aids in differentiating between various cardiomyopathies including Fabry's disease (3), amyloidosis (4), myocarditis (5), hypertrophic cardiomyopathy (6), takotsubo (7), or acute versus chronic ischemic cardiomyopathy (2, 8).

Although extremely informative, CMR is limited by its technical complexity and long acquisition times (9). Cardiac and respiratory motion make CMR particularly challenging. Images need to be acquired during a period where the patient is motionless, so the exam length heavily depends on the patients' heart rhythm and on compliance with breathing instructions (10). Alongside patient compliance, scanning parameters must be carefully chosen with respect to pulse sequence type, spatial orientation of the imaging volume, and cardiac triggering options (10). These complexities demand specialized training of the medical staff and impair the clinical utility and accessibility of CMR, despite its widely accepted role in diagnosing cardiac disease (9).

To address these limitations, several working groups have focused on the development of fast and user-friendly acquisition methods (11–34). One proposed approach is the use of "one-click" scans, where multiple cardiac parameters (such as T1 relaxation, T2 relaxation, or cardiac motion) are collected simultaneously with less prospective planning (22, 23, 35, 36). These techniques have been collectively called Simultaneous Multiparametric Acquisition and Reconstruction Techniques (SMART) (37). SMART involves the collective acquisition of quantitative CMR contrast parameters (e.g., T1 and T2) which would normally be acquired separately in a clinical CMR setting. These new methods may increase sampling efficiency during free-breathing, ECG-free acquisitions and focus on retrospectively recovering data to reconstruct several cardiac contrasts at once. This may include producing simultaneous T1 and T2 maps, cine series or more (12, 14, 16, 18, 19, 23, 38–40). The result is a faster CMR acquisition with less need for specialized training, breathing instructions, or ECG setup. The goal of this review is to: (1) summarize the theory behind SMART, explaining how they enable the acquisition and reconstruction of high-quality images with less scan time compared to traditional methods; and (2) provide examples for how these rapid sequences could be applied in clinical settings, demonstrating how their application can improve the efficiency of clinical CMR scanning.

Basics of multi-parametric sparse sampling methods

Multi-parametric methods exploit the inherent redundancy of images to reduce the required sampling rate. Since redundant data can be compactly represented in some transform domains, this notion is closely related to the concept of "compressibility." The redundancy that is present in conventional CMR acquisitions allows for reducing sampling rate requirements in SMART, resulting in decreased scan time. CMR's long acquisition times are primarily caused by the need for several types of images—such as bright or dark blood morphological images, cine images, parametric maps, late gadolinium enhancement (LGE) images, perfusion images, or more—which require different parameter settings, views, and various contrast types (41). This limitation is worsened by the need for repeat measurements over various cardiac cycles to meet data sampling requirements and by the relatively short periods during which cardiac motion is minimal (10). There is significant redundancy with respect to anatomical regions being repetitively scanned for various contrasts (**Figure 1A**). The goal of SMART is to optimize the efficiency of CMR scans by acquiring multiple CMR data (cardiac motion, T1 relaxation, T2 relaxation etc.) in a single acquisition that can be reconstructed into informative images using assumptions based on prior knowledge of the MR signal properties (**Figure 1B**) (42).

Sampling less MR data per reconstructed image typically results in reduced image quality (IQ), but this can be mitigated with alternative sampling trajectories (**Figure 2**) (42). Traditionally, MR data are acquired as signals on a Cartesian k-space grid and then reconstructed to an image using a Fast Fourier transformation (**Figure 2**) (10). When undersampled, this method leads to fold-over artifacts that may be detrimental to visual interpretation or quantitative analysis (**Figure 2**). Many newer techniques utilize alternative sampling trajectories which frequently sample through the center of k-space, such as radial, rosette or spiral trajectories. These trajectories are desirable because they allow detection and extraction of respiratory and cardiac motion, thus enabling newer techniques to be free-breathing or self-gated (35). This reduces scanning complexity for the technologist, as no ECG electrodes or respiratory navigators are required. Furthermore, it removes the need for monitoring breathing compliance, and eliminates the potential for cardiac mis-triggers or incomplete breath-holds. It also benefits pediatric patients or those who have difficulty holding their breath, and patients with abnormal cardiac rhythms.

So-called sparse reconstruction techniques can produce higher IQ with reduced scan time and comprehensive, co-registered images when they capture more information at once (42). Thus, three-dimensional (3D) acquisitions or those that simultaneously capture many features, such as varying MR

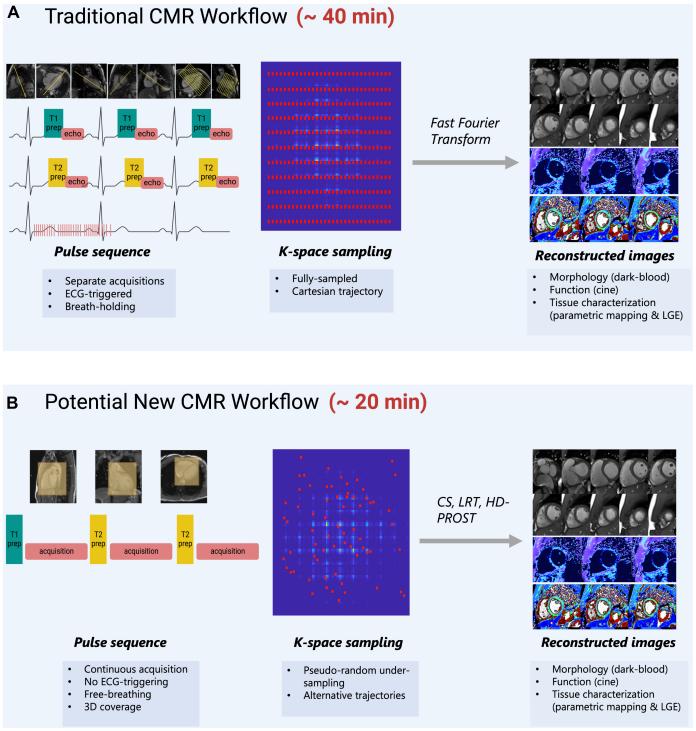

FIGURE 1
(A) Traditional CMR scanning workflow which requires separate image acquisitions to acquire images of different contrasts. Images are planned sequentially which requires time and specialized training to understand cardiac anatomy. ECG-triggers and breath-holding are needed to obtain images when motion is minimal. K-space is normally fully sampled and a fast-Fourier transform is used to obtain images with high image quality. **(B)** A potential new CMR workflow that is suggested by SMART-CMR. The novelty behind these SMART is to simplify CMR scanning by taking advantage of the redundancies which exist between images of different contrasts. Some SMART allow for imaging acquisitions without ECG-gating or breath-holding with whole-heart coverage. The acquisition planning is simplified, often simply requiring the placement of a volumetric box over the heart. For these methods to reduce scan time, pseudo-random under-sampling is often used in combination with alternative reconstruction approaches such as compressed-sensing (CS), low-rank tensor (LRT) methods, or high-dimensionality undersampled Patch based Reconstruction (HD-PROST).

contrasts, blood flow, and cardiac motion are characteristic of SMART. They effectively exploit the redundancy that exists in traditional CMR exams to achieve an efficient and nearly "all-in-one" image acquisition (42). This is also beneficial from a clinical standpoint as it allows the entire structure and function of the heart to be assessed with perfectly co-registered images across different MR contrast types.

Three methods, which are at the forefront of SMART, speed up MR acquisitions by undersampling (**Table 1**). These methods allow for recovery of CMR image integrity from data that were undersampled during their acquisition. The three key approaches are: Parallel Imaging (PI), Compressed Sensing (CS), and Low Rank Tensor (LRT) methods. These methods are commonly implemented alone or in combination.

Parallel imaging

Parallel imaging (PI) is widely used in clinical practice. PI allows for reduced data sampling by exploiting data redundancy available from phased array surface coils (**Figure 3**) (43). Phased array surface coils consist of several independent receiver coils arranged close to the region of interest (**Figure 3**). Each independent receiver coil is more sensitive to an anatomical area of the region of interest which is in closest proximity. Coil sensitivity maps are estimated and used to separate real signals from undersampling artifacts as the undersampled acquisition would typically lead to incoherent images if reconstructed using traditional methods (43).

Although PI improves the usability of CMR, scan time remains a significant limitation (9). While PI has allowed CMR scan time to be decreased 2- to 3-fold while maintaining diagnostic IQ (**Table 1** and **Figure 3**) with shorter breath-hold times (44), it is limited by the fixed geometry of the phased array coil elements and the loss of SNR at greater accelerations, where less data are acquired (43). Greater field strengths and dimensionality increase the baseline signal, allowing for more coherent images despite acceleration (43). Thus, the benefits of PI are appreciated in CMR using higher magnetic field

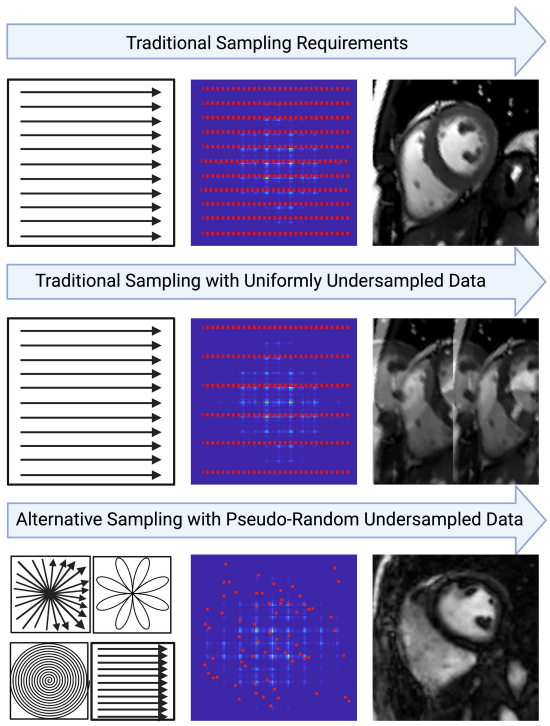

FIGURE 2
An example of how image quality may be affected from the way data is sampled in k-space. Traditional cartesian k-space sampling with fully sampled data results in high image quality. However, traditional k-space sampling with uniformly undersampled data results in coherent fold-over artifacts. Variable density pseudo-random undersampling allows artifacts to be incoherent in image space, approaching noise-like artifacts in some cases. This may allow the resulting image to retain diagnostic integrity despite heavy under-sampling. Oftentimes, variable density pseudo-random undersampling is achieved with alternative trajectories such as rosette, radial or spiral. The key benefits of these trajectories include the center of k-space being over-sampled which allows features like motion to be extracted and the incorporation of golden-angle sampling which strengthens the incoherence of artifacts in image space.

strengths and in exams that require a 3D or multi-dimensional component such as 2- or 3D cine imaging or angiography.

Compressed sensing

Compressed sensing (CS) is a reconstruction technique that exploits the sparsity of an image to recover it from far fewer samples than required by the Nyquist–Shannon sampling theorem. To successfully reconstruct an image, CS requires the image to be sparse in some domain (e.g., wavelet, finite difference, etc.) and the undersampling artifacts to be incoherent in the sparse domain (**Figure 4**) (45). CS has enabled many applications, including removing the need for patient breath-holding in 2D (46) or 3D cine imaging (47), accelerating parametric mapping acquisitions (48), acquiring 3D LGE images (49, 50), acquiring 3D MR angiography images (51–55), or acquiring higher dimensional CMR images such as 5D cardiac images (x, y, z spatial dimensions + respiratory motion + cardiac motion) (30, 56–60). CS has also recently been cleared by the United States Food and Drug Administration (FDA), allowing it to be used and tested in larger clinical settings (61–63).

For CS to successfully reconstruct an undersampled image, data must be sampled pseudo-randomly, and the reconstruction process must iteratively threshold the sparse domain and enforce data consistency with the acquired data in k-space (the sampling domain) to separate signals from noise and undersampling artifacts (**Figure 4**) (45). A sparse domain is a domain where the image can be compressed, meaning that few signals are representative of the whole image (**Figure 4**). The undersampling artifacts must be "incoherent" in this domain, meaning that undersampling in k-space will not affect the detection of "real signals" in the sparse domain (45). Once an appropriate sparse domain is selected, data is sampled pseudo-randomly in k-space, with the sampling rate defined by a set acceleration factor (**Figure 4**). After sampling, the goal of the CS reconstruction algorithm is to recover the "true signal" and remove the aliased signal which appears as noise (**Figure 4**) (45). This is done using an iterative, non-linear reconstruction framework (45) (**Figure 4**).

Certain parameters can be altered within the CS framework to enhance the resulting IQ. Like PI, CS is more reliable when the baseline signal is higher, e.g., with higher field strengths or higher dimensional imaging (3D or more) (45). The choice of the "sparse domain" and sampling trajectory also impacts the robustness of the technique (45). An important parameter in the CS reconstruction called regularization strength increases image sparsity in the sparse domain and thus attenuates more noise but also results in spatial blurring, making detection of edges such as the myocardial blood pool border more difficult (45). Clinical studies to date have shown that CS can reduce scan times by up to 90% (**Table 1**) and increase patient comfort, without a significant loss of diagnostic IQ or information. Before widespread clinical adoption however, standardization of CS techniques is required (**Figure 4**).

Low rank tensor methods

Low rank tensor (LRT) methods are yet another way to exploit CMR redundancy and save scan time. This method frames CMR as a tensor (**Figure 5A**) and reduces the redundancies which exist within this tensor representation (64). For example, CMR data is a tensor when visualized as still frame images grouped by T1 relaxation, T2 relaxation, and cardiac phase (**Figure 5A**). When visualized in this way, anatomical, contrast, and signal overlap can be observed between frames (**Figure 5A**). LRT methods use correlations between frames to recover CMR images from undersampled data (65). In this

sense, many MR features, such as respiratory or cardiac motion, can be viewed as higher dimensions within the LRT framework. This method has been applied to accelerate cardiac cine imaging (64, 66–71), visualization of contrast inflow (perfusion) (72), 5D flow (73), LGE (74), MR angiography (75), and parametric mapping (19, 25, 76). Like CS, LRT methods can be applied to remove the need for patient breath-holding or cardiac gating, making this another potentially useful method for difficult patient populations.

The key property that enables undersampling and scan time reduction in LRT methods is low rankness (64). Low rankness with respect to CMR means that along each dimension of the tensor (spatial, respiratory, cardiac, T1 relaxation, T2 relaxation, etc.), any datapoint can be obtained as a linear combination of other datapoints (64). In other words, a cardiac image at a specific cardiac phase with a specific contrast can be created by other images in different phases with different contrast weightings. The significance of this with respect to CMR scanning is that only a subset of CMR data is needed to extract higher-dimensional CMR data. However, to exploit these linear combinations, basis functions, i.e., functions which capture the signal behavior of each dimension (spatial, respiratory, cardiac, T1 relaxation, T2 relaxation, etc.), must be estimated (64) (**Figure 5B**). These can be estimated from the data itself or from Bloch equation simulations using the scan parameters (35).

In LRT methods, two different perspectives can be used separately or jointly to exploit CMR redundancy: global or local (77). Using an example of 2D cine images, a global

TABLE 1 Comparison of acquisition and reconstruction properties of sparse sampling techniques discussed in this manuscript.

	Parallel imaging	Compressed sensing	Low rank tensor methods	HD-PROST
Trajectory	Any	Trajectories which allow incoherent aliasing	(1) Trajectories which allow incoherent aliasing (2) Trajectories which continuously sample low-frequency information (e.g., the center of k-space)	Trajectories which allow incoherent aliasing
Redundancy	Coil domain	Any sparsifying domain	Tensor representation	Tensor representation
Acceleration	2–3 fold	4–5 fold	4–5 fold	2.5–6.5 fold
Requirements	(1) Phased-array coils (2) Sensitivity maps	(1) Pseudo-random data sampling (2) Pre-selected "sparse" domain (3) Pre-selected number of tuneable parameters	(1) Multi-dimensional CMR acquisition (2) Pseudo-random data sampling (3) Formation of tensor	(1) Multi-contrast CMR acquisition (2) Pseudo-random data sampling (3) Formation of tensor
Assumptions	(1) Coils are most sensitive to the imaging-area they are closest to (2) Coil sensitivities vary throughout the image	(1) CMR data is compressible (2) Pseudo-random data sampling allows undersampling artifacts to be separated from "true signal" (3) Undersampled CMR data can be recovered in a "sparse" domain	(1) CMR data has many spatio-temporal-contrast correlations (2) Pseudo-random data sampling allows undersampling artifacts to be separated from "true signal" (3) High-dimensional CMR data can be expressed as a LRT (4) Undersampled CMR data can be recovered from a LRT model	(1) CMR data has many spatio-temporal-contrast correlations (2) Pseudo-random data sampling allows undersampling artifacts to be separated from "true signal" (3) A multi-contrast image can be expressed as a LRT (4) Joint-contrast, undersampled CMR data can be recovered from a LRT model
Adjustable parameters	(1) Acceleration factor (limited by number of phased-array coils) (2) SENSE vs. GRAPPA	(1) "Sparse" domain (2) Tuneable parameters in the reconstruction	(1) Tensor constraints (global vs. local) (2) Tuneable parameters in the reconstruction	(1) Tuneable parameters in the reconstruction
Clinical validation studies	(44, 112–115)	(30, 49–53, 57, 116–118)	(73, 84, 104)	(18, 19, 75, 87, 105)
Technical literature	(119–123)	(45–48, 54–56, 59, 60, 124, 125)	(23, 64, 66, 69–72, 74, 76–78, 83, 85, 103, 126, 127)	(25, 36, 86)

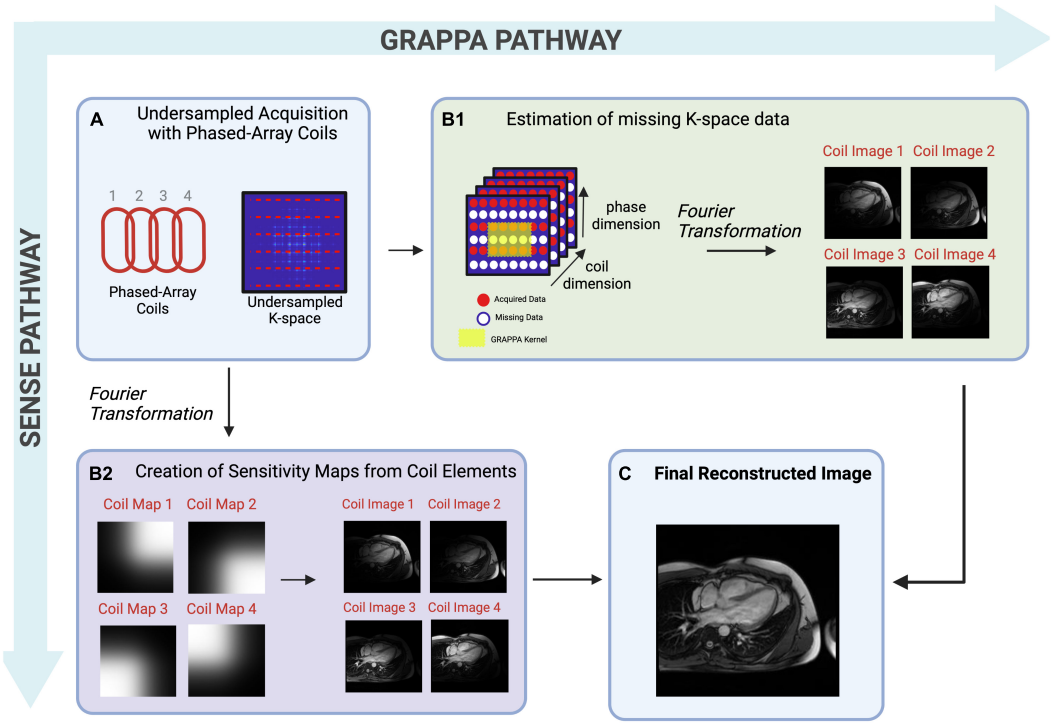

FIGURE 3
A pictorial example of multi-coil Parallel Imaging techniques describing both image-based SENSE (sensitivity encoding) or k-space based GRAPPA (generalized autocalibrating partial parallel acquisition)– two differing reconstruction techniques. **(A)** Pictorial representation of phased-array coils used to acquire undersampled data, and a graphical representation of undersampled k-space. The non-random undersampling method results in artifacts that are detrimental to visual inspection, therefore must be separated from real signals. **(B1)** Pictorial representation of k-space based GRAPPA. In this technique, reconstruction takes place in the k-space. The acquired MR signals fill in k-space for each coil, though many lines of k-space are missing due to undersampling. Missing points in k-space are then estimated iteratively using known data from the center of k-space, and local known data for each region, known as kernels. Once missing lines of k-space are filled, a Fourier transformation is performed, creating individual coil images from which the final reconstructed image will be created. **(B2)** Pictorial representation of image-based SENSE, in which reconstruction takes place in image space. A Fourier Transformation is performed which creates a coil sensitivity map for each coil element. These sensitivities are used to sort real signals from artifacts, creating an image for each coil, from which the final reconstructed image will be created. **(C)** The individual coil images are combined to create a final, reconstructed image.

approach may look at each still frame as a whole and search for correlations between each image (**Figure 6A**). This will often result in residual artifacts or spatial blurring because of the many different contrasts (from fat, muscle, blood pool, and air) that are present in each frame (77). Global LRT treats different tissue types jointly, so the accuracy of defining fine details in an image is reduced (77). A local approach may break each still frame into smaller "patches" and search for correlations that exist between these patches across dimensions (**Figure 6B**) (77, 78). This method retains more of the image detail information because the patches are more likely to contain a single tissue type with a single contrast (77, 78).

A major advantage of LRT methods is that they are adaptive and versatile (35). Unlike CS, LRT methods do not require the selection of a pre-defined sparse domain; they can look at all the existing CMR data to find redundancy (35). The advantage of this is less dependence on *a priori* decision making and potentially a larger reduction of scan time with a greater retention of the MR signal. In imaging tasks where precision is important, such as with parametric mapping, LRT methods may be better suited than CS because less signal is lost during the reconstruction process (35, 78). Like PI and CS, LRT methods work best with higher dimensional CMR applications (3D or more) since more redundancy exists at higher dimensions. For this reason, LRT methods have been successfully applied to create joint T1-T2 or T1-T2-cine images (19, 23, 39, 79–85), exploiting the overlap between these contrasts. The adaptive and versatile nature of LRT methods have made them a major focus in the development of SMART (19, 23, 25, 36, 38, 39, 75, 79–86).

High dimensionality, undersampled patch based reconstruction

High-dimensionality, undersampled patch-based reconstruction (HD-PROST) is a specific type of local-LRT regularization method which uses a patch-based perspective to exploit CMR redundancy (36) (**Figure 7**). Similar to local LRT

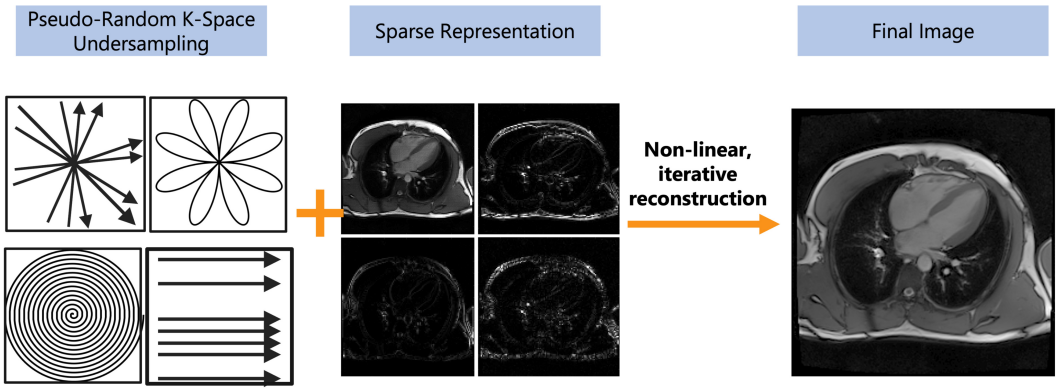

FIGURE 4
Depiction of the compressed sensing concept. Compressed sensing requires both a pseudo-random undersampling of k-space and for a sparse representation of the image in some transform domain (e.g., wavelet, finite difference, etc.). The pseudo-random sampling of k-space can be achieved with a variety of sampling trajectories such as radial, rosette, spiral, or cartesian. The under-sampled data undergoes a non-linear, iterative reconstruction to recover image integrity from the aliased image. The pseudo-random sampling of k-space allows undersampling artifacts to appear as noise and can be removed by thresholding in a sparse domain. The final image may have reduced image quality but should still be diagnostic.

methods, this patch-based approach breaks an image frame into "patches," but unlike local LRT methods, it searches for correlations both within a given patch and between patches (36). This allows CMR redundancy to be exploited to an even greater extent than the aforementioned methods, translating to both a further reduction in scan time and production of higher-quality images (65, 74, 75).

To date, only proof-of-concept studies exist to demonstrate the clinical potential of applying HD-PROST using an undersampled MR acquisition (**Table 2**) (19, 25, 36, 38, 39, 75, 79–82, 86, 87). Recently, an HD-PROST application which recovers 3D cine, T1, and T2, was tested in phantoms and 10 healthy volunteers and gave comparable results for ejection fraction (EF) as well as highly precise T1 and T2 measurements when compared to standard methods (19). In another study, a free-breathing 3D whole-heart sequence capable of visualizing the coronary vasculature was used (75). Both phantom and *in vivo* images had an excellent agreement in visualizing the coronary vasculature and its distal segments when compared with the fully sampled reference image (75). These images had a good quality despite shorter scan times (4 min and 35 s ± 44 s vs. 22 min and 30 s ± 4 min and 54 s for fully sampled image) (75). HD-PROST has also been applied to reconstruct water- and fat-suppressed LGE images (87). Although this study found HD-PROST images to be of diagnostic quality in 18/20 datasets with strong agreement in the location of enhancement when compared to standard LGE images, residual cardiac motion was still present (87). This may be due to over-regularization causing mismatches in patch-similarity, producing noisy signal variations that are like aliasing artifacts (36). Thus, further clinical studies are needed to help standardize the tuning of hyper-parameters for cardiac applications that intend to use HD-PROST or any of the sparse-sampling methods previously described.

Simultaneous multi-parametric acquisition and reconstruction techniques

Here, the SMART, which allow for simultaneously acquiring and reconstructing co-registered CMR images of different contrast weightings, with sparse sampling principles applied alone or in combination, are described.

3D single-parameter mapping

Some multi-parametric methods have focused on obtaining a single quantitative image contrast as part of a 3D or multi-cardiac-phase acquisition to increase the efficiency of parametric mapping CMR exams. Clinical CMR parametric mapping is limited by incomplete spatial coverage of the heart which decreases its sensitivity to detect regional myocardial abnormalities (37). Given the good agreement of mapping with LGE enhancement in visualizing focal lesions (88), complete coverage would likely increase the sensitivity of mapping and may even allow for avoiding contrast agent administration altogether.

In recent years, several groups have presented methods to obtain whole-heart T1 maps during a free-breathing acquisition. Han et al.'s (29) method exploits redundancy in the temporal

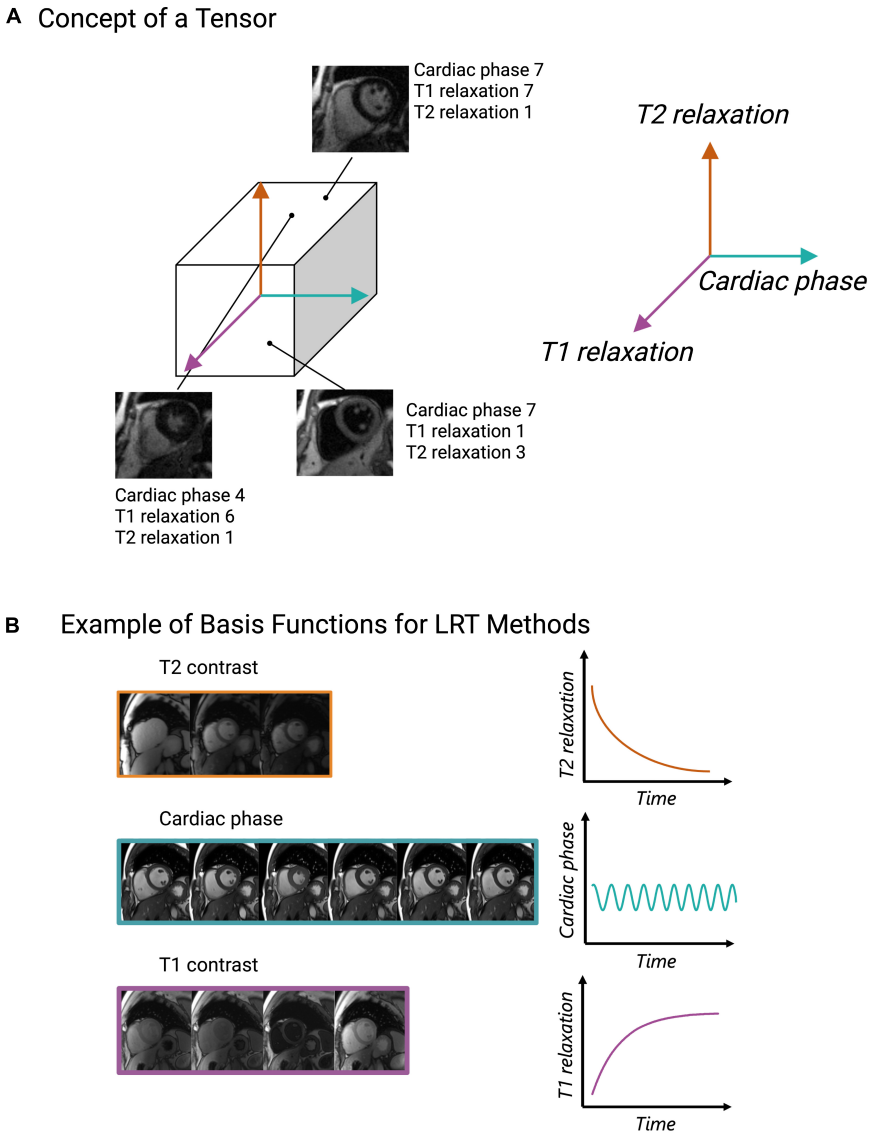

FIGURE 5
Depiction of the low rank tensor (LRT) concept. **(A)** Example of CMR images represented as a tensor with cardiac phase, T1 relaxation, and T2 relaxation representing different dimensions of the tensor. Once CMR data is organized in this way, any coordinate along the tensor will obtain an image with a various cardiac phase, T1 and T2 relaxation time. **(B)** Pictorial example of basis functions, which capture the signal behavior of each dimension (cardiac, T1 relaxation or T2 relaxation). These basis functions allow CMR data to be undersampled and for missing data to be recovered through various linear combinations of the sampled data.

domain (e.g., between image frames) to reduce scan time and obtain 40 short-axis slices with a spatial resolution of 1.9 × 1.9 × 4.5 mm. Their method requires a fairly lengthy imaging time of 14 min, but this time could be decreased by decreasing the number of slices acquired or lowering the spatial resolution (29). Nordio et al. (89) similarly developed a free-breathing 3D T1 mapping method which obtains 11 short-axis slices in 12 min. Their method incorporates an image-denoising step before T1 map fitting which improved the precision of their T1 maps when compared to Modified-Look-Locker-Inversion-Recovery (MOLLI) (89). However, their method depends on a 1D respiratory navigator which was shown to achieve a scan efficiency of only 36% when tested in 15 healthy subjects (89). In 2020, Guo et al. (90) presented a free-breathing 3D T1 mapping method which obtains nine short-axis slices in only 2 min. This method achieved high precision of T1 mapping values when compared to both Saturation recovery single-shot acquisition (SASHA) and MOLLI methods (coefficient of variations: 6.2 ±1.4%, 5.3 ± 1.1%, and 4.9 ± 0.8% for SASHA, MOLLI and the proposed 3D method, respectively) (90) in a highly accelerated scan time, demonstrating clinical feasibility of the technique.

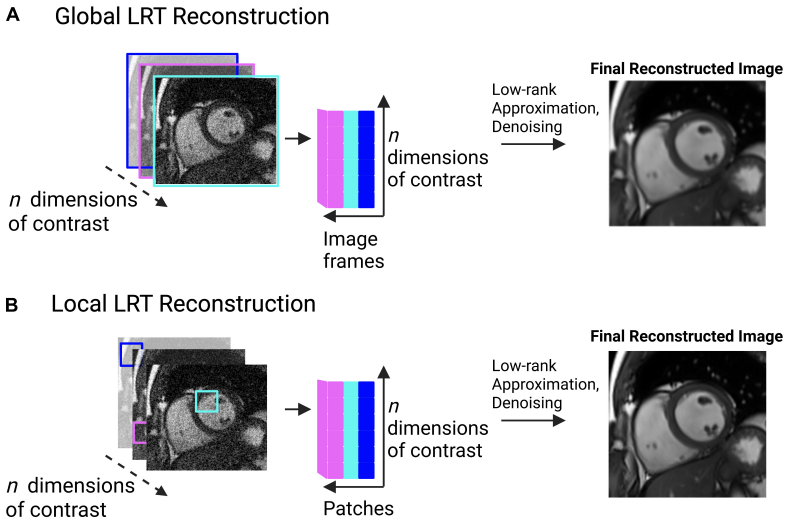

FIGURE 6
(A) Pictorial example of global low rank tensor (LRT) methods. This global method looks for image redundancy between entire image frames. This pictorial shows image frames identified across multiple image contrasts (e.g., T1, T2, etc.). Correlations are sought between the image frames, represented by the cartesian plane. Low-rank approximation and denoising are then applied to produce a final, reconstructed image. Spatial blurring or artifacts may be present in the resulting image due to the possibility of multiple tissue types being present in the image frame. **(B)** Pictorial example of local low rank tensor methods. This method breaks an image frame into "patches" and looks for image redundancy across image patches. The patches are unfolded in a matrix and a tensor is formed. Tensor decomposition through low-rank approximation allows for the image to be denoised, producing a final, reconstructed image. This method retains more detail information than the global method, as patches are more likely to contain a single tissue type, with a single contrast.

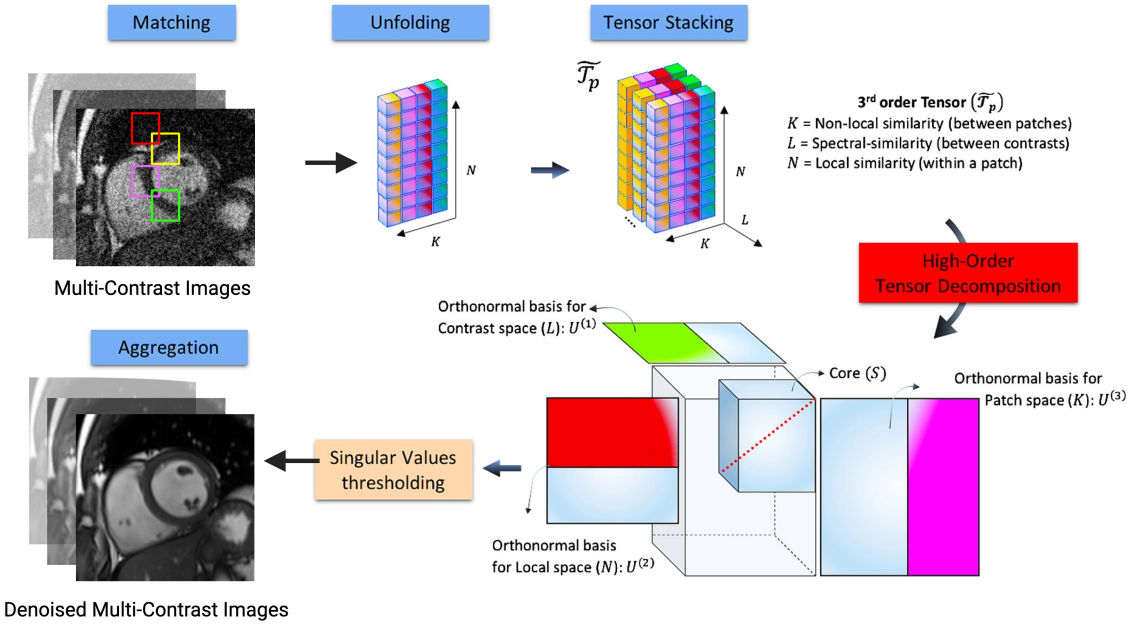

FIGURE 7
Flowchart describing the denoising HD-PROST optimization proposed by Bustin et al. (36). Multi-contrast images are denoised using 2D and 3D block matching, respectively, grouping similar 2D and 3D patches in the multi-contrast images. In a simple 2D matrix, these patches are then unfolded, and a third-order tensor is formed by stacking them in the contrast dimension. Through tensor decomposition, the high-order tensor can then be compressed. This is done by truncating multilinear singular vectors corresponding to small multilinear singular values. This process outputs denoised, multi-contrast images which are then used as prior knowledge in the joint MR reconstruction. Figure adapted from Bustin et al. (36).

TABLE 2 Comparison of SMART methods discussed in this manuscript.

	Motion compensation method	Parameters acquired	Recon. schema	Acquisition schema (trajectory, prep. pulse type and readout)	Scan time	Recon. rime
Akçakaya et al. (11)	Breath held and ECG triggered	T1, T2	Voxel-wise least squares curve fitting	Cartesian trajectory with SR pulse and T2 prep pulse and a single-shot bSSFP readout	13 heartbeats	NA
Blume et al. (12)	Navigator-gated and ECG triggered	T1, T2	PI (1.6x acceleration) and least squares curve fitting	Cartesian trajectory with IR pulse and T2 prep pulse and bSSFP readout	NA	NA
Guo et al. (14)	Navigator-gated and ECG triggered	3D, T1, T2	Curve fitting by Levenberg-Marquardt algorithms	Cartesian trajectory with SR pulse and T2 prep pulse and GRE readout	7.9 ± 1.4 min	NA
Multi-mapping (15)	Breath held and ECG triggered	T1, T2	PI (2x acceleration) and Dictionary generation and matching	Cartesian trajectory with IR pulse and T2 prep pulse and bSSFP readout	NA	NA
SATURN (16)	Navigator-gated and ECG triggered	T1, T2, T2*	PI (3 or 4x acceleration) and curve fitting	Cartesian trajectory with SR pulse and T2 prep pulse and spoiled GRE readout	18.5 s/slice	NA
3D-QALAS (17)	Breath held and ECG triggered	3D, T1, T2	PI (2x acceleration) and curve fitting	Cartesian trajectory with IR pulse and T2 prep pulse and GRE readout	15 heartbeats	NA
Milotta et al. (18)	Navigator-triggered retrospectively and ECG triggered	3D, T1, T2, water, fat fraction	PI (4x acceleration), HD-PROST, motion correction, and dictionary generation and matching	Cartesian trajectory with spiral-like profile order, IR pulse, T2 prep pulse, Dixon GRE acquisition	9 ± 1 min 48 s	27 min and 45 s
Qi et al. (19)	Free breathing, non-ECG gated	3D, T1, T2, cine	PI (2x acceleration), cardiac/respiratory binning, HD-PROST, dictionary generation and matching	Radial (golden angle) trajectory with IR pulse and T2 prep pulse and spoiled GRE readout	11.2 min	NA
CABIRIA (20)	Breath held and ECG triggered	T1, T2	PI (2x acceleration), and curve fitting	Cartesian trajectory with IR pulse and bSSFP readout	8 heartbeats/slice	NA
Deep-BLESS (21)	Breath held and ECG triggered	T1, T2	DL algorithm, PI (2x acceleration), CS	Radial trajectory (golden angle) with IR pulse and T2 prep pulse and spoiled GRE readout	11 heartbeats/slice	<1 s
Finger- printing (22)	Breath held and ECG triggered (newer adaptations are free-breathing and non-ECG triggered) (38, 39, 101)	3D, T1, T2, T2*, ECV, proton density, cine, fat fraction, water, T1 rho (22, 39, 81, 82, 95, 96)	Different frameworks have been proposed: all use dictionary generation and matching; some additionally incorporate PI, CS, LRT, HD-PROST (38, 79–82)	Spiral trajectory with IR pulse and T2 prep pulse (newer adaptations use radial or rosette trajectories)	Various acquisition times depending on sequence (16 heartbeats/slice (22), 7 min (38), 29.4 s/slice (39)	NA
Multi-tasking (23)	Free breathing and non-ECG gated	3D, T1, T2, T2*, ECV, fat fraction, cine	Cardiac/respiratory binning, PI, LRT	Radial trajectory with a hybrid T2IR preparatory pulse and GRE readout, and self-navigation with adequate temporal resolution to estimate motion basis-functions		

10.3389/fcvm.2022.953823

Recently, Bustin et al. (25) proposed a free-breathing technique, 3D Motion-Corrected Undersampled Signal matched (MUST)-T2, to obtain high spatial resolution (1.5 mm^3) 3D T2 maps in 8 min. Their method, which is similar to Ding et al.'s (26), uses a saturation pulse to reset the magnetization after every heart beat to increase scan efficiency and reduce the dependence on heart rate (25). When tested in a cohort of 25 patients with myocarditis, the method demonstrated a high sensitivity to detect edema (25). The isotropic spatial resolution is advantageous because it allows reformatting in any imaging view without a loss of resolution. Van Heeswijk et al. (33) developed a similar 3D T2-mapping approach with isotropic resolution (1.7 mm^3) but their method is slightly less efficient as a three-heartbeat waiting period is needed between magnetization recovery (scan time $\approx$ 18 min) (33). Milotta et al. (31) propose a similar technique which can obtain whole-heart T2 maps, dark- and bright-blood images in a free-breathing scan of 11 min with high spatial resolution. The 3D coverage and high-spatial resolution of the aforementioned methods may allow detection of the coronary arteries in addition to myocardial tissue characterization and morphological assessment, moving towards the direction of a comprehensive CMR exam.

Joint T1–T2

In traditional T1 and T2 parametric mapping, a preparatory pulse [inversion recovery (IR), saturation recovery (SR), combination of IR and SR, or T2 preparatory (T2prep)] is used before a readout with a pulse sequence to generate a single contrast. These readouts occur at several different time points after the preparatory pulse is applied, and later each voxel's signal intensity from the image series is fitted to a curve that describes the relaxation rate of the voxel (2). The acquisition is typically ECG-triggered with a breath-hold requirement for each obtained 2D slice. This method is not only lengthy but also depends on two major assumptions: (1) the voxels' signal intensity can be described only by the relaxation time being measured (or that the influence of other factors are negligible), and (2) the images in the series are co-registered (i.e., there is no physical displacement between the voxels of images acquired at different readout time points) (2). Since T1 and T2 provide complementary information when characterizing myocardial tissue (2), joint T1–T2 mapping may both overcome lengthy acquisition times and increase the diagnostic utility of parametric mapping by providing co-registered maps.

To simultaneously generate T1 and T2 maps, a combination of IR or SR and T2 prep pulses are typically used to generate T1 and T2 contrasts, respectively (**Table 2**) (35). Blume et al. (12) presented one of the first joint T1–T2 techniques which could acquire joint images using IR and T2prep pulses in an ECG-triggered, navigator-gated, free-breathing acquisition. Although their method was shown to measure precise T1 and T2 values in 19 healthy subjects, their method is inefficient—requiring almost 3 min to obtain a single 2D slice—as it requires dummy heartbeats during signal recovery (12). Guo et al. (14) and Hermann et al. (16) also presented navigator-gated, free-breathing approaches to obtain joint maps. Guo et al.'s (14) method was shown to be relatively fast, acquiring 3D joint T1–T2 maps with an average scan time of 8 min with moderate precision (coefficient of variations: 6.0 for T1 and 10.6 for T2). Hermann et al. (16) generated T2* maps in addition to T1 and T2, using an average acquisition time of 26.5 s/slice. Although these methods were shown to rapidly acquire joint maps, it should be noted that their techniques were tested mainly in a healthy subject population where breathing is relatively consistent. Navigator-based triggering depends on a steady breathing pattern which may not be found in all patients and could result in increased scan times in clinical settings.

In a different approach to navigator-triggering, Milotta et al. (18) acquired 2D low-resolution image navigators before running their 3D sequence to retrospectively isolate respiratory motion. The 2D image navigators are acquired rapidly and simplify the acquisition as they remove dependence on obtaining optimal respiratory-triggering windows, but they neglect to consider breathing motion in the anterior-posterior direction which may impact the robustness of the mapping technique (18). Their method additionally incorporates the HD-PROST framework to increase scanning efficiency, obtaining joint T1–T2 and water-fat maps over the whole heart with isotropic resolution in just 9 min (18). Qi et al. (19) take this one step further by removing the need for respiratory navigators altogether through use of a radial sampling schema. During reconstruction, the breathing motion is estimated using the k-space center of all radial spokes (19). Their method obtains 3D joint T1–T2-cine maps with isotropic resolution in 11.2 min (19).

Kvernby et al. (17) present another IR and T2prep technique, 3D-QALAS, which can acquire a stack of 13 2D short axis co-registered T1–T2 maps at end-diastole in an ECG-triggered acquisition of 15 heartbeats. This method was shown to detect T1 and T2 changes in a longitudinal study of patients who underwent valve replacement surgery (91) and was highly reproducible in a cohort of 23 patients with mixed pathologies, although it suffers from a lower precision compared to MOLLI and T2-Gradient-Spin-Echo (GraSE) techniques (92). CABIRIA, which similarly acquires joint 2D T1/T2 mapping images in a breath-hold of eight heartbeats, achieved high precision when tested in five healthy subjects but suffered from low repeatability (20). Their method continuously acquires data throughout eight cardiac cycles after a user-selectable timepoint after the R-wave in the ECG (20). This has the advantage of increasing the efficiency of data collection, ultimately reducing acquisition time. In contrast to the combination of IR and T2prep

pulses, Akçakaya et al. (11) used a combination of SR and T2prep pulses to generate 2D joint T1–T2 maps in a breath-hold of 13 heartbeats. Their method yielded improved T1/T2 accuracy but with lower precision compared to the IR based methods (11).

Other joint T1–T2 mapping approaches include Henningsson's (15). Multimapping, deep learning (DL) Bloch equation simulations (DeepBLESS) (21, 93), and Chow et al.'s (13) mSASHA. Multimapping is a joint T1/T2 method which generates a dictionary for each subject and then matches the acquired signal to this dictionary to generate T1–T2 maps (15). They only partially resolve these dictionaries in order to reduce the otherwise lengthy dictionary generation process (15). DeepBLESS is based on the Bloch equation simulations with the slice profile correction (BLESSPC) algorithm which was previously developed for MOLLI T1 mapping (21, 93, 94). mSASHA uses an ECG-trigger to acquire joint T1–T2 maps in 11 heartbeats. Their method demonstrated both high accuracy and precision when tested in 10 healthy subjects.

All aforementioned methods address key challenges of CMR, including the complexity of CMR scanning procedures and long scan times, but are limited to small sample sizes in mostly healthy subjects. Thus, despite the growing body of evidence, further clinical validation, feasibility, accuracy, and impact-on-outcome studies are required to verify the clinical potential of these SMART.

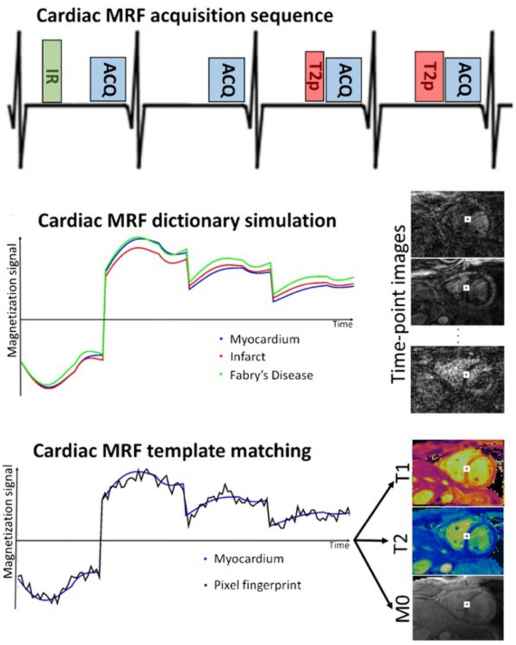

FIGURE 8
Example of the Fingerprinting workflow, including the dictionary matching process, and images obtained using the cardiac Fingerprinting sequence. This sequence simultaneously quantifies T1 and T2 in the myocardium. The figure shows acquisition of only 4-heartbeats of the 16-heartbeat acquisition method. In each heartbeat an inversion recovery (IR), T2 preparation (T2p), or no preparation pulse is used before the data acquisition (ACQ). Image taken from Cruz et al. (99).

Cardiac magnetic resonance fingerprinting

Cardiac magnetic resonance fingerprinting (cMRF) is a multi-parametric, rapid acquisition sequence for simultaneous acquisition of multiple quantitative tissue parameters. The traditional cMRF sequence quantifies T1, T2, and proton density (M0) using an ECG-triggered sequence with a breath-hold of 16 heartbeats (**Figure 8**) (22). Several variants of the sequence have been added over time, among them modifications for detecting and quantifying T1p, T2∗, and fat signal fraction (81, 82, 95, 96). Other developments include correcting for the confounding factors caused by the radiofrequency field (B1) (97), incorporating the ability for cMRF to acquire multiple cardiac slices at once (80), incorporating a 3D free-breathing, non-cardiac gated sequence with an acquisition time of 7 min (38) and more recently, incorporating a 2D joint T1–T2-cine sequence (**Table 2**) (39, 98).

Cardiac magnetic resonance fingerprinting attempts to capture the continuous and transient state of the magnetization history using various pulse sequence modules (e.g., IR, SR, T2prep pulses, varying flip angles and varying TR) that are sensitized to parameters of interest (e.g., T1 and T2) (22). The acquired signals are matched to a dictionary of possible signal evolutions to generate quantitative maps of interest (**Figure 8**) (22). cMRF dictionaries are generated using Bloch equations — a mathematical formula that calculates magnetization as a function of time with respect to T1 and T2 relaxation rates, and any other properties that can be modeled by the MR physics — to predict a range of possible spin behaviors and signal evolutions (22). In cardiac-triggered cMRF, dictionaries are made for each patient at the time of reconstruction, based on patient-specific patterns. They account for hardware parameters (B1 field inhomogeneity), acquisition parameters (pulse sequence type, echo time, flip angle, repetition time, readout type, etc.) and heart rate (22). This is critical as clinical parametric mapping is inherently susceptible to external factors (2). For a more thorough overview of the cMRF technique and its applications, the reader is directed to (98–100).

To save acquisition time, cMRF heavily undersamples data using radial, rosette, or spiral sampling trajectories (22). Radial or spiral trajectories are chosen so that the undersampling artifacts are incoherent in the spatial domain. Although each individual image is heavily undersampled, cMRF acquires hundreds of these poor-quality images, so that tissue signal patterns can still be identified and matched to the 'fingerprint' from the dictionary. More recently, cMRF has incorporated CS,

LRT or HD-PROST methods into its framework (39, 79–82, 98). LRT methods have been applied to the original cardiac-gated and breath-held cMRF technique to acquire multiple 2D T1–T2 slices simultaneously and to acquire joint T2–T2-cine images (80, 98). HD-PROST has similarly been applied to obtain joint T1–T2-cine images and 3D free-breathing and non-cardiac-gated cMRF images (38, 39). Recent clinical trials have demonstrated that cMRF gives highly reproducible T1 and T2 measurements that correlate well with standard mapping sequences (**Table 2**). The main advantage of combining undersampling methods with existing SMART methods is to recover images with higher IQ and greater image detail due to their effective recovery of undersampled data (98–100).

Though many studies have demonstrated the clinical potential of cMRF (99), there is still a need for larger, prospective clinical trials to validate the technique for clinical application. To date, the largest study consists of 58 healthy volunteers scanned at a single site on a 1.5T scanner (101). The aim of this study was to test the precision, repeatability, and IQ of cMRF maps compared to standard mapping techniques. The authors found that though cMRF measurements were slightly less precise than conventional sequences, they were reliable and cMRF images showed a more consistent IQ compared to conventional sequences (101). Recently, cMRF was also tested in a cohort of nine patients with amyloidosis and was found to achieve high diagnostic accuracy of amyloidosis detection (102). This study was the first to test the technique in a controlled clinical trial but with a small sample size. Future trials should include different patient populations to bring the cMRF technique into clinical practice and to help focus the optimization of cMRF developments.

The quantitative nature of cMRF lends itself well to CMR protocols for myocardial tissue characterization. Parametric mapping such as T1 and T2 are important for differentiating between edema, scar, fatty tissue, and other abnormalities such as the deposition of amyloid fibrils (2). The simultaneous acquisition of multiple contrasts and maps in cMRF reduces error caused by a mismatch of anatomical positions or the cardiac phase across different image types.

Cardiac magnetic resonance multitasking

Magnetic resonance multitasking is a free breathing multi-parametric sequence that can resolve cardiac motion, respiratory motion and myocardial relaxation properties, without the need for ECG triggering (**Figure 9**) (23). Its reconstruction framework allows for the incorporation of PI, CS, and LRT methods to decrease scan time (23). This allows a patient to lay-down and breath normally while the standard acquisition of cardiac cine, T1 and T2 mapping is acquired as opposed to the traditional breath-held and ECG triggered methods. Different variants of Multitasking sequences exist with varying acquisition times, but on average, Multitasking can acquire parameters in 1.5 min/slice or 15 min for a 3D ventricular stack, using a satisfactory in-plane spatial resolution of 1.4 × 1.4 × 8 mm (23, 103).

A previously published Multitasking acquisition scheme can be described as follows (23): T1 and T2 contrast data can be acquired simultaneously with radial sampling after five hybrid T2/IR preparation pulses, with a subset of k-space being sampled more frequently than the rest of k-space to obtain substantial temporal information for the retrospective cardiac and respiratory binning and to derive respiratory and cardiac subspaces used in the LRT reconstruction (**Figure 9A**). Binning refers to the retrospective data sorting into their motion states (respiratory and cardiac phases). The rest of the k-space is undersampled.

In the reconstruction process, Multitasking first sorts the motion states and then fits the dynamic image frames to T1 and T2 contrast weightings (23). The T1 and T2 maps are generated in a similar but slightly different fashion to cMRF. Multitasking generates a dictionary of T1 and T2 recovery curves using Bloch equations and then determines the T1 and T2 basis functions from this dictionary to perform a voxel-wise fitting of the acquired imaging signals (23). CS and LRT methods are then used to recover IQ from the undersampled dataset (23). Since images have been sampled across the entire T1/T2 recovery period, cine images can be created using many different variations of T1 and T2 contrast weighting. One can obtain dark-blood, bright-blood, T1-weighted, and T2-weighted cine series (**Figure 9A**) (23). If the recovery times for pericardium, fat, scar, edema, and myocardium are known, additional images can be created that either suppress or highlight these tissues—all from the same acquisition. This removes the need for specialized training by allowing a comprehensive exam to be obtained without ECG-gating and while the patient is breathing freely.

Several proof-of-concept studies have confirmed the versatility of the Multitasking framework (**Table 2**). Multitasking has been used to measure myocardial T1 and extracellular volumes (ECV) (104), myocardial T1 and T2 (23, 85), myocardial T1, T2, T2*, and fat-fraction (83) and carotid plaques and aortic strain in patients with thoracic aortic disease (84). These studies demonstrated that the Multitasking framework can produce high quality images with reproducible values that are in good agreement with reference values (**Table 2**). However, clinical studies with larger sample sizes are required to confirm these findings and validate this sequence for clinical use. While Multitasking has a strong clinical potential and can add additional contrasts such as T2*, its development is still ongoing, and more pre-clinical and clinical studies have yet

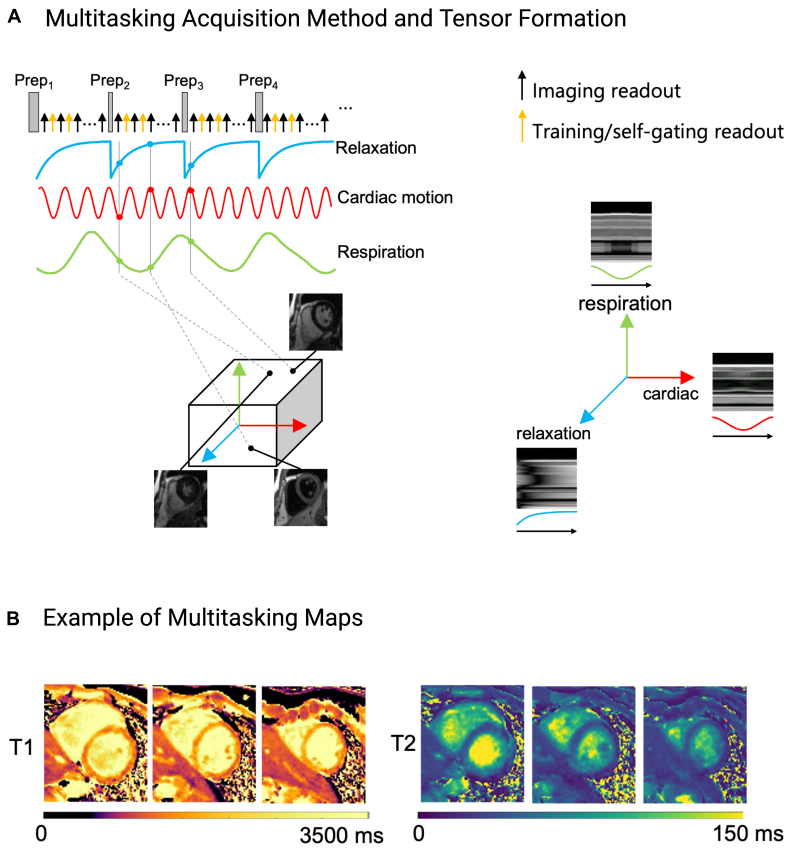

FIGURE 9
Example of the Multitasking acquisition method. **(A)** To capture T1 and T2 contrasts simultaneously, a hybrid T1/T2prep pulse is used in a continuous acquisition. Training/self-gating readouts are also acquired for retrospective cardiac and respiratory binning, and to estimate basis functions. Multi-dimensional information, namely cardiac and respiratory motion, and relaxation rate are extracted from the acquired data and sorted into a tensor. Each dimension in the tensor depicts cardiac motion, respiratory motion, T1 relaxation or T2 relaxation. One can choose any point within the tensor to obtain an image at a specific respiratory position, cardiac position, and relaxation position. **(B)** Example of the fitted Multitasking T1 and T2 maps. These maps are fitted after data are sorted into their tensor formation.

to show its ability to reliably quantify cardiac function, or T1 and T2 values in clinical settings.

Deep learning applications to simultaneous multi-parametric acquisition and reconstruction techniques

For SMART to be adopted into clinical practice, the issue of lengthy reconstruction times must be addressed. Reconstruction times of SMART have shown to vary from 3 min (105) to several hours (55). However, a clinical workflow may require even faster reconstruction speeds to troubleshoot any potential issues with the acquisition that could arise while the patient is still in the scanner. The speed of reconstruction for each method depends on several factors such as acquisition parameters [dimensionality of the acquisition (2D versus 3D), in-plane spatial resolution, undersampling factor, etc.], reconstruction parameters (number of iterations and other tuneable parameters), computer hardware parameters [random access memory, processing unit (graphics processing unit vs. central processing unit), etc.], and computing platform (computed unified device architecture, python, MATLAB, etc.) (55). Deep Learning (DL) may allow SMART to overcome some of their limitations by efficiently computing complex reconstruction tasks (**Figure 10**).

Deep learning has already been applied to cMRF for optimizing the dictionary-generation, image gridding and dictionary-signal-matching process used in cMRF's reconstruction of parametric maps (106, 107). Dictionary generation is a time-consuming and computationally heavy part of cMRF's reconstruction (22). DL reconstructions have been shown to speed up this process by more than sixfold (106), simply outputting T1/T2 values after the MRF signal time course and cardiac RR interval times are inputted to the network (**Figure 11**) (107). DL has also been applied to

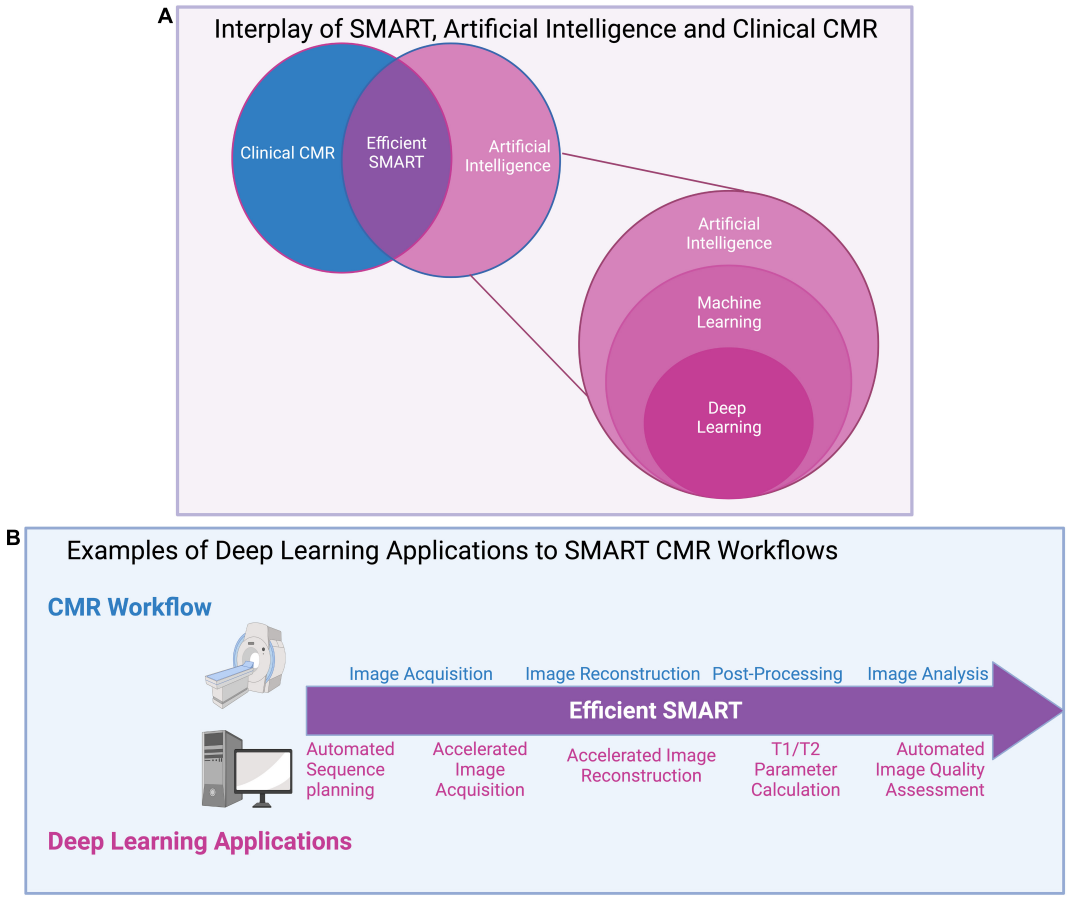

FIGURE 10
(A) Interplay of SMART, artificial intelligence (AI), and clinical CMR: A graphical overview of the relationships between artificial intelligence (AI) and its subsets, machine learning (ML) and deep learning (DL), as well as AI's potential impact on clinical CMR through SMART techniques. AI uses machines to perform tasks usually disposed to humans and covers all ML techniques. ML specifically investigates how computers learn from data, and DL, the most popular ML technique, automatically learns important features of data. **(B)** Examples of deep learning applications to SMART CMR workflows: DL has been applied at all stages of the CMR workflow, from image acquisition to analysis. Advantages to DL applications include reductions in input needed from clinicians through automated methods, and significant reductions in time for acquisition, reconstruction, and analysis. Challenges remain in applying DL to clinical settings, include computational limits, the lengthy training required for DL networks, and the "black box" nature of DL.

automated planning and sequence design, useful for reducing the complexity of scanning for technologists, though limited literature exists of cardiac applications (108).

Widespread application of DL to SMART is still limited. Their novelty and their current development status limit DL to a use mostly in small, exploratory studies, rather than large clinical validation trials. In addition to the signal-dictionary matching in cMRF, DL has been applied to quickly reconstruct T1 and T2 maps directly from cMRF images (107), reconstruct feature maps from multitasking images while accelerating reconstruction time by a factor of up to 3,000 (109), accelerate the acquisition of whole-heart magnetization transfer images fivefold (28), and has accurately estimated image IQ from other sequences in line with expert human reader ratings (110). Since DL has the potential to expedite the time-consuming and computationally demanding reconstruction processes of many SMART, its application will likely increase as SMART become more mature.

The use of DL is not without limitations. While DL may offer an increase in SMART reconstruction speeds, it requires a training stage which may not be easy or fast to conduct. Computational challenges such as the limits in processing capabilities to reconstruct long image sequences (111), and the need for labeled datasets in training (111) may complicate or restrict its general utility. Small datasets used for training DL networks may not accurately represent the diversity of the true population, preventing adoption in clinical practice (111). Furthermore, the "black box" nature of DL may limit a more rapid widespread adoption (111). The performance of other sparse sampling methods (PI, CS, LRT, HD-PROST) can be characterized using mathematical tools to understand how and when these methods fail, but this is more challenging with

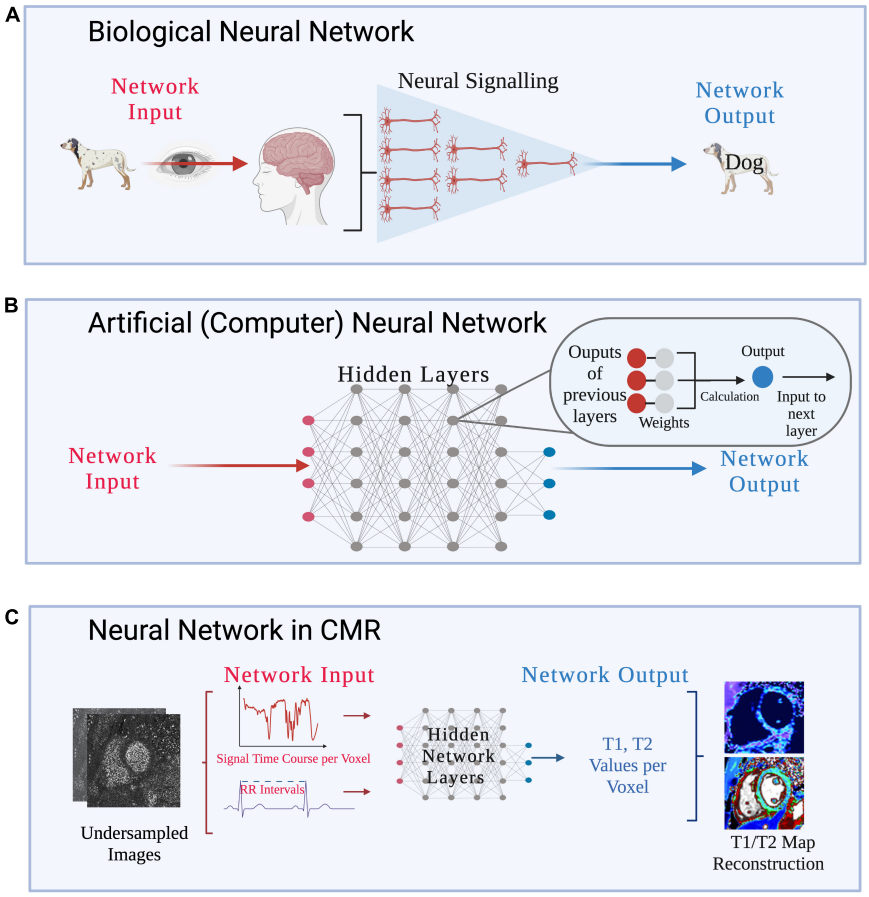

FIGURE 11
(A) Biological neural network: pictorial depiction of visual processing by interconnected neurons in the human brain. Figure design inspired by Zhu et al. (128). **(B)** Artificial (computer) neural network: pictorial of an artificial (computer) neural network as used in DL methods. Neural networks are composed of multiple hidden layers of interconnected nodes, which parallel the human brain's interconnected neural signaling pathways. Network inputs go through several layers of computations which not visible to the reader, and as such, these computations are known as hidden layers. Within each layer, filters are applied to the input, producing spatially dependent features which are then input to the next layer. The network aims to learn the optimal value of the filters, known as their weight, to generate features of maximum relevance to the task. If there are many layers, or computations, in the model, it is known as a deep neural network. **(C)** Neural network in CMR: a basic graphical representation of the deep neural network structure used to accelerate cardiac Fingerprinting (cMRF), as proposed by Hamilton and Seiberlich (106). After the network has been trained on simulated cMRF data, undersampled cMRF images are input and the network produces reconstructed T1/T2 maps. Specifically, for a given voxel, the measured cMRF signal time course and cardiac RR interval times from the ECG are input. The network then produces the estimated T1 and T2 values per voxel. This technique greatly accelerates reconstruction time from undersampled images, suggesting applications for rapid CMR reconstructions in clinical settings.

DL because the mathematical expressions inside the neural networks are hidden. This may be especially problematic when DL methods return reconstructions that look realistic but are in-fact inaccurate descriptions of the real pathology or anatomy. Ideally, clinicians should be able to understand DL's predictions before applying the results to clinical decision making (111). Minimizing bias in network design and ensuring training can be done with representative datasets and weighting will be critical to ensure DL networks do not simply replace manual bias with another form (109).

Despite its limitations, recent work supports the idea that SMART techniques will move toward DL reconstructions. The long manually intensive reconstructions currently experienced with SMART techniques only pushes CMR's time limitation from the foreground to the background (42). CMR will be unable to accommodate more patients without experiencing a reconstruction backlog, but this can be solved with DL (111).

Conclusion and future outlook

The application of SMART to clinical settings has the potential to change the current practice of CMR imaging. The ability of these techniques to acquire and then reconstruct different types of CMR images from a single image acquisition sequence simplifies the workflow for both the technologist and the patient. In the long term, this may allow CMR to be used in centers or locations without technologists specialized in cardiac

imaging. The benefit may also extend to patients living in remote areas, avoiding long commutes to specialized CMR centers. The significant shortening of scan times by using SMART compared to conventional CMR sequences may allow higher patient throughputs, reducing cost per scan and shortening CMR waitlists (9). The other added benefit for clinicians is the co-registration of SMART images, as various tissue characteristics or regional function can be reliably combined and thereby better inform therapeutic decisions. As part of a comprehensive CMR exam which includes morphology, function, and tissue characterization, SMART provides opportunity to obtain several of these parameters simultaneously. Some additional technical developments and eventually large, prospective, controlled clinical trials will be required to bring these techniques into clinical routine and identify areas where the techniques need to be optimized for clinical application. However, SMART addresses the issues of complicated imaging methods and long scan times in one way or another.

Author contributions

KE wrote and edited the manuscript, and created the figures and tables. KL assisted in drafting and editing text, and with creating figures. SR assisted in drafting text. MC assisted with idea conception and figure creation. MF assisted with text editing and is the senior author. All authors contributed to the article and approved the submitted version.

Conflict of interest

The authors declare that the research was conducted in the absence of any commercial or financial relationships that could be construed as a potential conflict of interest.

Publisher's note

All claims expressed in this article are solely those of the authors and do not necessarily represent those of their affiliated organizations, or those of the publisher, the editors and the reviewers. Any product that may be evaluated in this article, or claim that may be made by its manufacturer, is not guaranteed or endorsed by the publisher.

References

1. Seraphim A, Knott KD, Augusto J, Bhuva AN, Manisty C, Moon JC. Quantitative cardiac MRI. *J Magn Reson Imaging.* (2020) 51:693–711. doi: 10.1002/jmri.26789

2. Messroghli DR, Moon JC, Ferreira VM, Grosse-Wortmann L, He T, Kellman P, et al. Clinical recommendations for cardiovascular magnetic resonance mapping of T1, T2, T2* and extracellular volume: a consensus statement by the Society for Cardiovascular Magnetic Resonance (SCMR) endorsed by the European Association for Cardiovascular Imaging (EACVI). *J Cardiovasc Magn Reson.* (2017) 19:75. doi: 10.1186/s12968-017-0389-8

3. Sado DM, White SK, Piechnik SK, Banypersad SM, Treibel T, Captur G, et al. Identification and assessment of Anderson-Fabry disease by cardiovascular magnetic resonance noncontrast myocardial T1 mapping. *Circ Cardiovasc Imaging.* (2013) 6:392–8. doi: 10.1161/CIRCIMAGING.112.000070

4. Karamitsos TD, Piechnik SK, Banypersad SM, Fontana M, Ntusi NB, Ferreira VM, et al. Noncontrast T1 mapping for the diagnosis of cardiac amyloidosis. *JACC Cardiovasc Imaging.* (2013) 6:488–97. doi: 10.1016/j.jcmg.2012.11.013

5. Luetkens JA, Homsi R, Sprinkart AM, Doerner J, Dabir D, Kuetting DL, et al. Incremental value of quantitative CMR including parametric mapping for the diagnosis of acute myocarditis. *Eur Heart J Cardiovasc Imaging.* (2016) 17:154–61. doi: 10.1093/ehjci/jev246

6. Rowin EJ, Maron MS. The role of cardiac MRI in the diagnosis and risk stratification of hypertrophic cardiomyopathy. *Arrhythmia Electrophysiol Rev.* (2016) 5:197. doi: 10.15420/aer.2016:13:3

7. Eitel I, von Knobelsdorff-Brenkenhoff F, Bernhardt P, Carbone I, Muellerleile K, Aldrovandi A, et al. Clinical characteristics and cardiovascular magnetic resonance findings in stress (Takotsubo) cardiomyopathy. *JAMA.* (2011) 306:277–86. doi: 10.1001/jama.2011.992

8. Florian A, Jurcut R, Ginghina C, Bogaert J. Cardiac magnetic resonance imaging in ischemic heart disease: a clinical review. *J Med Life.* (2011) 4:330–45.

9. Roifman I, Paterson DI, Jimenez-Juan L, Friedrich MG, Howarth AG, Wintersperger BJ, et al. The state of cardiovascular magnetic resonance imaging in Canada: results from the CanSCMR Pan-Canadian Survey. *Can J Cardiol.* (2018) 34:333–6. doi: 10.1016/j.cjca.2017.12.026

10. Ginat DT, Fong MW, Tuttle DJ, Hobbs SK, Vyas RC. Cardiac imaging: part 1, MR pulse sequences, imaging planes, and basic anatomy. *Am J Roentgenol.* (2011) 197:808–15. doi: 10.2214/AJR.10.7231

11. Akçakaya M, Weingärtner S, Basha TA, Roujol S, Bellm S, Nezafat R. Joint myocardial T 1 and T 2 mapping using a combination of saturation recovery and T 2 -preparation: joint myocardial T 1 and T 2 mapping. *Magn Reson Med.* (2016) 76:888–96. doi: 10.1002/mrm.25975

12. Blume U, Lockie T, Stehning C, Sinclair S, Uribe S, Razavi R, et al. Interleaved T 1 and T 2 relaxation time mapping for cardiac applications. *J Magn Reson Imaging.* (2009) 29:480–7. doi: 10.1002/jmri.21652

13. Chow K, Hayes G, Flewitt JA, Feuchter P, Lydell C, Howarth A, et al. Improved accuracy and precision with three-parameter simultaneous myocardial T 1 and T 2 mapping using multiparametric SASHA. *Magn Reson Med.* (2022) 87:2775–91. doi: 10.1002/mrm.29170

14. Guo R, Chen Z, Herzka DA, Luo J, Ding H. A three-dimensional free-breathing sequence for simultaneous myocardial T 1 and T 2 mapping. *Magn Reson Med.* (2019) 81:1031–43. doi: 10.1002/mrm.27466

15. Henningsson M. Cartesian dictionary-based native T 1 and T 2 mapping of the myocardium. *Magn Reson Med.* (2022) 87:2347–62. doi: 10.1002/mrm.29143

16. Hermann I, Kellman P, Demirel OB, Akçakaya M, Schad LR, Weingärtner S. Free-breathing simultaneous T 1, T 2, and T 2 * quantification in the myocardium. *Magn Reson Med.* (2021) 86:1226–40. doi: 10.1002/mrm.28753

17. Kvernby S, Warntjes MJB, Haraldsson H, Carlhäll CJ, Engvall J, Ebbers T. Simultaneous three-dimensional myocardial T1 and T2 mapping in one breath hold with 3D-QALAS. *J Cardiovasc Magn Reson.* (2014) 16:102. doi: 10.1186/s12968-014-0102-0

18. Milotta G, Bustin A, Jaubert O, Neji R, Prieto C, Botnar RM. 3D whole-heart isotropic-resolution motion-compensated joint T 1 /T 2 mapping and water/fat imaging. *Magn Reson Med.* (2020) 84:3009–26. doi: 10.1002/mrm.28330

19. Qi H, Bustin A, Cruz G, Jaubert O, Chen H, Botnar RM, et al. Free-running simultaneous myocardial T1/T2 mapping and cine imaging with 3D whole-heart

coverage and isotropic spatial resolution. *Magn Reson Imaging.* (2019) 63:159–69. doi: 10.1016/j.mri.2019.08.008

20. Santini F, Kawel-Boehm N, Greiser A, Bremerich J, Bieri O. Simultaneous T 1 and T 2 quantification of the myocardium using cardiac balanced-SSFP inversion recovery with interleaved sampling acquisition (CABIRIA): cardiac relaxometry with CABIRIA. *Magn Reson Med.* (2015) 74:365–71. doi: 10.1002/mrm.25402

21. Shao J, Ghodrati V, Nguyen K, Hu P. Fast and accurate calculation of myocardial T 1 and T 2 values using deep learning Bloch equation simulations (DeepBLESS). *Magn Reson Med.* (2020) 84:2831–45. doi: 10.1002/mrm.28321

22. Hamilton JI, Jiang Y, Chen Y, Ma D, Lo WC, Griswold M, et al. MR fingerprinting for rapid quantification of myocardial T 1, T 2, and proton spin density: cardiac MR fingerprinting for T 1, T 2, and M 0 mapping. *Magn Reson Med.* (2017) 77:1446–58. doi: 10.1002/mrm.26216

23. Christodoulou AG, Shaw JL, Nguyen C, Yang Q, Xie Y, Wang N, et al. Magnetic resonance multitasking for motion-resolved quantitative cardiovascular imaging. *Nat Biomed Eng.* (2018) 2:215–26. doi: 10.1038/s41551-018-0217-y

24. Becker KM, Schulz-Menger J, Schaeffter T, Kolbitsch C. Simultaneous high-resolution cardiac T 1 mapping and cine imaging using model-based iterative image reconstruction. *Magn Reson Med.* (2019) 81:1080–91. doi: 10.1002/mrm.27474

25. Bustin A, Milotta G, Ismail TF, Neji R, Botnar RM, Prieto C. Accelerated free-breathing whole-heart 3D T 2 mapping with high isotropic resolution. *Magn Reson Med.* (2020) 83:988–1002. doi: 10.1002/mrm.27989

26. Ding H, Fernandez-de-Manuel L, Schär M, Schuleri KH, Halperin H, He L, et al. Three-dimensional whole-heart T 2 mapping at 3T: 3D myocardial T 2 mapping. *Magn Reson Med.* (2015) 74:803–16. doi: 10.1002/mrm.25458

27. Feng L, Liu F, Soultanidis G, Liu C, Benkert T, Block KT, et al. Magnetization-prepared GRASP MRI for rapid 3D T1 mapping and fat/water-separated T1 mapping. *Magn Reson Med.* (2021) 86:97–114. doi: 10.1002/mrm.28679

28. Fotaki A, Fuin N, Nordio G, Velasco Jimeno C, Qi H, Emmanuel Y, et al. Accelerating 3D MTC-BOOST in patients with congenital heart disease using a joint multi-scale variational neural network reconstruction. *Magn Reson Imaging.* (2022) 92:120–32. doi: 10.1016/j.mri.2022.06.012

29. Han PK, Marin T, Djebra Y, Landes V, Zhuo Y, El Fakhri G, et al. Free-breathing 3D cardiac T 1 mapping with transmit B 1 correction at 3T. *Magn Reson Med.* (2022) 87:1832–45. doi: 10.1002/mrm.29097

30. Ma L, Yerly J, Di Sopra L, Piccini D, Lee J, DiCarlo A, et al. Using 5D flow MRI to decode the effects of rhythm on left atrial 3D flow dynamics in patients with atrial fibrillation. *Magn Reson Med.* (2021) 85:3125–39. doi: 10.1002/mrm.28642

31. Milotta G, Ginami G, Bustin A, Neji R, Prieto C, Botnar RM. 3D whole-heart free-breathing qBOOST-T2 mapping. *Magn Reson Med.* (2020) 83:1673–87. doi: 10.1002/mrm.28039

32. Nezafat M, Nakamori S, Basha TA, Fahmy AS, Hauser T, Botnar RM. Imaging sequence for joint myocardial T 1 mapping and fat/water separation. *Magn Reson Med.* (2019) 81:486–94. doi: 10.1002/mrm.27390

33. van Heeswijk RB, Piccini D, Feliciano H, Hullin R, Schwitter J, Stuber M. Self-navigated isotropic three-dimensional cardiac T 2 mapping: self-navigated isotropic 3D cardiac T 2 mapping. *Magn Reson Med.* (2015) 73:1549–54. doi: 10.1002/mrm.25258

34. Weingärtner S, Shenoy C, Rieger B, Schad LR, Schulz-Menger J, Akçakaya M. Temporally resolved parametric assessment of Z-magnetization recovery (TOPAZ): dynamic myocardial T 1 mapping using a cine steady-state look-locker approach. *Magn Reson Med.* (2018) 79:2087–100. doi: 10.1002/mrm.26887

35. Qi H, Cruz G, Botnar R, Prieto C. Synergistic multi-contrast cardiac magnetic resonance image reconstruction. *Philos Trans R Soc Math Phys Eng Sci.* (2021) 379:20200197. doi: 10.1098/rsta.2020.0197

36. Bustin A, Lima da Cruz G, Jaubert O, Lopez K, Botnar RM, Prieto C. High-dimensionality undersampled patch-based reconstruction (HD-PROST) for accelerated multi-contrast MRI. *Magn Reson Med.* (2019) 81:3705–19. doi: 10.1002/mrm.27694

37. Friedrich MG. Steps and leaps on the path toward simpler and faster cardiac MRI scanning. *Radiology.* (2021) 298:587–8. doi: 10.1148/radiol.2021204084

38. Cruz G, Jaubert O, Qi H, Bustin A, Milotta G, Schneider T, et al. 3D free-breathing cardiac magnetic resonance fingerprinting. *NMR Biomed.* (2020) 33:e4370. doi: 10.1002/nbm.4370

39. Jaubert O, Cruz G, Bustin A, Schneider T, Koken P, Doneva M, et al. Free-running cardiac magnetic resonance fingerprinting: joint T1/T2 map and cine imaging. *Magn Reson Imaging.* (2020) 68:173–82. doi: 10.1016/j.mri.2020.02.005

40. Xanthis CG, Bidhult S, Greiser A, Chow K, Thompson RB, Arheden H, et al. Simulation-based quantification of native T1 and T2 of the myocardium using a modified MOLLI scheme and the importance of magnetization transfer. *Magn Reson Imaging.* (2018) 48:96–106. doi: 10.1016/j.mri.2017.12.020

41. Kramer CM, Barkhausen J, Bucciarelli-Ducci C, Flamm SD, Kim RJ, Nagel E. Standardized cardiovascular magnetic resonance imaging (CMR) protocols: 2020 update. *J Cardiovasc Magn Reson.* (2020) 22:17. doi: 10.1186/s12968-020-00607-1

42. Yang AC, Kretzler M, Sudarski S, Gulani V, Seiberlich N. Sparse reconstruction techniques in magnetic resonance imaging: methods, applications, and challenges to clinical adoption. *Invest Radiol.* (2016) 51:349–64. doi: 10.1097/RLI.0000000000000274

43. Niendorf T, Sodickson DK. Parallel imaging in cardiovascular MRI: methods and applications. *NMR Biomed.* (2006) 19:325–41. doi: 10.1002/nbm.1051

44. Plein S, Ryf S, Schwitter J, Radjenovic A, Boesiger P, Kozerke S. Dynamic contrast-enhanced myocardial perfusion MRI accelerated withk-t sense. *Magn Reson Med.* (2007) 58:777–85. doi: 10.1002/mrm.21381

45. Lustig M, Donoho D, Pauly JM. Sparse MRI: the application of compressed sensing for rapid MR imaging. *Magn Reson Med.* (2007) 58:1182–95. doi: 10.1002/mrm.21391

46. Usman M, Atkinson D, Odille F, Kolbitsch C, Vaillant G, Schaeffter T, et al. Motion corrected compressed sensing for free-breathing dynamic cardiac MRI: motion corrected compressed sensing. *Magn Reson Med.* (2013) 70:504–16. doi: 10.1002/mrm.24463

47. Usman M, Ruijsink B, Nazir MS, Cruz G, Prieto C. Free breathing whole-heart 3D CINE MRI with self-gated Cartesian trajectory. *Magn Reson Imaging.* (2017) 38:129–37. doi: 10.1016/j.mri.2016.12.021

48. Wang X, Roeloffs V, Klosowski J, Tan Z, Voit D, Uecker M, et al. Model-based T 1 mapping with sparsity constraints using single-shot inversion-recovery radial FLASH: model-based T 1 mapping with joint sparsity constraints. *Magn Reson Med.* (2018) 79:730–40. doi: 10.1002/mrm.26726

49. Kamesh Iyer S, Tasdizen T, Burgon N, Kholmovski E, Marrouche N, Adluru G, et al. Compressed sensing for rapid late gadolinium enhanced imaging of the left atrium: a preliminary study. *Magn Reson Imaging.* (2016) 34:846–54. doi: 10.1016/j.mri.2016.03.002

50. Basha TA, Akçakaya M, Liew C, Tsao CW, Delling FN, Addae G, et al. Clinical performance of high-resolution late gadolinium enhancement imaging with compressed sensing: high-resolution LGE with compressed sensing. *J Magn Reson Imaging.* (2017) 46:1829–38. doi: 10.1002/jmri.25695

51. Forman C, Piccini D, Grimm R, Hutter J, Hornegger J, Zenge MO. High-resolution 3D whole-heart coronary MRA: a study on the combination of data acquisition in multiple breath-holds and 1D residual respiratory motion compensation. *Magn Reson Mater Phys Biol Med.* (2014) 27:435–43. doi: 10.1007/s10334-013-0428-x

52. Forman C, Piccini D, Grimm R, Hutter J, Hornegger J, Zenge MO. Reduction of respiratory motion artifacts for free-breathing whole-heart coronary MRA by weighted iterative reconstruction: weighted iterative reconstruction for CMRA. *Magn Reson Med.* (2015) 73:1885–95. doi: 10.1002/mrm.25321

53. Nakamura M, Kido T, Kido T, Watanabe K, Schmidt M, Forman C, et al. Non-contrast compressed sensing whole-heart coronary magnetic resonance angiography at 3T: a comparison with conventional imaging. *Eur J Radiol.* (2018) 104:43–8. doi: 10.1016/j.ejrad.2018.04.025

54. Addy NO, Ingle RR, Wu HH, Hu BS, Nishimura DG. High-resolution variable-density 3D cones coronary MRA: high-resolution coronary MRA. *Magn Reson Med.* (2015) 74:614–21. doi: 10.1002/mrm.25803

55. Nam S, Akçakaya M, Basha T, Stehning C, Manning WJ, Tarokh V, et al. Compressed sensing reconstruction for whole-heart imaging with 3D radial trajectories: a graphics processing unit implementation: accelerated 3D radial imaging for whole heart. *Magn Reson Med.* (2013) 69:91–102. doi: 10.1002/mrm.24234

56. Feng L, Axel L, Chandarana H, Block KT, Sodickson DK, Otazo R. XD-GRASP: golden-angle radial MRI with reconstruction of extra motion-state dimensions using compressed sensing. *Magn Reson Med.* (2016) 75:775–88. doi: 10.1002/mrm.25665

57. Feng L, Coppo S, Piccini D, Yerly J, Lim RP, Masci PG, et al. 5D whole-heart sparse MRI: 5D whole-heart sparse MRI. *Magn Reson Med.* (2018) 79:826–38. doi: 10.1002/mrm.26745

58. Menchón-Lara RM, Royuela-del-Val J, Godino-Moya A, Cordero-Grande L, Simmross-Wattenberg F, Martín-Fernández M, et al. An efficient multi-resolution reconstruction scheme with motion compensation for 5D free-breathing whole-heart MRI. In: Cardoso MJ, Arbel T, Gao F, Kainz B, van Walsum T, Shi K, et al. editors. *Molecular Imaging, Reconstruction and Analysis of Moving Body Organs, and Stroke Imaging and Treatment (Lecture Notes in Computer Science).* (Vol. 10555), Cham: Springer International Publishing (2017). p. 136–45. doi: 10.1007/978-3-319-67564-0_14

59. Di Sopra L, Piccini D, Coppo S, Stuber M, Yerly J. An automated approach to fully self-gated free-running cardiac and respiratory motion-resolved 5D whole-heart MRI. *Magn Reson Med.* (2019) 82:2118–32. doi: 10.1002/mrm.27898

60. Cheng JY, Zhang T, Alley MT, Uecker M, Lustig M, Pauly JM, et al. Comprehensive multi-dimensional MRI for the simultaneous assessment of cardiopulmonary anatomy and physiology. *Sci Rep.* (2017) 7:5330. doi: 10.1038/s41598-017-04676-8

61. FDA. *510k Premarket Notification of Compressed Sensing Cardiac Cine (Siemens)*. Silver Spring, MD: FDA (2017).

62. FDA. *510k Premarket Notification of HyperSense (GE Medical Systems)*. Silver Spring, MD: FDA (2017).

63. FDA. *510k Premarket Notification of Compressed SENSE (Philips)*. Silver Spring, MD: FDA (2018).

64. Haldar JP, Liang ZP. Low-rank approximations for dynamic imaging. In: *Proceedings of the 2011 IEEE International Symposium on Biomedical Imaging: From Nano to Macro*. Chicago, IL: IEEE (2011). p. 1052–5. doi: 10.1109/ISBI.2011.5872582

65. Bustin A, Fuin N, Botnar RM, Prieto C. From compressed-sensing to artificial intelligence-based cardiac MRI reconstruction. *Front Cardiovasc Med.* (2020) 7:17. doi: 10.3389/fcvm.2020.00017

66. Lingala SG, Hu Y, DiBella E, Jacob M. Accelerated dynamic MRI exploiting sparsity and low-rank structure: k-t SLR. *IEEE Trans Med Imaging.* (2011) 30:1042–54. doi: 10.1109/TMI.2010.2100850

67. Pedersen H, Kozerke S, Ringgaard S, Nehrke K, Kim WY. k-t PCA: temporally constrained k-t BLAST reconstruction using principal component analysis: k-t BLAST using PCA. *Magn Reson Med.* (2009) 62:706–16. doi: 10.1002/mrm.22052

68. Zhao B, Haldar JP, Christodoulou AG, Liang ZP. Image reconstruction from highly undersampled (k, t)-space data with joint partial separability and sparsity constraints. *IEEE Trans Med Imaging.* (2012) 31:1809–20. doi: 10.1109/TMI.2012.2203921

69. Zhao B, Haldar JP, Brinegar C, Liang ZP. Low rank matrix recovery for real-time cardiac MRI. In: *Proceedings of the 2010 IEEE International Symposium on Biomedical Imaging: From Nano to Macro*. Rotterdam: IEEE (2010). p. 996–9. doi: 10.1109/ISBI.2010.5490156

70. Liu F, Li D, Jin X, Qiu W, Xia Q, Sun B. Dynamic cardiac MRI reconstruction using motion aligned locally low rank tensor (MALLRT). *Magn Reson Imaging.* (2020) 66:104–15. doi: 10.1016/j.mri.2019.07.002

71. Miao X, Lingala SG, Guo Y, Jao T, Usman M, Prieto C, et al. Accelerated cardiac cine MRI using locally low rank and finite difference constraints. *Magn Reson Imaging.* (2016) 34:707–14. doi: 10.1016/j.mri.2016.03.007

72. Otazo R, Candès E, Sodickson DK. Low-rank plus sparse matrix decomposition for accelerated dynamic MRI with separation of background and dynamic components: L+S reconstruction. *Magn Reson Med.* (2015) 73:1125–36. doi: 10.1002/mrm.25240

73. Walheim J, Dillinger H, Kozerke S. Multipoint 5D flow cardiovascular magnetic resonance - accelerated cardiac- and respiratory-motion resolved mapping of mean and turbulent velocities. *J Cardiovasc Magn Reson.* (2019) 21:42. doi: 10.1186/s12968-019-0549-0

74. Akçakaya M, Basha TA, Goddu B, Goepfert LA, Kissinger KV, Tarokh V, et al. Low-dimensional-structure self-learning and thresholding: regularization beyond compressed sensing for MRI reconstruction: LOST: regularization beyond CS for MR reconstruction. *Magn Reson Med.* (2011) 66:756–67. doi: 10.1002/mrm.22841

75. Bustin A, Ginami G, Cruz G, Correia T, Ismail TF, Rashid I, et al. Five-minute whole-heart coronary MRA with sub-millimeter isotropic resolution, 100% respiratory scan efficiency, and 3D-PROST reconstruction. *Magn Reson Med.* (2019) 81:102–15. doi: 10.1002/mrm.27354

76. Yaman B, Weingartner S, Kargas N, Sidiropoulos ND, Akcakaya M. Locally low-rank tensor regularization for high-resolution quantitative dynamic MRI. In: *Proceedings of the 2017 IEEE 7th International Workshop on Computational Advances in Multi-Sensor Adaptive Processing (CAMSAP)*. Willemstad: IEEE (2017). p. 1–5. doi: 10.1109/CAMSAP.2017.8313075

77. Trzasko J, Manduca A. Local versus global low-rank promotion in dynamic MRI series reconstruction. In: *Proceedings of the 19th Annual Meeting of ISMRM*. Montreal, QC (2011). p. 4371.

78. Zhang T, Pauly JM, Levesque IR. Accelerating parameter mapping with a locally low rank constraint: locally low rank parameter mapping. *Magn Reson Med.* (2015) 73:655–61. doi: 10.1002/mrm.25161

79. Cruz G, Qi H, Jaubert O, Kuestner T, Schneider T, Botnar RM, et al. Generalized low-rank nonrigid motion-corrected reconstruction for MR fingerprinting. *Magn Reson Med.* (2022) 87:746–63. doi: 10.1002/mrm.29027

80. Hamilton JI, Jiang Y, Ma D, Chen Y, Lo W, Griswold M, et al. Simultaneous multislice cardiac magnetic resonance fingerprinting using low rank reconstruction. *NMR Biomed.* (2019) 32:e4041. doi: 10.1002/nbm.4041

81. Lima da Cruz GJ, Velasco C, Lavin B, Jaubert O, Botnar RM, Prieto C. Myocardial T1, T2, T2*, and fat fraction quantification via low-rank motion-corrected cardiac MR fingerprinting. *Magn Reson Med.* (2022) 87:2757–74. doi: 10.1002/mrm.29171

82. Velasco C, Cruz G, Lavin B, Hua A, Fotaki A, Botnar RM, et al. Simultaneous T 1, T 2, and T 1ρ cardiac magnetic resonance fingerprinting for contrast agent–free myocardial tissue characterization. *Magn Reson Med.* (2022) 87:1992–2002. doi: 10.1002/mrm.29091

83. Cao T, Wang N, Kwan AC, Lee H, Mao X, Xie Y, et al. Free-breathing, non- ECG, simultaneous myocardial T 1, T 2, T 2 *, and fat-fraction mapping with motion-resolved cardiovascular MR multitasking. *Magn Reson Med.* (2022) 88:1748–63. doi: 10.1002/mrm.29351

84. Hu Z, Christodoulou AG, Wang N, Shaw JL, Song SS, Maya MM, et al. Magnetic resonance multitasking for multidimensional assessment of cardiovascular system: development and feasibility study on the thoracic aorta. *Magn Reson Med.* (2020) 84:2376–88. doi: 10.1002/mrm.28275

85. Mao X, Lee HL, Hu Z, Cao T, Han F, Ma S, et al. Simultaneous multi-slice cardiac MR multitasking for motion-resolved, non-ECG, free-breathing T1–T2 mapping. *Front Cardiovasc Med.* (2022) 9:833257. doi: 10.3389/fcvm.2022.833257

86. Mohsin YQ, Lingala SG, DiBella E, Jacob M. Accelerated dynamic MRI using patch regularization for implicit motion compensation. *Magn Reson Med.* (2017) 77:1238–48. doi: 10.1002/mrm.26215

87. Munoz C, Bustin A, Neji R, Kunze KP, Forman C, Schmidt M, et al. Motion-corrected 3D whole-heart water-fat high-resolution late gadolinium enhancement cardiovascular magnetic resonance imaging. *J Cardiovasc Magn Reson.* (2020) 22:53. doi: 10.1186/s12968-020-00649-5

88. Karur GR, Hanneman K. Cardiac MRI T1, T2, and T2* mapping in clinical practice. *Adv Clin Radiol.* (2019) 1:27–41. doi: 10.1016/j.yacr.2019.03.001

89. Nordio G, Bustin A, Henningsson M, Rashid I, Chiribiri A, Ismail T, et al. 3D SASHA myocardial T1 mapping with high accuracy and improved precision. *Magn Reson Mater Phys Biol Med.* (2019) 32:281–9. doi: 10.1007/s10334-018-0703-y

90. Guo R, Cai X, Kucukseymen S, Rodriguez J, Paskavitz A, Pierce P, et al. Free-breathing whole-heart multi-slice myocardial T 1 mapping in 2 minutes. *Magn Reson Med.* (2021) 85:89–102. doi: 10.1002/mrm.28402

91. Kvernby S, Rönnerfalk M, Warntjes M, Carlhäll CJ, Nylander E, Engvall J, et al. Longitudinal changes in myocardial T 1 and T 2 relaxation times related to diffuse myocardial fibrosis in aortic stenosis; before and after aortic valve replacement: myocardial relaxation times after AVR. *J Magn Reson Imaging.* (2018) 48:799–807. doi: 10.1002/jmri.25980

92. Kvernby S, Warntjes M, Engvall J, Carlhäll CJ, Ebbers T. Clinical feasibility of 3D-QALAS – Single breath-hold 3D myocardial T1- and T2-mapping. *Magn Reson Imaging.* (2017) 38:13–20. doi: 10.1016/j.mri.2016.12.014

93. Shao J, Zhou Z, Nguyen K, Finn JP, Hu P. Accurate, precise, simultaneous myocardial T1 and T2 mapping using a radial sequence with inversion recovery and T2 preparation. *NMR Biomed.* (2019) 32:e4165. doi: 10.1002/nbm.4165

94. Shao J, Rapacchi S, Nguyen KL, Hu P. Myocardial T1 mapping at 3.0 tesla using an inversion recovery spoiled gradient echo readout and bloch equation simulation with slice profile correction (BLESSPC) T1 estimation algorithm: FLASH-MOLLI with BLESSPC T1 mapping. *J Magn Reson Imaging.* (2016) 43:414–25. doi: 10.1002/jmri.24999

95. Jaubert O, Cruz G, Bustin A, Hajhosseiny R, Nazir S, Schneider T, et al. T1, T2, and fat fraction cardiac MR fingerprinting: preliminary clinical evaluation. *J Magn Reson Imaging.* (2021) 53:1253–65. doi: 10.1002/jmri.27415

96. Liu Y, Hamilton J, Eck B, Griswold M, Seiberlich N. Myocardial T 1 and T 2 quantification and water–fat separation using cardiac MR fingerprinting with rosette trajectories at 3T and 1.5T. *Magn Reson Med.* (2021) 85:103–19. doi: 10.1002/mrm.28404

97. Hamilton JI, Jiang Y, Ma D, Lo WC, Gulani V, Griswold M, et al. Investigating and reducing the effects of confounding factors for robust T1 and T2 mapping with cardiac MR fingerprinting. *Magn Reson Imaging.* (2018) 53:40–51. doi: 10.1016/j.mri.2018.06.018

98. Hamilton JI, Jiang Y, Eck B, Griswold M, Seiberlich N. Cardiac cine magnetic resonance fingerprinting for combined ejection fraction, T 1 and T 2 quantification. *NMR Biomed.* (2020) 33:e4323. doi: 10.1002/nbm.4323

99. Cruz G, Jaubert O, Botnar RM, Prieto C. Cardiac magnetic resonance fingerprinting: technical developments and initial clinical validation. *Curr Cardiol Rep.* (2019) 21:91. doi: 10.1007/s11886-019-1181-1

100. Eck BL, Flamm SD, Kwon DH, Tang WHW, Vasquez CP, Seiberlich N. Cardiac magnetic resonance fingerprinting: trends in technical development and

potential clinical applications. *Prog Nucl Magn Reson Spectrosc.* (2021) 122:11–22. doi: 10.1016/j.pnmrs.2020.10.001

101. Hamilton JI, Pahwa S, Adedigba J, Frankel S, O'Connor G, Thomas R, et al. Simultaneous mapping of T 1 and T 2 using cardiac magnetic resonance fingerprinting in a cohort of healthy subjects at 1. 5T. *J Magn Reson Imaging.* (2020) 52:1044–52. doi: 10.1002/jmri.27155

102. Eck BL, Seiberlich N, Flamm SD, Hamilton JI, Suresh A, Kumar Y, et al. Characterization of cardiac amyloidosis using cardiac magnetic resonance fingerprinting. *Int J Cardiol.* (2022) 351:107–10. doi: 10.1016/j.ijcard.2021.12.038

103. Mao, X, Serry FM, Hu Z, Kwan AC, Han F, Xie Y, et al. 3D Whole-ventricle, free-breathing, non-ECG, T1-T2-B1+ mapping and cine imaging with cardiac MR multitasking. In: *Proceedings of the Virtual Conference ISMRM* (2021).

104. Shaw JL, Yang Q, Zhou Z, Deng Z, Nguyen C, Li D, et al. Free-breathing, non-ECG, continuous myocardial T 1 mapping with cardiovascular magnetic resonance multitasking. *Magn Reson Med.* (2019) 81:2450–63. doi: 10.1002/mrm.27574

105. Bustin A, Hua A, Milotta G, Jaubert O, Hajhosseiny R, Ismail TF, et al. High-spatial-resolution 3D whole-heart MRI T2 mapping for assessment of myocarditis. *Radiology.* (2021) 298:578–86. doi: 10.1148/radiol.2021201630

106. Hamilton JI, Seiberlich N. Machine learning for rapid magnetic resonance fingerprinting tissue property quantification. *Proc IEEE.* (2020) 108:69–85. doi: 10.1109/JPROC.2019.2936998

107. Hamilton JI, Currey D, Rajagopalan S, Seiberlich N. Deep learning reconstruction for cardiac magnetic resonance fingerprinting T 1 and T 2 mapping. *Magn Reson Med.* (2021) 85:2127–35. doi: 10.1002/mrm.28568

108. Blansit K, Retson T, Masutani E, Bahrami N, Hsiao A. Deep learning–based prescription of cardiac MRI planes. *Radiol Artif Intell.* (2019) 1:e180069. doi: 10.1148/ryai.2019180069

109. Chen Y, Shaw JL, Xie Y, Li D, Christodoulou AG. Deep learning within a priori temporal feature spaces for large-scale dynamic MR image reconstruction: application to 5-D cardiac MR multitasking. In: Shen D, Liu T, Peters TM, Staib LH, Essert C, Zhou S, et al. editors. *Medical Image Computing and Computer Assisted Intervention – MICCAI 2019. (Lecture Notes in Computer Science).* (Vol. 11765), Cham: Springer International Publishing (2019). p. 495–504. doi: 10.1007/978-3-030-32245-8_55

110. Piccini D, Demesmaeker R, Heerfordt J, Yerly J, Di Sopra L, Masci PG, et al. Deep learning to automate reference-free image quality assessment of whole-heart MR images. *Radiol Artif Intell.* (2020) 2:e190123. doi: 10.1148/ryai.2020190123

111. Leiner T, Rueckert D, Suinesiaputra A, Baeßler B, Nezafat R, Išgum I, et al. Machine learning in cardiovascular magnetic resonance: basic concepts and applications. *J Cardiovasc Magn Reson.* (2019) 21:61. doi: 10.1186/s12968-019-0575-y

112. Feng L, Srichai MB, Lim RP, Harrison A, King W, Adluru G, et al. Highly accelerated real-time cardiac cine MRI using k - t SPARSE-SENSE: accelerated real-time cardiac cine MRI with k-t SPARSE-SENSE. *Magn Reson Med.* (2013) 70:64–74. doi: 10.1002/mrm.24440

113. Schwab F, Schwarz F, Dietrich O, Lanz T, Resmer F, Wichmann T, et al. Free breathing real-time cardiac cine imaging with improved spatial resolution at 3 T. *Invest Radiol.* (2013) 48:158–66. doi: 10.1097/RLI.0b013e31827f1b68

114. Hunold P, Maderwald S, Ladd ME, Jellus V, Barkhausen J. Parallel acquisition techniques in cardiac cine magnetic resonance imaging using TrueFISP sequences: comparison of image quality and artifacts. *J Magn Reson Imaging.* (2004) 20:506–11. doi: 10.1002/jmri.20125

115. Theisen D, Sandner TA, Bamberg F, Bauner KU, Schwab F, Schwarz F, et al. High-resolution cine MRI with TGRAPPA for fast assessment of left ventricular function at 3 Tesla. *Eur J Radiol.* (2013) 82:e219–24. doi: 10.1016/j.ejrad.2012.12.019

116. Jaspan ON, Fleysher R, Lipton ML. Compressed sensing MRI: a review of the clinical literature. *Br J Radiol.* (2015) 88:20150487. doi: 10.1259/bjr.20150487

117. Vermersch M, Longère B, Coisne A, Schmidt M, Forman C, Monnet A, et al. Compressed sensing real-time cine imaging for assessment of ventricular function, volumes and mass in clinical practice. *Eur Radiol.* (2020) 30:609–19. doi: 10.1007/s00330-019-06341-2

118. Wetzl J, Schmidt M, Pontana F, Longère B, Lugauer F, Maier A, et al. Single-breath-hold 3-D CINE imaging of the left ventricle using Cartesian sampling. *Magn Reson Mater Phys Biol Med.* (2018) 31:19–31. doi: 10.1007/s10334-017-0624-1

119. Tsao J, Boesiger P, Pruessmann KP. k-t BLAST andk-t SENSE: dynamic MRI with high frame rate exploiting spatiotemporal correlations. *Magn Reson Med.* (2003) 50:1031–42. doi: 10.1002/mrm.10611

120. Pruessmann KP, Weiger M, Scheidegger MB, Boesiger P. SENSE: sensitivity encoding for fast MRI. *Magn Reson Med.* (1999) 42:952–62. doi: 10.1002/(SICI)1522-2594(199911)42:5<952::AID-MRM16>3.0.CO;2-S

121. Pruessmann KP, Weiger M, Boesiger P. Sensitivity encoded cardiac MRI. *J Cardiovasc Magn Reson.* (2001) 3:1–9. doi: 10.1081/JCMR-100000143

122. Kellman P, Epstein FH, McVeigh ER. Adaptive sensitivity encoding incorporating temporal filtering (TSENSE). *Magn Reson Med.* (2001) 45:846–52. doi: 10.1002/mrm.1113

123. Griswold MA, Jakob PM, Heidemann RM, Nittka M, Jellus V, Wang J, et al. Generalized autocalibrating partially parallel acquisitions (GRAPPA). *Magn Reson Med.* (2002) 47:1202–10. doi: 10.1002/mrm.10171

124. Correia T, Cruz G, Schneider T, Botnar RM, Prieto C. Technical note: accelerated nonrigid motion-compensated isotropic 3D coronary MR angiography. *Med Phys.* (2018) 45:214–22. doi: 10.1002/mp.12663

125. Piccini D, Littmann A, Nielles-Vallespin S, Zenge MO. Spiral phyllotaxis: the natural way to construct a 3D radial trajectory in MRI: spiral phyllotaxis radial 3D trajectory. *Magn Reson Med.* (2011) 66:1049–56. doi: 10.1002/mrm.22898

126. Liang ZP. Spatiotemporal imagingwith partially separable functions. In: *Proceedings of the 2007 4th IEEE International Symposium on Biomedical Imaging: From Nano to Macro*. Arlington, VA: IEEE (2007). p. 988–91. doi: 10.1109/ISBI.2007.357020

127. Yaman B, Weingartner S, Kargas N, Sidiropoulos ND, Akcakaya M. Low-rank tensor models for improved multidimensional MRI: application to dynamic cardiac T_1 mapping. *IEEE Trans Comput Imaging.* (2020) 6:194–207. doi: 10.1109/TCI.2019.2940916

128. Zhu G, Jiang B, Tong L, Xie Y, Zaharchuk G, Wintermark M. Applications of deep learning to neuro-imaging techniques. *Front Neurol.* (2019) 10:869. doi: 10.3389/fneur.2019.00869

frontiers | Frontiers in Cardiovascular Medicine

TYPE Policy and Practice Reviews
PUBLISHED 23 January 2023
DOI 10.3389/fcvm.2022.991383

OPEN ACCESS

EDITED BY
Anthony G. Christodoulou,
Cedars-Sinai Medical Center, United States

REVIEWED BY
Edward DiBella,
The University of Utah, United States
Markus Henningsson,
Linköping University, Sweden

*CORRESPONDENCE
Anastasia Fotaki
✉ Anastasia.fotaki@kcl.ac.uk

†These authors have contributed equally to this work and share first authorship

SPECIALTY SECTION
This article was submitted to Cardiovascular Imaging, a section of the journal Frontiers in Cardiovascular Medicine

RECEIVED 11 July 2022
ACCEPTED 29 December 2022
PUBLISHED 23 January 2023

CITATION
Fotaki A, Velasco C, Prieto C and Botnar RM (2023) Quantitative MRI in cardiometabolic disease: From conventional cardiac and liver tissue mapping techniques to multi-parametric approaches.
Front. Cardiovasc. Med. 9:991383.
doi: 10.3389/fcvm.2022.991383

Quantitative MRI in cardiometabolic disease: From conventional cardiac and liver tissue mapping techniques to multi-parametric approaches

Anastasia Fotaki[1*†], Carlos Velasco[1†], Claudia Prieto[1,2,3,4] and René M. Botnar[1,2,3,4]

[1]School of Biomedical Engineering and Imaging Sciences, King's College London, London, United Kingdom, [2]School of Engineering, Pontificia Universidad Católica de Chile, Santiago, Chile, [3]Institute for Biological and Medical Engineering, Pontificia Universidad Católica de Chile, Santiago, Chile, [4]Millennium Institute for Intelligent Healthcare Engineering, Santiago, Chile

Cardiometabolic disease refers to the spectrum of chronic conditions that include diabetes, hypertension, atheromatosis, non-alcoholic fatty liver disease, and their long-term impact on cardiovascular health. Histological studies have confirmed several modifications at the tissue level in cardiometabolic disease. Recently, quantitative MR methods have enabled non-invasive myocardial and liver tissue characterization. MR relaxation mapping techniques such as T_1, $T_{1\rho}$, T_2 and T_2* provide a pixel-by-pixel representation of the corresponding tissue specific relaxation times, which have been shown to correlate with fibrosis, altered tissue perfusion, oedema and iron levels. Proton density fat fraction mapping approaches allow measurement of lipid tissue in the organ of interest. Several studies have demonstrated their utility as early diagnostic biomarkers and their potential to bear prognostic implications. Conventionally, the quantification of these parameters by MRI relies on the acquisition of sequential scans, encoding and mapping only one parameter per scan. However, this methodology is time inefficient and suffers from the confounding effects of the relaxation parameters in each single map, limiting wider clinical and research applications. To address these limitations, several novel approaches have been proposed that encode multiple tissue parameters simultaneously, providing co-registered multiparametric information of the tissues of interest. This review aims to describe the multi-faceted myocardial and hepatic tissue alterations in cardiometabolic disease and to motivate the application of relaxometry and proton-density cardiac and liver tissue mapping techniques. Current approaches in myocardial and liver tissue characterization as well as latest technical developments in multiparametric quantitative MRI are included. Limitations and challenges of these novel approaches, and recommendations to facilitate clinical validation are also discussed.

KEYWORDS

cardiometabolic disease, MRI, tissue characterization, mapping, multiparametric mapping

1. Introduction

Quantitative MRI (QMRI) measures physical tissue values, related to the nuclear spin of protons in water. It includes the T_1-, T_2-, T_2*-, $T_{1\rho}$ -relaxation times and the proton density. The respective parameter maps provide quantitative parameter values for each voxel, which carry information about the corresponding structural environment of the protons. QMRI can be used to assess microstructural alterations related to tissue remodeling and has emerged as valuable imaging modality for myocardial and hepatic tissue characterization (1, 2). QMRI has been incorporated in standardized diagnostic clinical protocols in various pathologies, including inflammatory cardiomyopathies (3), amyloidosis (4), Anderson-Fabry disease (5) and iron overload (1, 2, 6). It has also been proposed by both the European Association for the Study of the Liver and the American Association for the Study of Liver Disease as a non-invasive diagnostic tool for tissue characterization in Non-alcoholic Fatty Liver Disease (NAFLD) (7, 8). QMRI facilitates direct quantitative comparison of tissue maps in the same individual with chronic disease over time and allows more accurate longitudinal monitoring of the disease, thereby enabling an individualized characterization and more objective patient assessment.

Cardiometabolic disease, which describes a clustering of disorders that touch upon the interface between cardiovascular disease (hypertension, atherosclerosis) and metabolic disease states (insulin resistance, diabetes, adiposity, NAFLD) (9), is a chronic disease state and a major cause of morbidity worldwide. The reported prevalence is 33–35% in adults and is associated with an increased risk of adverse cardiovascular events and all-cause mortality (10, 11). Cardiometabolic disease is challenging for physicians to manage because it can be present for years before becoming clinically apparent. Histological and functional alterations have been observed in the heart and liver, in addition to the skeletal muscle, liver, pancreas, adipose tissue and microcirculation (12). Numerous studies suggest that QMRI may add valuable information by identifying microstructural tissue damage early in the disease process, allowing for instituting and maintaining optimum health behaviors and treatment strategies, at a time when it is likely to be most effective.

The objective of this review is to provide an overview of parametric QMRI in cardiac and hepatic tissue characterization in cardiometabolic disease. First, we describe cardiac and hepatic tissue structural changes that occur in the primary manifestations of cardiometabolic disease, namely in diabetes, hypertension and atherosclerosis, as a framework for understanding how QMRI can be utilized to assess these changes. Then, we describe single-parameter mapping techniques and their clinical applications in the corresponding disease states. Lastly, we describe emerging multiparametric approaches in heart and liver, which are promising for comprehensive understanding of this multi-faceted disease.

Abbreviations: CMR, cardiovascular magnetic resonance; T2DM, type 2 diabetes mellitus; ECV, extracellular volume; HTN, hypertension; IR, inversion recovery; LGE, late-gadolinium enhancement; LVH, left ventricular hypertrophy; MOLLI, modifier look-locker imaging; MRF, magnetic resonance fingerprinting; NAFLD, non-alcoholic fatty liver disease; NASH, non-alcoholic steatohepatitis; QMRI, quantitative magnetic resonance imaging; SR, saturation recovery.

2. Microscopic tissue alterations in cardiometabolic disease

2.1. Diabetic cardiomyopathy

Type 2 diabetes mellitus (T2DM) is estimated to affect 6% of the world's population (13) and is considered a coronary heart disease risk equivalent (14–17). The pathogenesis of the cardiac morbidity is multifactorial (18, 19). It has been proposed that metabolic modifications induced by hyperglycaemia, insulin resistance and hyperlipidaemia cause an aberrant use of fatty acids for energy generation (20). Fatty acid may saturate ß-oxidation and accumulate in the cytosol, leading to lipotoxic effects. Furthermore, hyperglycemia elicits reactive oxygen species and advanced glycation product formation, which lead to cardiac glucotoxicity. Both, the lack of fuel and lipo/gluco-toxicity as well as disturbances in mitochondrial energetics are triggering cardiac low-grade chronic inflammation, fibrosis and contractile dysfunction (21). Histological studies have confirmed corresponding changes in the myocardium of diabetic patients and animals, including the presence of diffuse myocardial and perivascular fibrosis (22–24; **Figure 1**), increased quantities of matrix collagen, inflammation, myocyte hypertrophy, myocardial steatosis and increased apoptosis (25–29). These pathophysiological changes often evolve quiescently to heart failure; and the prevalence of heart failure in T2DM is ranging from 19 to 26% (30, 31). It is therefore of clinical relevance to comprehend early alterations of cardiac tissue composition in T2DM and the progress from subclinical disease to more advanced disease stage manifesting clinically.

2.2. Hypertensive cardiomyopathy

Arterial hypertension is part of the constellation of disorders that constitute the cardiometabolic disease and is associated with an estimated 54% of strokes and 47% of ischemic heart disease worldwide (32, 33). The pathogenesis of hypertensive heart disease involves primarily cardiomyocyte hypertrophy, providing adaptive response to pressure overload (involving effects of growth factors, cytokines and neurohormones, and genetic predisposition) (34, 35). The alterations in the cellular and non-cellular (extracellular matrix) level induce structural remodeling of the myocardium with fibrosis of the muscle and perivascular space, medial hypertrophy of intramyocardial coronary vasculature, microangiopathy with decreased coronary reserve and development of epicardial coronary stenoses (36, 37). Myocardial fibrosis has been documented histologically in hypertensive hearts in subjects with hypertension (HTN) and left ventricular hypertrophy (LVH) (38). Myocardial fibrosis can be focal, referred to as replacement fibrosis, or diffuse, also known as interstitial fibrosis and is the most typical pattern in hypertensive heart disease (36) (**Figure 2**). Myocardial fibrosis predisposes patients to diastolic and systolic dysfunction, myocardial ischemia, and arrhythmias (39). It has been also demonstrated that treatment with inhibitors of angiotensin converting enzyme reduces collagen content and left ventricular stiffness with potential improvement in diastolic and systolic function, and perhaps outcomes (40). Thus, monitoring myocardial tissue alterations in hypertensive patients could enable risk stratification, inform treatment strategies, and monitor response.

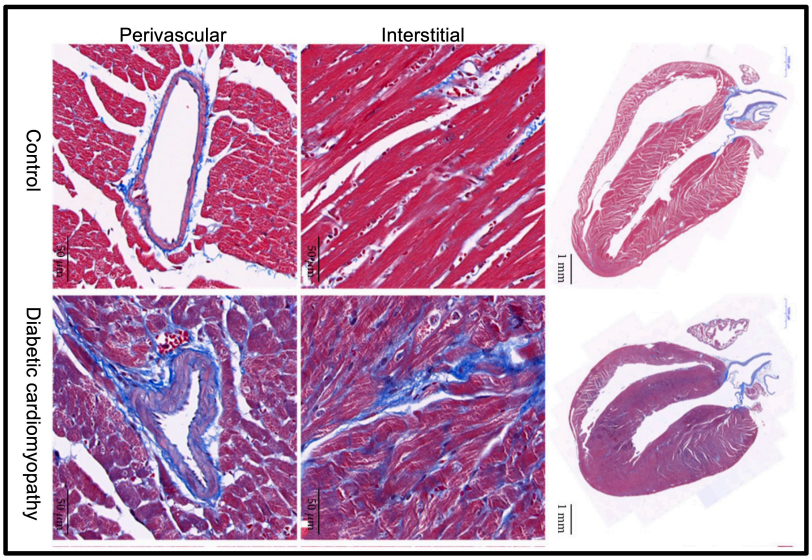

FIGURE 1
Fibrosis plays a crucial role in the development of diabetic cardiomyopathy. Representative images of Masson's trichrome staining of a longitudinal section of the heart of control and diabetic mice (scale bar 1 mm). Magnified views show extracellular collagen deposition in the interstitial (scale bar 50 μm) and perivascular (scale bar 50 μm) space. Compared to the control group, diabetic cardiomyopathy mouse hearts displayed markedly increased collagen content both in the interstitial and perivascular space. Adapted from Li et al. with permission (24).

2.3. Atherosclerotic cardiovascular disease

Atherosclerotic Cardiovascular Disease constitutes an important aspect of cardiometabolic syndrome and remains a leading cause of morbidity and mortality worldwide (41). The atherogenic process is primarily an inflammatory process and consists of several cellular and molecular interactions, including fatty tissue accumulation, platelet aggregation, abnormal vasomotor function, and can potentially culminate in atherosclerotic plaque formation, erosion, rupture or concomitant thrombus formation (42, 43), impeding blood flow and leading to tissue ischemia. In an acute ischemic event, the infarcted myocardial regions undergo a complex process of invasion, transformation and apoptosis of various cell types, including inflammatory cells and myofibrolasts, before remodeling to fibrotic scar tissue. Occasionally lipomatous metaplasia of the scar tissue ensues (44, 45). Fibrosis has also been histologically observed in non-infarcted regions of the heart as a result of left ventricular remodeling in patients with severe coronary atherosclerosis (46, 47). It is hypothesized that coronary artery stenosis, induced by atherosclerosis, impairs perfusion and causes chronic hypoxia with myocyte loss with consequent "reparative" collagen synthesis, contributing to interstitial collagen accumulation (48). Furthermore, there is ample evidence supporting the association of inflammation with the initiation and progression of atherosclerosis (43, 49). Atherectomy specimens have demonstrated the migration of the inflammatory cells in the arterial endothelium and that the inflammatory burden contributes to atherogenesis and adverse events (43).

2.4. Non-alcoholic fatty liver disease

NAFLD is considered the hepatic manifestation of the metabolic syndrome and constitutes one of the most common causes of chronic liver disease, with an estimated worldwide prevalence of around 25% (50). It is characterized by excessive fat accumulation in the hepatic tissue that is not attributable to consumption of alcohol (8). This condition may range histologically from simple non-alcoholic fatty liver, which is considered a benign condition, to non-alcoholic steatohepatitis (NASH), which additionally involves various stages of inflammation to tissue necrosis (8). Evidence from several studies suggests that all-cause mortality and more specifically cardiovascular-related mortality is higher in patients with NASH, and this is independent of the risk conferred by traditional risk factors and components of the metabolic syndrome (51–53). There is therefore a clinical need for reliable non−invasive biomarkers at the tissue level for the assessment of NAFLD and NASH (54).

3. Single-parameter mapping techniques in cardiometabolic disease

Parametric mapping requires the acquisition of a series of weighted images with different contrasts. These contrasts are generated by varying timing parameters such as echo times or inversion times. Fitting the series of weighted images to the corresponding signal model, in a pixel-wise manner, enables the generation of a quantitative map of the tissue relaxation, expressed in units of time (e.g., milliseconds). Single-parameter mapping techniques include T_1 mapping, T_2 mapping, T_2^* mapping and T1rho mapping. Extracellular volume can be generated from native (pre-contrast) and post contrast T_1 mapping. Proton density fat fraction (PDFF) is a ratio, expressed as a percentage, of the fraction of the MRI-visible protons attributable to fat divided by all MRI-visible protons in that region of the liver attributable to fat and water. A brief introduction to each of these maps and their application in cardiometabolic disease is given below. The latter is also summarized

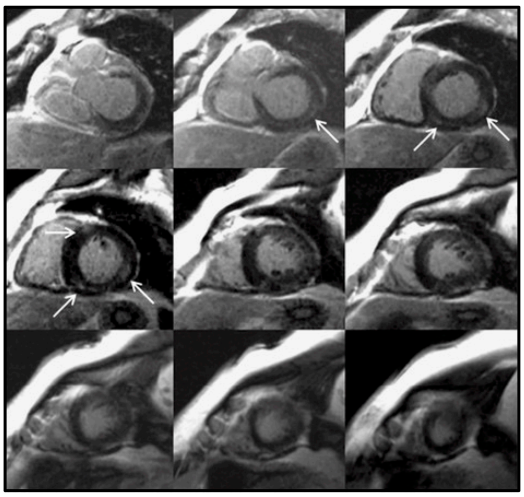

FIGURE 2
Focal myocardial fibrosis in a hypertensive patient. Late gadolinium enhancement in a 63-year-old female patient with longstanding hypertension. The arrows show an area of intramyocardial late gadolinium enhancement in the basal and mid inferoseptal and inferolateral segments. This is not the most typical fibrosis pattern in hypertension, which is usually diffuse. Adapted from Maceira et al. with permission (36).

in **Table 1**. The reader is referred to (55, 56) for further reading about the specific mapping techniques.

3.1. T_1 mapping

T_1 (spin-lattice) relaxation time is the characteristic tissue relaxation constant governing the recovery of longitudinal magnetization (M_z) back to its thermal equilibrium following a radiofrequency pulse. T_1 parametric mapping is conventionally achieved by applying magnetization preparation pulses (e.g., Inversion Recovery (IR) or Saturation Recovery (SR) pulses to encode T1 as in MOLLI (1) or in SASHA (57) respectively) preceding the readout to generate the desired T_1 contrast. The same preparation pulse type is typically applied several times with varying parameter settings, (e.g., inversion delay or saturation delay) to obtain different T_1 contrast weighted images, which are then used for pixel-wise parametric fitting to the expected signal behavior. The need for several weighted images for parametric fitting (e.g., ∼10 for T1 mapping) and the time required to allow for magnetization recovery reduce the efficiency of the sequence, usually limiting it to one or few 2D slices, especially in the case of cardiac imaging, where the readout is synchronized with the ECG and usually performed at the diastolic cardiac phase.

Native T_1 values are prolonged by tissue free water content and are typically shortened by fat and iron. Increased native T_1 values are seen in oedema and during inflammation (3). Increased T_1 values are also seen in areas of fibrosis, due to associated expansion of the extracellular space as seen for example in myocardial infarction (MI) and hepatic fibrosis (58). Controversial results about myocardial T_1 values in diabetic cardiomyopathy have been reported, some studies have concluded significantly increased native T_1 values in the myocardium of diabetic patients in comparison to controls (59–62) (**Figure 3**), while other studies have not found a significant difference (20, 63). Meta-analysis of the relevant studies did not show an association of diabetes with native T_1 time (64). With regards to arterial hypertension, several groups have shown that elevated T_1 values are found in hypertensive subjects with left ventricular hypertrophy (LVH) compared with those with normal left ventricular myocardial mass and controls (38, 65–67). These results suggest that hypertensive patients have increased myocardial fibrosis, but that this is triggered with the onset of LVH rather than earlier. This could also suggest that interstitial changes in early hypertension (pre-LVH) are non-existent or perhaps are small and not detectable with current applications of T_1 mapping technique. These findings have been confirmed by a meta-analysis (68). Additionally, in a cohort of patients with NAFLD versus healthy subjects, native liver T_1 values could differentiate steatotic from non-steatotic livers and showed a strong correlation with history of cardiovascular disease (69).

3.2. T_2 mapping

T_2 (spin-spin) relaxation time is the MR constant governing the decay of transverse magnetization ($M_{x,y}$) and is dependent on spin-spin interactions. T_2 parametric mapping is conventionally achieved by applying T2-preparation pulses, with different time durations, before the readout to encode T_2 (70) and generate the desired T_2 weighted images. T_2 mapping requires the acquisition of ∼3–4 T_2 weighted images including pause heartbeats to allow for magnetization recovery, which collectively reduces the efficiency of the sequence, usually limiting spatial resolution and coverage resulting in the acquisition of only one or a few 2D slices per CMR examination.

T_2 mapping detects tissue free water content and has been shown very useful for detection of myocardial inflammation and oedema in chronic and acute disease settings (71–76). T_2 mapping is also used for the differential diagnosis of acute myocardial infarction as it allows detection of the associated oedema and inflammation caused by the acute immune response (77). Jiang et al., demonstrated that diabetes status is related to increased T_2 values even in asymptomatic individuals, and this is associated with both left ventricular systolic and diastolic function (78). Furthermore, a recent study has demonstrated that there is good correlation between liver T_2 values and histology determined steatosis ($r = 0.780$, $p < 0.001$) and grade of steatosis ($r = 0.779$, $p < 0.001$). Interestingly, a higher correlation between the liver T_2 value and percentage of histological steatosis was observed ($r = 0.838$, $p < 0.001$), after adjusting for the fibrosis stage. A T_2 cut-off value of 65 ms [area under the curve (AUC) ± SE: 0.88 ± 0.07, 95% confidence interval (CI): 0.73–1.00, $p = 0.005$] could discriminate moderate/severe steatosis from none/mild steatosis with a sensitivity of 81%, specificity of 86%, positive predictive value of 85%, and negative predictive value of 82% (79).

3.3. T_2^* mapping

T_2^* time captures the dephasing in transverse magnetization (perpendicular to the strong magnetic field) due to the combined effect of field inhomogeneities and susceptibility induced distortions from the magnetised tissue (e.g., high content of paramagnetic materials such as iron) and the spin-spin relaxation related

TABLE 1 *In vivo* CMR studies with conventional single-parameter mapping techniques in patients with cardiometabolic disease.

References	Study design	Patient characteristics	Reference standards	CMR methods	Accuracy/Correlation
Permutt et al. (100)	Prospective cross-sectional	51 NAFLD adults	51 corresponding biopsies	PDFF	PDFF correlated with histology-determined steatosis, ($r2 = 0.54$, $P < 0.0001$)
Wong et al. (87)	Cross-sectional prospective	231 T2DM adults	945 non-diabetic patients referred for CMR	ECV	ECV: 30% (26.9, 32.7) T2DM vs 28.1% (25.0, 31) HV, $P < 0.001$
Idilman et al. (166)	Retrospective observational	70 NAFLD adults	Corresponding liver biopsies	PDFF	PDFF correlated with biopsy-determined steatosis, ($r = 0.86$, $P = 0.02$) PDFF correlated less strongly with biopsy-determined steatosis when fibrosis was present, ($r = 0.6$ vs $r = 0.859$, respectively; $P = 0.020$) PDFF correlated better in mild hepatic steatosis than that of moderate or severe steatosis ($r = 0.835$ and $r = 0.402$, respectively; $P = 0.003$) PDFF measurement of 15.03% (area under the curve, 0.95; 95% confidence interval: 0.91, 1.00) differentiates moderate or severe steatosis from mild or no hepatic steatosis, with a sensitivity of 93.0% and a specificity of 85.0%, and respective positive and negative predicted values of 91.0% and 88.0%
Tang et al. (104)	Prospective cross-sectional	77 NAFLD adults	77 corresponding biopsies	PDFF	PDFF was significantly correlated with histologic steatosis grade ($\rho = 0.69$, $P < 0.001$). Area under the receiver operating characteristic curves was 0.989 (95% confidence interval: 0.968, 1.000) for distinguishing patients with steatosis grade 0 ($n = 5$) from those with grade 1 or higher ($n = 72$); 0.825 (95% confidence interval: 0.734, 0.915) to distinguish those with grade 1 or lower ($n = 31$) from those with grade 2 or higher ($n = 46$); 0.893 (95% confidence interval: 0.809, 0.977) to distinguish those with grade 2 or lower ($n = 58$) from those with grade 3 ($n = 19$).
Shah et al. (89)	Cross-sectional prospective	11 T2DM obese adolescents	10 non-T2DM obese adolescents 12 HV		ECV: 37.6% (33.6%, 40.7%) T2DM obese vs 32.8% (27.8%, 34.5%) non-T2DM obese, $P = 0.03$ ECV: 26.4% (25.3%, 27.1%) T2DM obese vs 37.6% (33.6%, 40.7%) HV, $P = 0.03$ ECV was associated with hemoglobin A1c ($r = 0.76$, $P < 0.0001$)
Banerjee et al. (110)	Comparative prospective	90 NAFLD/NASH adults	Histological specimens within 1 month 7 HV	Native T1 and T2* Estimated cT1	cT1 correlated with increasing liver fibrosis $r_s = 0.68$, 95% CI 0.54–0.78, $p < 0.0001$
Kuruvilla et al. (38)	Cross-sectional prospective	20 HTN LVH, 23 HTN non-LVH	22 HV	Native T1 ECV	Native T1: 996 ± 32.5 ms HTN LVH vs 967.4 ± 35 ms HV, $P = 0.007$ Native T1: 974.0 ± 33.6 ms HTN non-LVH vs 976.4 ± 35 ms HV, P = not statistically significant ECV: 29% ± 3 HTN LVH vs 26% ± 2 HV, $P = 0.006$ ECV: 27% ± 2 HTN non-LVH vs 26% ± 2 HV, $P = 0.6$
Treibel et al. (67)	Observational prospective	40 well-controlled HTN adults	50 HV		Native T1: 997 ± 27 ms HTN with LVH vs 948 ± 31 ms HTN no LVH, $p < 0.001$ Native T1: 955 ± 30 ms HTN versus 965 ± 38 ms HV, $p = 0.16$ ECV: 27.1% ± 2.7 HTN vs 26.1 ± 2.4, $P = 0.06$ ECV: 28.8 ± 2.8% HTN LVH vs. 26.2 ± 2.2 HTN no LVH, $p < 0.01$)
Doycheva et al. (102)	Prospective cross-sectional	100 T2DM adults	None	PDFF	PDFF, median (IQR): 12.3 (9.2) T2DM NAFLD vs 2.7 (1.9) T2DM no NAFLD, $P < 0.0001$
Levelt et al. (20)	Cross-sectional prospective	46 T2DM adults	20 HV	Native T1 ECV	Native T1: 1,194 ± 32 ms T2DM vs 1,184 ± 28 ms HV, $P = 0.23$ ECV: 29% ± 2 T2DM vs 29% ± 3 HV, $P = 0.77$
Rodrigues et al. (66)	Observational prospective	88 HTN (41 normal LV; 15 Conc-REMDL; Conc-LVH 24; Ecc LVH 8	29 HV	Native T1 ECV	Native T1: 1,031 ± 35 ms HTN normal LV vs 1,024 ± 41 ms HV, p = reported as not statistically significant Native T1: 1,029 ± 45 ms HTN Conc-REMDL vs 1,024 ± 41 ms HV, p = reported as not statistically significant Native T1: 1,054 ± 41 ms HTN Conc-LVH vs 1,024 ± 41 ms HV, $p = 0.007$ Native T1: 1,062 ± 41 ms HTN Ecc-LVH vs 1,024 ± 41 ms HV, $p = 0.017$ ECV: 29% ± 4 HTN Conc-LVH vs 27% ± 3 HTN normal LV, $p < 0.0001$ ECV: 29% ± 4 HTN Conc-LVH vs 26% ± 3 HTN Conc-REMDL, $P = 0.012$, $p < 0.0001$ ECV: 30% ± 3 HTN Ecc-LVH vs 27% ± 3 HTN normal LV, $P = 0.6$ ECV: 30% ± 3 HTN Ecc-LVH vs 26% ± 3 HTN Conc-REMDL, $P = 0.021$
Swoboda et al. (61)	Case-controlled observational	100 T2DM adults (50 ACR+ve T2DM, 50 ACR-ve T2DM)	30 HV	Native T1 ECV	Native T1: 1,232 ± 36 ms T2DM vs 1,210 ± 47 ms HV, $P = 0.0.02$ Native T1: 1,253 ± 66 ms T2DM ACR +ve vs 1,232 ± 36 ms T2DM ACR-ve, $P = 0.05$ ECV: 25.1 ± 2.9 T2DM vs 23.3 ± 3 ms HV, $P < 0.0.001$ ECV: 27.2 ± 4.1 ms T2DM ACR+ve vs 25.1 ± 2.9 ms T2DM ACR-ve, $P = 0.004$

(Continued)

TABLE 1 (Continued)

References	Study design	Patient characteristics	Reference standards	CMR methods	Accuracy/Correlation
Van den Boomen et al. (68)	Systematic review and Meta-Analysis	831 HTN (739 no LVH HTN)	1101 HV	Native T1	HTN patients (with and without LVH) showed a significant difference between T1 values vs HV (SMD: 0.19; 95% CI 0.01–0.37; $I2 = 61\%$; $P = 0.04$) HTN patients without LVH showed no significant difference between the T1 values of HV and HTN patients (SMD: 0.03; 95% CI −0.07–0.13; $I2 = 2\%$; $P = 0.52$)
Shang et al. (63)	Cross-sectional prospective	38 T2DM adults	32 HV	Native T1 ECV	Native T1: 1,213.5 ± 57.5 ms T2DM vs 1,212.8 ± 41.4 ms HV, $P = 0.95$ ECV: 30.4 ± 2.9 T2DM vs 27.1 ± 2.4HV, $P < 0.001$ ECV correlated with duration of diabetes ($R = 0.539$, $P = 0.0005$)
Cao et al. (59)	Cross-sectional prospective	50 T2DM patients	50 BMI-matched HV	Native T1 and ECV	ECV: 27.4 ± 2.5% vs. 24.6 ± 2.2%, $p < 0.001$ native T1: 1,026.9 ± 30.0 ms T2DM vs. 1,011.8 ± 26.0 ms HV, $p = 0.022$ Native T1 values correlated with the hemoglobin A1c levels (standardized $\beta = 0.368$, $p = 0.008$) ECVs were associated with the HbA1c levels (standardized $\beta = 0.389$, $p = 0.002$)
Lam et al. (60)	Cross-sectional prospective	27 T2DM patients	10 HV	Native T1	Native T1: 1,056 ± 31 ms T2DM vs 1,016 ± 21 ms HV, $P = 0.00051$) Native T1 values correlated with the hemoglobin A1c levels ($\rho = 0.43$, $P = 0.0088$) ECV: 25% ± 0.03 T2DM vs 26% ± 0.02 HV, $P = 0.47$
Gulsin et al. (91)	Cross-sectional prospective	75 T2DM HFpEF adults	65 non-diabetic HFpEF adults	ECV	ECV: 28 ± 5 T2DM HFpEF vs 28 ± 5 non-diabetic HFpEF, $P < 0.683$
Chirinos et al. (90)	Retrospective cross-sectional	32 T2DM HFpEF adults	21 non-diabetic HFpEF adults		ECV: 30.4% T2DM HFpEF vs 27.1% non-diabetic HFpEF, $P = 0.10$
Kucukseymen et al. (62)	Retrospective observational	36 T2DM HFpEF obese adults	45 HV	Native T1	Native T1: 1,129 ± 25 ms T2DM HFpEF vs 1,071 ± 27 ms HV, $P < 0.001$ Native T1: 1,162 ± 37 ms T2DM HFpEF obese vs 1,071 ± 27 ms HV, $P < 0.0.01$
Arcari et al. (65)	Cross-sectional prospective	163 HTN	133 HV		Native T1: 1,102 ± 42 ms HTN vs 1,062 ± 39 ms HV, $P < 0.001$ Discrimination of HTN versus HV: AUC 0.98 (0.93–0.99)
Jiang et al. (78)	Prospective observational	135 T2DM adults	Age-, sex- and BMI-matched 55 HV	Native T1 Pre-contrast T2	Native T1: 1,242.6 ± 230.3 ms T2DM vs 1,209.2 ± 181.7 ms HV, $P = 0.439$ Pre-contrast T2: 41.79 ± 3.41 ms T2DM vs 40.48 ± 2.63 ms HV, $P = 0.009$ ECV: 32.61 ± 4.62 ms vs 27.53 ± 3.05 ms, $P < 0.001$
Bojer et al. (93)	Prospective cross-sectional	264 T2DM adults (207 without LGE, 29 ischemic LGE, 25 non-ischemic LGE, 3 both ischemic and non-ischemic LGE)	25 sex-matched HV	ECV	ECV: 32.2 ± 3.8 T2DM with LGE (ischemic and non-ischemic lesions) vs 28.8 ± 2.7 T2DM without LGE, $P < 0.0001$ ECV: 28.8 ± 2.7 T2DM without LGE vs 26.1 ± 1.5 HV, $P < 0.0001$ ± 3.1 T2DM with non-ischemic LGE vs 28.8 ± 2.7 T2DM without LGE, $P = 0.01$
Khan et al. (88)	Prospective observational	70 T2DM 76 pre-diabetic	296 HV		T2DM was associated with elevated ECV after adjusting for clinical and imaging covariates: β coefficient 1.33 (95% CI, 0.22–2.44); $P = 0.02$ ECV 30% Hazard Ratio for composite events, 3.31 (1.93–5.67), $P < 0.001$
Erden et al. (69)	Observational prospective	83 NAFLD adults	26 HV Liver biopsy for 44 patients		Native T1 MOLLI 3(3)3(3)5: 766.2 (561.2–2,210.2) vs 595.6 (457.6–644.6), $P < 0.001$ Native T1 MOLLI 5(3)3: 656.2 [502.9–1,028.1 vs 564.8 (445.4–605.4)], $P < 0.001$ Native T1 MOLLI 3(2)3(2)5: 744.6 (538.5–2221.5) vs 582.2 (464.0–637.4), $P < 0.001$ Native T1 MOLLI 5(3)3hrc: 638.3 (465.6–931.1) vs 556.8 (442.1–465.6), $P < 0.001$ T2 FLASH: 42.0 (33.2–44.1) NAFLD vs 41.4 (34.0–44.8), $P = 0.13$ T2 TrueFISP: 49.5 (39.4–55.1) NAFLD vs 49.1 (45.1–53.1), $P = 0.679$ Differentiating NAFLD and control group: Native T1 MOLLI 3(3)3(3)5 AUC: 0.976, Accuracy% (95%CI): 94.5 (90.2–98.8), Sensitivity% (95% CI): 92.8 (85.1–96.6), Specificity%: (95% CI) 100 (87.1–100), $P < 0.001$ Differentiating severe steatosis from mild/moderate steatosis Native T1 3(3)3(3)5: AUC: 0.995, Accuracy% (95%CI): 98.7 (96.3–100), Sensitivity% (95% CI): 100 (74.2–100), Specificity% (95% CI): 98.5 (92.1–99.7), $P < 0.001$
Laohabut et al. (92)	Retrospective cohort	188 T2DM adults undergoing CMR for ischemia or viability	551 non-T2DM adults undergoing CMR for ischemia or viability	Native T1 ECV	Native T1: 1,335 ± 75 T2DM vs 1,331 ± 58, $P = 0.516$ ECV: 30.0 ± 5.9 T2DM vs 28.8 ± 4.7, $P = 0.004$ High ECV (HR: 2.01, 95% CI: 1.03–3.93) was identified as independent predictors of cardiovascular events

(Continued)

TABLE 1 (Continued)

References	Study design	Patient characteristics	Reference standards	CMR methods	Accuracy/Correlation
Idilman et al. (79)	Retrospective observational	23 NAFLD adults (with NASH and without NASH)	Corresponding biopsy	Pre-contrastT2	Pre-contrast T2: 69 ± 7.37 ms NASH vs 61.73 ± 5.99 ms NAFLD without NASH, $p = 0.016$ Pre-contrast T2: 65.44 ± 8.56 NAFLD with lobular inflammation vs NAFLD without lobular inflammation 63.87 ± 5.1 ms, $p = 0.640$ Pre-contrast T2: 68.75 ± 9 NAFLD with portal inflammation vs 64.31 ± 7.3 ms, NAFLD without portal inflammation, $p = 0.347$ Pre-contrast T2 correlated with histology-determined steatosis: $r = 0.780$, $p < 0.001$ Pre-contrast T2 correlated with grade of steatosis: $r = 0.779$, $p < 0.001$ Liver T2 did not correlate with fibrosis stage: $r_s = -0.299$, $p = 0.165$ Liver T2 correlated with fibrosis stage after adjusting for steatosis: $r = -0.536$, $p = 0.012$ T2 value 65.01 ms discriminated moderate/severe from none/mid steatosis: (area under the curve [AUC] ± SE: 0.875 ± 0.073, 95% confidence interval [CI]: 0.73–1.00, $p = 0.005$), with a sensitivity of 81.3%, specificity of 85.7%, positive predictive value of 85%, and negative predictive value of 82.1%
Salvador et al. (64)	Systematic review and Meta-Analysis	5,053 T2DM		Native T1 ECV	T2DM is associated with a higher degree of MF assessed by ECV% (13 studies; mean difference: 2.09; 95% CI: 0.92–3.27) but not by native T1 (21.74; 95% CI: −1.27 to 44.75).

ACR+ve, albumin: creatinine ratio (indicating persistent micro-albuminuria) positive; ACR-ve, albumin: creatinine ratio (indicating persistent micro-albuminuria) negative; [AUC] ± SE, area under the curve ± standard error; BMI, body mass index; CMR, cardiac MRI; Conc-REMDL, concentric-remodelling; Conc-LVH, concentric left ventricular hypertrophy; cT1, corrected T1; Ecc LVH, eccentric left ventricular hypertrophy; ECV, extra-cellular volume; HbA1c, hemoglobin A1c; HTN, hypertension; HV, healthy volunteers; LGE, late gadolinium enhancement; LVH, left ventricular hypertrophy; MF, myocardial fibrosis; NAFLD, non-alcoholic fatty liver disease; PDFF, proton-density fat fraction; T2DM, type 2 diabetes mellitus.

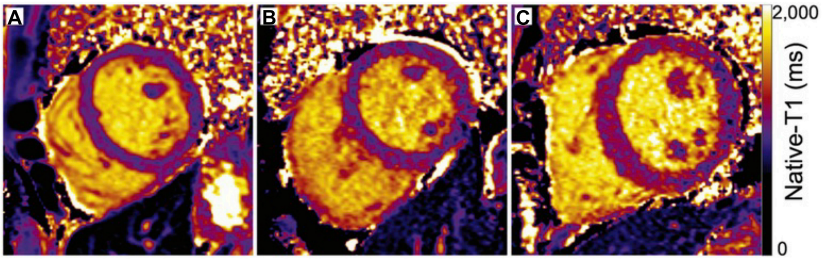

FIGURE 3
Maps of native-T1 relaxation times in **(A)** a healthy control and **(B)** a diabetic adult with normal left ventricular structural parameters demonstrate similar global mean T1 relaxation times (**A**: 1014 ms, **B**: 1023 ms). **(C)** In contrast, elevated native-T1 relaxation times within the septum, anterior wall, and inferior right ventricular insertion area of a diabetic adult with increased septal wall thickness (1.4 cm) and elevated mass-to-volume ratio (1.4 mg/ml) result in a longer mean left ventricular native-T1 time (**C**: 1,095 ms) compared to either **A** or **B**. Adapted from Lam et al. with permission (60).

dephasing. The T_2^* relaxation time values are always shorter than or equal to T_2. Routine evaluation of liver and heart iron content using T_2^* mapping is indicated in patients with suspected iron overload, for instance due to frequent transfusions in thalassaemia and sickle cell patients (80, 81). Increased iron can be co-existing in NAFLD and other chronic liver diseases (82) and emerging evidence suggests that liver iron deposition is associated with worse histopathological features of NASH and disease progression. T_2^* based imaging thus could be used clinically if integrated into clinical guidelines to identify such patients (83, 84). Additionally, iron may interfere with liver T_1 estimation and thus might contribute to lower accuracy in tissue characterization, if not corrected for.

3.4. Extracellular volume

The estimation of the extracellular volume (ECV) is based on the intravenous injection of extracellular gadolinium-based contrast agent (GBCA) with non-protein-bound volume distribution and can be measured using pre- and post-contrast T_1 mapping (85). The underlying principle is that the T_1 shortening effect of an extracellular GBCA is directly related to its tissue concentration. The relationship between ECV in the myocardium and blood is approximated by Equation 1, where the change in $1/T_1$ in the tissue and blood pool is used to determine contrast agent concentrations, the ratio of which yields an estimation of ECV, following a correction for red blood cell density in the blood pool (haematocrit, Hct).

$$\text{ECV myocardium} = \frac{\left(\frac{1}{T1\text{myo}_{\text{postGd}}} - \frac{1}{T1\text{myo}_{\text{native}}}\right)}{\left(\frac{1}{T1\text{blood}_{\text{postGd}}} - \frac{1}{T1\text{blood}_{\text{native}}}\right)} * (1 - \text{Hct})(86) \quad (1)$$

CMR studies have demonstrated, that ECV was significantly higher in HTN LVH subjects versus controls (0.29 ± 0.03 vs. 0.26 ± 0.02, $p < 0.01$) and HTN non-LVH subjects (0.29 ± 0.03 vs. 0.27 ± 0.02, $p = 0.05$) (38, 66). CMR studies showed controversial results with regards to the association of diabetes with increased ECV. Several studies demonstrated that increased ECV is present in diabetic subjects in comparison to controls (20, 59, 61, 63, 78, 87–92). This was found to weakly correlate with hemoglobin A1c levels

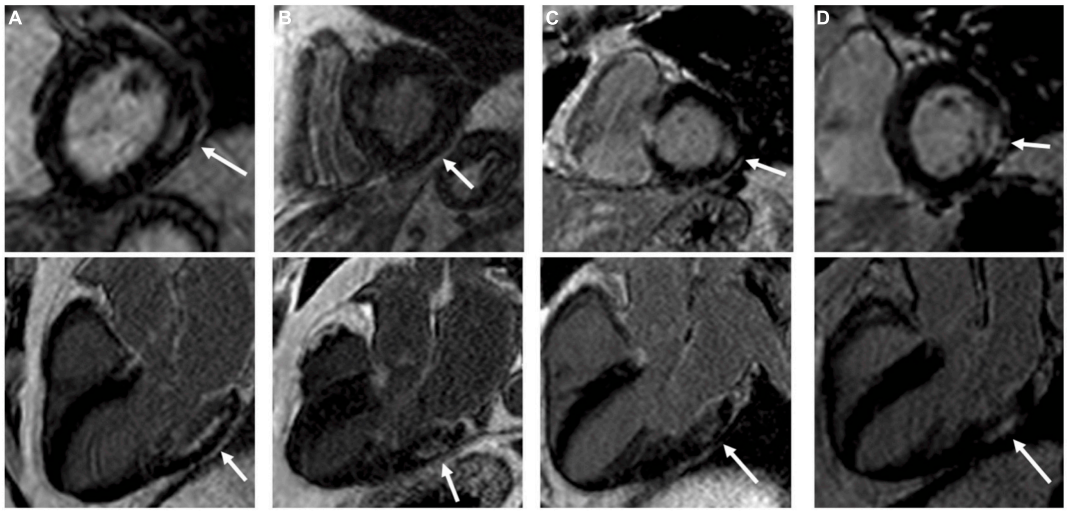

FIGURE 4
Four type 2 diabetes mellitus patients **(A–D)** with typical non-ischemic late gadolinium enhancement (LGE) lesions with left ventricular short-axis and long-axis images. Non-ischemic lesions are located mid-myocardial, basal and lateral or inferolateral. In segments with non-ischemic LGE lesions, the myocardium remains thick. Adapted from Bojer et al. with permission (93).

(59, 89) and the duration of diabetes (63). It was also associated with mortality and/or incident of heart failure admission (87), and constituted an independent risk factor for adverse cardiovascular outcomes (88, 92). It was also associated with late gadolinium enhancement (LGE) lesions that could not be explained by previous infarcts (non-ischemic LGE lesions) and prevalent complications of diabetes (retinopathy, autonomic neuropathy) (93; **Figures 4**, **5**). On the contrary, dissimilar results with regards to the association of diabetes with increased ECV have been suggested by other groups (20, 60, 88, 91, 94, 95). A recently published meta-analysis concluded that diabetes was associated with increased ECV but not with native T_1 increase and increased ECV was also associated with poor glycaemic control (64).

3.5. $T1_\rho$ mapping

$T1_\rho$ (T1rho) measures the spin-lattice relaxation in the rotating frame, and is a sensitive marker for probing macromolecular water interaction (96). $T_{1\rho}$ has been demonstrated to be sensitive to oedema and fibrotic scar in chronic myocardial infarction. Application of non-contrast $T1_\rho$ -mapping in CMR has been reported to discriminate between infarcted and healthy myocardium in animal models (97). Oedema also induces enhancement in $T1_\rho$ values, as demonstrated in the area-at-risk in acutely ischemic myocardium, in acute myocarditis and Takotsubo cardiomyopathy (98, 99). This mapping technique sequence is yet to be routinely used in clinical practice. Nevertheless, both oedema and fibrosis are present in the myocardium and liver in NAFLD and future clinical validation in this patient group is warranted to assess its clinical utility as a potential biomarker.

3.6. Proton density fat fraction

Proton density fat fraction (PDFF) is a ratio, expressed as a percentage, of the fraction of the MRI-visible protons attributable to fat divided by all MRI-visible protons in that region of the liver attributable to fat and water. Taking advantage of the chemical shift between fat and water, pulse sequences can be used to acquire images at multiple echo times at which fat and water signals have different phases relative to each other (2). MRI-determined PDFF correlates with histologically determined steatosis grade in patients with NAFLD and has been utilized for the assessment of NAFLD in T2DM patients (100, 101) (102). The diagnostic accuracy of MRI-PDFF was further validated by Idilman et al. (103) and Tang et al. (104), both of which demonstrated that MRI-based PDFF assessments correlated closely with histology as assessed by liver biopsy ($r = 0.82$) and explant *ex vivo* histology assessment ($r = 0.85$). Idilman et al. noted that the presence of hepatic fibrosis reduced the correlation between biopsy results and PDFF (103).

4. Multiparametric approaches in quantitative MR

Cardiac and liver QMRI, including T_1, T_2 and ECV mapping, have emerged as an approach to quantify tissue properties in cardiometabolic disease. Furthermore, in the past years, there has been a growing interest in alternative parameters that may add complementary information. For instance, several studies have shown that $T1_\rho$ could be an alternative for the detection of liver (105–107) and myocardium fibrosis (98, 108, 109) without the need of an external contrast agent injection. Nevertheless, at the moment, in clinical practice each quantitative parameter is investigated individually. As a result, sequential, lengthy scans are required to capture multiple parameters in order to accurately describe the various disease phenotypes of cardiometabolic disease (1, 110–112).

Simultaneous multiparametric QMRI, in which the parameters of interest are obtained from a single scan have recently gained attention. An important aspect of this approach is that the parameters should no longer be confounded by each other, promising reliable quantification of the individual parameters in shorter scan time. For

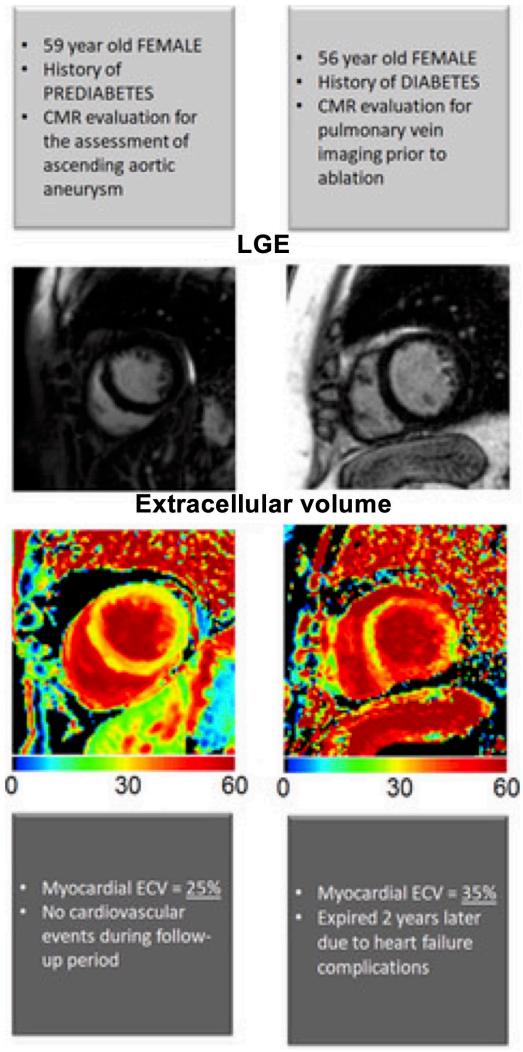

FIGURE 5
Late gadolinium enhancement images and extracellular volume fraction (ECV) maps by diabetic status. Example of two patients, with prediabetes and diabetes mellitus. Both patients had no late gadolinium enhancement (indicative of replacement fibrosis). The patient with diabetes mellitus had significantly higher amount of ECV (indicative of interstitial fibrosis) compared to the patient without diabetes mellitus. CMR indicates cardiac magnetic resonance. Adapted from Khan et al. with permission (88).

instance, liver T_1 values have been shown to depend strongly on iron content necessitating an additional measurement for liver iron, such as T_2*mapping, for interpretation of T_1 values (113). Recent studies in adult and pediatric patients with NAFLD also suggest that hepatic PDFF and T_2* are strongly correlated with each other *in vivo*. This relationship was observed using different MRI techniques and therefore PDFF and T_2* value should be considered together when interpreting each of those in human liver (114, 115). Finally, it has been observed that liver fat declines in patients with advanced fibrosis (burnt-out NASH), hence disease progress can be misinterpreted if NAFLD is screened with PDFF for steatosis only (102).

Several models of simultaneous multiparametric QMRI have been investigated in research studies, including methods like joint multiparametric mapping or transient-state imaging approaches (116, 117), magnetic resonance fingerprinting (MRF) (118) and magnetic resonance multitasking (119). Each of them follows a different technical approach, but with the shared goal of providing as many different parametric maps as possible within a single scan. A brief description of each of these and their potential to improve the clinical assessment of cardiometabolic disease is discussed hereafter.

4.1. Joint multiparametric mapping

In cardiac MRI, several 2D joint parametric mapping approaches have been proposed. With these approaches the acquisition sequence is generally designed to encode T_1 and T_2 simultaneously. Blume et al. (120) (steady-state) and Kvernby et al. (121) (transient state) employed interleaved T_2-preparation and Inversion Recovery (IR) preparation pulses for T_2 and T_1 encoding, respectively. Akçakaya et al. (122) and Guo et al. (123) also used T_2-preparation for T_2 encoding but replaced the IR by SR for T_1 encoding to make the sequence less dependent to heart rate variation. Another approach was proposed by Santini et al. (124); in this case, an IR pulse provides T_1 encoding, and the subsequent continuous balanced-Steady-State-Free-Precession readout provides the T_2 encoding.

The multiparametric maps from the aforementioned approaches are obtained after pixel-wise fitting to a sequence-dependent model. However, the need of resting periods for magnetization recovery and the use of breath-holds results in low spatial resolution, limited coverage, and motion artifacts if patients are unable to hold their breath. Applications for cardiac imaging, that sought to address these issues and to enable the acquisition in a clinically-feasible scan time have also been proposed (125) (126; **Figure 6A, B1, B2**). Those rely on "dictionary matching." Using this approach, a dictionary is generated which is a compendium of possible signal evolutions for a set of combinations of parameters of interest (such as T_1 or T_2), which can be calculated, for example with Bloch simulations (118) or the Extended Phase Graph (127) formalism. The "multi-parametric MR signal" of every pixel is then compared against all entries included in the dictionary by pattern matching (e.g., dot product or least square), to estimate the parameter combination that best represents the measured signal evolution. Dictionaries can also be employed to predict the signal evolution of the transient state; as proposed in MRF. There exist also several examples of multiparametric approaches which were proposed for liver imaging, including water/fat-separated T_1 mapping (MP-Dixon-GRASP) (128) along with PDFF imaging and water-specific T_1 mapping [T1(Water)] (PROFIT$_1$) (113). An alternative approach has been proposed by Pavlides et al. This includes T_1 mapping for fibrosis/inflammation imaging and T_2* mapping for liver iron quantification. The T_1 measurements of this method are adjusted for the iron level, as high iron levels in the presence of fibrosis can lead to "pseudo-normal" T_1 values. This was achieved by integrating the results from shortened-MOLLI T_1 maps and T_2^* maps in an algorithm that allows to correct for the bias introduced by elevated iron in the T_1 measurements, yielding iron−corrected T_1 maps (110, 129). In total, seventy−one patients with suspected NAFLD were recruited within 1 month of liver biopsy and the performance of multiparametric magnetic resonance for the assessment of NASH and fibrosis was evaluated using histology as reference standard (130; **Figure 7**). Fibrosis stage as analysed on biopsy correlated with MRI-estimated inflammation and fibrosis (r_s = 0.51, P < 0.0001). The AUC using this multi-parametric approach for the diagnosis of cirrhosis was 0.85 (95% CI: 0.76–0.95; P = 0.0002) and for the diagnosis of mild vs significant NAFLD was

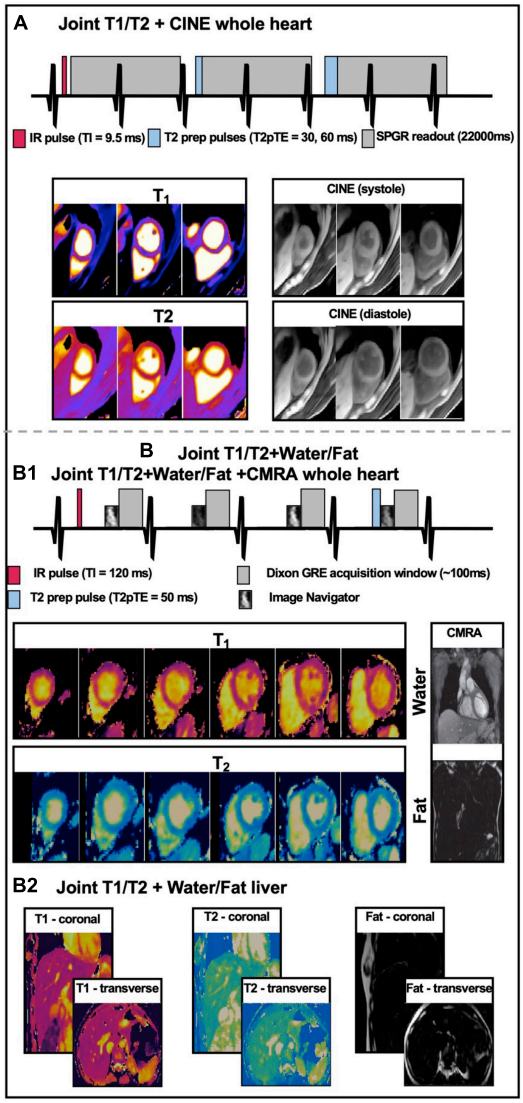

FIGURE 6
Simplified sequence diagram and corresponding images for three multi-parametric acquisition frameworks. **(A)** Short-axis T_1 and T_2 maps, and CINE images at apical, mid-ventricular, and basal levels obtained from a single joint T_1/T_2 + CINE free-running whole-heart scan. Figure adapted with permission from Qi et al. (128). **(B1)** Short-axis T_1 and T_2 map slices and a representative slice of water and fat CMRA images, obtained from a single joint whole-heart T_1/T_2 mapping + Water/FAT CMRA whole heart free-breathing isotropic scan. **(B2)** Representative coronal and transverse slices of joint T_1, T_2 maps and Fat images from a 3D isotropic free-breathing liver acquisition.

0.89 (95% CI: 0.80–0.98%; $P < 0.0001$). This prospective pilot study demonstrated the potential of multiparametric QMRI to assess the overall disease severity in patients with NAFLD.

4.2. Magnetic resonance fingerprinting

Most of joint multiparametric approaches presented above are based on steady state imaging and/or discrete sampling of few timepoints along the exponential signal decay, followed by magnetization recovery of the signal and then fit to a certain signal model. There are, however, alternatives like MRF (118) that rely on transient state imaging to generate co-registered multiparametric maps in a single highly efficient scan. In MRF, acquisition parameters such as flip angle and/or repetition time vary pseudo-randomly (**Figure 8A1**) throughout the scan to generate a unique signal evolution for every tissue, the so-called "fingerprint," defined by different combination of T_1, T_2 and other parameters of interest, when encoded. Parametric encoding can also be increased by interleaving magnetization preparation (e.g., IR or T_2-preparation) blocks at certain timepoints, similarly to the joint steady-state multiparametric approaches described above (**Figure 8A2**). In order to obtain a high temporal resolution (i.e., a large number or timepoints in the signal evolution) in an efficient manner, high acceleration factors and thus, highly undersampled images are obtained (**Figure 8B**). In parallel, a dictionary containing a sufficiently large and representative number of combinations of parameters of interest (e.g., T_1 or T_2) is generated using the specific acquisition parameters (**Figure 8C**).

The "fingerprint" of every voxel is then compared against all the possibilities or entries included in the dictionary by pattern matching to estimate the parameter combination that best explains the measured signal evolution (**Figure 8D**). In this way, multiparametric co-registered quantitative maps are generated within a single scan (**Figure 8E**). This dictionary can be reutilized in the subsequent scans provided that the acquisition parameter patterns remain unchanged, which is, however, not the case for cardiac imaging due to subject-specific heart rate variations.

Hamilton et al. (131) proposed for the first time the application of the MRF framework for an ECG-trigged scan for simultaneous T_1, T_2 and M_0 characterization of myocardial tissue. However, given the high flexibility that MRF provides for the extension of the sequence to encode additional parameters, several works have been proposed to extend cardiac MRF to multiparametric assessment, including simultaneous cardiac T_1/T_2 maps and PDFF, simultaneous T_1, T_2 and $T1\rho$ cardiac MRF and simultaneous T_1, T_2, PDFF and T_2^* acquisition (132) (133, 134).

Some of these approaches have been evaluated in healthy subjects (135, 136) and small patient cohorts (137) (138) (139).

For liver imaging, Chen et al. (140) proposed a robust MRF framework where T_1 and T_2 2D maps are obtained on a 3T scanner. This framework has been further extended to include 2D T_1, T_2, T_2^* and PDFF mapping in a 14s breath-hold acquisition (141) and initial clinical validation against histological grading from liver biopsies in a cohort of 56 patients with diffuse liver disease has been performed (142). Further advances include evaluating T_1, T_2, T_2^*, PDFF and $T_{1\rho}$ mapping (143).

Future clinical validation studies of the aforementioned methods for comprehensive cardiac and liver tissue characterization in cardiometabolic disease are anticipated.

4.3. Magnetic resonance multitasking

Magnetic resonance multitasking is an alternative approach that enables multiparametric assessment along with the visualization of cardiac and respiratory motion from a single scan. This technique is based, by definition, on a continuous acquisition in which all the possible signal evolutions that are taking place due to different image dynamics (i.e., how the signal would evolve throughout the acquisition due to magnetization relaxation, cardiac or respiratory motion, contrast agent pharmacokinetics or any other cause)

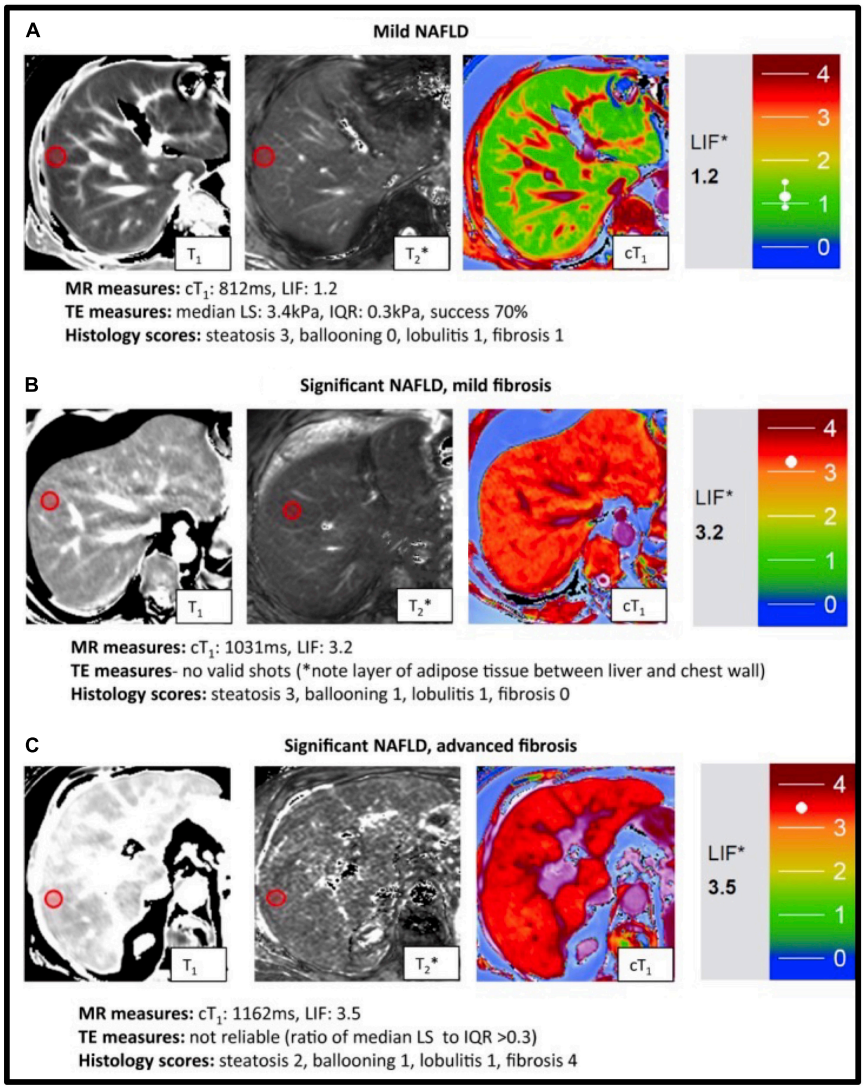

FIGURE 7
Representative magnetic resonance data with the corresponding transient elastography (TE) and histology data from patients with known or suspected non-alcoholic fatty liver disease NAFLD. T1, T2* mapping values were used to derive the calculated corrected T_1 maps (cT1) maps and Liver Inflammation and Fibrosis (LIF) scores. Patients were classified based on biopsy findings, using the Fatty Liver Inhibition of Progression (FLIP) algorithm (92), as having: mild disease **(A)**, significant disease/mild fibrosis **(B)** and significant disease/advanced fibrosis **(C)**. Red circles indicate typical regions of interest. There was a significant association between histological fibrosis and MRI LIF scores. Adapted from Pavlides et al. with permission (130).

are stacked as extra temporal dimension or "tasks" in a high dimensional low rank tensor. In the original work, Christodoulou et al. proposed (119) a cardiac MR multitasking approach where a T_2-IR prepared free-breathing acquisition leads to simultaneous and motion-resolved T_1, T_2 and functional assessment within a single ~60 s ECG-free scan. At Nyquist sampling rate, the high number of time dimensions considered for this matter would require prohibitive scan times. Christodoulou et al. exploited the low-rank property of the generated tensor, thus the redundant and highly spatio-temporally correlated information is leveraged during the image reconstruction step (**Figure 9**). Feasibility of the proposed technique has been shown in myocardial T_1 and ECV mapping (144) and of multi-slice motion-resolved joint T_1/T_2 cardiac mapping in a single 3-min free-breathing scan (145). Furthermore, in a recent work, Wang et al. (146) proposed the feasibility of simultaneous 3D quantification of water specific T_1, PDFF and T_2^* in a single 5-min scan. Future studies with larger patient cohorts for both heart and liver are warranted for robust clinical validation.

4.4. Technical challenges of quantitative MR

Parametric mapping has been widely adopted in clinical practice and constitutes a complementary imaging biomarker in several pathologies. In the theoretical realm, parameters maps depend on the interaction of physics (MRI signal) and the underlying tissue biology. Nevertheless, in clinical practice, several limitations need to be acknowledged, as most mapping techniques depend on several confounding factors. Relaxation time is the result of the combination of the subject, hardware, acquisition, reconstruction algorithm, and map analysis that were used; consequently, all steps in obtaining a relaxation time can add bias or uncertainty to its measurement.

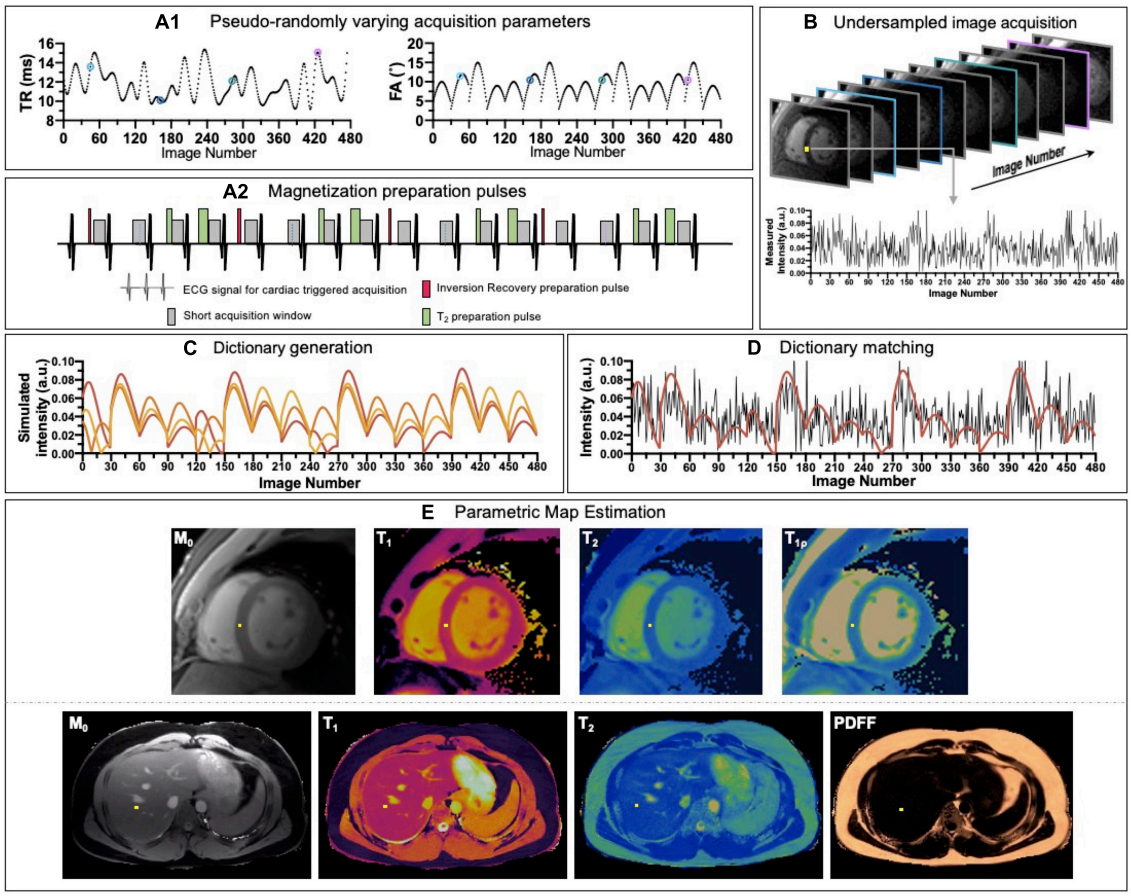

FIGURE 8
Schematic overview of a cardiac/liver MRF framework. **(A1)** Acquisition parameters such as repetition time (TR) and variable flip angles (FA) may be pseudo-randomly varied throughout acquisition and **(A2)** magnetization preparation pulses are introduced to increment contrast weighing on the desired parameters. **(B)** Highly undersampled images are obtained, and **(C)** a dictionary of different signal evolutions for a range of T_1/T_2 (and other parameters of interest) combinations are calculated in parallel. **(D)** Matching the temporal evolution of the signal measured with the dictionary will provide **(E)** inherently co-registered parametric maps of the scanned region.

A comprehensive review on this scope can be found in Ogier et al. (147). In brief, patients' heart rate, breathing pattern along with scanner characteristics, such as magnetic field and coils array affect the derived map. With regards to the acquisition and reconstruction techniques, well-established confounding factors include the pulse sequence choice, which is known to affect the quantification of the parameter to be mapped, due to the particular technical and physical limitations of chosen sequence (148). For instance, for T_1 mapping, different sequences such as MOLLI, shMOLLI, SASHA or SAPPHIRE show different accuracy and precision, as shown by Roujol et al. (149), and dedicated comparative studies have been done to determine which offers better diagnostic power (150). This is also the case for T_2 mapping, where the use of dedicated T_2-prep pulses is known to provide significantly underestimated T_2 values compared to spoiled gradient echo and multi-echo spin echo sequences (151). Prior work has also suggested steady-state preparation schemes to reduce the oscillations that occur in the transient state of steady state free precession due to off-resonance, and the linear flip angle approach was shown to have a superior performance in the presence of large off-resonance frequencies (152). Furthermore, k-space readout, be it linear or centric, has been shown to affect accuracy and precision in T_2 mapping (148). Similarly, T1rho relaxation is dependent on the applied spin-locking frequency. Additionally, the widely used MOLLI T_1-mapping sequence is recognized to be confounded by alterations in T_2, and linear T2prepared balanced steady state free precession values are confounded by T_1. On some occasions, parameter estimation errors arise when estimating a single parameter without taking into account the effect of other parameters that are inherently coupled; T_2-prepared sequences will be more prone to T_2^* susceptibility artifact due to imperfect refocusing of the signal during the preparation whereas T_1 quantification in the presence of iron will be biased and a corrected T_1 (cT_1) is required (130). Other sources of quantification variability such as magnetization transfer (153) or partial volume (154) may affect accuracy and precision. Promisingly, some of these effects can be eliminated or diminished with multi-parametric sequences such as MRF or CMR Multitasking, where several parameters of interest are estimated at the same time for each voxel, removing mis-registration inaccuracies and reducing estimation biases, furthermore multiple corrections can be included on the framework (119, 155–158). Unfortunately, the reproducibility of the aforementioned techniques is still impacted by confounding factors. In particular, multitasking and fingerprinting techniques, where modeling of the signal evolution is utilized to calculate the parameters, error liability is possible where not all influences on signal evolution are included in the model (148) (e.g., the cumulative effect of magnetisation transfer in MOLLI sequence, partial volume,

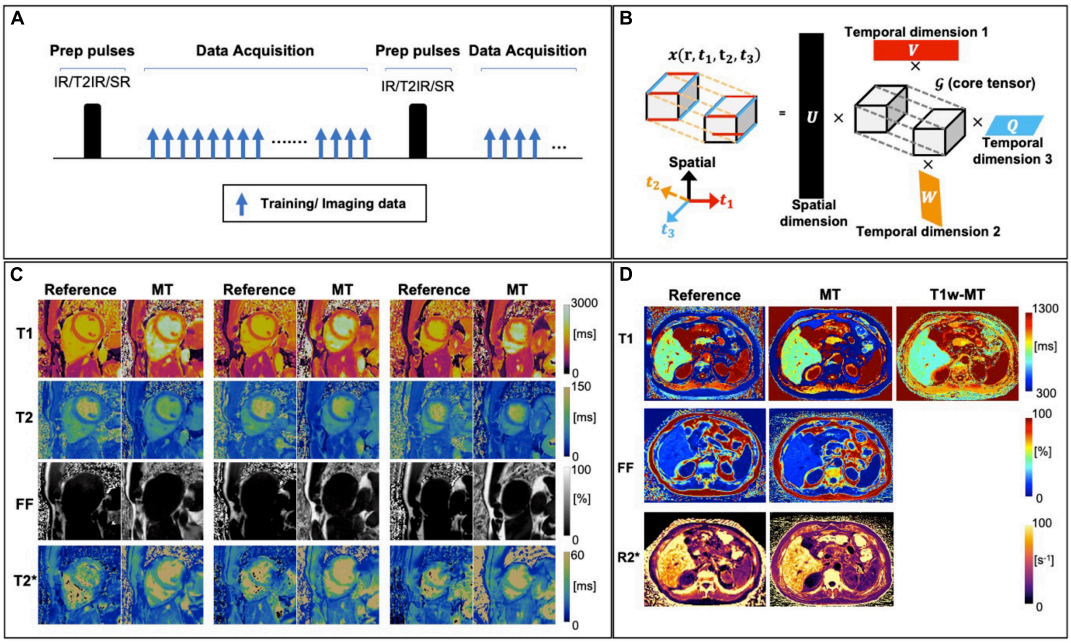

FIGURE 9
(A) A generic sequence diagram for Multitasking technique. The continuous acquisition cycles through different preparation modules (e.g., IR, T_2-IR, and SR), with FLASH excitations filling the entire recovery period. The training and imaging data are collected in an interleaved way, for resolving temporal and spatial information, respectively. **(B)** An illustration of multi-dimensional image. In this example, the image tensor contains one spatial dimension *r* and three temporal dimensions (can be T1/T2/T2* relaxation, resp motion, cardiac motion, etc.) and its low−rank tensor structure can be explicitly expressed through tensor factorization between 4 sets of basic functions (U, V, W, Q) and a core tensor $\mathcal{G}$. **(C)** Representative reference and Multitasking cardiac T_1, T_2, FF, and T_2^* maps from a healthy volunteer. **(D)** Representative reference and Multitasking liver T1, T1w (water T1), FF, and R2* maps from a patient with non-alcoholic steatohepatitis. Adapted from Cao et al. (59) and Wang et al. (146).

off-resonance effects, magnetisation transfer) (158). Considering those effects on dictionary generation can minimize imperfections. Additionally, the increase of the number of parameters to be estimated for a given number of data points also leads to an increase in the complexity of the acquisition/reconstruction and may affect accuracy and precision as well as increasing computational demands.

4.5. Future perspectives for clinical integration of QMRI in cardiometabolic disease

Significant progress has been made to-date to better understand the histological alterations of cardiac and hepatic tissue in cardiometabolic disease and their potential correlation to QMRI techniques. The quantification of cardiac fibrosis in T2DM has been extensively studied with T1 mapping and ECV methods and this has been associated with adverse cardiovascular events. Several pilot studies have also demonstrated myocardial fibrosis in hypertension. Parametric tissue characterization has demonstrated hepatic fibrosis, steatosis and inflammation in proof-of-principle studies in NAFLD. Nevertheless, the scope of QMRI in cardiometabolic disease has not been fully investigated. This is attributed primarily to two factors. Firstly, the standardization of the existing clinical single-parametric mapping techniques has been suboptimal and current guidelines suggest the generation of site-specific normal ranges. Validation and subsequent standardization of the new methods has not been performed either and is a crucial step to enhance clinical uptake. Furthermore, the reproducibility and robustness of the proposed methods needs to be ensured in multi-center and multi-vendor studies. The design of prospective, longitudinal studies tailored to the relevant clinical questions, incorporating the novel technologies available, is also mandatory to expedite clinical adoption (159). Efforts toward reproducibility and standardization can often be accelerated through an overarching international organization that many parties trust, such as the Quantitative Image Biomarker Alliance of the Radiological Society of North America and the Quantitative MR Study of the International Society for Magnetic Resonance in Medicine (ISMRM).

Additionally, advanced acquisition schemes often come at the cost of lengthy acquisition and post-processing times. Further applications of multi-parametric QMRI that incorporate deep-learning based approaches demonstrate promising results at no extra time-cost either at acquisition or image processing level and would augment the diagnostic information (160–162). This could also allow the exploration of additional contrast weightings, including for example tissue diffusion. Furthermore, in view of the multi-organ manifestations of cardiometabolic disease, studies investigating simultaneously the liver and cardiac tissue are anticipated, to gain insight into the pathophysiology of cardiac-liver axis (140).

5. Limitations

Ongoing research in cardiometabolic disease has discovered novel mechanistic pathways across various organ systems, including cardiac and skeletal muscle, pancreas, liver, adipose tissue and microcirculation. An elaborate review on inter-organ pathogenetic

interrogation and multimodality imaging perspective is out of scope of this article and has been covered elsewhere (4). Additional MRI techniques that have been applied in cardiometabolic disease include magnetic resonance elastography and magnetic resonance spectroscopy. Magnetic resonance elastography has been primarily utilized for the evaluation of liver stiffness. It relies on the demonstration of propagating shear waves within the liver employing a phase-contrast type sequence (163). Magnetic Resonance spectroscopy investigates cardiac and hepatic metabolism *in vivo* by measuring proton signals as a function of their resonance frequency. By using the gyromagnetic properties of ^{1}H, ^{31}P, ^{13}C, and ^{23}Na, Magnetic Resonance Spectroscopy relates energy metabolism to (dys)function of the heart (164, 165). This article, which focuses on relaxation and proton-density fat fraction mapping techniques, cannot elaborate on the aforementioned methods due to space constraints. The reader is directed to (163–165) for deeper insights into the physics and applications of the respective methodology.

6. Conclusion

Cardiometabolic disease is a cluster of complex diseases that involve changes in the physiology of myocardial and hepatic tissue. Quantitative MR imaging is a valuable tool to characterize this disease, although a single quantitative parameter may not provide sufficient information. Simultaneous multiparametric MRI has demonstrated the feasibility of obtaining fast, co-registered multiple parametric maps within a single short MR scan and is promising for comprehensive understanding of the disease. QMRI frameworks are currently at a transition point between development and clinical adoption. Inclusion of standardization agreements, quality control protocols, and reproducibility assessment are essential for the clinical validation and uptake of these new promising techniques to gain further insight into cardiometabolic disease.

Author contributions

AF, CV, and CP devised and wrote the manuscript. CP and RB reviewed the manuscript. All authors contributed to the article and approved the submitted version.

Acknowledgments

The authors acknowledge financial support from the BHF PG/18/59/33955 and RG/20/1/34802, EPSRC EP/P001009, EP/P032311/1, EP/P007619/1, and EP/V044087/1, Wellcome EPSRC Centre for Medical Engineering (NS/A000049/1), ICN2021_004, Fondecyt 1210637, Fondecyt 1210638, ANID Basal FB210024, and Millennium Nucleus NCN19_161.

Conflict of interest

The authors declare that the research was conducted in the absence of any commercial or financial relationships that could be construed as a potential conflict of interest.

Publisher's note

References

1. Messroghli D, Moon J, Ferreira V, Grosse-Wortmann L, He T, Kellman P, et al. Clinical recommendations for cardiovascular magnetic resonance mapping of T1, T2, T2* and extracellular volume: a consensus statement by the society for cardiovascular magnetic resonance (SCMR) endorsed by the European association for cardiovascular imaging (EACVI). *J Cardiovasc Magn Reson.* (2017) 19:75.

2. Thomaides-Brears H, Lepe R, Banerjee R, Duncker C. Multiparametric MR mapping in clinical decision-making for diffuse liver disease. *Abdom Radiol.* (2020) 45:3507–22. doi: 10.1007/s00261-020-02684-3

3. Ferreira V, Schulz-Menger J, Holmvang G, Kramer C, Carbone I, Sechtem U, et al. Cardiovascular magnetic resonance in nonischemic myocardial inflammation: expert recommendations. *J Am Coll Cardiol.* (2018) 72:3158–76. doi: 10.1016/j.jacc.2018.09.072

4. Dorbala S, Ando Y, Bokhari S, Dispenzieri A, Falk R, Ferrari V, et al. ASNC/AHA/ASE/EANM/HFSA/ISA/SCMR/SNMMI expert consensus recommendations for multimodality imaging in cardiac amyloidosis: part 1 of 2—evidence base and standardized methods of imaging. *Circ Cardiovasc Imaging.* (2021) 14:e000029.

5. Deva D, Hanneman K, Li Q, Ng M, Wasim S, Morel C, et al. Cardiovascular magnetic resonance demonstration of the spectrum of morphological phenotypes and patterns of myocardial scarring in Anderson-Fabry disease. *J Cardiovasc Magn Reson.* (2016) 18:14. doi: 10.1186/s12968-016-0233-6

6. Pennell D, Udelson J, Arai A, Bozkurt B, Cohen A, Galanello R, et al. Cardiovascular function and treatment in β-thalassemia major: a consensus statement from the American heart association. *Circulation.* (2013) 128:281–308. doi: 10.1161/CIR.0b013e31829b2be6

7. European Association for the Study of the Liver (EASL), European Association for the Study of Diabetes (EASD), European Association for the Study of Obesity (EASO). EASL–EASD–EASO clinical practice guidelines for the management of non-alcoholic fatty liver disease. *J Hepatol.* (2016) 64:1388–402.

8. Chalasani N, Younossi Z, Lavine J, Diehl A, Brunt E, Cusi K, et al. The diagnosis and management of non-alcoholic fatty liver disease: practice guideline by the American gastroenterological association, American association for the study of liver diseases, and American college of gastroenterology. *Gastroenterology.* (2012) 142:1592–609.

9. McCarthy C, Chang L, Vaduganathan M. Training the next generation of cardiometabolic specialists. *J Am Coll Cardiol.* (2020) 75:1233–7.

10. Mechanick J, Farkouh M, Newman J, Garvey W. Cardiometabolic-based chronic disease, adiposity and dysglycemia drivers. *J Am Coll Cardiol.* (2020) 75:525–38.

11. Hirode G, Wong R. Trends in the prevalence of metabolic syndrome in the United States, 2011–2016. *JAMA.* (2020) 323:2526–8. doi: 10.1001/jama.2020.4501

12. Kumar V, Hsueh W, Raman S. Multiorgan, multimodality imaging in cardiometabolic disease. *Circ Cardiovasc Imaging.* (2017) 10:e005447. doi: 10.1161/CIRCIMAGING.117.005447

13. James W. The epidemiology of obesity: the size of the problem. *J Intern Med.* (2008) 263:336–52.

14. Tancredi M, Rosengren A, Svensson A, Kosiborod M, Pivodic A, Gudbjörnsdottir S, et al. Excess mortality among persons with type 2 diabetes. *N Engl J Med.* (2015) 373:1720–32.

15. Cavender M, Steg P, Smith S, Eagle K, Ohman E, Goto S, et al. Impact of diabetes mellitus on hospitalization for heart failure, cardiovascular events, and death: outcomes at 4 years from the reduction of atherothrombosis for continued health (REACH) registry. *Circulation.* (2015) 132:923–31. doi: 10.1161/CIRCULATIONAHA.114.014796

16. Boudina S, Abel ED. Diabetic cardiomyopathy revisited. *Circulation.* (2007) 115:3213–23.

17. Heydari B, Juan Y, Liu H, Abbasi S, Shah R, Blankstein R, et al. Stress perfusion cardiac magnetic resonance imaging effectively risk stratifies diabetic patients with suspected myocardial ischemia. *Circ Cardiovasc Imaging.* (2016) 9:e004136. doi: 10.1161/CIRCIMAGING.115.004136

18. Fisher B, Gillen G, Lindop G, Dargie H, Frier B. Cardiac function and coronary arteriography in asymptomatic type 1 (insulin-dependent) diabetic patients: evidence for a specific diabetic heart disease. *Diabetologia.* (1986) 29:706–12. doi: 10.1007/BF00870280

19. Rubler S, Dlugash J, Yuceoglu Y, Kumral T, Branwood A, Grishman A. New type of cardiomyopathy associated with diabetic glomerulosclerosis. *Am J Cardiol.* (1972) 30:595–602.

20. Levelt E, Mahmod M, Piechnik S, Ariga R, Francis J, Rodgers C, et al. Relationship between left ventricular structural and metabolic remodeling in type 2 diabetes. *Diabetes.* (2016) 65:44–52.

21. Lorenzo-Almorós A, Tuñón J, Orejas M, Cortés M, Egido J. Lorenzo Ó. Diagnostic approaches for diabetic cardiomyopathy. *Cardiovasc Diabetol.* (2017) 16:28.

22. Zeng M, Zhang N, He Y, Wen Z, Wang Z, Zhao Y, et al. Histological validation of cardiac magnetic resonance T1 mapping for detecting diffuse myocardial fibrosis in diabetic rabbits. *J Magn Reson Imaging.* (2016) 44:1179–85. doi: 10.1002/jmri.25268

23. Konduracka E, Gackowski A, Rostoff P, Galicka-Latala D, Frasik W, Piwowarska W. Diabetes-specific cardiomyopathy in type 1 diabetes mellitus: no evidence for its occurrence in the era of intensive insulin therapy. *Eur Heart J.* (2007) 28:2465–71. doi: 10.1093/eurheartj/ehm361

24. Li K, Zhai M, Jiang L, Song F, Zhang B, Li J, et al. Tetrahydrocurcumin ameliorates diabetic cardiomyopathy by attenuating high glucose-induced oxidative stress and fibrosis via activating the SIRT1 pathway. *Oxid Med Cell Longev.* (2019) 2019:6746907. doi: 10.1155/2019/6746907

25. Heerebeek LV, Hamdani N, Handoko ML, Falcao-Pires I, Musters RJ, Kupreishvili K, et al. Diastolic stiffness of the failing diabetic heart. *Circulation.* (2008) 117:43–51.

26. Jellis C, Wright J, Kennedy D, Sacre J, Jenkins C, Haluska B, et al. Association of imaging markers of myocardial fibrosis with metabolic and functional disturbances in early diabetic cardiomyopathy. *Circ Cardiovasc Imaging.* (2011) 4:693–702. doi: 10.1161/CIRCIMAGING.111.963587

27. Rijzewijk L, van der Meer RW, Smit JW, Diamant M, Bax JJ, Hammer S, et al. Myocardial steatosis is an independent predictor of diastolic dysfunction in type 2 diabetes mellitus. *J Am Coll Cardiol.* (2008) 52:1793–9.

28. Taegtmeyer H, McNulty P, Young M. Adaptation and maladaptation of the heart in diabetes: part I. *Circulation.* (2002) 105:1727–33.

29. Anderson E, Rodriguez E, Anderson C, Thayne K, Chitwood W, Kypson A. Increased propensity for cell death in diabetic human heart is mediated by mitochondrial-dependent pathways. *Am J Physiol Heart Circ Physiol.* (2011) 300:H118–24. doi: 10.1152/ajpheart.00932.2010

30. Ng A, Auger D, Delgado V, van Elderen S, Bertini M, Siebelink H, et al. Association between diffuse myocardial fibrosis by cardiac magnetic resonance contrast-enhanced T(1) mapping and subclinical myocardial dysfunction in diabetic patients: a pilot study. *Circ Cardiovasc Imaging.* (2012) 5:51–9. doi: 10.1161/CIRCIMAGING.111.965608

31. Jia G, Hill M, Sowers J. Diabetic cardiomyopathy. *Circ Res.* (2018) 122:624–38.

32. Lawes C, Vander Hoorn S, Rodgers A. Global burden of blood-pressure-related disease, 2001. *Lancet.* (2008) 371:1513–8. doi: 10.1016/S0140-6736(08)60655-8

33. Zhou D, Xi B, Zhao M, Wang L, Veeranki S. Uncontrolled hypertension increases risk of all-cause and cardiovascular disease mortality in US adults: the NHANES III linked mortality study. *Sci Rep.* (2018) 8:9418. doi: 10.1038/s41598-018-27377-2

34. Díez J, González A, López B, Querejeta R. Mechanisms of disease: pathologic structural remodeling is more than adaptive hypertrophy in hypertensive heart disease. *Nat Clin Pract Cardiovasc Med.* (2005) 2:209–16. doi: 10.1038/ncpcardio0158

35. Coelho-Filho O, Mongeon F, Mitchell R, Moreno H Jr, Nadruz W Jr, Kwong R, et al. Role of transcytolemmal water-exchange in magnetic resonance measurements of diffuse myocardial fibrosis in hypertensive heart disease. *Circ Cardiovasc Imaging.* (2013) 6:134–41. doi: 10.1161/CIRCIMAGING.112.979815

36. Maceira A, Mohiaddin R. Cardiovascular magnetic resonance in systemic hypertension. *J Cardiovasc Magn Reson.* (2012) 14:28.

37. Berk B, Fujiwara K, Lehoux S. ECM remodeling in hypertensive heart disease. *J Clin Invest.* (2007) 117:568–75.

38. Kuruvilla S, Janardhanan R, Antkowiak P, Keeley E, Adenaw N, Brooks J, et al. Increased extracellular volume and altered mechanics are associated with LVH in hypertensive heart disease, not hypertension alone. *JACC Cardiovasc Imaging.* (2015) 8:172–80.

39. McLenachan J, Dargie H. Ventricular arrhythmias in hypertensive left ventricular hypertrophy. Relationship to coronary artery disease, left ventricular dysfunction, and myocardial fibrosis. *Am J Hypertens.* (1990) 3:735–40. doi: 10.1093/ajh/3.10.735

40. Díez J, Querejeta R, López B, González A, Larman M, Martínez Ubago J. Losartan-dependent regression of myocardial fibrosis is associated with reduction of left ventricular chamber stiffness in hypertensive patients. *Circulation.* (2002) 105:2512–7. doi: 10.1161/01.cir.0000017264.66561.3d

41. Saam T, Ferguson M, Yarnykh V, Takaya N, Xu D, Polissar N, et al. Quantitative evaluation of carotid plaque composition by in vivo MRI. *Arterioscler Thromb Vasc Biol.* (2005) 25:234–9.

42. Pant S, Deshmukh A, Gurumurthy G, Pothineni N, Watts T, Romeo F, et al. Inflammation and atherosclerosis–revisited. *J Cardiovasc Pharmacol Ther.* (2014) 19:170–8. doi: 10.1177/1074248413504994

43. Paoletti R, Gotto A, Hajjar D. Inflammation in atherosclerosis and implications for therapy. *Circulation.* (2004) 109(Suppl. 1):III20–6.

44. Ertl G, Frantz S. Healing after myocardial infarction. *Cardiovasc Res.* (2005) 66:22–32.

45. Lücke C, Schindler K, Lehmkuhl L, Grothoff M, Eitel I, Schuler G, et al. Prevalence and functional impact of lipomatous metaplasia in scar tissue following myocardial infarction evaluated by MRI. *Eur Radiol.* (2010) 20:2074–83. doi: 10.1007/s00330-010-1791-x

46. Volders P, Willems I, Cleutjens J, Aren J, Havenith M, Daemen M. Interstitial collagen is increased in the non-infarcted human myocardium after myocardial infarction. *J Mol Cell Cardiol.* (1993) 25:1317–23. doi: 10.1006/jmcc.1993.1144

47. Orlandi A, Francesconi A, Marcellini M, Ferlosio A, Spagnoli L. Role of ageing and coronary atherosclerosis in the development of cardiac fibrosis in the rabbit. *Cardiovasc Res.* (2004) 64:544–52. doi: 10.1016/j.cardiores.2004.07.024

48. Silver M, Pick R, Brilla C, Jalil J, Janicki J, Weber K. Reactive and reparative fibrillar collagen remodelling in the hypertrophied rat left ventricle: two experimental models of myocardial fibrosis. *Cardiovasc Res.* (1990) 24:741–7. doi: 10.1093/cvr/24.9.741

49. Ehara S, Ueda M, Naruko T, Haze K, Itoh A, Otsuka M, et al. Elevated levels of oxidized low density lipoprotein show a positive relationship with the severity of acute coronary syndromes. *Circulation.* (2001) 103:1955–60.

50. Estes C, Razavi H, Loomba R, Younossi Z, Sanyal A. Modeling the epidemic of nonalcoholic fatty liver disease demonstrates an exponential increase in burden of disease. *Hepatology.* (2018) 67:123–33. doi: 10.1002/hep.29466

51. Ekstedt M, Franzén L, Mathiesen U, Thorelius L, Holmqvist M, Bodemar G, et al. Long-term follow-up of patients with NAFLD and elevated liver enzymes. *Hepatology.* (2006) 44:865–73.

52. Rafiq N, Bai C, Fang Y, Srishord M, McCullough A, Gramlich T, et al. Long-term follow-up of patients with nonalcoholic fatty liver. *Clin Gastroenterol Hepatol.* (2009) 7:234–8.

53. Söderberg C, Stål P, Askling J, Glaumann H, Lindberg G, Marmur J, et al. Decreased survival of subjects with elevated liver function tests during a 28-year follow-up. *Hepatology.* (2010) 51:595–602. doi: 10.1002/hep.23314

54. Kim D, Kim W, Kim H, Therneau T. Association between noninvasive fibrosis markers and mortality among adults with nonalcoholic fatty liver disease in the United States. *Hepatology.* (2013) 57:1357–65. doi: 10.1002/hep.26156

55. Balaban R, Peters D. Basic principles of cardiovascular magnetic resonance. 3rd ed. In: Manning W, Pennell D editors. *Cardiovascular magnetic resonance*. Philadelphia, PA: Elsevier (2019). p. 1–14.

56. Manning W, Pennell D. *Cardiovascular magnetic resonance*. Amsterdam: Elsevier (2010).

57. Chow K, Flewitt J, Green J, Pagano J, Friedrich M, Thompson R. Saturation recovery single-shot acquisition (SASHA) for myocardial T(1) mapping. *Magn Reson Med.* (2014) 71:2082–95. doi: 10.1002/mrm.24878

58. Diao K, Yang Z, Xu H, Liu X, Zhang Q, Shi K, et al. Histologic validation of myocardial fibrosis measured by T1 mapping: a systematic review and meta-analysis. *J Cardiovasc Magn Reson.* (2016) 18:92–92. doi: 10.1186/s12968-016-0313-7

59. Cao Y, Zeng W, Cui Y, Kong X, Wang M, Yu J, et al. Increased myocardial extracellular volume assessed by cardiovascular magnetic resonance T1 mapping and its determinants in type 2 diabetes mellitus patients with normal myocardial systolic strain. *Cardiovasc Diabetol.* (2018) 17:7. doi: 10.1186/s12933-017-0651-2

60. Lam B, Stromp T, Hui Z, Vandsburger M. Myocardial native-T1 times are elevated as a function of hypertrophy, HbA1c, and heart rate in diabetic adults without diffuse fibrosis. *Magn Reson Imaging.* (2019) 61:83–9. doi: 10.1016/j.mri.2019.05.029

61. Swoboda P, McDiarmid A, Erhayiem B, Ripley D, Dobson L, Garg P, et al. Diabetes mellitus, microalbuminuria, and subclinical cardiac disease: identification and monitoring of individuals at risk of heart failure. *J Am Heart Assoc.* (2017) 6:e005539. doi: 10.1161/JAHA.117.005539

62. Kucukseymen S, Neisius U, Rodriguez J, Tsao C, Nezafat R. Negative synergism of diabetes mellitus and obesity in patients with heart failure with preserved ejection fraction: a cardiovascular magnetic resonance study. *Int J Cardiovasc Imaging.* (2020) 36:2027–38. doi: 10.1007/s10554-020-01915-4

63. Shang Y, Zhang X, Leng W, Chen L, Lei X, Zhang T, et al. Assessment of diabetic cardiomyopathy by cardiovascular magnetic resonance T1 mapping: correlation with left-ventricular diastolic dysfunction and diabetic duration. *J Diabetes Res.* (2017) 2017:9584278. doi: 10.1155/2017/9584278

64. Salvador D, Gamba M, Gonzalez-Jaramillo N, Gonzalez-Jaramillo V, Raguindin P, Minder B, et al. Diabetes and myocardial fibrosis: a systematic review and meta-analysis. *JACC Cardiovasc Imaging.* (2022) 15:796–808.

65. Arcari L, Hinojar R, Engel J, Freiwald T, Platschek S, Zainal H, et al. Native T1 and T2 provide distinctive signatures in hypertrophic cardiac conditions—comparison of uremic, hypertensive and hypertrophic cardiomyopathy. *Int J Cardiol.* (2020) 306:102–8. doi: 10.1016/j.ijcard.2020.03.002

66. Rodrigues J, Amadu A, Dastidar A, Szantho G, Lyen S, Godsave C, et al. Comprehensive characterisation of hypertensive heart disease left ventricular phenotypes. *Heart.* (2016) 102:1671–9.

67. Treibel T, Zemrak F, Sado D, Banypersad S, White S, Maestrini V, et al. Extracellular volume quantification in isolated hypertension - changes at the detectable limits? *J Cardiovasc Magn Reson.* (2015) 17:74. doi: 10.1186/s12968-015-0176-3

68. van den Boomen M, Slart R, Hulleman E, Dierckx R, Velthuis B, van der Harst P, et al. Native T1 reference values for nonischemic cardiomyopathies and populations with increased cardiovascular risk: a systematic review and meta-analysis. *J Magn Reson Imaging.* (2018) 47:891–912. doi: 10.1002/jmri.25885

69. Erden A, Kuru OZD, Peker E, Kul M, Ozalp Ates FS, Erden I, et al. MRI quantification techniques in fatty liver: the diagnostic performance of hepatic T1, T2, and stiffness measurements in relation to the proton density fat fraction. *Diagn Interv Radiol.* (2021) 27:7–14. doi: 10.5152/dir.2020.19654

70. Brittain J, Hu B, Wright G, Meyer C, Macovski A, Nishimura D. Coronary angiography with magnetization-prepared T2 contrast. *Magn Reson Med.* (1995) 33:689–96.

71. Greulich S, Mayr A, Kitterer D, Latus J, Henes J, Steubing H, et al. T1 and T2 mapping for evaluation of myocardial involvement in patients with ANCA-associated vasculitides. *J Cardiovasc Magn Reson.* (2017) 19:6. doi: 10.1186/s12968-016-0315-5

72. Mayr A, Kitterer D, Latus J, Steubing H, Henes J, Vecchio F, et al. Evaluation of myocardial involvement in patients with connective tissue disorders: a multi-parametric cardiovascular magnetic resonance study. *J Cardiovasc Magn Reson.* (2016) 18:67. doi: 10.1186/s12968-016-0288-4

73. Puntmann V, D'Cruz D, Smith Z, Pastor A, Choong P, Voigt T, et al. Native myocardial T1 mapping by cardiovascular magnetic resonance imaging in subclinical cardiomyopathy in patients with systemic lupus erythematosus. *Circ Cardiovasc Imaging.* (2013) 6:295–301.

74. Puntmann V, Isted A, Hinojar R, Foote L, Carr-White G, Nagel E. T1 and T2 mapping in recognition of early cardiac involvement in systemic sarcoidosis. *Radiology.* (2017) 285:63–72.

75. Guo Q, Wu L, Wang Z, Shen J, Su X, Wang C, et al. Early detection of silent myocardial impairment in drug-naive patients with new-onset systemic lupus erythematosus: a three-center prospective study. *Arthritis Rheumatol.* (2018) 70:2014–24. doi: 10.1002/art.40671

76. Zhang Y, Corona-Villalobos C, Kiani A, Eng J, Kamel I, Zimmerman S, et al. Myocardial T2 mapping by cardiovascular magnetic resonance reveals subclinical myocardial inflammation in patients with systemic lupus erythematosus. *Int J Cardiovasc Imaging.* (2015) 31:389–97.

77. Giri S, Chung Y, Merchant A, Mihai G, Rajagopalan S, Raman S, et al. T2 quantification for improved detection of myocardial edema. *J Cardiovasc Magn Reson.* (2009) 11:56.

78. Jiang L, Wang J, Liu X, Li Z, Xia C, Xie L, et al. The combined effects of cardiac geometry, microcirculation, and tissue characteristics on cardiac systolic and diastolic function in subclinical diabetes mellitus-related cardiomyopathy. *Int J Cardiol.* (2020) 320:112–8. doi: 10.1016/j.ijcard.2020.07.013

79. Idilman I, Celik A, Savas B, Idilman R, Karcaaltincaba M. The feasibility of T2 mapping in the assessment of hepatic steatosis, inflammation, and fibrosis in patients with non-alcoholic fatty liver disease: a preliminary study. *Clin Radiol.* (2021) 76:709.e13–8. doi: 10.1016/j.crad.2021.06.014

80. Kirk P, Roughton M, Porter J, Walker J, Tanner M, Patel J, et al. Cardiac T2* magnetic resonance for prediction of cardiac complications in thalassemia major. *Circulation.* (2009) 120:1961–8.

81. Wood J, Enriquez C, Ghugre N, Tyzka J, Carson S, Nelson M, et al. MRI R2 and R2* mapping accurately estimates hepatic iron concentration in transfusion-dependent thalassemia and sickle cell disease patients. *Blood.* (2005) 106:1460–5. doi: 10.1182/blood-2004-10-3982

82. Pilling L, Tamosauskaite J, Jones G, Wood A, Jones L, Kuo C, et al. Common conditions associated with hereditary haemochromatosis genetic variants: cohort study in UK biobank. *BMJ.* (2019) 364:L6157.

83. Middleton M, Heba E, Hooker C, Bashir M, Fowler K, Sandrasegaran K, et al. Agreement between magnetic resonance imaging proton density fat fraction measurements and pathologist-assigned steatosis grades of liver biopsies from adults with nonalcoholic steatohepatitis. *Gastroenterology.* (2017) 153:753–61. doi: 10.1053/j.gastro.2017.06.005

84. Nelson J, Wilson L, Brunt E, Yeh M, Kleiner D, Unalp-Arida A, et al. Relationship between the pattern of hepatic iron deposition and histological severity in nonalcoholic fatty liver disease. *Hepatology.* (2011) 53:448–57. doi: 10.1002/hep.24038

85. Moon J, Messroghli D, Kellman P, Piechnik S, Robson M, Ugander M, et al. Myocardial T1 mapping and extracellular volume quantification: a society for cardiovascular magnetic resonance (SCMR) and CMR working group of the European society of cardiology consensus statement. *J Cardiovasc Magn Reson.* (2013) 15:92. doi: 10.1186/1532-429X-15-92

86. Flett A, Hayward M, Ashworth M, Hansen M, Taylor A, Elliott P, et al. Equilibrium contrast cardiovascular magnetic resonance for the measurement of diffuse myocardial fibrosis. *Circulation.* (2010) 122:138–44.

87. Wong T, Piehler K, Kang I, Kadakkal A, Kellman P, Schwartzman D, et al. Myocardial extracellular volume fraction quantified by cardiovascular magnetic resonance is increased in diabetes and associated with mortality and incident heart failure admission. *Eur Heart J.* (2014) 35:657–64. doi: 10.1093/eurheartj/eht193

88. Khan M, Yang E, Nguyen D, Nabi F, Hinojosa J, Jabel M, et al. Examining the relationship and prognostic implication of diabetic status and extracellular matrix expansion by cardiac magnetic resonance. *Circ Cardiovasc Imaging.* (2020) 13:e011000. doi: 10.1161/CIRCIMAGING.120.011000

89. Shah R, Abbasi S, Neilan T, Hulten E, Coelho-Filho O, Hoppin A, et al. Myocardial tissue remodeling in adolescent obesity. *J Am Heart Assoc.* (2013) 2:e000279.

90. Chirinos J, Bhattacharya P, Kumar A, Proto E, Konda P, Segers P, et al. Impact of diabetes mellitus on ventricular structure, arterial stiffness, and pulsatile hemodynamics in heart failure with preserved ejection fraction. *J Am Heart Assoc.* (2019) 8:e011457. doi: 10.1161/JAHA.118.011457

91. Gulsin G, Kanagala P, Chan D, Cheng A, Athithan L, Graham-Brown M, et al. Differential left ventricular and left atrial remodelling in heart failure with preserved ejection fraction patients with and without diabetes. *Ther Adv Endocrinol Metab.* (2019) 10:2042018819861593.

92. Laohabut I, Songsangjinda T, Kaolawanich Y, Yindeengam A, Krittayaphong R. Myocardial extracellular volume fraction and T1 mapping by cardiac magnetic resonance compared between patients with and without type 2 diabetes, and the effect of ECV and T2D on cardiovascular outcomes. *Front Cardiovasc Med.* (2021) 8:771363. doi: 10.3389/fcvm.2021.771363

93. Bojer A, Sørensen M, Vejlstrup N, Goetze J, Gæde P, Madsen P. Distinct non-ischemic myocardial late gadolinium enhancement lesions in patients with type 2 diabetes. *Cardiovasc Diabetol.* (2020) 19:184. doi: 10.1186/s12933-020-01160-y

94. Vasanji Z, Sigal R, Eves N, Isaac D, Friedrich M, Chow K, et al. Increased left ventricular extracellular volume and enhanced twist function in type 1 diabetic individuals. *J Appl Physiol.* (2017) 123:394–401. doi: 10.1152/japplphysiol.00012.2017

95. Ambale-Venkatesh B, Liu C, Liu Y, Donekal S, Ohyama Y, Sharma R, et al. Association of myocardial fibrosis and cardiovascular events: the multi-ethnic study of atherosclerosis. *Eur Heart J Cardiovasc Imaging.* (2019) 20:168–76.

96. Muthupillai R, Flamm S, Wilson J, Pettigrew R, Dixon W. Acute myocardial infarction: tissue characterization with T1ρ-weighted MR imaging—initial experience. *Radiology.* (2004) 232:606–10. doi: 10.1148/radiol.2322030334

97. Musthafa H, Dragneva G, Lottonen L, Merentie M, Petrov L, Heikura T, et al. Longitudinal rotating frame relaxation time measurements in infarcted mouse myocardium in vivo. *Magn Reson Med.* (2013) 69:1389–95.

98. Han Y, Liimatainen T, Gorman R, Witschey W. Assessing myocardial disease using T(1ρ) MRI. *Curr Cardiovasc Imaging Rep.* (2014) 7:9248.

99. Bustin A, Toupin S, Sridi S, Yerly J, Bernus O, Labrousse L, et al. Endogenous assessment of myocardial injury with single-shot model-based non-rigid motion-corrected T1 rho mapping. *J Cardiovasc Magn Reson.* (2021) 23:119. doi: 10.1186/s12968-021-00781-w

100. Permutt Z, Le T, Peterson M, Seki E, Brenner D, Sirlin C, et al. Correlation between liver histology and novel magnetic resonance imaging in adult patients with non-alcoholic fatty liver disease–MRI accurately quantifies hepatic steatosis in NAFLD. *Aliment Pharmacol Ther.* (2012) 36:22–9. doi: 10.1111/j.1365-2036.2012.05121.x

101. Bannas P, Kramer H, Hernando D, Agni R, Cunningham A, Mandal R, et al. Quantitative magnetic resonance imaging of hepatic steatosis: validation in ex vivo human livers. *Hepatology.* (2015) 62:1444–55.

102. Doycheva I, Cui J, Nguyen P, Costa E, Hooker J, Hofflich H, et al. Non-invasive screening of diabetics in primary care for NAFLD and advanced fibrosis by MRI and MRE. *Aliment Pharmacol Ther.* (2016) 43:83–95.

103. Idilman I, Keskin O, Celik A, Savas B, Elhan A, Idilman R, et al. A comparison of liver fat content as determined by magnetic resonance imaging-proton density fat fraction and MRS versus liver histology in non-alcoholic fatty liver disease. *Acta Radiol.* (2016) 57:271–8. doi: 10.1177/0284185115580488

104. Tang A, Tan J, Sun M, Hamilton G, Bydder M, Wolfson T, et al. Nonalcoholic fatty liver disease: MR imaging of liver proton density fat fraction to assess hepatic steatosis. *Radiology.* (2013) 267:422–31.

105. Allkemper T, Sagmeister F, Cicinnati V, Beckebaum S, Kooijman H, Kanthak C, et al. Evaluation of fibrotic liver disease with whole-liver T1rho MR imaging: a feasibility study at 1.5 T. *Radiology.* (2014) 271:408–15. doi: 10.1148/radiol.13130342

106. Chen W, Chen X, Yang L, Wang G, Li J, Wang S, et al. Quantitative assessment of liver function with whole-liver T1rho mapping at 3.0T. *Magn Reson Imaging.* (2018) 46:75–80. doi: 10.1016/j.mri.2017.10.009

107. Singh A, Reddy D, Haris M, Cai K, Rajender Reddy K, Hariharan H, et al. T1rho MRI of healthy and fibrotic human livers at 1.5 T. *J Transl Med.* (2015) 13:292.

108. van Oorschot J, El Aidi H, Jansen of Lorkeers SJ, Gho JM, Froeling M, Visser F, et al. Endogenous assessment of chronic myocardial infarction with T(1rho)-mapping in patients. *J Cardiovasc Magn Reson.* (2014) 16:104. doi: 10.1186/s12968-014-0104-y

109. Witschey W, Zsido G, Koomalsingh K, Kondo N, Minakawa M, Shuto T, et al. In vivo chronic myocardial infarction characterization by spin locked cardiovascular magnetic resonance. *J Cardiovasc Magn Reson.* (2012) 14:37. doi: 10.1186/1532-429X-14-37

110. Banerjee R, Pavlides M, Tunnicliffe E, Piechnik S, Sarania N, Philips R, et al. Multiparametric magnetic resonance for the non-invasive diagnosis of liver disease. *J Hepatol.* (2014) 60:69–77.

111. Hoffman D, Ayoola A, Nickel D, Han F, Chandarana H, Shanbhogue K. T1 mapping, T2 mapping and MR elastography of the liver for detection and staging of liver fibrosis. *Abdom Radiol.* (2020) 45:692–700. doi: 10.1007/s00261-019-02382-9

112. Schaapman J, Tushuizen M, Coenraad M, Lamb H. Multiparametric MRI in patients with nonalcoholic fatty liver disease. *J Magn Reson Imaging.* (2021) 53:1623–31.

113. Thompson R, Chow K, Mager D, Pagano J, Grenier J. Simultaneous proton density fat-fraction and R 2 * imaging with water-specific T1 mapping (PROFIT1): application in liver. *Magn Reson Med.* (2021) 85:223–38. doi: 10.1002/mrm.28434

114. Mamidipalli A, Hamilton G, Manning P, Hong C, Park C, Wolfson T, et al. Cross-sectional correlation between hepatic R2* and proton density fat fraction (PDFF) in children with hepatic steatosis. *J Magn Reson Imaging.* (2018) 47:418–24.

115. Bashir M, Wolfson T, Gamst A, Fowler K, Ohliger M, Shah S, et al. Hepatic R2* is more strongly associated with proton density fat fraction than histologic liver iron scores in patients with nonalcoholic fatty liver disease. *J Magn Reson Imaging.* (2019) 49:1456–66. doi: 10.1002/jmri.26312

116. Gomez P, Molina-Romero M, Buonincontri G, Menzel M, Menze B. Designing contrasts for rapid, simultaneous parameter quantification and flow visualization with quantitative transient-state imaging. *Sci Rep.* (2019) 9:8468. doi: 10.1038/s41598-019-44832-w

117. Sbrizzi A, Heide O, Cloos M, Toorn A, Hoogduin H, Luijten P, et al. Fast quantitative MRI as a nonlinear tomography problem. *Magn Reson Imaging.* (2018) 46:56–63.

118. Ma D, Gulani V, Seiberlich N, Liu K, Sunshine J, Duerk J, et al. Magnetic resonance fingerprinting. *Nature.* (2013) 495:187–92.

119. Christodoulou A, Shaw J, Nguyen C, Yang Q, Xie Y, Wang N, et al. Magnetic resonance multitasking for motion-resolved quantitative cardiovascular imaging. *Nat Biomed Eng.* (2018) 2:215–26.

120. Blume U, Lockie T, Stehning C, Sinclair S, Uribe S, Razavi R, et al. Interleaved T(1) and T(2) relaxation time mapping for cardiac applications. *J Magn Reson Imaging.* (2009) 29:480–7. doi: 10.1002/jmri.21652

121. Kvernby S, Warntjes M, Haraldsson H, Carlhall C, Engvall J, Ebbers T. Simultaneous three-dimensional myocardial T1 and T2 mapping in one breath hold with 3D-QALAS. *J Cardiovasc Magn Reson.* (2014) 16:102.

122. Akcakaya M, Weingartner S, Basha T, Roujol S, Bellm S, Nezafat R. Joint myocardial T1 and T2 mapping using a combination of saturation recovery and T2 -preparation. *Magn Reson Med.* (2016) 76:888–96. doi: 10.1002/mrm.25975

123. Guo R, Chen Z, Herzka D, Luo J, Ding H. A three-dimensional free-breathing sequence for simultaneous myocardial T1 and T2 mapping. *Magn Reson Med.* (2019) 81:1031–43.

124. Santini F, Kawel-Boehm N, Greiser A, Bremerich J, Bieri O. Simultaneous T1 and T2 quantification of the myocardium using cardiac balanced-SSFP inversion recovery with interleaved sampling acquisition (CABIRIA). *Magn Reson Med.* (2015) 74:365–71. doi: 10.1002/mrm.25402

125. Qi H, Bustin A, Cruz G, Jaubert O, Chen H, Botnar R, et al. Free-running simultaneous myocardial T1/T2 mapping and cine imaging with 3D whole-heart coverage and isotropic spatial resolution. *Magn Reson Imaging.* (2019) 63:159–69. doi: 10.1016/j.mri.2019.08.008

126. Milotta G, Bustin A, Jaubert O, Neji R, Prieto C, Botnar R. 3D whole-heart isotropic-resolution motion-compensated joint T1 /T2 mapping and water/fat imaging. *Magn Reson Med.* (2020) 84:3009–26. doi: 10.1002/mrm.28330

127. Weigel M. Extended phase graphs: dephasing, RF pulses, and echoes - pure and simple. *J Magn Reson Imaging.* (2015) 41:266–95. doi: 10.1002/jmri.24619

128. Feng L, Liu F, Soultanidis G, Liu C, Benkert T, Block K, et al. Magnetization-prepared GRASP MRI for rapid 3D T1 mapping and fat/water-separated T1 mapping. *Magn Reson Med.* (2021) 86:97–114. doi: 10.1002/mrm.28679

129. Tunnicliffe E, Banerjee R, Pavlides M, Neubauer S, Robson M. A model for hepatic fibrosis: the competing effects of cell loss and iron on shortened modified Look-Locker inversion recovery T1 (shMOLLI-T1) in the liver. *J Magn Reson Imaging.* (2017) 45:450–62. doi: 10.1002/jmri.25392

130. Pavlides M, Banerjee R, Tunnicliffe E, Kelly C, Collier J, Wang L, et al. Multiparametric magnetic resonance imaging for the assessment of non-alcoholic fatty liver disease severity. *Liver Int.* (2017) 37:1065–73.

131. Hamilton J, Jiang Y, Chen Y, Ma D, Lo W, Griswold M, et al. MR fingerprinting for rapid quantification of myocardial T1, T2, and proton spin density. *Magn Reson Med.* (2017) 77:1446–58. doi: 10.1002/mrm.26216

132. Jaubert O, Cruz G, Bustin A, Schneider T, Lavin B, Koken P, et al. Water-fat Dixon cardiac magnetic resonance fingerprinting. *Magn Reson Med.* (2020) 83:2107–23.

133. Velasco C, Cruz G, Lavin B, Hua A, Fotaki A, Botnar R, et al. Simultaneous T1, T2, and T1rho cardiac magnetic resonance fingerprinting for contrast agent-free myocardial tissue characterization. *Magn Reson Med.* (2022) 87:1992–2002. doi: 10.1002/mrm.29091

134. Lima da Cruz GJ, Velasco C, Lavin B, Jaubert O, Botnar RM, Prieto C. Myocardial T1, T2, T2*, and fat fraction quantification via low-rank motion-corrected cardiac MR fingerprinting. *Magn Reson Med.* (2022) 87:2757–74. doi: 10.1002/mrm.29171

135. Hamilton J, Pahwa S, Adedigba J, Frankel S, O'Connor G, Thomas R, et al. Simultaneous mapping of T1 and T2 using cardiac magnetic resonance fingerprinting in a cohort of healthy subjects at 1.5T. *J Magn Reson Imaging.* (2020) 52:1044–52.

136. Liu Y, Hamilton J, Rajagopalan S, Seiberlich N. Cardiac magnetic resonance fingerprinting: technical overview and initial results. *JACC Cardiovasc Imaging.* (2018) 11:1837–53.

137. Jaubert O, Cruz G, Bustin A, Hajhosseiny R, Nazir S, Schneider T, et al. T1, T2, and fat fraction cardiac MR fingerprinting: preliminary clinical evaluation. *J Magn Reson Imaging.* (2021) 53:1253–65.

138. Cavallo A, Liu Y, Patterson A, Al-Kindi S, Hamilton J, Gilkeson R, et al. CMR fingerprinting for myocardial T1, T2, and ECV quantification in patients with nonischemic cardiomyopathy. *JACC Cardiovasc Imaging.* (2019) 12:1584–5. doi: 10.1016/j.jcmg.2019.01.034

139. Eck B, Seiberlich N, Flamm S, Hamilton J, Suresh A, Kumar Y, et al. Characterization of cardiac amyloidosis using cardiac magnetic resonance fingerprinting. *Int J Cardiol.* (2022) 351:107–10. doi: 10.1016/j.ijcard.2021.12.038

140. Chen Y, Jiang Y, Pahwa S, Ma D, Lu L, Twieg M, et al. MR fingerprinting for rapid quantitative abdominal imaging. *Radiology.* (2016) 279:278–86. doi: 10.1148/radiol.2016152037

141. Jaubert O, Arrieta C, Cruz G, Bustin A, Schneider T, Georgiopoulos G, et al. Multi-parametric liver tissue characterization using MR fingerprinting: simultaneous T1, T2, T2*, and fat fraction mapping. *Magn Reson Med.* (2020) 84:2625–35. doi: 10.1002/mrm.28311

142. Fujita S, Sano K, Cruz G, Fukumura Y, Kawasaki H, Fukunaga I, et al. MR fingerprinting for liver tissue characterization: a histopathologic correlation study. *Radiology.* (2022) 306:150–9. doi: 10.1148/radiol.220736

143. Velasco C, Cruz G, Jaubert O, Lavin B, Botnar R, Prieto C. Simultaneous comprehensive liver T1, T2, T2*, T1rho, and fat fraction characterization with MR fingerprinting. *Magn Reson Med.* (2022) 87:1980–91. doi: 10.1002/mrm.29089

144. Shaw J, Yang Q, Zhou Z, Deng Z, Nguyen C, Li D, et al. Free-breathing, non-ECG, continuous myocardial T1 mapping with cardiovascular magnetic resonance multitasking. *Magn Reson Med.* (2019) 81:2450–63. doi: 10.1002/mrm.27574

145. Mao X, Lee H, Hu Z, Cao T, Han F, Ma S, et al. Simultaneous multi-slice cardiac MR multitasking for motion-resolved, Non-ECG, free-breathing T1-T2 mapping. *Front Cardiovasc Med.* (2022) 9:833257. doi: 10.3389/fcvm.2022.833257

146. Wang N, Cao T, Han F, Xie Y, Zhong X, Ma S, et al. Free-breathing multitasking multi-echo MRI for whole-liver water-specific T1, proton density fat fraction, and R2* quantification. *Magn Reson Med.* (2022) 87:120–37. doi: 10.1002/mrm.28970

147. Ogier A, Bustin A, Cochet H, Schwitter J, van Heeswijk R. The road toward reproducibility of parametric mapping of the heart: a technical review. *Front Cardiovasc Med.* (2022) 9:876475. doi: 10.3389/fcvm.2022.876475

148. Chow K, Hayes G, Flewitt J, Feuchter P, Lydell C, Howarth A, et al. Improved accuracy and precision with three-parameter simultaneous myocardial T(1) and T(2) mapping using multiparametric SASHA. *Magn Reson Med.* (2022) 87:2775–91. doi: 10.1002/mrm.29170

149. Roujol S, Weingartner S, Foppa M, Chow K, Kawaji K, Ngo L, et al. Accuracy, precision, and reproducibility of four T1 mapping sequences: a head-to-head comparison of MOLLI, ShMOLLI, SASHA, and SAPPHIRE. *Radiology.* (2014) 272:683–9. doi: 10.1148/radiol.14140296

150. Child N, Suna G, Dabir D, Yap M, Rogers T, Kathirgamanathan M, et al. Comparison of MOLLI, shMOLLLI, and SASHA in discrimination between health and disease and relationship with histologically derived collagen volume fraction. *Eur Heart J Cardiovasc Imaging.* (2018) 19:768–76. doi: 10.1093/ehjci/jex309

151. Baessler B, Schaarschmidt F, Stehning C, Schnackenburg B, Maintz D, Bunck A. A systematic evaluation of three different cardiac T2-mapping sequences at 1.5 and 3T in healthy volunteers. *Eur J Radiol.* (2015) 84:2161–70. doi: 10.1016/j.ejrad.2015.08.002

152. Deshpande V, Chung Y, Zhang Q, Shea S, Li D. Reduction of transient signal oscillations in true-FISP using a linear flip angle series magnetization preparation. *Magn Reson Med.* (2003) 49:151–7. doi: 10.1002/mrm.10337

153. Schmierer K, Scaravilli F, Altmann D, Barker G, Miller D. Magnetization transfer ratio and myelin in postmortem multiple sclerosis brain. *Ann Neurol.* (2004) 56:407–15.

154. Gonzalez Ballester M, Zisserman A, Brady M. Estimation of the partial volume effect in MRI. *Med Image Anal.* (2002) 6:389–405.

155. Ma D, Coppo S, Chen Y, McGivney D, Jiang Y, Pahwa S, et al. Slice profile and B1 corrections in 2D magnetic resonance fingerprinting. *Magn Reson Med.* (2017) 78:1781–9. doi: 10.1002/mrm.26580

156. Cruz G, Jaubert O, Schneider T, Botnar R, Prieto C. Rigid motion-corrected magnetic resonance fingerprinting. *Magn Reson Med.* (2019) 81:947–61.

157. Deshmane A, McGivney D, Ma D, Jiang Y, Badve C, Gulani V, et al. Partial volume mapping using magnetic resonance fingerprinting. *NMR Biomed.* (2019) 32:e4082.

158. Hilbert T, Xia D, Block K, Yu Z, Lattanzi R, Sodickson D, et al. Magnetization transfer in magnetic resonance fingerprinting. *Magn Reson Med.* (2020) 84:128–41.

159. Abdallah L, de Matos R, March e Souza YPD, Vieira-Soares D, Muller-Machado G, Pollo-Flores P. Non-alcoholic fatty liver disease and its links with inflammation and atherosclerosis. *Curr Atheroscler Rep.* (2020) 22:7.

160. Chen Y, Fang Z, Hung S, Chang W, Shen D, Lin W. High-resolution 3D MR fingerprinting using parallel imaging and deep learning. *Neuroimage.* (2020) 206:116329.

161. Cohen O, Zhu B, Rosen M. MR fingerprinting deep reconstruction network (DRONE). *Magn Reson Med.* (2018) 80:885–94.

162. Gomez P, Cencini M, Golbabaee M, Schulte R, Pirkl C, Horvath I, et al. Rapid three-dimensional multiparametric MRI with quantitative transient-state imaging. *Sci Rep.* (2020) 10:13769. doi: 10.1038/s41598-020-70789-2

163. Tang A, Dzyubak B, Yin M, Schlein A, Henderson W, Hooker J, et al. MR elastography in nonalcoholic fatty liver disease: inter-center and inter-analysis-method measurement reproducibility and accuracy at 3T. *Eur Radiol.* (2022) 32:2937–48. doi: 10.1007/s00330-021-08381-z

164. McGavock J, Lingvay I, Zib I, Tillery T, Salas N, Unger R, et al. Cardiac steatosis in diabetes mellitus. *Circulation.* (2007) 116:1170–5. doi10.1161/CIRCULATIONAHA.106.645614

165. Bizino M, Hammer S, Lamb H. Metabolic imaging of the human heart: clinical application of magnetic resonance spectroscopy. *Heart.* (2014) 100:881–90. doi10.1136/heartjnl-2012-302546

166. Idilman IS, Aniktar H, Idilman R, Kabacam G, Savas B, Elhan A, et al. Hepatic steatosis: quantification by proton density fat fraction with MR imaging versus liver biopsy. *Radiology.* (2013) 267:767–75. doi: 10.1148/radiol.13121360

Frontiers in
Cardiovascular Medicine

Innovations and improvements in cardiovascular treatment and practice

Focuses on research that challenges the status quo of cardiovascular care, or facilitates the translation of advances into new therapies and diagnostic tools.

Discover the latest Research Topics

See more →

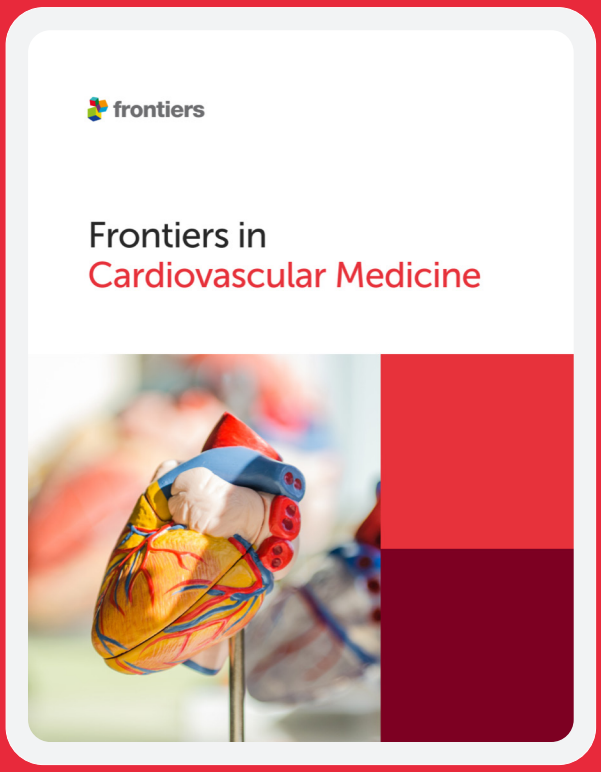

Frontiers

Avenue du Tribunal-Fédéral 34
1005 Lausanne, Switzerland
frontiersin.org

Contact us

+41 (0)21 510 17 00
frontiersin.org/about/contact